MECHANISM OF INSTABILITIES OF EXOTHERMIC

HYPERSONIC BLUNT-BODY FLOWS

by

John B. McVey

B. S., Lehigh University (1955)
M. S., Lehigh University (1956)

Submitted in Partial Fulfillment
of the Requirements for the

Degree of Doctor of Science

at the
Massachusetts Institute of Technology

June 1967

Signature of Author ....
Department of Mechanical Engineering

Certified by ....
T. Y. Toong
Thesis Supervisor

Accepted by ....
Warren M. Rohsenow
Chairman, Departmental Committee
on Graduate Students

MECHANISM OF INSTABILITIES OF EXOTHERMIC
HYPERSONIC BLUNT-BODY FLOWS

John B. McVey

Submitted to the Department of Mechanical
Engineering in June 1967 in partial fulfillment
of the requirement for the degree of Doctor of Science

ABSTRACT

An experimental and analytical investigation of the regular, periodic

instability observed in exothermic hypersonic blunt-body flows has been

conducted. A ballistic range instrumented with submicrosecond spark

schlieren photographic equipment and ionization probes has been used to

identify the distinguishing flow field characteristics about hypersonic

spheres fired into lean acetylene-oxygen mixtures and stoichiometric hy-

drogen-air mixtures. The variation of the instability wavelength with

initial gas state, body size, and body velocity has been recorded. The

boundaries of the several observed flow regimes have been established.

An instability mechanism is proposed and is shown to be consistent with

the experimental results and with the significant gas dynamic wave inter-

action processes. The instability originates in the induction zone which

separates the bow shock and the exothermic reaction front in the nose

region of the flow field. The instability arises from the effect on

the chemical reaction rate of entropy waves which are generated by the

interaction of compression waves with the bow shock wave. The compression

waves are generated by the time-varying reaction rate. This type of

instability can be expected to be present in any hypersonic combustion

process wherein strong shock waves are present.

Thesis Supervisor: T. Y. Toong

Title: Professor of Mechanical Engineering

ACKNOWLEDGMENTS

MECHANISM OF INSTABILITIES OF EXOTHERMIC

HYPERSONIC BLUNT-BODY FLOWS

TABLE OF CONTENTS

TABLE OF CONTENTS (Cont'd.)

LIST OF TABLES

LIST OF FIGURES

RESULTS, CONCLUSIONS AND RECOMMENDATIONS

1. The flow field about hypersonic spheres moving through lean acetylene-oxygen and stoichiometric hydrogen-air gas mixtures at speeds on the order of the Chapman-Jouguet speed and at sufficiently high gas pressures is unstable. At moderate pressures, the instability generates a regular, periodic wave pattern easily observed by means of schlieren photography. At higher pressures, the instability generates a turbulent schlieren pattern.

2. The regular, periodic schlieren wave pattern is produced by:

(a) a corrugation of the boundary separating the hotter reacted gas from the colder unreacted gas. The corrugations, which are frozen in the flow, generate a prominent train of vertical striations, nearly equally spaced, and appearing alternately dark and bright on the photographs.

(b) compression waves propagating in the inviscid wake and the entropy waves generated by the interaction of the compression waves with the bow shock wave. The waves produce a fish-scale like pattern in the inviscid wake between the bow shock and the corrugated reacted gas boundary.

3. The periodic instability is generated by the interactions of the reaction front and the bow shock with compression waves and contact discontinuities propagating within the induction zone in the nose region

1

of the flow field. The instability arises from the sensitivity of the induction time to penturbations in the state of the shocked gas.

4. The wavelength of the instability is a strong function of the induction time of the exothermic gas mixture. It is a weak function of the sphere diameter. The instability can exist whenever strong shocks appear in exothermic gas mixtures.

5. The several distinctly different schlieren patterns created by the instability define four flow regimes: (1) Wake combustion regime; (2) Turbulent regime; (3) Stable regime; (4) Periodic regime. The boundaries of the periodic regime, within which the regular, periodic instability is observed, are strong functions of the sphere diameter and velocity and of the initial gas pressure and mixture ratio. The range of First Damkohler numbers based on induction time, sphere radius, and velocity for which the instability is observed lies between 0.1 and 1.0. The Chapman-Jouguet speed and the second explosion limit condition do not define any of the flow field regime boundaries. The theoretical and experimental results suggest that the characteristics of the temperature rise marking the end of the induction period is a factor in determining the boundaries.

6. It is recommended that the conditions required for the existence of the regular periodic instability be investigated by an experimental and analytical program. Experiments should be conducted with exothermic gas mixtures which have an induction zone behavior significantly different

2

from that of the hydrogen-oxygen and hydrocarbon-oxygen reaction; a carbon monoxide-oxygen system is an example. Analytical calculations of the variation of the temperature rise at the end of the induction period with initial gas state should be carried out to determine if this quantity is responsible for the periodic regime boundaries.

7. It is recommended that the degree to which the presence of the instability increases the extent of the exothermic reaction in the flow field about the sphere be investigated. Since the instability is probably nondestructive, the instability, particularly the turbulent mode, can possibly be used to promote the combustion process in hypersonic air-breathing engine combustors.

INTRODUCTION

The characteristics of the combustion process in gaseous systems wherein the reaction front propagates with a supersonic rate with respect to the unburned gas is of interest to at least two fields of study: (1) detonation wave research, the objective of which is to determine the mechanisms responsible for the development, structure and stability of detonation waves; (2) supersonic combustion research, the object of which is to develop a hypersonic air breathing engine in which supersonic flow is maintained at all points within the device.

Research on detonation waves has been carried out for over forty years yet the processes which govern the characteristics of such waves are not fully understood. A survey of the state of detonation wave research which contains an extensive bibliography is found in Ref. 1. In recent years it has become apparent that self sustained detonation waves are intrinsically unstable and that if sufficiently refined instrumentation is employed, the wave will be found to be three-dimensional and time dependent. Such a state of affairs has long been recognized for waves propagating in mixtures near the detonability limits. Under these conditions the scale of the instability is large and easily observed; "spinning" detonation waves are examples. At conditions removed from the detonability limits, the instability scale becomes extremely small. Some experimental evidence indicates the instability retains a regular,

periodic behavior; this has been termed multi-headed spin. Other evidence suggests the gas flow behind the wave front is randomly turbulent. The experimental difficulties involved in examining the structure of such waves, coupled with their apparent structural complexity, has made extremely difficult the identification of the mechanism responsible for the instabilities.

Research and development of supersonic combustion ramjet engines has only recently grown to a significant scale. Ideally, the goal of this program is to develop an engine in which the flow remains at a high supersonic Mach number throughout. The cycle efficiency of such a design can be shown to be higher than for a conventional design and other advantages accrue, such as reduced structural cooling loads. If it were possible to inject, mix and burn the fuel while the through-flow maintains a high velocity, then the static conditions which govern the chemical reaction rates would not be radically different from those found in present designs. However, either by design or unavoidable circumstances, strong shocks will most likely exist in local regions of the flow. In these regions conditions will be generated similar to those found in detonation waves. Thus the nature of the instabilities associated with such conditions will be of interest to the designers of these devices. Furthermore, it may prove that by controlled use of unsteady chemical kinetic-gas dynamic interactions, the overall reaction rate in supersonic combustors can be promoted.

Recently, two groups conducted experiments in which conditions similar to those found in detonation waves were generated by firing projectiles into quiescent detonable gases. Ruegg and Dorsey (Ref. 2) fired spheres into hydrogen-air mixtures and observed the flow field by means of schlieren photography. Later they reported briefly on results obtained with methane-air and pentane-air mixtures (Ref. 3). Struth, Behrens, and Wecken (Ref. 5) performed similar experiments and included work with gases which underwent endothermic reactions (carbon tetrachloride and benzene)(Ref. 5). Later they performed experiments with conical projectiles (Ref. 6). The experiments indicated that under a wide range of conditions the flow field, as in the case of self sustained detonations, is highly unstable. In the case of the spherical projectiles and exothermic gas mixtures, under certain conditions, the instability generates a highly regular, periodic flow field structure which is easily observed (e.g.,Fig. 1). The fact that the flow field structure is easily resolved and is so highly regular as opposed to the very small scale, complex structure of self sustained detonation waves suggests that the ballistic range can be used with advantage to study the mechanisms of the instabilities observed in exothermic hypersonic flows. A program of this type is reported herein.

The previous investigators have reported evidence that the length of the induction zone behind the normal segment of the bow shock is the

characteristic length which determines the wavelength of the observed

regular instability. They suggest that under some conditions an

acoustic instability exists and that under other conditions periodic

ignition occurs. (The conclusions drawn by these authors are discussed

in detail in the section entitled, "Instability Mechanism.") The

fundamental difference between the two types of theories is that the

role of chemical kinetics does not enter into the evaluation of the

frequency behavior of the acoustic (or hydrodynamic) model whereas a

"periodic ignition" model implies by definition that kinetics controls

the instability period or frequency. Thus, if the instability is purely

hydrodynamic, no information concerning the instability mechanism can

be gained by a study of the frequency behavior; the frequency is de-

termined by the geometry of the system. The results of this study indi-

cate that the observed regular instability is the result of strong gas

dynamic-chemical kinetic interactions and is not of the acoustic type.

The type of behavior observed in these experiments can exist in any

exothermic hypersonic flow involving the gas mixtures of the type used

(hydrogen-air, hydrocarbon-oxygen) wherein strong shock waves are present.

In these experiments, the blunt body serves merely to generate and to

stabilize a strong shock in the gas. A sphere generates an axially

symmetric field; such flow fields are particularly well suited to study

by optical methods. As will be shown, the wavelength of the instability

is only a weak function of the sphere diameter; the characteristic

length which determines the wavelength is, as noted previously, the induction zone length.

The similarities and differences between these instabilities and those associated with the most commonly observed exothermic hypersonic flow, detonation waves, should be pointed out. The simplest and most effective method by which the detonation wave instability can be observed is the soot technique wherein a helical pattern is produced on a soot covered wall as the spinning wave propagates through a tube. Detonations exhibiting multi-headed spin produce a "fish-scale" or cellular pattern. The wavelength of the instability is characterized by the size of the cell. The first success in theoretically predicting the instability frequency was achieved by Fay (Ref. 7) and Manson (Ref. 8) who showed that the spin frequency corresponds to frequency of transverse acoustic wave in the hot product gas behind the wave front. The higher spin frequencies observed at higher pressures and for mixture conditions removed from the detonation limits correspond to the higher acoustic harmonics. The characteristic length entering the analyses is the tube diameter; neither the induction zone length nor any other parameter characteristic of the chemistry appears. The transverse vibrations are a manifestation of the instability of the detonation wave structure; however, since the theory is hydrodynamic, no information on the mechanism of the instability is gained.

Numerous mathematical analyses have been performed to determine under what conditions an exothermic plane wave is stable (see Ref. 1). The approach usually involves the determination of whether or not small disturbances existing within the structure of a detonation wave are amplified or damped; the wave structure is usually assumed to be one-dimensional and is specified by an assumed rate chemistry. Since it has now been determined experimentally that self-sustained detonations are always observed to be unstable, what is desired is an analysis which will describe the asymptotic behavior of the small disturbances as they grow to finite amplitude. Lacking this, on the basis of experimented results, various models of the three-dimensional, finite amplitude, time dependent disturbances have been proposed. Much work has been published in the Russian literature and is reviewed in the book by Shchelken and Troshin (Ref. 9). The structure proposed involves collisions of triple shock configurations which generate local regions of intense temperature and pressure leading to the presence of discrete detonations "heads" which generate the observed instability patterns. The application of this experimentally derived structure to the prediction of instability wavelengths for specified gas conditions is still in an embryonic stage. Some authors claim the model supports the connection between the observed cell size and a chemical reaction time (Ref. 10) and that the discrete structure observed is "a characteristic of the front itself and is independent of the external conditions," i.e., tube geometry (Ref. 11). The

9

relationship between this model and the spin frequencies predicted by the acoustic theory in which the tube geometry is a determining factor remains to be explained. In the study reported herein the complex geometry associated with the perturbed plane wave is avoided and the prediction of the instability wavelength which should be observed for a given proposed instability mechanism is quite straightforward.

A number of experiments with detonation waves indicate that under some conditions the flow is turbulent. White (Ref. 12) obtained such evidence with the use of an interferometer and Opel (Ref. 13) by means of schlieren photography. Recent experiments employing other techniques indicate that a regular periodicity persists on a very small scale in detonations occurring under conditions far removed from the detonability limits (Refs. 7 and 14). Thus there is a question as to whether the detonations under any conditions indeed exhibit a random turbulence or whether the optical records merely appear turbulent due to the tortuous path followed by the light rays while traversing the detonation front.

In these ballistic range experiments reported herein both turbulent and periodic flow patterns are observed and there is no question that the two cases represent a distinctly different behavior of the reaction front. The appearance of the flow field drastically changes from periodic to turbulent as the flow conditions pass through well defined boundaries.

In the following text, a description of the ballistic range and associated equipment used in the experiments is given. The characteristic

flow field features which appear in the schlieren photographs are then identified. A review of the principles involved in schlieren analysis is given in Appendix I. The experimental results concerning the factors effecting the various observed flow field regimes and data on the behavior of the instability wavelength are then presented. Finally, an instability mechanism is proposed and is discussed in light of the experimental results. Supporting gas dynamic and chemical kinetic calculations are given in Appendices II, III, IV.

SECTION I

DESCRIPTION OF EXPERIMENTAL APPARATUS

The experiments were conducted in a ballistic range instrumented

with schlieren photographic equipment and an ionization probe. An

overall view of the equipment is given in Fig. 2.

The design of the ballistic range components was based on designs

developed for use in the Re-entry Simulation Range, Lincoln Laboratory,

Massachusetts Institute of Technology. The ballistic range consists of

a specially designed .50 caliber smooth-bore gun barrel and electrically

operated breech which fires the projectile into a blast tank where the

motion of the powder gases is retarded. The projectile passes through a

sabot catcher and diaphragm, continues past a shadowgraph station into

the test section where the schlieren equipment and ionization probe are

located. The projectile then continues through an uninstrumented section

and impacts on a steel plate. The overall length of the range is

approximately 25 feet; the diameter of the test section is 6 inches.

The projectiles used are solid aluminum spheres having a Grade 200

finish. The majority of the tests were performed with 1/2 inch spheres

which did not require the use of sabots. The sabots used with the

smaller diameter spheres are 1/2 inch long nylon cylinders having a

1/2 inch diameter and are recessed at one end to accept the projectile.

The sabots are cut lengthwise to promote their break-up so they can be

easily separated from the projectile. Standard .50 caliber cartridge

cases are filled with fast burning rifle powder; both Hercules 2400 and Du Pont 4227 are used. The muzzle velocities produced in the experiments ranged from 4500 to 7500 feet per second. The maximum attainable velocity with the 1/2 aluminum spheres is probably on the order of 8000 fps. With the use of light-weight plastic projectiles, higher velocities could be attained. The velocity scatter at any given powder charge is approximately 400 fps or 6% under average conditions. This could be improved with the use of wadding to pack the powder in the cartridge cases and thereby maintain a more even burning rate. The barrel is mounted in a recoil absorbing traversing mechanism. The barrel is bore sighted on the impact plate and requires realignment only after the range is dismantled. The scatter of the projectiles on the impact plate is generally limited to a one inch diameter circle. The breech is remotely operated so that the test cell can be vacated during testing.

The blast tank was fabricated from a heavy-walled 18 inch diameter steel pipe. A single replaceable baffle plate having a 3/4 inch diameter opening is located at the mid-plane. During testing, the blast tank is pumped down to pressures of 100 mm Hg or less. If a low test section pressure is to be used, the effectiveness of the blast tank in retarding the powder gases is critical since the retarding effect of the test gas itself is small. Under these conditions, the blast tank pressure is usually raised to approximately the test section pressure. At test section

pressures, above 150 mm Hg, the blast tank is usually evacuated to less than 1 mm Hg. The effect of the blast tank pressure on muzzle velocity is small; the difference in velocities between a blast tank pressure of 100 mm Hg and 1 mm Hg is less than the muzzle velocity scatter cited above.

A second baffle located outside the blast tank and having a replaceable 5/8 inch diameter opening serves as the sabot catcher. If a saboted projectile is used, the blast tank pressure is raised to 100 mm Hg in order to promote separation of the sabot and the projectile. Separation was effected in approximately 85% of the runs involving sabots.

The test section gas is separated from the blast tank gas by a one mil mylar diaphragm. At test section pressures on the order of 50 mm Hg or less there is evidence that the debris from the ruptured diaphragm remains in the vicinity of the projectile as it passes the schlieren station which is located approximately two feet downstream of the diaphragm holder. Since most tests were performed at pressures higher than 50 mm Hg, this does not present a significant problem. In some of the photographs of runs made at higher pressures, tiny particles and the Mach waves generated by them can be observed. Whether these are particles of unburned powder or debris from the diaphragm has not been determined.

The projectile velocity is determined by measuring the time interval required for the ball to pass from the shadowgraph station to the

schlieren station. The shadowgraph station is comprised of a point

spark light source, a single focusing lens and a camera with a pin hole

aperture covered by a blue filter. The lens focuses the spark light on

the pin hole; the filter eliminates the need for a capping shutter. The

purpose of the shadowgraph is to record the location of the projectile

at the instant the timing device is triggered. A trigger signal is pro-

vided by the projectile's breaking a light beam which is monitored by a

phototube. The light beam is produced by a high intensity D. C. lamp.

The schlieren station is located 13 inches downstream of the shadow-

graph station. The distances between a reticle on the shadowgraph

station window and reticles on the schlieren mirror window were measured

by photographing a calibration bar which was positioned along the center-

line of the test section. The calibration bar contains accurately

machined reference points such that the errors introduced in the velocity

measurements due to errors in the measurement of the distance between

measuring points is negligible--less than 0.1%.

The schlieren system is a double pass system utilizing a single

6 inch diameter spherical mirror having a 48 inch radius of curvature.

The mirror is located inside the test section, three inches off the

center line. Because of the severe environment created by the detonating

gases, the mirror surface is protected by a one inch thick optical quality

glass cover whose surfaces are ground and polished to the same tolerances

as the mirror surface. After each set of runs, the glass cover is

cleaned by overnight immersion in aqua-regia. Pitting of the glass

surface due to debris churned up by the exploding gases gradually

accumulated over the duration of the program, but the quality of the

photographs was not markedly effected.

The remaining components of the schlieren system are grouped outside

of the test section at the end of a cross arm, approximately 42 inches

from the centerline of the test section. An optical arrangement which

made possible the exposing of two photographs along virtually the same

optical path is employed. The arrangement of the components is shown

in Fig. 3. Two complete schlieren systems, one along a vertical axis,

the other along the horizontal axis are shown. The light rays are de-

flected along the third axis to the schlieren mirror by a four-sided

pyramidical mirror, not visible in Fig. 3. Light enters the test section

through a one inch diameter, 1/8 inch thick commercial quality glass

window. With this system, the rays incident to the and reflected from

the schlieren mirror must travel slightly off-axis in order to strike

opposite faces of the pyramidical mirror. In such a double pass system,

a slight amount of parallax is introduced. The parallax is minimized

by having the incident and reflected bundle of rays strike the pyramid

as close to the apex as the dimensions of the bundle cross section

allows. For this reason, a lens is used to bring the incident rays to

focus on the pyramid face, and the knife-edge, where the reflected rays

form a second image of the light source, is placed as close as possible

to the opposite face of the pyramid. The latter requirement could be relaxed by the introduction of another lens such that the reflected image of the light source could be successively focused on the pyramid face and then on the knife edge, but it was felt that the gains would be offset by the deterioration of the picture quality accompanying the introduction of another lens in the reflected ray optical path. Because of the geometry of the light source (a line source rather than a point source), the parallax could be reduced if the four-sided pyramid were replaced by a two-sided mirror and a single rather than dual schlieren system used. For this reason, the dual system was used only when wave propagation rates or other time dependent effects were being studied, and the single system used when the flow field geometry was being studied.

The light source is formed by a spark discharge between two 0.020 inch tungsten electrodes embedded in a 0.020 inch groove machined in a fuzed quartz block. The electrode gap is of the order of 0.10 inches. The groove is used to stabilize the position of the spark discharge. A line source is used rather than a point source in order to achieve greater illumination; the spark illumination is critical for the f/8 schlieren mirror. A low inductance, 1/4 microfarad pulse capacitor charged to 4000 volts is connected to the tungsten electrodes by 1/4 inch diameter copper leads. The light from the line source is focused on interchangeable slits by a 1 inch focal length microscope eyepiece. The slit widths used range from 0.006 to 0.020 inches; the slit used depends on the

balance between light intensity and schlieren sensitivity desired. The

time duration of the spark as measured by the width of the voltage vs.

time output of a type 1P21 phototube was found to be approximately 0.25

μ sec. The trace width was measured at the point where the voltage rise

was e^{-1} of the maximum. This spark duration is satisfactory for the

projectile velocities encountered in these tests although it does not

provide sufficient resolution to measure the detachment distance with

confidence. The triggering signal for the schlieren spark sources is

generated either by use of a preset oscilloscope delayed trigger or by

the output of a phototube which is focused on the intersection of the

test section centerline and the schlieren system optical axis. Under

the conditions of the experiments, the self luminosity in the nose region

of the projectile is sufficient to produce a strong phototube output.

The knife-edge consists of a section of 0.010 inch shim shock

connected to a micrometer drive. The knife-edge can be oriented both

parallel to and vertical to the flow field axis and can be inserted

from either direction to produce either a bright or a dark bow shock.

For most of the runs a vertical knife-edge position, i.e., oriented

normal to the flow field axis, was used.

The schlieren systems are equipped with a high intensity lamp which

can be inserted in the optical path to replace the spark light source

for alignment and focusing purposes. The primary alignment was achieved

by adjustment of the orientation of the schlieren mirror, which is

mounted internally by means of a three-legged telescope-type installation.

Despite the use of an extremely rugged construction, the shock and deto-

nation waves generated at the higher pressures occasionally cause mis-

alignment of the mirror. Alignment is easily checked by illuminating

the spark gap and viewing the knife-edge and spark gap by eye through

the objective lens.

Achromatic telescope objective lenses were used as objective lenses

to focus the test section image. A series of lenses having focal lengths

from 20 to 34.5 inches were used to provide different magnifications.

The cameras were mounted on a track such that the film plane could be

positioned at the focal plane. Commercial 4 x 5 view cameras equipped

with Polaroid backs were used together with 3000 speed Polaroid Type 57

film. Electrically operated Packard shutters are fitted to the cameras.

The shutters are remotely opened in the darkened room test cell imme-

diately before firing.

Since the event to be photographed is highly luminous, considerable

effort was expended in developing a reliable optical and photographic

system which could produce unfogged photographs. The self-luminosity

is characterized by a delay of approximately 500 μ sec between the time

the projectile passes the schlieren station and is photographed and the

time of the appearance of significant radiation from the hot products

of reaction. The duration of the self-luminosity is of the order of

0.05 sec. Thus an electrically operated capping shutter having a closing

time of 500 μ sec was required to eliminate all fogging. Unfortunately, no convenient system is commercially available. The Beckman-Whitley capping shutter which uses detonator caps to shatter a glass block and the Jarall-Ash collapsing foil shutters were judged to be too bulky, too expensive, and too time consuming to operate. A program to develop a lead vapor capping shutter (Ref. 15) was unsuccessful since the light radiated from the vaporizing lead was itself sufficient to fog the 3000 speed Polaroid film. The system used is a mechanical system in which a taut 0.020 inch piano wire pulls a 0.010 brass shim across the optical path. The shutter is activated by discharging a high voltage capacitor through a 0.006 inch steel wire which is used to restrain the piano string. Approximately 1200 μsec were required for the shutter to block a 3/4 inch diameter aperture. This is sufficiently fast to eliminate most of the fogging for the test conditions used. The range of test conditions was restricted, however, since richer mixtures and higher pressure mixtures produced more self-luminosity.

In addition to the capping shutter, filters are used to reduce the effects of the self-luminosity. Most of the radiation from the hot gases is of a wave length of 5000 angstroms and higher. The radiation from the spark is predominantly in the blue and ultra-violet regions--below 5000 angstroms. Also, the film is more sensitive to the high energy, short wavelength radiation. Unfortunately, glass lenses and windows block

the ultra-violet radiation, hence the useable portion of the spectrum lies between 3000 and 5000 angstroms. A Kodak Wratten Filter No. 34 which has a peak transmittance at 4200 angstroms and zero transmittance between 5000 and 6400 was used in all of the experiments.

The ionization probe which is used to detect the location and, in some cases, the motion of the reacted gas boundary is mounted beside the schlieren phototube such that it is within the field of view of the schlieren system. The probe used in most of the test runs consists of two parallel 0.030 inch steel electrodes spaced 0.060 inches centerline to centerline. The probe projects approximately 1/4 inch from the tip of a 1/2 inch diameter supporting rod. The plane through the electrode centerlines was oriented parallel to the optical axis; as a result the probe silhouette observed in the photographs appears as that of a single wire. The probe electrodes are connected in series with a 45 volt battery and a 500 ohm resistor. The voltage drop across the resistor was recorded by an oscilloscope. Typical outputs were of the order of 1 volt indicating an effective resistance across the electrode gap of 0.025 meg ohms. The capacitance of the circuit was estimated to be 100 picofarads resulting in a calculated circuit rise time on the order of $3 \, \nu$ sec.

The triggering circuit for the schlieren and shadowgraph spark sources is based on the use of a specially designed spark modulator which converts the 10 to 30 volt gate or delay trigger output of the oscilloscope into

a 4000 volt square wave having a duration on the order of 0.1 μsec. The electronic circuitory involves the use of a hydrogen thyratron to control the high voltage discharge and a pulse forming network to shape the square wave. This pulse is applied to a third or "tickler" electrode which, in the case of the line source, projects into the mid-point of the gap formed by the tungsten electrodes. The discharge from the tickler electrode to the ground electrode induces the breakdown of the primary gap. The delay between the input to the oscilloscope and the rise on the output of a phototube viewing the spark light is typically 0.4 μsec. Most of this delay is accounted for by the delay built into the oscillo-scope gate output.

Tektronix Type 555 dual beam oscilloscopes are used as the basic timing and recording devices. The oscilloscopes were calibrated periodically by use of crystal controlled Tektronix Type 181 Time Mark Generator. Non-linear sweep rates and errors in measurements of oscillo-scope traces are the dominant source of error in the projectile velocity measurements and limit the accuracy to approximately $\pm$ 3%. The velocity is determined by dividing the distance the projectile moves between the shadowgraph and schlieren stations by the time interval. The distance is measured from the position of the ball relative to the reticles as recorded by the photographs and the known distance between reticles. The time interval is found by measuring the oscilloscope trace length which is determined by the time of the gate outputs to the

22

spark modulator.   As noted above, there is a delay on the order of 0.4 sec between the gate output and the observation of spark light--the two delays are nearly equal and, therefore, tend to cancel any errors intro- duced.   The time interval was typically in the vicinity of 180 μ sec for the gas mixtures used.   When the dual schlieren system is used, the time between schlieren sparks is measured by monitoring the sparks by a photo- tube.

The gases used in the experiments were obtained from Airco commer- cial cylinders.   The gases are mixed in a rotating mixing tank usually within six hours of their use.   Previous work on the determination of the detonation wave speeds of the gas mixtures indicated that a mixing time of approximately two minutes was sufficient to insure a homogeneous mixture.   Usually much longer mixing times were used in the experiments. The gas volumes are measured by means of partial pressures; the gases are assumed to be ideal.   The test section is evacuated to a pressure of from 100 to 300 microns of Hg before each run; the test gases therefore typically contain 0.10% residual gases.

SECTION 2

IDENTIFICATION OF FLOW FIELD FEATURES

The characteristics of exothermic hypersonic blunt-body flow field which are distinguishable on schlieren photographs are shown schematically in Fig. 4. These features are discussed below. Throughout this discussion reference is made to methods of interpreting schlieren photographs of axisymmetric flow fields and to detailed flow field calculations. These details are discussed in Appendix I and IV. Reference is also made to the features of inert or relatively unreactive flows which are described in standard texts (e.g., Ref. 16) and which are outlined in the following paragraph.

The most prominent feature of the hypersonic flow about a sphere is the nearly parabolic bow shock wave which is normal to the flight axis on the axis and which far downstream approaches the Mach angle corresponding to the body velocity. Other than within the viscous boundary layer, the flow is subsonic with respect to the ball only in a limited portion of the nose region (behind the strong segment of the bow shock). The sonic lines which bound the subsonic region can be very roughly approximated by lines extending upstream from the center of the sphere to the bow shock and inclined at an angle of 45 deg with respect to the axis. The gas velocity with respect to the ball immediately downstream of the bow shock on the centerline corresponds to the value behind a normal shock; the velocity decays to zero at the stagnation point in a

very nearly linear manner. The boundary layer separates from the body
shortly after the section of maximum body diameter (the body shoulder).
The free shear layers converge to form a neck or section of minimum
diameter. A wake shock which turns the flow more or less parallel to
the flight axis originates at the neck and trails downstream joining the
bow shock far downstream. A weak shock also may emanate from the point
where the boundary layer separates from the body. This recompression shock
is due to overexpansion of the flow about the body; the shock turns the
flow parallel to the converging shear layers. The viscous flow, which
includes the boundary layer, shear layer and the core of the wake down-
stream of the neck, may be either laminar or turbulent depending on the
Reynolds number of the flow. For the experiments conducted on the study,
transition to turbulence appeared to occur at the wake neck. As discussed
below, all of the features visible on schlieren photographs of nonreacting
flows are retained in the exothermic flows studied herein.

Bow Shock Wave

For the exothermic mixtures employed in these experiments, the bow
shock retains the more or less parabolic shape characteristic of non-
reactive flows. For relatively nonreactive gases such as air it has been
shown that the bow shock shape for supersonic flow fields about spheres
can be correlated over a wide range of conditions by simple expressions
involving the Mach number and the density ratio across a normal shock

at that Mach number. Korkan (Ref. 17) gives the following correlation:

$$\frac{r}{D} = A \left(\frac{x}{D} \right)^{n}$$

$$A = \frac{1.52}{(\rho_s/\rho_o)^{0.2}} + \frac{1}{M_o^2} \tag{1}$$

$$n = \frac{0.76}{(\rho_s/\rho_o)^2} + \frac{1}{2M_o^2} + 0.44$$

This correlation was found to apply also in the case of exothermic mixtures if a density ratio, $\frac{\rho_{ave}}{\rho_c}$, indicative of the extent of reaction in the nose region were used in evaluating the parameters A and n. For example, for Run No. 87 (Fig. 5) the density ratio for which the correlation provides a good representation of the observed shock shape is 0.200 whereas the unreacted value is 0.182 and the fully reacted value is approximately 0.265. A comparison of the shock profile given by the correlation with the experimental profile for conditions of Run No. 87 (Hydrogen-air, Φ = 1.0, M_o = 5.10, p = 0.396 atm) is shown in Fig. 6. This shock shape correlation is used in the analysis of the instability mechanism to obtain an estimate of the velocity in the inviscid wake near the body shoulder.

In all cases, at points sufficiently far downstream of the shock apex, the angle of the shock wave with respect to the flight axis approaches the Mach angle corresponding to the given ball velocity. An oblique detonation wave stabilized by the body was **never** observed. Such waves could theoretically exist for cases where the projectile velocity is greater than the Chapman-Jouguet speed. These waves would be charac-

terized by a "bow shock wave" whose minimum inclination would be that

for which the normal component of the free stream gas velocity with re-

spect to the bow shock wave is equal to the Chapman-Jouguet speed. These

shock angles would be much greater than the Mach angle and would be

readily observed.

In cases where the projectile velocity is less than the Chapman-

Jouguet speed, a self-sustained detonation could develop in the wake

of the projectile and eventually overtake the projectile. This was ob-

served in several cases; Fig. 7 is an example. The detonation wave is

observed to be somewhat curved and to exhibit a turbulent appearance in

the schlieren photograph. The interaction of the detonation wave and

the partially reacted wake gases was not studied; Behrens, et. al., present

some data on this phenomena (Ref. 4). In some cases, photographs were

obtained after the detonation wave had passed the ball. In these cases,

no bow shock wave was observed indicating the Mach number of the reacted

gas behind the detonation wave relative to the projectile was less than

unity. This is consistent with the Chapman-Jouguet model which specifies sonic

flow (with respect to the wave front) behind a plane detonation wave.

In cases where the schlieren photographs do not indicate the pre-

sence of turbulence in the inviscid region of the flow field, the bow

shock retains the smooth, continuous shape characteristic of nonreactive

flows. In cases where a turbulent effect does exist, the bow shock be-

comes distinctly wrinkled and the contour in the nose region becomes

fuzzy indicating the presence of strong disturbances (Figs. 7 and 8).

The wrinkling is probably due to the impingement of weak shock waves

generated by nonuniform, locally intense exothermic reaction.

Shear Layers, Viscous Wake, Wake Shock and Recompression Shocks

As is the case of non-reactive supersonic blunt-body flows, for

the flow fields having non-turbulent reaction zones, the boundary layer

is observed to separate shortly after the section of maximum diameter.

The resulting shear layer converges to form a neck followed by a viscous

wake (Figs. 9 and 10). A wake shock originates in the neck region and

trails downstream. The shear layer cannot be observed in the case of

turbulent reaction because it is masked by the strong schlieren effects

generated by the turbulence (Fig. 8).

For those runs where the Mach number is sufficiently low that the

fluid in the boundary layer does not undergo significant exothermic

reaction until after the neck region is reached, the schlieren effect

of the hydrodynamic turbulence becomes significantly enhanced as heat

release occurs (Figs. 11 and 12). The effect of the chemical reaction

on the hydrodynamic turbulence was not studied in this program.

In many of the photographs (e.g., Fig. 12), recompression shocks

resulting from overexpansion of the flow near the shoulder of the body

can be seen. In many cases these shocks are located asymmetrically

with respect to the flight axis because of imperfections in the body

surface caused by the wearing action of the gun barrel.

Reacted Gas Boundary

Chemical reaction occurs in the stagnation region, where the residence time of the gas elements is infinite, and exists in a limited region of the inviscid wake. The extent of the region depends essentially on the temperature and pressure levels in the shocked gas and the reactivity of the gas mixture. The reaction zone, or more precisely the region wherein the gas has undergone exothermic reaction, is observed to be a region bounded by a smooth surface or a corrugated surface, or it is observed to be a turbulent region with an indefinite boundary. These reaction zone configurations, which provide a basis for classifying the various flow regimes, are illustrated in Figs. 8, 12, 13, and 14 which are discussed below.

The experimental basis for identifying this region as a reaction zone are the results of the ionization probe measurements, the boundary velocity measurements made by use of the dual schlieren photographs, and the interpretation of the schlieren photograph shadings.

The ionization probe was used in conjunction with the photographs to determine in what region of the flow field the ionization level reached detectable limits. In these experiments, ionization can be produced either thermally or by the production of ionized species in

the chemical reaction process. Both of these conditions exist behind a reaction front. For those runs where the probe was positioned such that the tip did not intersect the reaction zone boundary, no signal was recorded; for those cases where probe intersected the boundary, a finite deflection of the oscilloscope beam was recorded for times later than the intersection time.

An example of a case where the reaction zone does not extend to the probe and thus no probe signal is recorded is given in Fig. 15. No deflection of the oscilloscope trace is noted at the time the probe passes through the bow shock. The shock heating is insufficient to produce detectable ionization levels. The normal component of the approach flow at the intersection point is estimated to be 3.2 in this case. (The top trace in the oscillograph is used to measure the ball velocity and is not pertinent to this discussion.)

An example of a case where the reaction zone does not initially extend to the probe but where it reaches the probe after a delay is shown in Fig. 16. Here a probe signal is recorded beginning approximately 70 μ sec (or equivalently 9 ball diameters) after the ball passes the probe station. The probe output is recorded by the lower traces on the oscillographs. During the delay period the reaction zone has grown laterally either through expansion or through the molecular transport processes associated with subsonic flame propagation. The initial oscillating nature of the signal is caused by the corrugated surface of the reaction

30

zone immersing varying lengths of the probe electrodes with ionized gas. The normal component of the bow shock Mach number, which determines the temperature and pressure of the gas immediately behind the shock, is estimated to be 3.5.

An example of a case where the gas immediately behind the bow shock wave undergoes exothermic reaction is shown in Fig. 17. Here a signal is recorded approximately $2\,\mu$sec after the second picture was taken. The normal component of the bow shock Mach number at the intersection point in this case is estimated to be 3.6.

If the corrugated boundary of Fig. 13 is a reacted gas boundary, it should move in the streamwise direction with the local gas velocity. On the other hand, if this region represents a series of propagating compression waves, the boundary should move in the streamwise direction with a velocity equal to or greater than the sum of the acoustic speed and local gas velocity. From the dual schlieren photographs such as Fig. 17, it is possible to obtain the average velocity with which the reaction zone boundary moves in the direction of flight between the time the two photographs were taken. As discussed in the following paragraphs, it is indeed observed that the boundary moves with the local gas velocity. For Run 157 (Fig. 17) a typical local gas velocity in the inviscid wake as measured by a stationary observer will be shown to be approximately 700 fps in the direction of the motion of the ball. On the other hand, the acoustic speed in a gas having a temperature of

2500 R, molecular weight of 31.6 and a specific heat ratio of 1.4 is on

the order of 2300 fps. Thus the difference between the gas velocity and

the propagation rate of rate of compression waves is quite large and it

is possible to distinguish between the motion of a contact discontinuity

and a compression wave with certainty.

It should be noted that in the inviscid wake downstream of the

missile, the unreacted gas is relatively cool due to the temperature re-

duction associated with the expansion of the gas about the missile.

Therefore, the propagation rate of the reaction front in the inviscid

wake, measured relative to the local gas velocity, is quite small. A

reaction zone boundary in the wake should therefore appear to be frozen

in the wake. Based on the calculations of Appendix IV, at all locations

downstream of the major diameter of the ball, expansion should have cooled

the gas sufficiently to freeze the induction reactions associated with

shock heating; any propagation of the reaction front would be due to

molecular transport and can be expected to be quite small.

By identifying the peculiarities in the reacted gas boundary in

Fig. 17, a specific point on the boundary can be located on both photo-

graphs. In this particular case, the boundary irregularities are quite

distinct, particularly on the original photographs, and the corresponding

points can be located with reasonable certainty. The photographs were

exposed at a 12 μ sec interval. This is the time required for the ball

to move approximately 1.5 diameters. In Fig. 18 the average boundary

streamwise velocity during this time interval is plotted as a function

of the average position downstream of the shock apex. The end points

of the horizontal bars represent the positions of the given point in the

two photographs. The velocity is measured relative to the laboratory

observer, not relative to the ball. If the reacted gas boundary is

frozen in the flow, this is the velocity with which the disturbed gas

drifts past the stationary observer. Note that the measured velocities

of from 400 to 700 fps are small relative to the ball velocity of

5540 fps. In this coordinate system, the variation of the streamwise

velocity due to expansion and to the effect of the wake shock is

emphasized. The points corresponding to the lowest three plotted values

of $(\frac{y}{D})$ are located upstream of the wake shock in both of the photo-

graphs and therefore the indicated velocity variation can be due only to

expansion. The expansion of the gas causes an increase in the velocity

of the gas measured relative to the ball but a decrease velocity measured

relative to the stationary observer. The effect of the wake shock is to

abruptly increase the wake velocity measured by the stationary observer.

The rounded shape of the curve shown in Fig. 18 is due to the averaging

associated with the measurements being taken over a relatively large

time interval.

The velocity of the reacted gas boundary measured relative to the ball (not relative to the stationary observer as plotted in Fig. 18), is the quantity which relates the wavelength of the instability (as measured by the separation of the boundary corrugations) to the instability frequency: $f = \frac{V_w}{\lambda}$. Under a given set of conditions, the instability frequency is a constant but the wake velocity, V_w, is a function of the axial and radial coordinates. Therefore, the measured wavelength can be expected to vary with distance downstream of the ball. The spacing of the striations appears in the photographs, however, to be remarkably constant. This is a consequence of the fact that the variation of the wake velocity relative to the ball in the inviscid wake downstream of the body shoulder is actually quite small. For Run 157 (Fig. 18), the wake velocity varies by 300 fps compared to the ball velocity of 5540 fps, a variation of 5.4 percent. This is undetectable in the photographs. Based on a velocity of defect of 700 fps, the appropriate wake velocity to be used to relate frequency and wavelength is, for the case of this illustration, 87 percent of the ball velocity. The error introduced in any analysis by use of the ball velocity rather than an appropriate wake velocity is small. As detailed in the section entitled "Instability Mechanism," a wake velocity estimated by use of the bow shock correlation given earlier in this section is used as the appropriate wake velocity.

The magnitude of the reacted gas boundary velocity measured by means of the dual schlieren photographs is confirmed by the probe measurements.

As mentioned previously, in cases where the probe tip grazes the reacted gas boundary, the probe signal oscillates due to the periodically varying depth of penetration of the probe into the ionized gas. This results from the motion of the corrugated boundary. The average boundary velocity can be found by dividing the measured wavelength by the measured oscillation period. For the case of Run 157 (Fig. 17) the average of the peak to peak and trough to trough periods is approximately 15.9 μ sec and the measured wavelength to diameter ratio is 0.211 (Table I). This results in an average velocity of 630 fps which compares favorably with the 400 to 700 fps detected by the dual schlieren technique. For the case of Run 139 (Fig. 16), the probe measurements yield a boundary velocity of 570 fps.

The boundary velocity was also measured by monitoring the output of a phototube which viewed the image produced by a continuous schlieren light source. That is, the camera film-holder was replaced by a phototube, the field of view of which was limited to a narrow verticle slit of a height approximately equal to the width of the reacted gas region. The spark light source was replaced by a high intensity lamp. The phototube output oscillates as the striations produced by the schlieren effect drift past the slit. The phototube output for Run 142 is given in Fig. 19. In this case, the average period of oscillation is approximately 30 μ sec and the average wavelength to diameter ratio is 0.57. The resulting wake velocity is 780 fps.

The measured values of reacted gas boundary velocity, which are in the neighborhood of 700 fps, agree with the analytically predicted value of the gas velocity at the corresponding region in the flow field of an unreacting gas. The analytical prediction is based on the flow field calculations detailed in Appendix IV and summarized in Fig. 20. The Mach number in the inviscid wake at a radial distance of 0.8 diameters (the reacted gas boundary radius for Run 157) at an axial position of, for example, 1.3 diameters downstream of the bow shock apex is approximately 3.2. For the acetylene-oxygen mixture used in Run 157 this corresponds to a velocity of 4730 fps. The wake velocity observed by a stationary observer would be 630 fps which agrees fairly well with the experimental observations. The wake velocity corresponding to a Mach number of 3.4, the limit of the calculations shown in Fig. 20, would be 530 fps.

In view of the large difference between these calculated gas velocities and the boundary velocity which would be observed if the boundary were produced by propagating compression waves, it is apparent that the boundary is a contact discontinuity, fixed to the fluid particles.

Further evidence that the boundary under consideration is a boundary between reacted and unreacted gas is provided by the schlieren photographs. The direction of the density change across the corrugated boundary can be deduced from examination of the schlieren shadings; see Figs. 13 and 21. The knife-edge used in Fig. 13 was inserted in the direction

opposite from that in Fig. 21, accounting for the bright bow shock in

Fig. 13 compared to the dark bow shock in Fig. 21. (The dark outline

on the upper half of the bow shock in Fig. 13 is produced either by an

inadvertant horizontal knife-edge effect caused by one of the apertures

not being large enough to pass the light rays which are strongly deflected

in the vertical plane by the bow shock, or by a shadowgraph effect caused

by the film not being positioned precisely at the objective lens focal

point.) As pointed out in Appendix I, the very prominent alternating

dark and bright bands characterizing the reaction zone are accounted for

entirely by its corrugated boundary and the density change across the

boundary. Streamwise periodic density changes within the volume of

reacted gas need not exist to produce this strong regular schlieren

pattern; indeed such density fluctuations do not exist. If a segment

of the corrugated boundary is chosen for examination in which the width

of the boundary is increasing in the downstream direction, then, if the

density on the inside of the surface is less than that on the outside,

the shading should be opposite that of the bow shock. (The bow shock

is an envelope whose width is increasing in the downstream direction but

whose density change is in the opposite sense from that across the reac-

tion front.) This is seen to be the case in the photographs, confirming

that the density inside the corrugated boundary is less than that outside

the boundary, as would necessarily be the case for an exothermic reaction

front boundary.

In certain cases where the instability wavelength is short, striations are observed even in the nose region (e.g., Fig. 22). It was originally thought, early in the program before the cause of the vertical striations had been determined, that these waves observed in the nose region were oscillating shock waves. However, early work with the dual schlieren apparatus (Runs 30 through 47, Table I), where the time between exposures was held to a fraction of the instability period, failed to produce an example of the wave propagating upstream; i.e., from the ball to the bow shock. This, of course, is consistent with the fact that the striation is caused by the corrugated edge of the reaction front and that such striations will always flow downstream.

In addition to the above experimental evidence that the boundary under consideration is the reaction zone boundary, there is analytical confirmation, for the nonturbulent cases, that the boundary profile is determined by the ignition delay characteristics of the fuel-oxidizer combination used. This is discussed in Appendix IV where the experimentally observed and analytically predicted profiles for the case of a Mach 5.0 sphere moving through a stoichiometric hydrogen-air mixture are compared.

Inviscid Wake

For those cases where the reaction zone boundary is corrugated or where the reaction zone is turbulent, there exists in the inviscid wake

a pattern of two sets of smoothly curved wave fronts which extend from the reaction zone to the bow shock and which cross one another to yield a net-like pattern. These waves have been identified as pressure waves and entropy waves as noted in Fig. 4. As discussed below, this identification is based on the results of the schlieren analysis, on the magnitudes of the wave propagation rates as determined by the dual schlieren photographs, and on the results flow field analysis (Appendix IV).

As noted in the previous section, the corrugated reaction zone boundary is fixed in the flow and moves with the local gas velocity. Inspection of photographs such as Fig. 13 and 21 indicates that one set of waves (the entropy waves) attaches to the reaction zone boundary at a given point on each corrugation. The other set (the compression waves) appears indistinct near the reaction zone boundary in all the photographs, and it is not possible to establish by the photographs that these waves do or do not attach to that boundary. Both sets of waves extend to the bow shock surface. The actual joining of the waves at the bow shock is, in general, indistinct on the photographs. By examination of the photographs wherein the instability is observed to be irregular (e.g., Fig. 23), it is concluded that each wave in one set corresponds to a particular wave in the second set, and that the corresponding waves have a common point at the bow shock. The waves which are fixed to the reaction zone boundary, which moves with the local gas velocity, must themselves

move with the gas velocity and, therefore, must be contact discontinuities

or entropy waves. Such waves could be generated by the interaction of

compression waves with the bow shock. This would account for the one-to-

one correspondence between waves in each set and the apparent joining

of the waves at the bow shock. If the waves of the second set are com-

pression waves, their propagation speed relative to the gas velocity

must be equal to or greater than the acoustic speed. This is found to be

the case by examination of the dual photographs such as Fig. 17.

The pertinent data from Fig. 17 is reproduced schematically in Fig. 24.

The positions of a single point on the reaction front boundary have been

located in the dual photographs and are sketched in Fig. 24 together with

the entropy waves emanating from that point. Compression waves have been

sketched in the figure at the intersection of the entropy waves and the

bow shock. The angle of inclination of the entropy waves, bow shock and

compression waves are those measured in Fig. 17. The distance ΔS_S ,

moved by the intersection point along the bow shock is then measured;

the distance, ΔS_P , moved by the compression wave normal to itself can

then be calculated from the geometry of the interaction. The average

propagation rate of the compression wave relative to the ball can then be

calculated using the known time interval of 11.9 μ sec. The gas velocity

behind the bow shock measured relative to the ball can be approximated

by use of the oblique shock relations using the average value of the bow

shock inclination along the intersection path. The compression wave

propagation rate relative to the gas velocity is the difference between

the velocity of the wavefront with respect to the ball and the gas

velocity relative to the ball. These values calculated for

points located 2.5 and 4.9 diameters downstream of the bow shock apex

for Run 157 are 1,400 fps and 1,000 fps, respectively. The acoustic

speed at these locations was calculated to be 1,375 and 1,345. The

agreement between the observed and calculated values is reasonable con-

sidering the error amplification which results when taking the difference

between two large quantities. The measured propagation rates of the two

sets of waves thus support the contention that they are entropy waves and

compression waves.

The direction of the density change across such waves is known--

the density must increase across a compression wave and decrease across

the contact discontinuity generated by the interaction compression wave

and the bow shock. (This interaction is treated in detail in Appendix II.)

The direction of the density change can also be deduced from the shadings

of the schlieren photographs. As discussed in Appendix I, the shading

of the compression wave must be opposite from the shading of the bow

shock since both are compression waves but have opposite slopes measured

with respect to the flow field axis. Examination of the photographs

indicates this to be the case. The shading of the entropy wave should

be the same as that of the bow shock since both have slopes of the same

sign, and in both cases the light ray passes from a medium of low density to a medium of high density when crossing the wave. (In Appendix II it is shown that the gas on the upstream side of the contact discontinuity is hotter than that on the downstream side.) In the photographs the entropy wave appears as a double band, the downstream band having the proper relative brightness. The double band is probably related to the structure of the wave as discussed in Appendix I.

It is apparent from the symmetry of the flow field that the waves originate in the nose region. A further test of whether these waves represent compression and entropy waves would be to construct the contours which such waves would exhibit as time progresses. Such a calculation has been carried out; the details are given in Appendix IV. An infinitesimal pressure pulse was assumed to be generated at the stagnation point and its location at later times corresponding to an arbitrarily chosen time interval was plotted. The location of the infinitesimal contact discontinuity generated by the interaction of the pressure pulse with the bow shock was also plotted. The results of the calculation are shown in Fig. 25.

The developing shapes of the compression and entropy waves are seen to correspond to the shapes observed in the photographs. The entropy waves remain attached to the stagnation point and undergo a severe bending in the downstream region as they traverse the inviscid wake. This bending is particularly noticeable in the schlieren photographs of the low Mach

number runs (e.g., Fig. 26) where the reaction zone does not extend far into the inviscid wake.

The shape of the compression waves is determined primarily by the location of the source of the disturbance. The distortion of these waves due to the variation of acoustic speed and flow velocity throughout the flow field is small. The waves have the appearance of a set of concentric rings centered about the nose of the ball.

Based on the above observations that the compression waves appear to radiate almost as concentric rings from the origin of the disturbance and that the entropy waves owe their shape to the "stretching" caused by their being attached to the rapidly moving compression wave-bow shock intersection point while simultaneously being fixed to the slowly moving fluid elements, it is concluded that any periodic disturbance distributed symmetrically and located in the nose region of the flow field will produce a wave pattern in the inviscid region having the characteristics observed in the photographs.

If the two sets of waves do represent compression waves and entropy waves, then a specific relationship should exist between the angles of intersection of the bow shock, the compression wave and the entropy wave or contact discontinuity. Also, another wave, the reflection of the compression wave from the bow shock, should exist. A schematic representation of the shock interaction is given in Fig. 27. The reflected wave is not shown in this figure. In Fig. 27a the shock interaction

is shown as seen in a coordinate system fixed with respect to the ball.

The steady state configuration, i.e., in a coordinate system fixed with

respect to the point of intersection, is shown in Figs. 27b and 27c.

The details of the interaction are considered in Appendix II where it is

shown that the reflected wave is a rarefaction wave and that all the

waves are weak. A weak rarefaction wave cannot be expected to be visible

in the schlieren photographs. As discussed in Appendix II, a discrepancy

of from 10 to 30° exists between the analytically predicted and experi-

mentally observed inclinations of the entropy wave. The experimentally

observed configuration can be analytically generated for an interaction of

the type assumed in Fig. 27, only if the propagation rate of the compression

wave with respect to the local gas velocity is assumed to be less than

the acoustic speed. Such an assumption does not correspond to physical

reality and therefore some other, as yet undetermined, explanation must

exist for the discrepancy. This is further discussed in Appendix II.

Although the interaction analysis fails to explain the precise ob-

served angular relationship among the waves at the intersection point,

it is felt that the discrepancy is not severe enough to suggest that the

observed waves are not compression and entropy waves. The discrepancy

is probably due to some unaccounted for effect such as distortions caused

by the following powder gases or the effects of the exothermic reactions

in the wake. The conclusion drawn from the measurements reported in this

section is that the waves indeed represent propagating compression waves

and the entropy waves generated by the interaction of the compression

waves with the bow shock.

SECTION 3

EXPERIMENTAL DATA

The recorded experimental data is composed primarily of schlieren photographs of the hypersonic flow field about spheres fired into lean acetylene-oxygen mixtures and stoichiometric hydrogen-air mixtures. Argon and helium were used as diluents in several runs. Velocity measurements were recorded for each run and ionization probe data were recorded in a large number of cases.

The primary objective of the tests was to obtain data on the variation of the instability wavelength with the controllable experimental parameters (initial gas state, sphere velocity and diameter). It became apparent early in the program that the regular instability could exist only under a limited range of conditions; therefore, a number of runs were made also with the objective of determining the boundaries of the various flow regimes.

The principal data obtained from the experiments are presented in Table 1. A selected number of photographs from which the data have been taken are reproduced herein and are discussed throughout the following text. Most of the data of Table 1 has been used in the preparation of figures which summarize the data. Some of the data is questionable because of suspected unreliable oscilloscope calibrations or weak or irregular schlieren patterns which makes measurement of the flow field characteristics difficult. Such data is so identified by notes in the

"Remarks" column of Table 1. Those runs in which dual schlieren photo-
graphy was employed and those in which probe measurements were recorded
also are specified. Unless otherwise noted, the data of Table 1 was
obtained with the use of a half-inch unsaboted sphere.

Flow Field Regimes

Four different flow field regimes can be distinguished for hypersonic
blunt bodies moving in a gas mixture capable of undergoing exothermic
reaction. The regimes are characterized by the nature of the chemical
reaction zone as observed on schlieren photographs. The regimes are
defined as·follows: (A discussion of the details observed in the photo-
graphs referred to is included in the text below.)

1) Wake Combustion Regime. Only the fluid in the boundary layer is
heated sufficiently to permit the exothermic reaction to be initiated.
The effects of the reaction are observed in the turbulent viscous wake
where the chemical heat release results in the enhancement of turbulent
schlieren effect. See Fig. 11.

2) Turbulent Regime. Chemical reaction spreads throughout a large
portion of the inviscid wake and exhibits a definitely turbulent appearance.
See Fig. 8.

3) Stable Regime. Chemical reaction spreads throughout a large
portion of the inviscid wake but the flow within the reaction zone is
non-turbulent and the reacted gas boundary is smooth. See Fig. 14.

4) Periodic Regime. The region of reacted gas is characterized by strong regularly spaced, dark and bright vertical striations. The reacted gas boundary has a corrugated appearance and compression and entropy waves can be observed propagating in the inviscid wake. See Fig. 1.

The location of these flow regimes in terms of the laboratory controlled parameters mixture pressure and the ball Mach number is given in Fig. 28 for the case of 1/2 inch diameter spheres fired into a mixture of 15 moles of O_2 to 1 mole of C_2H_2. This gas mixture was used to generate a regime plot because the controllable parameters could be easily varied over a range wide enough to observe all the significant boundaries. Richer acetylene-oxygen mixtures generated excessive self-luminosity which produced fogging of the film. In the case of the hydrogen-air mixtures, the pressure level required to observe the high pressure boundaries exceeded the levels where the effects of the shock waves disturbed the alignment of the optical equipment. The data obtained for the hydrogen-air mixtures (Fig. 29) indicates the same general regime boundaries exist for that mixture as for the acetylene-oxygen mixture although, of course, the locations of the boundaries on a pressure-Mach number plot differs from those of Fig. 28.

Acetylene-Oxygen; 1/2 Inch Diameter Spheres

Fig. 28 indicates, as expected, that at low Mach numbers, regardless of the pressure levels, the chemical reaction is confined to the viscous wake. As seen in Fig. 11, there appears to be no effect of the reaction on the flow field other than the increased wake temperature made apparent by the enhanced turbulent schlieren effect. For most of the runs made in this program, the Reynolds number of the flow was such that the viscous wake should become turbulent at the neck. In Fig. 11 the schlieren sensitivity is relatively weak such that the turbulence cannot be observed immediately downstream of the neck. However, approximately two diameters downstream of the neck exothermic reaction becomes sufficiently great that turbulent flow is clearly observed. The effect of the heat release on the turbulence intensity and on the turbulence statistics was not investigated. The effect observed in Fig. 11 is primarily an enhancement of the schlieren effect caused by the substantially increased density fluctuations caused by the heat release.

At somewhat higher speeds the reaction zone begins to spread laterally into the inviscid wake. The boundary of the reacted gas downstream of the ball can in some cases be distinguished from the shear layers. In Fig. 12 the faint shear layers lie inside of the smooth reacted gas boundary. The hot reacted gases again enhance the schlieren effect of the turbulent gases. Also observed in this photo are weak recompression

shocks emanating from the body shoulder; the existence of these shocks is, of course, not dependent on the exothermic reaction.

If the pressure is sufficiently low, the reaction zone continues to spread laterally into the inviscid wake as the Mach number is increased and no instability of the flow is observed. Thus, at low pressure there is no sharp demarcation between the wake combustion regime and the stable combustion regime. It was observed, however, that at the very low pressures required to bypass the regime of periodic oscillations in the acetylene-oxygen mixtures (below 0.066 atm) the stability of the flow was easily upset by influences of the gunpowder gases. At these low pressures it was necessary to maintain a pressure of at least 0.1 atm in the blast tank in order to retard the motion of the powder gases and prevent these disturbances which cause the reacted gas boundary to wrinkle and thereby exhibit a turbulent appearance.

At higher pressures, as the Mach number is increased above a certain minimum, the periodic instability regime, of which Fig. 1 is typical, is encountered. Within this regime, as the Mach number is further increased, the wavelength of the instability decreases. (The variation of the wavelength with ball speed and mixture pressure is discussed in detail in the following sub-section.) Throughout most of the periodic regime the schlieren photographs exhibit a quite regular structure. The deviations from this regular behavior which occur near the regime

boundaries are discussed in the following paragraphs. At the lowest

Mach numbers at which the regular instability is observed, the wave-

length becomes quite long and the wave form takes on a somewhat different

appearance (Figs. 19 and 30) from that observed at the higher speeds.

This different appearance is solely the result of the increased wavelength

and does not represent a change in the mode of oscillation. This is

further discussed in the section on the instability mechanism.

At these low Mach numbers, and at the highest pressures at which

tests were run with the acetylene-oxygen mixture, a gross distortion of

the wave form is observed (Fig. 23). The wavelength of the instability

becomes random as does the transverse dimension of the reacted gas boundary.

The strength of the compression and entropy waves in the inviscid wake

as inferred from the distinctness of their schlieren traces is also

variable. It is observed that the widest regions of the reacted gas region

are joined with the strongest entropy waves.

At the boundary between the periodic regime and the wake combustion

and stable combustion regimes, the amplitude of the boundary corrugation

is observed to be markedly reduced, and the schlieren pattern produced

by the corrugations is relatively weak. In some cases the instability

is observed to die out and then reappear. This is illustrated in Fig. 5.

These low pressure regime boundaries are fairly well defined, although

as indicated by the arrows in Figs. 28 and 29, there is a certain amount

of scatter.

As indicated in the regime plots, the regular instability is observed

to exist at velocities both above and below the Chapman-Jouguet speed.

In other words, from the results of these experiments, the Chapman-

Jouguet speed has no significance in determining the shape of boundaries

of any of the flow regimes. For the two mixtures studied it does provide

an indication of the approximate missile speed required to observe the

periodic instability. As discussed in the section on the instability

mechanism, the instability is due to nonequilibrium effects; the parameter

governing the conditions under which the instability can exist is the

First Damkohler number based on the induction time of the reaction. On

the other hand, the Chapman-Jouguet speed is determined by purely

equilibrium calculations. Therefore, it should not be expected that the

Chapman-Jouguet speed is a quantity useful in the interpretations of

these experiments. The similar location of the regime boundaries with

respect to the Chapman-Jouguet speed for the two mixtures cannot be

construed as an indication that this will be the case for all exothermic

mixtures.

At the higher pressures, as the Mach number is increased an abrupt

transition from the periodic to the turbulent regime takes place. To

produce such a strong schlieren pattern (as observed in Fig. 8) this

turbulent schlieren effect must be produced by a disturbance of the reacted

gas boundary across which a large change in the index of refraction occurs.

This disturbance could be created by a wrinkling of the boundary,similar to flame wrinkling, in which case the reacted gas itself need not necessarily be turbulent. On the other hand, the entire volume of reacted gas could be turbulent with the strong schlieren effect being produced by the hot turbulent gas ingesting the cold outer gas at the boundary. A schlieren photograph cannot distinguish between the two cases; i.e., it is not known whether or not the instability actually generates hydrodynamic turbulence.

The pattern of entropy waves and compression waves in the inviscid wake, a characteristic of the regular instability, is again observed in the turbulent regime; however, the spacing of the waves is random. The compression waves must be stronger than those generated in the periodic case since a noticeable distortion of the bow shock profile occurs due to the wave interaction process (Fig. 8). Also characteristic of the turbulent case is the fuzzy appearance of the bow shock wave in the region. The fact that the bow shock wave is so strongly effected in a random manner suggests that the gas passing through the shock does gain a significant random velocity component and that all throughout the volume of the reacted gas region does possess a certain turbulent component. On the other hand, the turbulent appearance of the schlieren photographs is certainly not a random turbulence.

As the boundary of the periodic regime is approached by lowering the pressure at constant Mach number, the turbulent pattern more and

more suggests the evenly spaced vertical striations of the periodic

regime. This is illustrated by Fig. 31 where conditions, except for the

reduced pressure, are nearly equal to those for Run 128, pictured in Fig. 8.

Figure 31 suggests that the turbulent pattern is caused by a distortion

of a corrugated boundary. Again, however, such photographs actually

provide no information on whether the distortion is caused by the growth

of turbulence within the reacted gas or by a wrinkling of the gas inter-

face (an instability of the reacted gas boundary itself).

As the pressure is further reduced, other conditions remaining

fixed, the flow becomes periodic. This is illustrated in Fig. 33 where

the characteristic periodic oscillation is observed under conditions

similar to those in Fig. 31 except for the reduced pressure. Note,

however, that the wavelength of the instability is decidedly shorter than

the wavelength associated with the turbulence of Fig. 31.

Another example of a run near the boundary of the periodic and

turbulent regimes is shown in Fig. 32. Here the flow is observed to be

intermittently turbulent and periodic.

Within the turbulent regime, if the velocity is increased with

other conditions remaining the same, the characteristics of the flow

change to only a small degree. The turbulence spreads through a greater

lateral extent as would be expected and the scale of the turbulence

decreases (Fig. 34). In Fig. 34 there is also a noticeable difference

between the schlieren effect produced by the turbulence near the body and that produced downstream of the body. This suggests that the wrinkling of the reacted gas boundary does not persist with time but instead is damped out. If the wrinkling were due to the spreading of hydrodynamic turbulence, the wrinkling should persist because it is unlikely that the decrease in temperature and pressure due to expansion would greatly effect the turbulence intensity.

Above a certain Mach number, the regime plot, Fig. 28, indicates the periodic instability is no longer observed; the flow appears to be either turbulent or stable. The data trend indicates that the slope of the turbulent/periodic boundary becomes small at the high Mach numbers and that there is a minimum pressure below which the turbulent regime is not encountered.

Finally, it is interesting to note that at velocities in the vicinity of the Chapman-Jouguet speed, as the pressure is increased, the character of the flow changes from a stable flow to one exhibiting a well ordered periodic behavior and then to a turbulent behavior. Studies of the structure of detonation waves have produced evidence that such waves are unstable and that at low pressures a coarse structured, well organized, periodic behavior exists (spin). As the pressure is increased, the characteristic multi-headed spin instability wavelength decreases until the scale becomes so small that the structure can no longer be

resolved. At the same time, other experimental evidence has been obtained

that suggests that the flow becomes turbulent. The question arises as

to whether the turbulent detonations and those exhibiting multi-headed

spin are one and the same, the classification depending upon the resolving

power of the instrumentation. For the experiments conducted in this

program, however, it is apparent that for exothermic blunt body flows,

the turbulent regime and the high frequency periodic regime are funda-

mentally different and are sharply divided.

Acetylene-Oxygen; 3/8 and 1/4 Inch Diameter Spheres

A limited number of runs were performed with spheres of 3/8 and

1/4 inch diameter. It was observed that the diameter has a strong effect

on the location of the regime boundaries. It was found that if a regime

plot is constructed using the product of the pressure and diameter as

the ordinate, it is possible to fit the few data points for the smaller

diameter spheres onto the same plot with the half-inch spheres (Fig. 35).

The arrows again indicate that the specified data points, according to

the observed character of the reaction zone, should lie on the other

side of the boundary. The boundaries shown are those of Fig. 17. The

agreement is very good, although there are too few data points to draw

any firm conclusions. The agreement suggests, however, that the induc-

tion time, which is inversely proportional to pressure, plays the major

role in determining the conditions under which the periodic instability

can exist. It further suggests that the other factors which determine

the shape of the regime boundaries are relatively insensitive to changes

in pressure and diameter. These other factors are discussed in the section

on instability wavelength. The fact that the induction time does not by

itself determine the regime boundary is illustrated by a comparison of

the contour of a line of constant Damkohler number based on induction

time, shown as a dashed line in Fig. 35, with the regime boundaries.

Hydrogen-Air; 1/2 Inch Diameter Spheres

The regime plot for the stoichiometric hydrogen-air mixtures

(Fig. 29) indicates that relatively higher pressures are required to ob-

serve the periodic instability in this mixture than in the acetylene-

oxygen mixture. As shown, no runs were made at pressures sufficiently

high to observe the turbulent regime. Photographs exhibiting the turbu-

lent regime were obtained in lean hydrogen-oxygen mixtures ($H_2:O_2$, $\Phi = 0.25$)

in which no diluent was used. The periodic behavior is observed for the

stoichiometric hydrogen-air mixture again at velocities both above and

below the Chapman-Jouguet speed.

The published results of Ruegg and Dorsey (Ref. 2) and Struth,

Behrens, and Wecken (Ref. 4) illustrate the effect of pressure and

diameter on the regime boundaries for this mixture. The data are shown

in Fig. 36 where the ordinate is the pressure-diameter product and the

solid regime boundaries are taken from Fig. 29. The turbulent regime

was observed by Ruegg and Dorsey with 0.785 inch diameter spheres fired into gas at a pressure of 0.55 atm. At the low Mach numbers, long wavelength surges were observed which created strong deformation of the bow shock. Struth, et. al., did not observe the instability above the Chapman-Jouguet speed with their 9mm spheres. This is in contrast to the observations reported herein (Fig. 29).

Instability Wavelength

The instability wavelength, measured in ball diameters, for the lean acetylene-oxygen mixtures is shown in Fig. 37, and for stoichiometric hydrogen-air mixtures in Fig. 38. The wavelength is defined as the distance between striations on the schlieren photographs measured at axial locations in the vicinity of the rear edge of the ball. The gas velocity in this region of the inviscid wake, which is of the order of 80 to 90 percent of the free stream velocity, further increases due to expansion by only a small fraction of the free stream velocity and therefore the measured wavelength is relatively insensitive to the measurement position chosen. The wavelength appears to the eye to be constant downstream of the ball.

Acetylene-Oxygen; 1/2 Inch Diameter Spheres

The details of the variation of the wavelength with pressure and velocity will be discussed with reference to the data for half-inch

spheres fired into the 1:15 acetylene-oxygen mixtures. As noted previously, this mixture was chosen for study since the pressure and velocity could be varied over relatively wide ranges within the limits of capability of the equipment. The data obtained for an ambient gas pressure of 0.132 atm (100 mm Hg) is shown by the circles in Fig. 37. As noted on the regime plot, at this pressure the periodic instability was observed up to a Mach number of 6.0. Under this condition, the pressure behind the bow shock, assuming chemically frozen flow in thermal equilibrium, is 5.75 atmospheres and the temperature 1940° K (3500° R). As the velocity is decreased, the wavelength increases steadily until a Mach number of 5.28 is reached. At this point a gap in the data exists, the next data point being at Mach 5.0 where the wavelength is 25 percent higher than at the previous point. There is no apparent change in the wave-form across the gap. It is not certain whether the gap actually exists or whether it is a result of scatter in the data. As discussed below, the gap does appear to exist at other pressure levels.

As the velocity is further decreased, the wavelength continues to increase until at a Mach number of 4.92, where the wavelength is approximately three times longer than at Mach 6.0, a sudden decrease in wave-length is observed. A marked change in the schlieren effect is also observed since the anomalously short wavelength or high frequency is accompanied by a reduced amplitude of the boundary corrugation. (Compare

Fig. 9 with Fig. 13.) As will be noted in the section on the instability

mechanism, this anomalously high frequency may be caused by the effect

of reflected waves which generate a pattern having a wavelength twice

the expected wavelength. This high frequency behavior persists for a

short Mach number interval during which the wavelength rapidly increases.

Then another abrupt increase in the frequency apparently occurs. The

amplitude of the boundary corrugations is so small and the striations

so extremely weak that the wavelength cannot be measured with accuracy;

two such points corresponding to Run Nos. 251 and 220 are located near

Mach 4.9 on Fig. 37. In these cases the entropy waves in the inviscid

wake produce a stronger effect than the boundary corrugation and it is

the relatively close spacing of these waves which suggests that a second

abrupt increase change in frequency has occurred. This effect was not

observed at other pressure levels.

As the Mach number is decreased below Mach 4.75, the instability is

no longer observed for runs made at 100 mm Hg. The normal shock conditions

corresponding to this Mach number are a pressure downstream of the shock

of 3.6 atm and a temperature of 1360° K (2470° R).

As indicated on the regime plot, at lower pressures the Mach number

interval through which the instability is observed is shorter than at

100 mm Hg. At pressure of 0.098 atm (75 mm Hg) the instability was ob-

served at a Mach number of 5.55 but was not observed in the case of two

runs made between Mach 5.55 and Mach 5.34. In one of these runs the flow was stable; in the other a weak irregular, intermittent pattern was observed. Thus a gap in the data exists similar to that observed at a pressure of 100 mm Hg. Between Mach 5.34 and 5.20 the instability wavelength increases; the wavelength is observed to be longer than that for a pressure of 100 mm Hg. As the Mach number is further decreased, the anomalous high frequency behavior is observed and then the flow becomes stable.

At a pressure of 0.198 atm (150 mm Hg), the highest Mach number at which the regular instability is observed is Mach 5.33. At this high Mach number range there is virtually no separation between the wavelengths observed at this pressure and at a pressure of 100 mm Hg. This is in conflict with the proposed model of the instability mechanism which predicts that the wavelength is inversely proportional to pressure. As the Mach number is decreased, once again there is evidence of an abrupt increase in the wavelength (near Mach 5.15). The increase in the wavelength magnitude is a smaller percentage than observed at the lower pressure, and it is therefore even more difficult to determine if this apparent jump is real or is due to data scatter. In one of the photographs (Fig. 39), the instability exhibits an intermittent behavior in which two different wavelengths appear to exist at different times. Unfortunately, a horizontal knife edge was used in this run and resolution

of the flow field structure is quite poor. However, a change in the form of the corrugated reacted gas boundary can be observed in Fig. 39 in the vicinity of the point where the trailing wake shock crosses the reacted gas boundary. Other photographs wherein a horizontal knife edge was used do not exhibit this peculiarity. This is the only photograph out of over 250 which suggests that a transition from one frequency to another can occur; previous investigators have reported observing such a transition (Ref. 4).

As the Mach number is further decreased, the wavelength increases but again there is no significant separation between this data and that for the lower pressure. Between a Mach number of 4.80 and 4.65 the anomalous high frequency is observed; three such data points are included on Fig. 37. For the run at Mach 4.71, shown in Fig. 15, the schlieren effect is very weak and the wavelength measurement is questionable. The value plotted in Fig. 37 is less than that of the other two points suggesting that this is a case corresponding to the second abrupt frequency jump cited in the discussion of the runs made at 100 mm Hg pressure. However, the schlieren characteristics of the photograph do not correspond to those runs, and it is believed that the shorter wavelength is due to measurement errors. It is observed in Fig. 15 that the spacing of the vertical striations in the reacted gas appears to change intermittently from the small value corresponding to the anomalously high frequency to twice that value. This is indicated in Fig. 37 by the vertical line

joining two points, one having twice the wavelength of the other. As discussed in the section of the instability mechanism, this effect is believed to be due to the varying effectiveness of the entropy waves in generating the boundary corrugation. In Fig. 40, this double-valued effect is again observed in a section of the wake, this time with alternately spaced uneven wavelengths. Measurements indicate that the sum of the uneven lengths is twice the wavelength in the region of the wake where the spacing is even. Both values joined by a vertical line are again shown in Fig. 37.

At the very low Mach numbers the long wavelength is observed (Figs. 19 and 30). The spacing of the waveforms is somewhat irregular as indicated by the vertical lines in Fig. 37. Below Mach 4.4 the flow was observed to be stable.

At higher pressures, the regular periodic instability is observed only over a short Mach number range due to the transition to the turbulent regime. There again is very little separation of the wavelength data from that taken at the lower pressures, particularly in the Mach 4.86 to 5.0 range. Also it is apparent from this data that the transition to the anomalous high frequency mode occurs at lower Mach numbers as the pressure is increased. At a pressure of 0.230 atm (175 mm Hg), Fig. 41 indicates transition occurs at a Mach number in the vicinity of 4.65. Note that two sets of entropy waves are observed in the invi-

scid wake but the reacted gas boundary, the corrugations of which are formed by the action of the entropy waves, still displays the fundamental wavelength. This phenomenon is further discussed in the section on the instability mechanism.

At the highest pressure for which tests were made in the acetylene-oxygen mixtures, 0.264 atm (200 mm Hg), the regular instability waveform was observed in only one case. In other runs the waveform exhibited severe transverse distortions as shown in Fig. 23.

To summarize the most important points of the foregoing, it was observed in the tests made with half-inch spheres fired into 1:15 $C_2H_2:O_2$ mixtures that the wavelength of the regular instability increases with decreasing Mach numbers, the increase becoming quite rapid at the lowest Mach numbers for which the instability was observed. At a given Mach number, the wavelength was in general smaller for high pressures, but this was not a strong effect. Two significant anomalies were observed in the otherwise regular trend of increasing wavelength with decreasing Mach number:

(1) In the Mach number range from 5.0 to 5.4, a gap exists in the data wherein the observed wavelength appears to undergo an abrupt increase of 15 to 25 percent as the Mach number is decreased. This apparent effect may be generated by data scatter, but the effect was observed at three different pressure levels.

(2) At a certain low Mach number, which decreases with increasing

pressure, an apparent transition to a higher frequency occurs. As dis-

cussed later, this is believed to be merely an effect of wave reflections

on the reacted gas boundary corrugations, the observed wavelength being

twice the value that would be observed in the absence of the reflections.

Acetylene-Oxygen; 1/4 Inch Diameter Spheres

The instability wavelength data obtained for one-quarter inch

diameter spheres fired into 1:15 $C_2H_2:O_2$ mixtures at a pressure of 0.264

atm (200 mm Hg) is shown in Fig. 42. Shown for comparison purposes is the

data for one-half inch spheres at 100 mm Hg pressure. In the latter data,

the wavelengths measured in the cases of the anomalous high frequency

were doubled to produce the continuous trend shown.

According to theory, the data should lie on a common curve since

the Damkohler number is the same for both sets of runs. It is seen that

the data for the smaller spheres lies slightly above the other data. The

slight separation is small but is significant when compared to the separa-

tion obtained when varying pressure at constant diameter.

Hydrogen-Air; 1/2 Inch Diameter Spheres

The instability wavelength data obtained for stoichiometric hydro-

gen-air mixtures is shown in Fig. 38. Again it can be seen that the

separation of the low pressure data from the high pressure data is less

than would be expected from the inverse proportionality relationship of the induction times. One case of the anomalous high frequency was observed. No runs were made at Mach numbers sufficiently low to observe the long wavelength instability.

SECTION 4

INSTABILITY MECHANISM

This section contains a discussion of the proposed mechanism which

generates the regular, periodic instability. The similarities and dif-

ferences between this flow and that of a one-dimensional detonation are

first discussed. The probable physical cause of the instability of these

exothermic flows is reviewed. The suggestions of previous investigators

regarding the instability mechanism is then reviewed. Equations describ-

ing the wavelength of these acoustic theories are derived and the results

of the experiments and theory are compared. The gas dynamics of the

pertinent wave interaction processes is examined and an instability

mechanism consistent with the results of these considerations is pro-

posed. The experimental wavelength behavior is then compared with

theoretical wavelength prediction. The proposed mechanism is shown to

be consistent with physical processes which could lead to the existence

of the several flow regimes discussed in the previous section. The

probable process by which the reacted gas boundary corrugations are

formed is discussed. Finally, an expression for the induction time of

hydrogen-oxygen mixtures is derived by comparison of theory with experi-

ments. This expression is then compared with induction time correlations

derived by other experimental methods.

In this discussion it will be shown that the induction zone length

along the central streamline is the proper length over which occur the

interactions responsible for the periodic striations. On reviewing the
work that has been done on determination of induction times, it is
apparent that there is significant scatter in the experimental data and
often the conditions (mixture ratio and percent diluent) used in shock
tube and other types of experiments differ significantly from the condi-
tions of the balistic range experiments. Therefore, apparent agreement
between the experimentally observed instability wavelength and that
predicted theoretically based on induction time correlations cannot
alone be regarded as sufficient evidence that a proposed instability
mechanism is indeed the correct mechanism. At the very least, the model
must also be consistent with the laws of gas dynamics. In particular,
the interaction of pressure waves or entropy waves with the boundaries
of the induction zone should be examined to determine if the wave
reflections at the boundaries are consistent with the model of, for
example, a closed-ended or open-ended organ pipe. Also, the proposed
mechanism should contain, or at least be consistent with, some feedback
mechanism by which the instability is maintained. Therefore, in
addition to comparing the theoretically predicted and experimentally
observed wavelength behavior, a significant portion of this section
is devoted to examining these other considerations.

Shock Induced Combustion

As noted in the section on identification of flow field features,
examination of the wave patterns in the schlieren photographs indicates

that the instability originates in the nose region of the flow field. A gas particle in the free stream approaching the nose region, specifically a particle on the axis of symmetry, first encounters a normal shock, then after a time interval equal to the induction time, passes through a reaction front at which point there is an abrupt rise in temperature. The gas continues to the stagnation point, where it reaches the equilibrium temperature due to its infinite residence time. The principle feature of the flow, the shock separated from the reaction front by an induction zone is similar to that which would exist in a one-dimensional model of a normal detonation wave.

The criteria which determine the stability of the exothermic hypersonic blunt-body flow field cannot be expected to be the same as that for the normal detonation because of the radically different boundary conditions characterizing the two problems. In the case of the flow field about the sphere, the existence of the bow shock is determined primarily by the presence of the body; the shock exists whether or not the gas is capable of exothermic reaction. In the case of the detonation wave, the existence of the shock and of the reaction front are interdependent--the two are closely coupled. The strong interdependence leads to a complex instability of the detonation wave apparently involving severe departures from one dimensionality (Ref. 1). This instability, now believed to be always present in self-sustained detonations, is as

yet not understood satisfactorily. The flow field in the nose region

of a blunt body moving in a detonable mixture more closely resembles

that of an overdriven detonation than that of a self-sustained detonation.

In the case of the overdriven wave, some agent other than the chemical

reaction, such as a piston or an expanding driver gas, is to a large

part responsible for the existence of the primary shock wave. This

other agent is relatively insensitive to effects of nonuniformities of

the primary shock, and thus there is a weaker feedback mechanism through

which instabilities can be sustained. Strongly overdriven detonations

can exhibit stable, one-dimensional structures (Ref. 12).

Although the detailed criteria which determine the stability of

the flow field about the ball and the flow field of a self-sustained

detonation probably differ, the most likely physical cause of the

instability is the same. This is the sensitivity of the reaction

front location or, equivalently, the sensitivity of the instantaneous

rate of chemical energy release, to disturbances effecting the strength

of the bow shock. The reaction front location is determined by the

induction time. The induction time is quite sensitive to changes in

strength of the bow shock and typically exhibits a dependence on the

temperature and pressure of the shocked gas of the form:

$$\tau = \frac{A}{p} \exp(E/RT)$$

A - constant

p - pressure

T - temperature

For small disturbances and for an isentropic relationship between pressure and temperature, the following relationship exists (Ref. 1):

$$\frac{\Delta \tau}{\tau} = - \left(\frac{\gamma}{\gamma - 1} + \frac{E}{RT} \right) \frac{\Delta T}{T} \tag{2}$$

Under conditions of these experiments, which are close to the conditions existing behind the shock in self-sustained detonations, the bracketed term is of the order of 10. Thus temperature fluctuations behind a disturbed bow shock will produce induction time fluctuations of a ten-times larger magnitude. This suggests that the observed instability could be caused by the amplification of disturbances in the induction zone which separates the reaction front and the bow shock in the nose region of the flow field.

Previous Work

Before pursuing this reasoning, the work of previous investigators will be reviewed. Ruegg and Dorsey (Ref. 2) suggest that the instability is due to longitudinal oscillations "between the sphere and the (bow shock) wave" and that such an oscillation would exhibit a period:

$$T = \frac{4\Delta}{n C_3} \tag{3}$$

$\mathcal{T}$ — oscillation period

Δ — shock detachment distance

n — integer

C_3 — velocity of sound between the
wave and the sphere

They suggest that the value of C_3 to be used should lie between the

value behind an adiabatic shock wave and that behind a Chapman-Jouguet

detonation.   They indicate that under the conditions of their experiments

this model gives a period of oscillation on the order of 10^{-5} sec which

is on the same order as the observed periods.   This period is somewhat

larger than but of the same order as the induction time.   They do not

attempt to deduce the mechanism of the instability from these observa-

tions.   (The primary result of their work is quantitative data on

induction times derived from the measured separation between the bow

shock and the reaction front.)

In a later discussion (Ref. 18), Ruegg and Dorsey identify

the regular striations observed in their schlieren photographs as being

the effect of a "strong acoustic oscillations" which generates waves

in the nose region which "propagate between the flame front and shock

wave, and are there reflected and returned to the flame in proper phase

to prevent damping of the disturbance." A linear relationship between

the wavelength/diameter ratio and the period, which is calculated by

dividing the separation distance between the reaction front and the

shock by the speed of sound in the unreacted gas behind the shock, is

cited as evidence that the oscillation is an acoustic effect. The plot

contains seven data points. The "visible propagation of waves between

the combustion and shock fronts" (observed by means of schlieren

photographs) is given as evidence that "acoustic waves at the front

of the missile are responsible for the oscillations." The "waves"

referred to, e.g., Fig. 22 of this report, have been identified herein

as the schlieren effect caused by the corrugated edge of the reacted

gas boundary and, as pointed out in the part of Section 2 dealing with

the reacted gas boundary, were never observed (by the dual schlieren

technique) to oscillate but were observed only to propagate from the

shock to the reaction front.

Behrens, Struth and Wecken (Ref. 4) compared the period of

the oscillation observed in their experiments with the induction times

obtained for stoichiometric hydrogen-air mixtures by Ruegg and Dorsey.

The oscillation period was obtained by dividing the observed wavelength

by an appropriate flow velocity (the missile velocity less the wake

velocity defect (Ref. 5)). They note that under certain conditions the

comparison is favorable, but that under other conditions (other

hydrogen-oxygen mixtures) the comparison is not favorable. For those

cases where the comparison is favorable, they refer to the vertical

striations in the reacted gas as a shock pattern which results from a

buildup of an acoustic oscillation; the buildup being due to

"resonance....(between) the induction frequency and the vibration

frequency." To explain the wide range of frequencies observed, they

"have to assume that there exists quite a continuous range, or dense

spectrum, of acoustic frequencies in the gas column before the missile."

They do not elaborate by describing a specific model but rather prefer

to present their observations in these general terms. For those cases

where the comparison between the period of oscillation and the induction

time is in poor agreement, they suggest that acoustic oscillations

exist. The frequency of these oscillations is determined by the

expression for the frequency of acoustic oscillations in a pipe closed

at both ends:

$$\nu = \frac{n c}{2(\Delta - \Delta_k)} \tag{4}$$

ν - frequency

n - integer

$\Delta - \Delta_k$ - distance between the combustion
wave and the sphere

c - the mean velocity of sound between
these space limits

They do not attempt to make a quantitative comparison between experiment

and theory because they were not able to measure $\Delta - \Delta_k$ in their photographs.

Note that the length over which the oscillations occur is stated to be

the distance between the sphere and the reaction front as opposed to the distance between the shock and the reaction front.

In summary, previous workers suggested that the wavelength of the vertical striations is related to the period of oscillations of one-dimensional acoustic waves propagating over a length equal to either the induction zone length , the detachment distance, or the distance between the sphere and the reaction front.

Acoustic Oscillations

The period of oscillation, T, of an acoustic wave on the central streamline in the nose region is the sum of the time required to propagate in the forward direction or toward the bow shock, t_f, plus the time required to propagate in the backward direction, t_b. The period of an acoustic wave oscillating in the unreacted gas between the reaction front and the bow shock will be designated T_u and the period of oscillation in the reacted gas T_R.

The separation of the reaction front from the bow shock is fixed by the induction time τ. A linear velocity decay behind the bow shock (a good approximation in an unreacting gas) with a velocity gradient in the unreacted region equal to that found in the case of no reaction is assumed such that (Fig. 43a):

$$v = \frac{\Delta' - x}{\Delta'} v_s \qquad (5)$$

75

then

$$\frac{\Delta'}{v_s} \int_0^{\Delta u} \frac{dx}{\Delta' - x} = \int_0^{\tau} dt \qquad (6)$$

and

$$1 - \frac{\Delta u}{\Delta'} = e^{-\frac{v_s}{\Delta'}\tau} \qquad (7)$$

The characteristic flow time appearing in this expression can be written as

$$\frac{\Delta'}{v_s} = \frac{\Delta'/R \times R}{v_o \times \rho_o/\rho_s} \qquad (8)$$

Employing an empirical correlation for detachment distance (Ref. 19)

$$\frac{\Delta'}{R} = 0.88 \left(\frac{\rho_o}{\rho_s}\right)^{1.053} \qquad (9)$$

this becomes

$$\frac{\Delta'}{v_o} = \frac{R}{v_o} \times 0.88 \left(\frac{\rho_o}{\rho_s}\right)^{0.053} \qquad (10)$$

Over the Mach number range of interest the density ratio across a normal shock is nearly constant meaning that the induction zone length depends almost exclusively on the first Damköhler number, $D \equiv \frac{\tau}{R/v_o}$:

$$\frac{\Delta u}{\Delta'} = 1 - e^{-\frac{\tau v_o}{RB}} = 1 - e^{-\frac{1}{B}D} \qquad (11)$$

where $B \equiv 0.88 \left(\frac{\rho_o}{\rho_s}\right)^{0.053} \approx$ const. for $4 < M_o < 6$

76

Since the acoustic speed in the unreacted gas, c_u, varies by a negligible amount with x, the velocity with which the wave propagates in the forward direction is

$$v_{prop} = - \left[c_u - v_s \left(1 - \frac{x}{\Delta'} \right) \right] \tag{12}$$

and the time required for the wave to propagate from the reaction front to the shock is

$$t_f = - \int_{\Delta_u}^{0} \frac{dx}{c_u \left[1 - \frac{v_s}{c_u} \left(1 - \frac{x}{\Delta'} \right) \right]}$$

$$= \frac{\Delta'}{v_s} \ln \frac{1 - M_s \left(1 - \frac{\Delta_u}{\Delta'} \right)}{1 - M_s} \tag{13}$$

where M_s = Mach number downstream of the bow shock

Similarly,

$$t_b = - \frac{\Delta'}{v_s} \ln \frac{\frac{c_u}{v_s} + \left(1 - \frac{\Delta_u}{\Delta'} \right)}{\frac{c_u}{v_s} + 1}$$

$$= - \frac{\Delta'}{v_s} \ln \frac{1 + M_s \left(1 - \frac{\Delta_u}{\Delta'} \right)}{1 + M_s} \tag{14}$$

and thus

$$T_u = \frac{\Delta'}{v_s} \ln \frac{1 + M_s}{1 - M_s} \frac{1 - M_s \left(1 - \frac{\Delta_u}{\Delta'} \right)}{1 + M_s \left(1 - \frac{\Delta_u}{\Delta'} \right)} \tag{15}$$

To determine the period of acoustic waves oscillating in the reacted gas, it is necessary to approximate the distance of the reaction front from the surface of the sphere, Δ_R in Fig. 43b, or equivalently, the the detachment distance Δ, taking account of the effects of heat release.

77

Assuming the effective density between the shock and the sphere to be:

$$\rho_{ave} = \rho_u \frac{\Delta u}{\Delta} + \rho_R \frac{\Delta R}{\Delta}$$

$$= \rho_u \left[\frac{\Delta u}{\Delta} \left(1 - \frac{T_u}{T_R} \right) + \frac{T_u}{T_R} \right]$$

(16)

which assumes that pressure and gas constant undergo no change across

the reaction front such that $\dfrac{\rho_R}{\rho_u} = \dfrac{T_u}{T_R}$, then the ratio of detachment

distances can be approximated as

$$\frac{\Delta}{\Delta'} \approx \frac{\rho_u}{\rho_{ave}} = \frac{1}{\frac{\Delta u}{\Delta} \left(1 - \frac{T_u}{T_R} \right) + \frac{T_u}{T_R}}$$

(17)

or by rearranging terms,

$$\frac{\Delta'}{\Delta} = \frac{T_R}{T_u} - \frac{\Delta u}{\Delta'} \left(\frac{T_R}{T_u} - 1 \right) = \frac{T_R}{T_u} \frac{1 - \frac{\Delta u}{\Delta'}}{1 - \frac{\Delta u}{\Delta}}$$

(18)

The gas velocity in the reacted gas is assumed to decay linearly

to zero from the value v_R found immediately behind the reaction front:

$$v = v_R \left(\frac{1 - \frac{x}{\Delta}}{1 - \frac{\Delta u}{\Delta}} \right)$$

(19)

Neglecting compressibility effects and gas constant changes as before,

and evaluating Eq. (1) at $x = \Delta'$

$$v_R = \frac{T_R}{T_u} v_u = \frac{T_R}{T_u} \left(1 - \frac{\Delta u}{\Delta'} \right) v_s$$

$$= \frac{\Delta'}{\Delta} \left(1 - \frac{x}{\Delta} \right) v_s$$

(20)

where Eq. (18) has been used.

Assuming the acoustic speed in the reacted gas, C_R , does not vary

with x, the forward propagation speed of an acoustic wave is

$$\nu_{prop} = -\left[c_R - \frac{\Delta'}{\Delta}\nu_s\left(1 - \frac{x}{\Delta}\right)\right] \tag{21}$$

and the forward propagation time is then

$$t_f = -\frac{1}{\nu_s}\int_\Delta^{\Delta u} \frac{dx}{\frac{c_R}{\nu_s} - \frac{\Delta}{\Delta'}\left(1 - \frac{x}{\Delta}\right)}$$

$$= \frac{\Delta'}{\nu_s}\, \ln\, \frac{\frac{c_R}{\nu_s} - \frac{\Delta - \Delta u}{\Delta'}}{\frac{c_R}{\nu_s}} \tag{22}$$

Similarly, the backward propagation time is

$$t_b = \frac{\Delta'}{\nu_s}\, \ln\, \frac{\frac{c_R}{\nu_s} + \frac{\Delta - \Delta u}{\Delta'}}{\frac{c_R}{\nu_s}} \tag{23}$$

and the period of an acoustic oscillation in the reacted gas is

$$T_R = \frac{\Delta'}{\nu_s}\, \ln\, \frac{\frac{c_R}{\nu_s} + \frac{\Delta - \Delta u}{\Delta'}}{\frac{c_R}{\nu_s} - \frac{\Delta - \Delta u}{\Delta'}} \tag{24}$$

Assuming $c_R = \sqrt{\frac{T_R}{T_u}}\, c_u$ this can be written

$$T_R = \frac{\Delta'}{\nu_s}\, \ln\, \frac{\sqrt{\frac{T_R}{T_u}} + M_s \frac{\Delta - \Delta u}{\Delta'}}{\sqrt{\frac{T_R}{T_u}} - M_s \frac{\Delta - \Delta u}{\Delta'}} \tag{25}$$

As will be discussed later in this section, the instability produces a periodic fluctuation in the chemical reaction rate, the end result of which is to create the corrugated reacted gas boundary. This boundary, as noted in Section 2, is fixed to the fluid elements and therefore moves downstream with the local velocity of the inviscid wake, ν_w .

79

The wavelength of the corrugations is then related to the period of

oscillation by the simple relation:

$$\lambda = T v_w$$ (26)

The applicability of this expression can easily be visualized by con-

sidering the process as viewed in a coordinate system fixed with respect

to the ball.

As noted in Section 2, the inviscid wake velocity downstream of the

ball at radial distances typical of the reacted gas boundary radius

varies little with downstream distance and is on the order of 85 percent

of the free-stream velocity. The error introduced by deriving the

instability wavelength from the period by use of the free-stream velocity,

v_o , instead of v_w would be small. The error in the wavelength trend

(variation of λ with free-stream Mach number) would be negligible

because of the similarity of the flow field over the Mach number

range of interest. Nevertheless, an estimate of v_w based on the

correlation for bow shock profiles discussed in Section 2 was used in

calculating the instability wavelength. The wake velocity was assumed

to be equal to the velocity behind the bow shock at the axial coordinate

of the body shoulder; at $\frac{x}{D} = \frac{1}{2} (1 + \frac{b}{R})$. For a typical case, the

value of $\frac{v_w}{v_o}$ so calculated varied from 0.82 at $M_o = 4.4$ to 0.84

at $M_o = 5.6$.

By combining Eqs. (15) and (25) with Eq. (26) the wavelength to
diameter ratios can then be written for acoustic oscillations in the
unreacted and reacted gases as:

$$\left(\frac{\lambda}{D}\right)_u = \frac{v_w}{v_0}\frac{B}{2}\ln\frac{1+M_s}{1-M_s}\frac{1-M_s\left(1-\frac{\Delta u}{\Delta}\right)}{1+M_s\left(1-\frac{\Delta u}{\Delta'}\right)} \tag{27}$$

$$\left(\frac{\lambda}{D}\right)_R = \frac{v_w}{v_0}\frac{B}{2}\ln\frac{\sqrt{\frac{T_R}{T_u}}+M_s\frac{\Delta-\Delta u}{\Delta'}}{\sqrt{\frac{T_R}{T_u}}-M_s\frac{\Delta-\Delta u}{\Delta'}} \tag{28}$$

The wavelength/diameter ratios calculated by these equations for
the case of a one-half inch diameter sphere fired into a 1:15 mol
ratio acetylene-oxygen mixture at a pressure of 0.132 atmosphere are
given in Fig. 44. The induction time was estimated from the correlation

$$\log_{10}\left([O_2]\,\tau\right) = -9.88 + \frac{17,100}{2.302\,RT} \tag{29}$$

$[O_2]$ - oxygen concentration, mol/liter

τ - induction time, sec

T - temperature, $^\circ$K

which was obtained by extrapolation of the shock tube data of
Kistiakowsky and Richards (Ref. 20). They suggest the expression

$$\log_{10}\left([O_2]\,\tau\right) = -10.58 + \frac{17,100}{2.302\,RT} \tag{30}$$

for stoichiometric $C_2H_2:O_2$ mixtures. Their experimental data indicates

a trend toward increasing $\hat{c}$ as the oxygen-acetylene ratio is increased. The maximum ratio reported in their work was 7.7:1; Eq. (29) was obtained by extrapolating to a ratio of 15:1.

The ratio of the temperature of the reacted gas to the temperature of the unreacted gas, $\dfrac{T_R}{T_u}$, along the central streamline was found by assuming the temperature rise due to reaction to be 50 percent of the ratio of the equilibrium temperature rise. The magnitude of the assumed ratio has a small effect on $(\dfrac{\lambda}{D})_u$, entering only in the calculation of the wake velocity. The effect on $(\dfrac{\lambda}{D})_R$ is relatively strong but does not alter the trend exhibited— $(\dfrac{\lambda}{D})_R$ increasing with increasing Mach number.

The lack of agreement between predicted wavelengths (Fig. 44) and observed wavelength (Fig. 37) for the case of acoustic oscillation in the reacted gas is severe. The calculations show that the thickness of the reacted gas layer in the nose region increases rapidly with Mach number above Mach 4.0 due to the rapid decrease in induction time. The decrease of induction time with increasing temperature is much faster than the increase in acoustic speed; hence the length/acoustic speed ratio increases with Mach number resulting in the wavelength trend shown. It is concluded that the regular instability observed in the photographs is not associated with an acoustic oscillation in the reacted gas.

Since the thickness of the layer of unreacted gas in the nose region decreases rapidly with increasing Mach number, the theoretical wavelength characteristic of an acoustic oscillation in the unreacted gas resembles the experimental trend, particularly at the higher Mach numbers (Fig. 44). The discrepancy between the calculated and observed wavelengths at any given Mach number could easily be accounted for by an inaccuracy in the induction time correlation. It is apparent, however, that $(\frac{\lambda}{D})_u$ does not exhibit the sharp rise in magnitude observed in the experiments at low Mach numbers. This is a result of the fact that below a certain Mach number, approximately Mach 4.0 in this case, virtually the entire nose region is composed of unreacted gas, and therefore there is practically no increase in the length over which acoustic oscillations occur as the Mach number is further decreased. The very small increase in calculated wavelength is due to the decrease in the acoustic speed resulting from the lower adiabatic shock temperature and to the slight increase in detachment distance which results from the decreasing Mach number.

The apparent agreement between experiment and theory at high Mach number and poor agreement at low Mach numbers led previous investigators (Ref. 4) to the unsatisfactory suggestion that different mechanisms prevail in the high and low Mach numbers ranges. As shown below, however, the purely acoustic model is incompatible with the physics of

the interactions between a compression wave and a shock wave. An

equally simple model which gives good agreement between experiment

and theory and which is consistent with the physics of the interaction

processes is easily developed.

Gas Dynamics of Wave Interactions

The interaction between a compression wave and the bow shock wave

for conditions typical of the experiments is shown schematically in

Fig. 45. In Fig. 45a a weak shock wave of Mach number 1.05 is depicted

as approaching a stationary Mach 5.0 bow shock. (A Mach 1.05 shock was

selected for these sample calculations since the changes across such a

shock were large enough to provide reasonable numerical accuracy and

yet the wave could be considered a weak shock. The magnitude of 1.05

is arbitrary and has no special significance.) The conditions down-

stream of the bow shock, Region 2, and downstream of the propagating

weak shock, Region 1, given in the table of Fig. 45 were obtained from

normal shock tables for a constant γ = 1.4 process. The situation after

the interaction is depicted in Fig. 45b. The interaction of two normal

shock waves of the same family, (the over-taking of shock waves) in

gases having an adiabatic exponent $\gamma \leq 5/3$ always results in a

transmitted shock wave and a reflected (in general weak) rarefaction

wave with a contact discontinuity between them (Ref. 21, p. 178).

The interaction is shown on an $x-t$ diagram in the lower right

section of Fig. 46. In this diagram, time increases in the downward

direction. The right-hand boundary of the diagram represents the position

of the bow shock. The incident weak shock, labelled P, interacts with

the bow shock reflecting a weak rarefaction, R, and a contact disconti-

nuity, CD. The other waves shown in Fig. 46 will be discussed later.

The conditions in the region between the reinforced bow shock

and the reflected wave, Region 3, given in the table, were calculated

by the method outlined in Ref. 21, p. 182. The weak rarefaction wave

propagating back into Region 1 causes a slight reduction in temperature

and pressure. Across the contact discontinuity which separates the gas

which has passed through the undisturbed Mach 5.0 bow shock (Region 3B)

from that which has passed through the reinforced (Mach 5.064) shock

(Region 3A) there is a sharp rise in temperature. The effect of these

disturbances on the induction time of the shocked gas is also shown in

the table. There is a substantial decrease in induction time due to the

effect of the incident weak shock ($\dfrac{t_1}{t_2}$ = 0.80) and a further sub-

stantial reduction after the interaction occurs ($\dfrac{t_{3A}}{t_2}$ = 0.68). The

effect of the reflected rarefaction wave is very small ($\dfrac{t_{3B}}{t_2}$ = 0.82

compared to $\dfrac{t_1}{t_2}$ = 0.80).

This example illustrates that because the reflected acoustic wave

is extremely weak, it can play only a minor role in the maintenance of

the instability. On the other hand, the contact discontinuity generated by the interaction is a relatively strong disturbance which, taken together with the sensitivity of the induction time to this disturbance, provides a mechanism through which the instability can be sustained. Indeed, as discussed below, the effect of the shortened induction time of the hot gas behind the contact discontinuity is to generate a second compression wave which begins the next cycle of the instability.

Studies of one-dimensional interactions of pressure and entropy waves with flame fronts have shown that the effects of the interactions, i.e., the nature of the reflected and transmitted waves, can be deduced by determining the effect of the incident waves on the heat release at the reaction front (Ref. 22). If the heat release at the front is increased, pressure waves will propagate in both the upstream and down-stream directions. The pressure waves are created by the increased volume occupied by the gases passing through the front after the increase in the energy release rate has occurred. In the case where the Mach number of the gases approaching the reaction front is small (in a coordinate system fixed to the reaction front) and where the change in the specific heat ratio, γ , across the reaction front is small, the strength of the shocks so generated is related to the change in the reaction rate by (Ref. 22):

$$\Delta w = \frac{\gamma - 1}{\gamma} \Delta P \left(v_2 - v_1 \right) + \frac{\gamma}{\gamma - 1} \frac{P_1 \left(1 + \frac{\Delta P}{P_1} \right)}{\sqrt{\frac{\gamma + 1}{2\gamma} \frac{\Delta P}{P_1} + 1}} \frac{c_2 + c_1}{\gamma} \frac{\Delta P}{P_1} \quad (31)$$

where $\quad w \quad$ = heat release per unit reaction
front area

$\quad \Delta P \quad$ = pressure rise across shock

$\quad 1, 2 \quad$ = conditions upstream and downstream
of the reaction front

Under the restrictions given, the upstream and downstream propagating

shocks are equal strength.

In the problem under study, the change in the energy release rate,

which creates the compression wave, is caused by the effect of the

reduced induction time of the gases which have passed through the

reinforced bow shock; the situation is shown schematically in Fig. 47.

The conditions a short time after a compression wave has interacted

with the bow shock are shown in Fig. 47a. (The reflected rarefaction

wave has been neglected.) The reaction front is located downstream of

the bow shock at the distance which the gas behind the undisturbed

bow shock moves in a time, $\tilde{t}_1$, equal to its induction time. The

contact discontinuity produced by the shock interaction is shown

propagating downstream. After the contact discontinuity has moved a

distance determined by the induction of the gas behind the contact

discontinuity, $\tilde{t}_{3A}$, a reaction front will exist at that location as

well as at the location determined by $t = t_1^n$. The reaction rate is

thereby effectively doubled. The situation a short time later is depicted

in Fig. 47b. The shock waves generated by the doubling of the reaction

rate are shown propagating both upstream and downstream. Later, after

the contact discontinuity passes the location determined by $t = t_1^n$,

no unreacted gas exists at that position and a single reaction front

exists at the location determined by $t = t_{3o}^n$. The reaction rate is

halved when the front located at $t = t_1^n$ is extinguished and rarefaction

waves are generated (Fig. 47c).

An $x - t$ representation of the interaction is also shown in Fig. 47.

The times corresponding to the three schematic representations discussed

above are indicated by the hash marks on the left-hand edge of the plot;

this edge represents the position of the undisturbed reaction front.

The effect of the contact discontinuity, CD , with the hotter gas

behind it is to generate a second reaction front, RF . At the instant

the second reaction front appears, weak shocks, P , are produced which

propagate both upstream and downstream. The upstream propagating shock

further raises the temperature and pressure of the unreacted gas causing

the second reaction front to move upstream . This effectively increases

the reaction rate and therefore is accompanied by the generation of a

train of weak compression waves. The effect of these waves is small

and is neglected. The downstream propagating shock also raises the

temperature and pressure of the gas behind itself, and thus causes

the originally undisturbed reaction front also to begin to move upstream
after the shock reaches the front. The compression waves so generated
are shown in the figure but their effect is small and is neglected.
The contact discontinuity now separates unreacted and reacted gas.
After the contact discontinuity reaches the original reaction front, no
additional unreacted gas reaches this front, and the reaction at this
location is extinquished. The sudden decrease in energy release rate
causes a rarefaction wave, R , to be generated.

According to this simple model, the strength of the shock wave
generated by the effect of the contact discontinuity on the reaction
front would be independent of the strength of the control discontinuity.
The shock strength depends on the change in the rate of energy release
at the reaction front; according to the model this change results from
the doubling of the rate which would exist in the absence of the instability.
The strength of the shock reaching the bow shock would, however, depend on
the strength of the contact discontinuity. For example, if the contact
discontinuity were weak, then $\tilde{c}_{3A} \approx \tilde{c}_{1}$ and the shock would be immedi-
ately followed by the rarefaction which is generated by the halving of
the reaction rate. The two waves would interact, and the shock would
decay before the shock reaches the bow shock. On the other hand, if
$\tilde{c}_{3A} \gg \tilde{c}_{1}$ the compression wave would reach the bow shock before the
rarefaction had caught up--its strength would be undiminished.

Regardless of the exact details of the interactions, it is clear from the standpoint of the physics of the interactions that it is much more likely that the strong effects of the contact discontinuity on the reaction front are responsible for the feedback which closes the cycle of events than are the weak effects of the rarefaction wave which is reflected from the bow shock.

Proposed Instability Mechanism

The complete cycle of events for the instability model composed of the effects of the interaction of a compression wave with the bow shock and the subsequent effects on the reaction front of the contact discontinuity so generated is shown in Fig. 48. An x-t diagram, not drawn to scale, is shown in Fig. 46. The beginning of the cycle is shown at a time when the contact discontinuity approaches the undisturbed reaction front. A zone of decreasing entropy follows the contact discontinuity as indicated later in Steps 5 and 6. In Step 2 the hot gas behind the contact discontinuity begins to react at a second front upstream of the original reaction front position, thereby increasing the overall rate of reaction and generating shock waves which propagate both upstream and downstream. At a somewhat later time, the contact discontinuity, now with reacted gas behind it, reaches the position of the downstream or original reaction front, causing the reaction at this front to be extinguished. Rarefaction waves are generated as a result

of the decreased overall reaction rate. A short time later, Step 3, the entropy zone, begins to penetrate the remaining reaction front causing the reaction rate to diminish and causing the front to begin to recede. The weak rarefaction wave which results from the gradually decreasing reaction rate is neglected. At a later time, the compression wave interacts with the bow shock reflecting a weak rarefaction and generating a contact discontinuity (Step 4). The reflected rarefaction has a negligible effect on the gas through which its propagates, as illustrated in the example of Fig. 45. In Step 5 the incident rarefaction generated by the extinguishing of the original reaction front penetrates the bow shock, restoring the bow shock to its initial strength and generating a zone of decreasing entropy. A chain of weak pressure waves are reflected during the penetration; their effects are negligible. The cycle of events is completed as the contact discontinuity followed by the zone of decreasing entropy approaches the undisturbed reaction front (Step 6).

For purposes of clarity, the contact discontinuity, CD , and zone of decreasing entropy, Z , (a broadened entropy wave) have been shown as being separate and distinct; however, as noted at the end of the preceding subsection, it is just as likely that the two will be merged into a single wave having steep front and a shallow tail. In this case the incident compression wave, P , and rarefaction wave, R , would also

be merged; the rarefaction would catch up with the weak shock causing

it to decay. This situation was first suggested during analysis of the

shadings of the schlieren photographs when it was observed that the

entropy waves in the inviscid wake were composed of a double band--a

dark band followed immediately by a light band (or vice versa).

The period of the cycle of events for this model (hereafter referred

to as the P-C D model) is longer than that of the acoustic model, since

the time required for the wave front to propagate from the bow shock

to the reaction front is determined by the gas velocity alone. Using

Eq. (5) for the gas velocity:

$$t_b = \int_0^{\Delta u} \frac{dx}{v_s \left(1 - \frac{x}{\Delta'}\right)}$$

$$= -\frac{\Delta'}{v_s} \ln \left(1 - \frac{\Delta u}{\Delta'}\right) \tag{32}$$

The forward propagation time is given by Eq. (13). Thus the period is

$$T_{P-CD} = \frac{\Delta'}{v_s} \ln \frac{1 - M_s \left(1 - \frac{\Delta u}{\Delta'}\right)}{(1 - M_s)\left(1 - \frac{\Delta u}{\Delta'}\right)} \tag{33}$$

and the wavelength observed in the wake is given by

$$\left(\frac{\lambda}{D}\right)_{P-CD} = \frac{v_w}{v_o} \frac{B}{R} \ln \frac{1 - M_s \left(1 - \frac{\Delta u}{\Delta'}\right)}{(1 - M_s)\left(1 - \frac{\Delta u}{\Delta'}\right)} \tag{34}$$

In Fig. 44 the wavelength trend predicted by this model for the

lean acetylene-oxygen mixtures is compared with those predicted by the

acoustic models. The wavelength is observed to increase much more rapidly

with decreasing Mach number for the P-C D model than for the acoustic

model. This is due to the rapid increase in the time required for

the contact discontinuity to reach the reaction front as the reaction

front recedes into the low velocity region near the stagnation point.

The period of oscillation predicted by the P-C D model thus remains a

strong function of the induction time as the induction time becomes long.

As noted previously, this is not so for the acoustic model in which case

the period is more or less proportional to the induction zone length

which asymptotically approaches the detachment distance as the induction

time becomes long.

The predicted wavelength trend for the P-C D model is compared

with experimental measurements in lean acetylene-oxygen mixtures in

Fig. 49. The experiments indicate an even more rapid increase of the

wavelength with decreasing Mach number than does the theory. This

could easily be due to the induction time exhibiting a faster increase

with temperature at the low temperatures than that given by Eq. (29).

The linear dependence of $\log_k ([O_2] \tau)$ on reciprocal temperature was

observed by Kistiakowsky and Richards (Ref. 20) to apply over a tempera-

ture range from 2200°K to 1300°K. The temperature at the Mach number of

4.7 where the experimental curves steepen is 1350°K. It is quite

possible that at lower temperatures a three body chain breaking reaction

becomes important and causes faster increase in induction time than

would otherwise be the case. This is observed in the hydrogen-oxygen reaction. Kistiakowsky and co-workers identify the rate limiting reaction for the acetylene-oxygen induction zone reactions as the same as that for the hydrogen-oxygen reaction in the temperature range from 1300 to 2200°K (Refs. 20 and 23). The gratifying quantitative agreement between the magnitudes of the theoretical and experimental wavelengths at the higher Mach numbers must be regarded as for fortuitous in view of the crudity of the expression for induction times used in the theoretical model.

Although there is good agreement between the experiments and theory with respect to the behavior of the wavelength with changing Mach number, the experiments fail to exhibit clearly the strong pressure dependence prescribed by any theory which specifies the induction time as the characteristic time. According to the induction time correlations, there is an inverse relationship between induction time and pressure. The lack of separation of the data in the Mach number range from 4.8 to 5.0 as the pressure is varied from 100 to 175 mm Hg is particularly noticeable in Fig. 37. For the runs made at pressure of 100 and 150 mm Hg where there is sufficient data to represent the experimental trend in Fig. 49, the separation indicated by the theory is significantly greater than that experimentally observed in the Mach number range from 4.7 to 5.3. It is difficult to perform conclusive tests on the

dependence of the wavelength on the induction time by conducting experiments over a wide pressure range with Mach number fixed, however, because of the transitions to the turbulent and stable flow regimes which occur (Fig. 28).

It is possible to demonstrate the dependence of instability wavelength on induction time by plotting the wavelength as a function of the reaction zone width, Fig. 50. The reaction zone width is a direct measure of the induction time as discussed in Appendix IV, "Flow Field Calculations." The shorter the induction time, the wider the reaction zone appears on the schlieren photographs. For purposes of Fig. 50, the reaction zone width is defined to be the distance between the envelopes drawn through the peaks of the corrugated reacted gas boundary, measured perpendicular to the axis of symmetry two diameters downstream of the nose of the ball.

The data shown in Fig. 50 includes shots made in hydrogen-oxygen mixtures and acetylene-oxygen mixtures for both one-half inch and one-quarter inch diameter projectiles. Most of the data lies in a band which bends sharply upward as the width to diameter ratio decreases to unity. A significant number of data points lie below the band in this region; these represent runs exhibiting the anomalous high frequency behavior noted earlier in the section on experimental results. The fact that there is a relatively small scatter in the data irrespective

of changes in pressure, Mach number, ball diameter and gas mixture indicates that the reaction zone width and the instability wavelength are strong functions of the same variable; i.e., the induction time.

It should be pointed out with regard to the instability mechanism that although the sphere diameter, D , is a convenient length to use in nondimensionalizing the wavelength measurements, the sphere diameter has only a small influence on the wavelength. The significant length in the problem is, as pointed out previously, the induction zone length, which is determined by the induction time and by the velocity of the gas behind the shock on the centerline. The induction time depends on the temperature and pressure of the gas behind the shock; these properties change by only a very small degree as the gas proceeds from the shock to the stagnation point. Therefore the influence of the ball diameter enters only through its effect on the gas velocity on the centerline. The velocity was assumed to exhibit a linear decrease from the shock to the stagnation point (Eq. 1). In cases where the induction zone length is small, the change in velocity in the induction zone would be small and thus the wavelength should be found to be nearly independent of the ball diameter. This is illustrated by evaluating the analytical expression for the wavelength, Eq. (34), at the limit where Δu becomes small.

By algebraic rearrangement, Eq. (34) can be written

$$\frac{\lambda}{D} = \frac{v_w}{v_o} \frac{B}{R} \ln \left[1 + \frac{\frac{\Delta u}{\Delta'}}{(1 - M_s)(1 - \frac{\Delta u}{\Delta'})} \right] \qquad (35)$$

In the limit as $\frac{\Delta u}{\Delta'} \rightarrow 0$,

$$\frac{\lambda}{D} \rightarrow \frac{v_w}{v_o} \frac{B}{R} \frac{\frac{\Delta u}{\Delta'}}{1 - M_s} \qquad (36)$$

Substituting the shock detachment distance correlation, Eq. (2), this becomes

$$\lambda \rightarrow \frac{v_w}{v_o} \frac{\Delta u}{(\frac{\rho_o}{\rho_3})(1 - M_s)} \qquad (37)$$

The factor $\frac{v_w}{v_o}$ introduces only a slight dependence on diameter; the other factors in the expression are independent of diameter.

Development of Reacted Gas Boundary Corrugations

The most likely process by which the corrugations of the reacted gas boundary are produced is discussed below. Before proceeding, the considerations which determine the location of the reacted gas boundary in the absence of the instability will be outlined. The calculation of this reaction front profile is considered in detail in Appendix IV.

The positions of the reaction front, the bow shock and a single streamline for typical flow confitions are shown in Fig. 51. The dashed

lines in this figure, which give the experimental profiles, will not be

considered in this discussion. The streamline shown is the limiting

streamline, outside of which no streamlines intersect the reaction front

and inside of which all streamlines intersect the reaction front.

Neglecting diffusion, the limiting streamline, therefore, is coincident

with the reacted gas boundary downstream of the point labeled F where

the induction zone reactions freeze. For streamline inside the limiting

streamlines, the end-of-induction condition is reached before the reactions

freeze due to expansion. By following the progress of the induction zone

reactions along several of these streamlines, the points where the end-

of-induction condition are reached can be plotted and the reaction front

profile sketched by joining the points. See Appendix IV for further

details.

In general terms, the corrugations are formed, in the region up-

stream of the body shoulder, by the reaction front proceeding outward

from the flow field axis to a greater extent in the hot gas behind the

contact discontinuity than it does in the cold gas ahead of the contact

discontinuity. Two hypothetical reacted gas boundaries are shown in

Fig. 52: (1) the (inner) boundary representing that boundary which

would exist if the flow were stable; (2) the (outer) boundary which

represents the maximum transverse extent to which the reacted gas boundary

could proceed for a given decrease in induction time. The decrease in

induction time of concern is that due to the increased temperature behind

the contact discontinuities associated with the instability.

The points at which the reacted gas boundaries becomes coincident

with a streamline due to freezing of the reaction is indicated by the

points labeled F.

The contours of compression waves, P_1 to P_4, generated by the

instability are shown as solid lines in the figure. The contact

discontinuities generated by the interaction of the compression waves

with the bow shock wave are shown as dashed lines. The contact dis-

continuities extend from the bow shock to the central streamline

near the stagnation point; only the segment from the bow shock to the

stable reacted gas boundary is shown in the figure. The compression

wave contour P_1 was generated by assuming the wavefront to be coinci-

dent with the bow shock along a short segment near the axis. Another

segment was then located by determining the progress of the assumed

segment over a time interval equal to the period of the instability.

In accordance with the P-C D model, motion of the contact discontinuities,from

the bow shock to the outer reacted gas boundary was determined by the

gas motion; motion of the compression wave from the reaction front to

the bow shock was determined by application of Huygens principle. The

instability period was determined from the assumed separation on the

stagnation streamline of the bow shock and outer reacted gas boundary.

As shown, the compression wave contour P_1 is found to be practically coincident with the bow shock over a significant transverse distance, then it begins to bend away from the shock at an increasing rate. The point where P_1 intersects the outer reacted gas boundary locates a point on the contact discontinuity generated by P_2. (It is the interaction of this contact discontinuity with the reaction front that generates the compression wavelets which form the wavefront P_1.) The intersection of the contact discontinuity with the bow shown determines a point on P_2, etc. The wave contours for values of $\frac{x}{D} < 1.0$ were developed by following the reaction of selected segments as described above; those shown for $\frac{x}{D} > 1.0$ were sketched. It can be seen that the compression wave rapidly develops from the normal wave on the axis of symmetry into the wave shape observed in the downstream region of the photographs.

The reacted gas is shown in the figure by the cross-hatched areas. The protrusions of reacted gas beyond the inner reacted gas boundary are bounded on the downstream edge by a contact discontinuity which separates hot gas on its upstream side from cold gas on its downstream side. The location of the upstream edge of the protrusion would be determined by the r ate of decrease of the temperature of the hot gas behind the contact discontinuity. The upstream edge shape shown in the figure was sketched arbitrarily, but the spear-shaped protrusions of reacted gas must result.

The protrusions would generate a saw-tooth silhouette on a schlieren photograph as shown by the insert. That is, the undercutting of the protrusion by unreacted gas would not appear on the photographs (although the undercutting would determine the lightness or darkness of the schlieren effect). This general shape of the reacted gas boundary is observed in Fig. 1.

It is apparent in photographs such as Figs. 1 and 13, that the shape of the boundary corrugations changes as the flow expands downstream of the body shoulder. The slope of the downstream edge of the corrugation (the edge having a slope opposite that of the bow shock) becomes smaller and the slope of the upstream edge becomes larger. This effect is due to the difference in the velocity of the gas at the peak of the corrugation and at the trough--the velocity at the trough being the greater. This difference in velocity is due to the hot reacted gas attaining a higher velocity when expanded to a given pressure than the colder unreacted gas. Thus the base of the protrustion of hot gas moves downstream faster than the peak, causing the protrusion to change its appearance from that of leaning downstream to that of leaning upstream. The beginning of this development is illustrated in Fig. 52 by the two downstream corrugations, the configurations of which were sketched on the basis of the above reasoning--they were not calculated.

The effect of the hot gas closer to the flow field axis moving faster than the cold gas exterior to the reacted gas boundary is particularly

noticeable in the photographs of the long wavelength instability such as Figs. 19 and 30. In these cases the amplitude of the corrugation is large and a large difference exists between the velocity of the peak and of the trough of the "corrugation." For the first several wavelengths downstream of the ball there is a distinct separation between the protrusions, but soon thereafter the base of one protrusion appears as though it is drawn into the next.

It is of interest to note that the corrugations serve as a means of joining the expanding cold outer gas with the expanding hot inner gas without the formation of a vortex sheet. If the boundary were a streamline, a shear layer would necessarily exist at the boundary. This is the case for the stable flow; e.g., Fig. 14. However there is no means of detecting the shear layer in the schlieren photographs.

Examination of the photographs indicates that the amplitude of the corrugation decreases as the Mach number increases. Because the wavelength decreases with increasing Mach number, the amplitude trend also manifests itself as a decrease in amplitude with decreasing wavelength (compare Figs. 10 and 13). As the Mach number increases, the two reacted gas boundaries shown in Fig. 52 would move farther out in the inviscid wake. A reduction in the corrugation amplitude implies that the separation distance between the two boundaries decreases as they move outward. The separation distance is determined by the strength of the

contact discontinuities as they sweep over the region between the two

boundaries; the stronger the contact discontinuity, the larger the

separation. The results of the shock interaction calculations, Appendix

II, do indeed indicate that the strength of the contact discontinuity

is smaller in the outer region of the inviscid wake. The strength

decreases due to the change in the geometry of the interaction between

the compression wave and the bow shock. For a given bow shock strength,

the contact discontinuity generated by the interaction is strongest

when the compression wave is parallel to the bow shock; the contact

discontinuity strength decreases as the angle between the two waves

increases. As can be seen in Fig. 52, this angle does increase as the

interaction point moves outward along the bow shock.

The foregoing theory of how the corrugations are formed can be

extended to suggest a plausible cause of the anomalous high frequency

behavior reported previously and the observation of two characteristic

instability wavelengths in the same photograph. These effects may be

a manifestation of wave reflections which have been neglected in the

cycle of events listed in Fig. 48. In Fig. 41, the corrugated reacted

gas boundary exhibits a well defined wavelength of a magnitude which is

in agreement with that predicted by the P-C D model. However, a double

set of entropy waves appears in the inviscid wake. In the usual case,

each entropy wave in the inviscid wake corresponds to one striation

in the reacted gas region since the corrugation of the reacted gas boundary

is caused by the greater transverse advance of the reaction front into

the hot gas behind the contact discontinuity. In Fig. 41 one set of

entropy waves apparently has a greater effect on corrugating the

reacted gas boundary than does the other. The effect of the second set

in producing a corrugation can be seen immediately behind the ball,

but the effect is washed out as the flow proceeds downstream.

The uneven spacing of the entropy waves and the dominance of one

set in producing the prominent striations in the reacted gas leads one

to suspect the effect is due to a weak and previously neglected wave

reflection. If circumstances were such that the spacing were even and that

the extent of the corrugation produced by each set were the same, then

it would appear as if an oscillation with twice the expected frequency

were occurring. Figure 40 illustrates such a case. (Notice that to the

right of the reticle the striations are, indeed, evenly spaced. The

wavelength is half the expected value. To the left of the reticle,

the striations are unevenly spaced. The wavelength, defined as the

distance between similarly appearing points on the boundary, is equal

to the expected value. At the far left of the photo, the striations

again appear to be evenly spaced.) Cases where the wavelength is

observed to be regular throughout have been referred to as those

exhibiting an anomalously high frequency; e.g. Fig. 9. If the data for

these runs were replotted in Figs. 37 and 50, using a wavelength twice

that recorded in Table I, then a more regular data distribution would

result. As noted previously these data can be identified not only by

the anomalously high frequency but also by the low amplitude of the

boundary corrugation observed in the photographs.

The wave most likely responsible for producing the second set of

entropy waves is the compression wave which is generated in Step 2 of

Fig. 48 and which propagates from the reaction front toward the ball

surface. This compression wave is reflected from the ball surface and

would be amplified upon passing through the reaction front (Ref. 22).

It would then interact with the bow shock as does the primary compression

wave in the P-C D model. From the limited number of runs in which the

high frequency behavior was observed (less than 10 runs out of 200),

It is apparent that only under certain circumstances are conditions

suitable for the reflected wave to produce an effect on the reacted

gas boundary and to generate the second set of entropy waves observed.

Thus it may be that under certain circumstances a resonant condition

exists which results in an abnormally strong reflected wave reaching

the bow shock. This speculation is supported by the observation that

the anomalously high frequency exists in only a very small Mach number

range for any given pressure, and by the observation that, except for

the single case cited (Fig. 41), the timing is always such that the

reflected compression wave and the primary compression wave reach the

bow shock at equally spaced time intervals such that the entropy waves

are observed to be equally spaced.

Existence of the Periodic Instability

As indicated by the regime plot, Fig. 28, it is not possible to

conduct experiments over a wide pressure range since the flow becomes

stable at low pressures and turbulent at high pressures. This sensitivity

of the existence of the regular instability mode to the pressure level

is a problem different from that of the prediction of the frequency

of the instability under given conditions. However, if the proposed

model is to be consistent with the actual gas dynamic processes, then

some plausible explanation of this effect should be contained within

the framework of the model.

Energy is fed into the instability at that point in the cycle when

the reaction rate abruptly increases due to the onset of reaction in

the hot gas behind the contact discontinuity. The magnitude of the

energy release is reflected by the strength of the shock waves generated,

Eq. (31). To explain the presence of the lower boundary of the regime

plot below which the flow is stable, the value of $\Delta\omega$ in Eq. (31),

the units of which are (energy) (length)$^{-2}$ (time)$^{-1}$, must be pressure sen-

sitive. The value of $\Delta\omega$ depends on the magnitude of the temperature

rise which occurs at the end of the induction period. This temperature

rise must indeed be pressure sensitive, since the exothermic termolecular

recombination reactions increase more rapidly with rising pressure than

do the bimolecular endothermic dissocation reactions. This effect is,

of course, responsible for the increase in the equilibrium temperature

rise of exothermic reactions with increasing pressure. Whether this

effect is strong or weak in the highly nonequilibrium condition which

exists at the end of the abrupt temperature rise is not known. Little

work has been published on solutions of the equation governing the

exothermic region of the hydrogen-air or acetylene-oxygen reactions.

According to the regime plot, the instability dies out as pressure

is decreased, but as pressure is increased a turbulent appearance is

generated. Since it is not possible to differentiate between true

turbulent flow and a wrinkled reacted gas boundary by use of schlieren

photography, it is difficult to speculate on the mechanism by which

such turbulence is generated. However, as mentioned in the section

describing the flow field regimes, several of the photographs suggest

that the turbulent appearance is produced by a wrinkling of the boundary

of the reacted gas, just as the vertical striations characteristic of

the regime of regular oscillations are a schlieren effect produced by a

regular, periodic distortion (a corrugation) of the surface of the

reacted gas boundary. The wrinkling of flame fronts has been studied

extensively (Ref. 24, 25), however, there is not complete agreement on the cause. The two causes most widely subscribed to are, (1) that the instability of the flame front is due to the hydrodynamic instability of a fluid containing an interface across which there is a density change; and (2) that the instability is caused by differences in the diffusion coefficients of the fuel and oxidizer which tend to produce inhomogeneities in the mixture. Both phenomena would be intensified by an increase in the magnitude of the property changes across the reaction front boundary. If the turbulent appearance of the reacted gas in the schlieren photographs is due to a wrinkling of the boundary, then the same reasoning used to explain the presence of the low pressure boundary in the regime plot would also apply at the high pressure boundary. The increased pressure results in a greater magnitude of the property changes across the reaction front which results in a greater instability of the reaction front.

Induction Time of Hydrogen-Oxygen Mixtures

By use of Eq. (34) for the theoretical instability wavelength for the P-C D model, it is possible to obtain an expression for induction times based on the experimental ballistic range data. In Fig. 53, the experimental data for the hydrogen-air runs are shown together with the theoretical curves predicted by use of Eq. (34) with an induction time correlation given by:

$$\log_{10}\left([O_2]\,\tau\right) = -9.90 + \frac{15,100}{2.30RRT} \tag{38}$$

This correlation is that which yields the best fit to the data for runs

made at an ambient pressure of 300 mm Hg. The conditions behind the

shock generated by these runs lie in the following ranges:

$$1400 < T\,(°K) < 1880$$
$$9.9 < p\,(atm) < 13.6$$
$$0.0126 < [O_2]\,(mols/liter) < 0.0135$$
$$[H_2]/[O_2] = 2$$

A comparison between this expression and other experimentally

determined correlations is given in Fig. 54. There is good agreement

between these experiments and the data obtained by Ruegg and Dorsey,

Strehlow and Cohen, and an extrapolation of the data of Miyama and

Takeyama. The data of Ruegg and Dorsey (Ref. 2) was obtained by

observing by means of schlieren photography the separation distance

between the shock wave and reaction front in ballistic range experiments

carried out in stoichiometric hydrogen-air mixtures with pressures

behind the shock of from 3 to 12 atmospheres. The data of Strehlow

and Cohen (Ref. 26) is based on use of schlieren photography to determine

the separation between the shock front and the reaction zone in shock tubes

containing hydrogen-oxygen mixtures highly diluted with inert gases.

The pressure range covered by their experiments was not specified.

109

The data of Miyama and Takeyama (Ref. 27) is based on the detection of

OH absorption and the detection of the pressure change associated with

chemical reaction is shock tube. Hydrogen-oxygen mixtures highly

diluted with inert gases were studied. The pressure behind the shock

varied from 4.5 to 5.6 atm. Among their results, they obtained evidence

that under the conditions of their experiments at temperatures above

1100°K the induction times determined by OH absorption detection and by

pressure change were the same.

The induction times obtained from these experiments lie significantly

above the data of Schott end Kinsey and of White and Moore. Schott and

Kinsey (Ref. 28) based their measurements on the detection of OH absorp-

tion in highly dilute hydrogen-oxygen mixtures in a shock tube with

pressures behind the shock on the order of 0.1 atmosphere. White and

Moore (Ref. 29) based their measurements on the use of an interferometer

to measure the separation between the shock and reaction fronts in

undiluted hydrogen-oxygen mixtures. A shock tube having a converging-

diverging section was used to produce a stable wave structure. The

pressure behind the shock front was on the order of 0.12 atm. The

data of Mullaney et al. (Ref. 30) is based on experiments similar to

those of White and Moore; pressures behind the shock are less than

0.1 atmosphere.

The induction time correlation required to bring about agreement between the theoretically predicted and experimentally observed instability wavelengths is thus seen to be in good agreement with induction time correlations obtained by other experimental techniques, particularly with those obtained by experiments at relatively high pressures.

In summary, in this section a model of the high frequency regular periodic instabilities associated with exothermic hypersonic blunt-body flows has been developed. The model is composed of the interaction of a compression wave with the bow shock wave in the nose region of the flow field and the subsequent effect of the contact discontinuity generated by this interaction on the rate of chemical energy release at the reaction front. The model has been shown to predict a wavelength trend that is consistent with the experimental measurements carried out in stoichiometric hydrogen-air mixtures and lean acetylene-oxygen mixtures with the exception that the experiments do not clearly produce the pressure effect which the model predicts. The model has been shown to be consistent with the probable explanation for the existence of the corrugated reacted gas boundary and with effects which could possibly be responsible for the existence of the flow field regime boundaries.

REFERENCES

1. Oppenheim, A. K., Manson, N., and Wagner, H. Gg., "Recent Progress in Detonation Research," AIAA Journal, Vol. I, 1963, pp. 2243-2252.

2. Ruegg, F. W., and Dorsey, W. W., "A Missile Technique for the Study of Detonation Waves," Journal of Research of the National Bureau of Standards, Vol. 66C, 1962, pp. 51-58.

3. Ruegg, F. W., and Dorsey, W. W., Tenth Symposium (International) on Combustion, The Combustion Institute, Pittsburgh, 1965, pp. 476-7.

4. Behrens, H., Struth, W., and Wecken, F., "Studies of Hypervelocity Firings into Mixtures of Hydrogen with Air or Oxygen," Tenth Symposium (International) on Combustion, The Combustion Institute, Pittsburgh, 1965, pp. 245-252.

5. Struth, W., Behrens, H., and Wecken, F., "Untersuchung Chemischer Reaktionen bei Einschuss in Reagierande Gase oder Gasemische mit Hohen Geschwindigkeiten," Deutsch-Franzosisches Forschungsinstitut Technische Mitteilung T 9/63, Saint Louis, France, June 1963.

6. Behrens, H., and Struth, W., "Verbrennungsvorgange bei Hochgeschwindigkeitsschussen mit Kegelgeschossen in Knallgas," Technische Mitteilung T 41/64, Deutsch-Franzosisches Forschungsinstitut, Saint Louis, France, 1964.

7. Fay, J. A., "A Mechanical Theory of Spinning Detonation," Journal of Chemical Physics, Vol. 20, 1952, pp. 942-950.

8. Manson, N., "Propagation des Detonations et des Deflagrations dans les Melanges Gaseux," L'Office National d'Etudes et de Recherches Aeronautiques; Diverse No. 1, Paris, 1947, Transl. ASTIA AD 132-808.

9. Shchelkin, K. I., and Troshin, Ya K., "Gasdynamics of Combustion," Moscow, 1963, Translation: NASA TTF-231, 1964.

10. Shchelkin, K. I., and Troshin, Ya K., "Non-stationary Phenomena in the Gaseous Detonation Front," Combustion and Flame, Vol. 7, June 1963, pp. 143-151.

11. Soloukhin, K. I., "Multiheaded Structure of Gaseous Detonation," Combustion and Flame, Vol. 10, March 1966, pp. 51-58.

12. White, D. R., "Turbulent Structure of Gaseous Detonation," Physics of Fluids, Vol. 4, 1964, pp. 465-480.

13. Opel, G. L., M. S. Thesis, Massachusetts Institute of Technology, Cambridge, Mass., 1959.

14. Duff, R. E., "Investigation of Spinning Detonation and Detonation Stability," Physics of Fluids, Vol. 4, 1961, pp. 1427-1433.

15. Edgerton, H. E., and Strabala, F. I., "Rapid Closing Electronically-Operated Shutter," The Review of Scientific Instruments, Vol. 27, 1956, p. 162.

16. Hayes, W. D., and Probstein, R. F., "Hypersonic Flow Theory," Academic Press, New York, 1959.

17. Korkan, K. D., "Comments on Bow Shock Shape about a Spherical Nose," AIAA Journal, Vol. 4, 1966, pp. 381-382.

18. General Discussion on Detonations, Ninth Symposium (International) on Combustion, Academic Press, New York, 1963, pp. 476-477.

19. Ridyard, H. W., and Storer, E. M. "Stagnation-point Shock Detachment of Blunt Bodies in Supersonic Flow," Journal of Aerospace Sciences, 29, 1962, pp. 751-752.

20. Kistiakowsky, G. B., and Richards, L. N., "Emission of Vacuum Ultraviolet Radiation from Acetylene-Oxygen and Methane-Oxygen Reactions in Shock Waves," Journal of Chemical Physics, Vol. 36, 1962, pp. 1707-1714.

21. Courant, R., and Friedrichs, K. O., "Supersonic Flow and Shock Waves," Interscience Publishers, New York, 1948.

22. Chu, B. T., "Mechanism of Generation of Pressure Waves at Flame Fronts," NACA TN 3683, 1956.

23. Glass, G. P., Kistiakowsky, G. B., Micheal, J. V., and Niki, H., "The Oxidation Reactions of Acetylene and Methane," Tenth Symposium (International) on Combustion, The Combustion Institute, Pittsburgh, 1965, pp. 513-522.

24. Lewis, B., and Von Elbe, G., "Combustion Flames and Explosions of Gases," Academic Press, New York, 1961, pp. 301-310.

25. Williams, F. A., "Combustion Theory," Addison Wesley, Reading, Mass., 1965, Chapter 7.

26. Strehlow, R. A., and Cohen, A., "Initiation of Detonation," Physics of Fluids, Vol. 5, 1962, pp. 97-101.

27. Miyama, H., and Takeyama, T., "Kinetics of Hydrogen-Oxygen Reaction in Shock Waves," Journal of Chemical Physics, Vol. 41, 1964, pp. 2287-2290.

28. Schott, G. L., and Kinsey, J. L., "Kinetic Studies of Hydroxyl Radicals in Shock Waves. II. Induction Times in the Hydrogen-Oxygen Reaction," Journal of Chemical Physics, Vol. 29, 1958, pp. 1177-1182.

29. White, D. R., and Moore, G. E., "Structure of Gaseous Detonation. IV. Induction Zone Studies in H_2-O_2 and CO-O_2 Mixtures," Tenth Symposium (International) on Combustion, The Combustion Institute, Pittsburgh, 1965, pp. 785-795.

30. Mullaney, G. J., et. al., "Determination of Induction Times in One Dimensional Detonations (H_2, C_2H_2 and C_2H_4)," AIAA Journal, Vol. 3, 1965, pp. 873-875.

31. Ladenburg, W. R., et. al., eds., "Physical Measurements in Gas Dynamics and Combustion," Vol. IX, of High Speed Aerodynamics Series, Princeton University Press, Princeton, N.J., 1954.

32. Joos, G., "Theoretical Physics," Hafner Publishing Co., New York, 1950, p. 393.

33. Chernyi, G. G., "Introduction to Hypersonic Flow," Academic Press, New York, 1961.

34. Shapiro, A. H., "The Dynamics and Thermodynamics of Compressible Fluid Flow," Vol. I., The Ronald Press Company, New York, 1953.

35. "Equations, Tables and Charts for Compressible Flow," NACA Report
    1135, 1953.

36. Nicholls, J. A., Adamson, T. C., and Morrison, R. B., "Ignition
    Time Delay of Hydrogen-Oxygen-Diluent Mixtures at High Temperatures,"
    AIAA Journal, Vol. 1, pp. 2253-2257, 1963.

37. Duff, R. E., "Calculation of Reaction Profiles Behind Steady-State
    Shock Waves," Journal of Chemical Physics, Vol. 28, 1958, pp. 1193-
    1197.

38. Ferri, A., Libby, P.A., and Zakkay, V., "Theoretical and Experimental
    Investigation of Supersonic Combustion," Third ICAS Congress, Stock-
    holm, Sweden, 1962.

39. Momtchiloff, I. N., Taback, E. D., and Buswell, R. F., "Kinetics
    in Hydrogen-Air Flow Systems, I, Calculation of Ignition Delays
    for Hypersonic Ramjets," Ninth Symposium (International) on Combus-
    tion, Academic Press, New York, 1963, pp. 220-230.

40. Brokaw, R. S., "Analytic Solutions to the Ignition Kinetics of the
    Hydrogen-Oxygen Reaction,"Tenth Symposium (International) on Combus-
    tion, The Combustion Institute, Pittsburgh, 1965, pp. 269-278.

41. Kondratiev, V. N., "Kinetics of Chemical Gas Reactions," Academy
    of Sciences, Moscow, 1958, (English Translation) AEC-tr-4493,
    February 1962, pp. 678-682.

42. McBoede, B. J., et. al., "Thermodynamic Properties to 6000° K for
    210 Substances Involving the First 18 Elements," NASA SP-3001, 1963.

43. Sedney, R., and Kahl, G. D., "Interferometeric Study of the Hypersonic Blunt Body Problem," Journal of Planetary and Space Sciences, Vol. 4, 1961, pp. 337-351.

44. Shapiro, A. H., "The Dynamics and Thermodynamics of Compressible Fluid Flow," Vol. II, The Ronald Press, New York, 1955, p. 684.

45. Officer, C. B., "Introduction to the Theory of Sound Transmission," McGraw-Hill, New York, 1958.

46. Kaufman, F., and Del Creco, F. P., "Fast Reactions of OH Radicals," Ninth Symposium (International) on Combustion, The Combustion Institute, Academic Press, New York, 1963, pp. 659-666.

47. Baldwin, R. R., Ninth Symposium (International) on Combustion, The Combustion Institute, Academic Press, New York, 1963, p. 667.

LIST OF SYMBOLS

A Constant
Bow shock correlation parameter, Eq. (1)

a Acoustic speed
Shock reflection coefficient parameter, Eq. II-(3)

B Density function, Eq. (11)
Relative brightness (APPENDIX I)

BS Bow shock

b Shock reflection coefficient parameter, Eq. II-(4)

CD Contact discontinuity

c Acoustic speed
Concentration

c^* Acoustic s eed at M = 1.0

D Diameter
First Damkohler similarity group

E Activation energy

F Freezing point

$K_g(T)$ Equilibrium constant

k Nondimensional specific reaction rate, Eq. III-(3)
Constant

k' Specific reaction rate

M Mach number

M^* Dimensionless speed, v/c^*

n Integer
Bow shock correlation parameter, Eq. (1)
Index of refraction (APPENDIX I)

P	Pressure
R	Body radius Gas constant Rarefaction wave
RF	Reaction front
r	Radial coordinate
P	Compression wave, shockwave
s	Path length Entropy
T	Temperature
TT	Period
t	Time
v	Velocity
W	Reaction zone width
x	Axial coordinate measured from shock apex Mol fraction
$\bar{x}$	Ratio of O_2 to H_2
y	Transverse coordinate
Z	Entropy zone
z	Transverse coordinate
α	Angle of incidence (APPENDIX I) Ratio of Reaction rates, Eq. III-(17)
γ	Ratio of specific heats
$\triangle$	Detachment distance

$\triangle'$ Detachment distance, unreacted gas, Fig. 43

δ Streamline inclination with respect to flowfield axis

δ' Transformation constant, Eq. III-(2)

ϵ Angular deflection

θ Wave inclination with respect to flowfield axis

λ Wavelength
Time constant

μ Mach angle

ν Frequency

ρ Density

τ Induction time

Φ Equivalence ratio

ω Rate of chemical energy release

Subscripts

b Backward rate

f Forward rate

i Condition at end of induction period

M Third body

n_1 Normal to compression wave 1

R Condition behind reaction front

S Condition behind shock

u Condition in unreacted gas

w Wake

o Condition in undisturbed gas

APPENDIX I

INTERPRETATION OF SCHLIEREN PHOTOGRAPHS

The schlieren photographs reproduced in this report were used to determine the location of the various wave fronts in the flow field and the direction of the gas density change across these fronts. Location of the shock waves or entropy waves which produce a given schlieren pattern in an axisymmetric flow field is straightforward since the light rays which are bent to the greatest extent are those tangent to the fronts. The view produced is thus a cross-sectional view of the flow field in a plane through the axis of symmetry, normal to the undisturbed light rays. Care must be exercised, however, in determining the direction of the density change; i.e., whether the density increases or decreases across a given discontinuity. The necessary considerations are detailed below.

The schlieren system employed in the experimental apparatus is a double pass system utilizing a single spherical mirror. As illustrated in Fig. 55a, the light source and the knife edge are located slightly off the optical axis near the center of curvature of the mirror. Both the light rays incident to and reflected from the mirror are shown in this figure; in the remaining sketches only the reflected rays are shown. When a region of changed index of refraction is located in the light path, the rays are bent in accordance with the laws of optics.

A brightened or darkened image is produced on the viewing screen depending on the direction of bending and on orientation of the knife edge. For example, the effect of placing a glass wedge in the test area is shown in Fig. 51b. The light rays are deflected onto the knife edge and are cut off, thus producing a darkened imagine on the screen. If the knife edge were inserted from the right instead of from the left, a brightened image would be produced. Also, if the wedge were pointed in the opposite direction, the image would be brightened rather than darkened.

The bending of the light rays can be either due to (1) refraction at a boundary separating two media of different refractive index or (2) to the curvature developed by a light ray on passing through a medium having a refractive index gradient in a direction normal to the ray (Ref. 31).

The magnitude of the former effect is governed by Snell's law of refraction

$$n_1 \sin \alpha_1 = n_2 \sin \alpha_2 \qquad \text{I-(1)}$$

where: n - refractive index

         α - angle between normal to boundary and light ray

and the subscripts refer to the two media. It is this effect which produces the deflection of a light ray on passing through a glass wedge. The direction of the deflection which produces the brightening or darkening on the schlieren screen is thus dependent on the boundary

geometry and on the direction of the change in the refractive index on crossing the boundary. It is this effect which is primarily responsible for the patterns observed on schlieren photographs of axisymmetric supersonic flows. In the gas dynamic case, the variation of the index of refraction with gas density is given by an expression of the form

$$n = 1 + k\rho \qquad \text{I-(2)}$$

where

$$\rho = \text{gas density}$$

$$k = \text{constant (typical value} = 0.000292 \text{ for air at STP.)}$$

The magnitude of the angular deflection, ϵ, produced by a refractive index gradient in a direction, x, normal to the direction of the light ray, z, is governed by the expression (Ref. 31, p. 9):

$$\epsilon = \int_{z_1}^{z_2} \frac{\partial}{\partial x} \ln n \, dz \qquad \text{I-(3)}$$

where the integration is performed throughout the test area or, effectively, between the flow boundaries. In the case of the glass wedge, no deflection due to this cause would be produced if the glass were homogeneous. In the aerodynamic case, however, streamwise density gradients are usually present which can produce a ray deflection.

These two effects which produce schlieren patterns both derive from the basic law of physical optics known as Fermat's law. The law states that light propagation takes place along a path such that the

first variation of the optical path is zero (Ref. 32): $\delta \int_{S_1}^{S_2} n\,ds = 0.$
Eq. I-(3) is the form taken by the Euler's equation for the variational
equation. Snell's law replaces the Euler equation at a surface of dis-
continuity (Ref. 31). Since both effects derive from the same basic law,
it can be expected that under certain conditions both effects can be
evaluated by a single calculation. That this is so for the aerodynamic
case is demonstrated below.

In the gas dynamic case, which is the Euler equation of the varia-
tional problem, Eq. I-(3) can be written as

$$\mathcal{E} = \int_{z_1}^{z_2} \frac{\partial}{\partial x}\left(n - n_o\right) dz \qquad\qquad \text{I-(4)}$$

where: n_o is the refractive index of undis-
turbed gas

since the value of n given by Eq. I-(2) is very close to unity. The
form of Eq. I-(4) and the fact that Snell's law deals with the boundaries
of the flow field suggests that the expression

$$\mathcal{E}_{TOT} = \frac{\partial}{\partial x} \int_{z_1}^{z_2} \left(n - n_o\right) dz \,, \qquad\qquad \text{I-(5)}$$

where the derivative has been brought outside the integral sign, can be
used to evaluate the total angular deflection of the light ray. Note
that Leibnitz' rule cannot be rigorously applied since the integrand is
discontinuous at the boundaries. This is readily demonstrated in the
following paragraph for the case of the wedge (Fig. 55c).

Considering the deflection of the ray through one surface of the

wedge (Fig.55c), Eq. I-(1) can be written as

$$n_1 \sin \alpha_1 = n_2 \sin (\alpha_1 - \epsilon)$$ I-(6)

$$\text{where: } \epsilon = \alpha_2 - \alpha_1$$

Expanding and rearranging terms:

$$\epsilon \approx \sin \epsilon = \frac{(n_2 - n_1 \cos \epsilon) \sin \alpha_1}{\cos \alpha_1} \approx (n_2 - n_1) \tan \alpha_1 \quad \text{I-(7)}$$

for $\epsilon \ll 1$.

Evaluating Eq. I-(5) for the upper surface of the wedge

$$\epsilon_{TOT} = \frac{2}{\partial x} \int_{z_1}^{0} (n_2 - n_1) dz$$

$$= - (n_2 - n_1) \frac{\partial z_1}{\partial x}$$

$$= (n_2 - n_1) \tan \alpha_1 \quad \text{I-(8)}$$

which is the same expression as obtained by application of Snell's law,

Eq. I-(7).

From the foregoing it is concluded that the total angular deflection

of a light ray can be evaluated by determining the gradient of the total

optical path of the ray. By substituting Eq. I-(2) into Eq. I-(5), and

noting that the brightness of the image on the viewing screen is propor-

tional to the angular deflection of the ray, the following expression

is obtained:

$$B = \text{CONST} \frac{2}{2x} \int_{z_1}^{z_2} \Delta\rho \, dz \qquad \text{I-(9)}$$

where   = Relative brightness

Use of Eq. I-(9) to predict the characteristics of a schlieren

photograph of a hypersonic sphere is illustrated in Fig. 56. A vertical

knife edge orientation is assumed. Only the effect of the bow shock wave

on the image plane brightness is examined. Fig. 56a shows the section

produced by the plane $z = 0$ which is effectively the plane seen on the

viewing screen. The location of a typical plane $y = y_0$ containing the light

rays to be examined in detail is specified.

The plane $y = y_0$ is shown in Fig. 56b. The intersection of the bow

shock with the plane $y = 0$ is shown as a dashed line; the intersection

with the plane $y = y_0$ is shown as a solid line. The paths of selected

light rays are shown with the deflection angles much exaggerated. The

path of the undeflected ray is shown as a dashed line. The basis for

sketching the ray paths as shown is provided in Figs. 56c and 56d. In

Fig. 56c is shown the integrated light path in the plane $y = y_0$ for all

values of x. This curve is constructed by considering how the term

$\int_{z_1}^{z_2} \Delta\rho \, dz$ must behave based on the known behavior of the flow field.

Between $x = 0$ and $x = x_1$, $\Delta\rho$ is zero since the flow is undisturbed. At

$x = x_1$, the bow shock is encountered and $\int_{z_1}^{z_2} \Delta\rho \, dz$ begins to take on con-

126

tinuously greater positive values due to the progressively greater values of $z_2 - z_1$, as defined by the solid contour of Fig. 56b. The $\int_{z_1}^{z_2} \Delta \rho \, dz$ grows at a decreasing rate with increasing χ because of the parabolic shape of the contour. At the same time, the average value of $\Delta \rho$ must decrease with increasing χ due to expansion of the flow. At large values of χ the mean value of $\Delta \rho$ must decrease to zero or become slightly negative as the pressure decays to ambient (the gas temperature will be greater than ambient and the density less due to the heightened entropy caused by the shock). Hence the value of $\int_{z_1}^{z_2} \Delta \rho \, dz$ must be zero initially, must be positive in the intermediate region, must have smaller gradients with increasing χ, and must finally decrease to zero.

Having established the shape of the $\int_{z_1}^{z_2} \Delta \rho \, dz$ curve, the streamwise gradient can be sketched as shown in Fig. 56d. The principal features are the abrupt change in brightness at $\chi = \chi_1$, and the brightness inversion in the downstream region. If the knife edge were positioned such that the bow shock is dark, then somewhat downstream the inviscid flow field should appear brightened; far downstream it should appear to have the brightness of the background. The brightening can be seen in Fig. 21. If the knife edge were reversed such that the bow shock is bright, the streamwise expansion causes a darkening as illustrated by Fig. 13. The inversion is most noticeable in the vicinity of the sphere where the streamwise density gradients are large due to rapid expansion about the ball.

The utility of using Eq. I-(9) to predict the relative brightness

characteristics of the photographs becomes apparent if one would attempt

to predict the separate effects of boundary refraction (Snell's law) and

of ray curvature due to continuous streamwise density gradients for the

example of Fig. 56. To estimate which effect predominates along a path

such as $\chi = \chi_\beta$ would require numerical calculations.

Corrugated Reacted Gas Boundary

The alternate dark and bright bands which characterize the reacted

gas zone in the case of the regular periodic instability (e.g., Fig. 21)   .

are accounted for in the analysis given in Fig. 57. The distinct, highly

contrasting bands are a result of the sawtooth edge of the reaction zone

refracting the light in the manner accounted for by Snell's law. The

boundary geometry and the direction of density change across the boundary

cause the refraction. Streamwise density gradients within the volume

and the refraction at the bow shock boundary effect the magnitude of

the $\int_{z_1}^{z_2} \rho \, dz$ but have little effect on its streamwise gradient.

The direction of the density change across the sawtooth or corru-

gated boundary can be determined by noting whether the image is brightened

or darkened at a given location. Choosing a zone in which the sawtooth

edge diverges in the downstream direction, it is seen that the shading

is in the opposite sense from that of the bow shock. The bow shock

diverges in the downstream direction and the density increases when pro-

ceeding from the free stream into the inviscid wake. To produce the

128

observed shading, the density must decrease when passing across the corrugated boundary from the inviscid wake. The suggestion that the volume within the corrugated boundary contains reacted gas is thus supported.

Inviscid Wake - Pressure Waves and Entropy Waves

The two distinct families of waves observed in the inviscid wake in the case of the regular periodic instability are shown schematically in Fig. 58a. A knife edge position producing a darkened bow shock is assumed. The waves identified as compression waves in the schematic appear as bright bands on the photographs. They are bounded on either side by a background brightness equivalent to that produced by an undisturbed inviscid wake. On the other hand, the entropy waves appear as dark bands bounded on the downstream edge by the background brightness and on the upstream side by a bright band (e.g., Fig. 21). The pressure waves extend from the bow shock to the vicinity of the corrugated boundary of the reaction zone where they become indistinct. The entropy waves extend from the bow shock to the reaction zone boundary where they assume a definite position with respect to the boundary corrugations.

The contours of the waves in the plane $y = y_0$ are shown in Fig. 58b and the relative density profile along the centerline of this plane is shown in Fig. 58c. In the latter figure, the decay of the density change caused by the entropy wave is shown to be rapid, whereas the

decay of the density change due to the pressure wave is shown to be gradual. A rapidly decaying wave will produce both positive and negative streamwise density gradients having somewhat the same magnitudes. The schlieren record will then be a double band, one bright and one dark. A gradually decaying wave will produce a single band since the density gradient in the decay region will not differ greatly from that of the background, and the schlieren record caused by the decay will be too weak to be detectable. Although the assumed decay rates will generate the observed schlieren patterns, it is questionable that the two waves can have significantly different decay characteristics, particularly near the bow shock. The entropy wave is generated by the interaction of the compression wave with the bow shock and therefore its spatial structure would be determined by the compression wave structure; the structures of the two waves would be expected to be similar.

The integrated optical path and the relative brightness derived from Figs. 58b and 58c are given in Figs. 58d and 58e.

APPENDIX II

SHOCK INTERACTION ANALYSIS

The prominent inviscid wake wave pattern which characterizes the regular periodic instability is produced by the interaction with the bow shock wave of compression waves (or weak shock waves) generated by the unstable nose region flow. The compression waves and the entropy waves (slip lines, contact discontinuities) produced by the interaction are visible on the schlieren photographs and form the observed net-like wave pattern. The reflections of the compression waves are not visible in the photographs. The calculations carried out to determine the geometry of the interaction process, the nature of the reflected wave, and the strengths of the several waves, are detailed hereunder. The calculations indicate that the compression wave must be a very weak wave, virtually an acoustic wave, and that the reflected wave is a rarefaction wave and cannot be expected to be visible in the schlieren photographs. The predicted and observed wave interaction geometries are not in agreement; there is a small but significant discrepancy, the reason for which is as yet not known. Calculations of the relative magnitudes of the density changes across the compression waves and across the contact discontinuities do not explain the greater schlieren effect produced by the contact discontinuities. The observed decrease in the amplitude of the reacted gas boundary corrugations with in-

creasing projectile velocity is shown to be consistent with the predicted

shock interaction behavior.

Geometry of Shock Interaction

The interaction is shown schematically in Fig. 27. The interaction

as observed in a coordinate system fixed to the ball, or as depicted in

one of the instantaneous schlieren photographs, is sketched in Fig. 27a.

The compression wave, labeled an acoustic wave, propagates downstream,

from left to right, sweeping along the bow shock and generating an in-

finitesimal contact discontinuity. The contact discontinuity is fixed

to the fluid elements and therefore trails behind the faster propagating

acoustic wave. The process as observed in this coordinate system is

unsteady; to facilitate the analysis, the interaction is transformed

to a stationary system.

Before proceeding, the parameters which characterize the interaction

and which are measured in the unsteady system will be indicated. They

are:

M_∞ - Free stream Mach number

Θ_1 - Bow shock angle

Θ_3 - Compression wave inclination

Θ_{CD} - Contact discontinuity inclination

These four quantities completely determine the interaction; i.e., all

flow field quantities can be calculated with these values given. How-

ever, in order to proceed with the calculation in the most straight-
forward manner, it is convenient to assume the magnitude of the propaga-
tion rate (or the strength) of the compression wave and to reserve one
of the measured quantities as a check on the assumption. The compression
wave speed was measured by the dual schlieren pictures and found to be
on the order of the acoustic speed, and therefore this value is assumed
for the first step in the iteration. The angle Θ_{c_D} is used to check the
assumption.

The steady state coordinate system is that system in which the
interaction point, O , is stationary. Therefore, the transformation
involves subtracting the velocity of the interaction point from all other
velocities. The direction of the velocity vector is given by the slope
of the bow shock at the intersection point. The magnitude of the velo-
city of the intersection point depends on the gas velocity and acoustic
speed behind the bow shock and on the angle between the bow shock and
compression wave, $\Theta_1 + \Theta_3$. It can be seen by reference to Fig. 27a that
if the acoustic wave is nearly parallel to the bow shock, as would be
the case in the nose region of the ball, then the velocity of the inter-
section point becomes nearly infinite. In this case, of course, one
has a case of the interaction of normal waves which is treated by other
means. (See Fig. 45.)

The velocity of the intersection point is given by

$$\frac{v_0'}{a_0} = \frac{v_{nss}'}{\sin(\theta_1 + \theta_3)}$$

II-(1)

v_{nss}' = Velocity of compression
wave normal to itself.

The interaction in the transformed coordinate system is shown in
Fig. 27b and again in Fig. 27c where the system has been rotated such
that the transformed free stream velocity is parallel to the x-axis.
The variables in this system are denoted by primes. The interaction
then takes on the more familiar geometry of the interaction of two waves
of the same family. For the interactions typical of these experiments,
however, the primary shock inclination, θ_1, is quite steep and the flow
deflection across the shock approaches the maximum possible deflection
for the given free stream Mach number. The weak compression wave
appears to be inclined upstream with respect to the free stream, but must,
of course, be inclined downstream with respect to the flow immediately
ahead of it. (This is discussed further below.) The contact discon-
tinuity must be parallel to the streamlines downstream of the bow shock.
Shown in Fig. 27c is the calculated inclination of the contact dis-
continuity and the position of the contact discontinuity as observed
in the schlieren photograph. There is a discrepancy of 9.3°. In the
case assumed here, where the compression wave is an acoustic wave,
the flow in all regions downstream of the bow shock is uniform.

Since all waves are stationary in the transformed coordinate system

of Fig. 27c, the **normal** component of Mach number of the gas approaching

the acoustic wave (Wave 3) must be unity (M'_{n3} = 1.0) since this is

the assumed basis of the transformation. Furthermore, the inclination

of the compression wave to the approaching flow must be between the

normal to the flow and the Mach angle. In the case where the compression

wave is assumed to be an acoustic wave, the Mach angle is 90°, hence

the acoustic wave must be normal to the flow. This is seen not to be

the case in the construction of Fig. 27c where the angle between a

streamline and the wave front is calculated to be 99°. This is indica-

tive either of errors in the measurement of the wave angles or that the

compression wave is not an acoustic wave; both possibilities are con-

sidered below.

The most likely measurement error would involve the inclination

of the compression wave, since the schlieren effect produced by this

wave is relatively weak near the bow shock (see Figs. 13 or 26). The

bow shock angle is easily measured and the free stream velocity measure-

ments are considered reliable. The measured inclination angle of the

contact discontinuity is subject to question, but this value has not as

yet entered the analysis. With the compression wave assumed to be

acoustic, then a value of the inclination, θ_3 , can be calculated for

which the wave is normal to the flow. This angle is found to 31.7° in

contrast to the measured value of 41.3° (Fig. 27a). The calculated parameters in the primed coordinate system corresponding to this compression wave angle of 31.7° compared to those given in Fig. 27c are:

Quantity	Compatible System	Figure 27c
Shock inclination, $\Theta_1{}'$	62.8°	62.3°
Acoustic wave inclination, $\Theta_3{}'$	59.0°	49.9°
Mach No. after shock, $M_1{}'$	1.0	1.03
Contact discontinuity inclination, Θ_{CD}	31.0°	31.1°
Observed C.D. inclination	22.3°	21.8°

It is seen that the change of 9.6° in the inclination of the acoustic wave produces changes in the calculated angles of less than 1°. The discrepancy between the observed and calculated inclinations of the contact discontinuity remains essentially unchanged. That a change in the inclination of the acoustic wave should indeed produce a very small change in the calculated inclination of the contact discontinuity can be inferred by reference to Fig. 27a. The contact discontinuity inclination is primarily determined by the rate at which the intersection point moves along the bow shock. This in turn depends strongly on the propagation rate of the compression wave but only weakly on its inclination except when the angle between the bow shock and the compression wave is quite small. It is therefore concluded that the discrepancy between the observed and measured inclinations of the contact dis-

continuity cannot be attributed to errors in measurements of the compression wave inclination.

If the compression wave were assumed to be of finite amplitude rather than of infinitesimal amplitude as heretofore assumed, there exists a wide range of values of compression wave inclination angle which satisfy the requirement that the compression wave lie between the normal to the flow and the Mach line. This is a result of the rapid decrease of the Mach angle as the flow Mach number increases from unity. For example, if the compression wave is assumed to be a Mach 1.1 shock, the geometry conditions are compatible for all compression wave angles, $\varnothing_3$, below 35°. In these cases, however, another consideration becomes important. In the steady state reference system for compression waves of finite strength, the flow downstream of the compression wave remains supersonic for only a very limited range of wave strengths. If the flow does not remain supersonic throughout, no solution to the interaction problem exists in which the various regions can be joined by a wave configuration of the type considered. The configuration is shown in detail in Fig. 59; the construction of which is similar to that of Fig. 27c but wherein the reflected wave has been included. No satisfactory configuration has been found which can provide for the possibility of subsonic flow behind the compression wave and which is at the same compatible with the observation that the waves are only slightly curved

and therefore of nearly uniform strength throughout their transverse extent. Furthermore, no deflection of the bow shock is observed at the intersection point; this would necessarily be the case if the wave were a stronger shock. Such a break is observed in the cases where the reaction zone appears turbulent; apparently much stronger disturbances are generated in this case. (See Figs. 7 and 8.) From these considerations it is concluded that the compression wave strength is sufficiently small such that the flow behind the compression wave remains supersonic.

Using the measured values of θ_1 and M_0 for any given run and values of θ_3 in the neighborhood of the measured value, the range of compression wave strengths for which the flow remains supersonic throughout was found to be extremely small. Typically, values of M_1' smaller than 1.03 were required to satisfy the supersonic flow requirement. It is, therefore, concluded that the compression wave is extremely weak; it is virtually an acoustic wave. The discrepancy between the observed and calculated contact discontinuity slopes cannot therefore be the result of any difference between the actual compression wave strength and the assumed infinitesimal strength.

Regardless of the above considerations, the discrepancy could not be resolved by assuming a value for the compression wave propagation speed higher than the acoustic speed. This can be visualized in Fig. 27a by observing that if the propagation rate of the compression wave were higher, then the interaction point 0 would move along the bow shock at

a faster rate. The velocity of the gas which has passed through the disturbed portion of the bow shock would increase by only a small amount due to the increased compression wave strength. The contact discontinuity would therefore be effectively stretched and would lie closer to the bow shock. This change in slope is in the opposite sense to that required to explain the discrepancy. A decrease in the propagation rate below the acoustic speed would be required. This, of course, is not possible from a physical standpoint.

Calculations were carried out to determine if the discrepancy were due to the perfect gas assumption or to the assumption of two-dimensional flow. As expected, however, calculations using thermodynamic data accounting for specific heat variation produced results which differed only insignificantly from the constant γ calculations. The two-dimensional relations apply strictly only in the immediate vicinity of the intersection point. The effect of the bending of the contact discontinuity due to three-dimensional effects was estimated by determining its contour for a conical flow field having the same shock radius as the bow shock. The effect was small and tended to incline the contact discontinuity even more, slightly increasing the discrepancy.

The variation of the measured and calculated wave interaction parameters with distance downstream of the shock apex for a typical case is shown in Fig. 60. It is seen that the measured contact discontinuity

slope increases continuously, whereas the calculated value remains nearly constant. Thus the discrepancy increases with increasing downstream distance. As noted previously, to explain the discrepancy in terms of the preceding analysis, an effect must occur which produces the same result as would a decrease in the acoustic speed. The effect has not been determined.

Reflected Wave

Since the strength of the compression wave is small, the character of the reflected wave can be determined by use of expressions for the reflection coefficients of disturbances which interact with shock waves. Analytic expressions for the reflection coefficient for a perfect gas with constant specific heats for a two-dimensional interaction with uniform flow upstream of the bow shock are given by Chernyi (Ref. 33) as:

$$\lambda = \frac{a-b}{a+b} \qquad \text{II-(2)}$$

$$a = 2\frac{\tan(\theta_1 - \delta_1)}{\tan \mu_1}\left[1 - \frac{\gamma-1}{2} M_1^2 \sin^2(\theta_1 - \delta_1)\left(\frac{p_1}{p_0} - 1\right)\right] \qquad \text{II-(3)}$$

$$b = 1 + \frac{p_1}{p_c}\frac{\tan^2(\theta_1 - \delta_1)}{\tan^2 \mu_1} - \gamma M_1^2 \sin^2(\theta_1 - \delta_1)\left(\frac{p_1}{p_0} - 1\right) \qquad \text{II-(4)}$$

where $\lambda \equiv \frac{p_{3R} - p_1}{p_2 - p_1}$ = reflection coefficient

$\mu \cong$ Mach angle

and the other symbols are defined in Fig. 59.

The parameters in these expressions can be related to the free stream

Mach number, M_0', and bow shock angle, Θ_1', through the following:

$$\frac{P_1}{P_0} = \frac{(\gamma+1)M_0'^2 \sin^2\Theta_1'}{(\gamma-1)M_0'^2 \sin^2\Theta_1' + 2} \qquad \text{II-(5)}$$

$$M_1'^2 \sin^2(\Theta_1'-\delta_1')\left(\frac{P_1}{P_0}-1\right) = \frac{(\gamma+1)M_0'^2 \sin^2\Theta_1'}{2\gamma M_0'^2 \sin^2\Theta_1' - (\gamma-1)} \qquad \text{II-(6)}$$

$$\tan^2\mu_1' = \frac{1}{M_1'^2-1} \qquad \text{II-(7)}$$

$$\tan(\Theta_1'-\delta_1') = \frac{\tan\Theta_1'}{\frac{P_1}{P_0}} \qquad \text{II-(8)}$$

A plot of the variation of the reflection coefficient as a function

of the upstream Mach number, M_0', and the flow deflection angle,

$\Theta_1'-\delta_1'$, is given in Fig. 61 (Fig. 4.7 of Ref. 33). It is seen that the

reflection coefficient can be either positive or negative and that the

value decreases rapidly near the limiting value of $\Theta_1'-\delta_1'$. This limit

is approached as the Mach number behind the bow shock approaches unity.

It is this branch of the curves that is of interest in the problem at

hand. In terms of Eqs. II-(2) to II-(4), the rapid decrease in Λ

is the result of the rapid increase to infinity of $\tan\mu_1'$, as M_1' approaches

unity. From the expressions for the parameters a and b, it is apparent

that a approaches zero and b remains finite and non-zero as $\tan\mu_1'$ becomes

large. Thus Λ approaches -1 in the limit. In this case the compression

wave is reflected as an expansion wave of equal strength.

The value of the reflection coefficient on the nearly vertical leg

of the curves of Fig. 61 can be determined approximately by evaluating

the flow parameters required by Eqs. II-(2) and II-(3), except for $\tan \mu_1'$,

in the limiting case where $M_1' = 1$. The exact value of $\tan \mu_1'$ is then

used with the resulting expression to evaluate λ. The limiting value

of the shock angle for sonic flow used in Eqs. II-(5) to II-(7) is given

by the relation

$$\sin^2 \theta_1^* = \frac{1}{4 \gamma M_0'^2} \left\{ (\gamma+1) M_0'^2 - (3-\gamma) + ([\gamma+1][(\gamma+1) M_0'^4 - 2(3-\gamma) M_0'^2 + (\gamma+9)])^{1/2} \right\} \qquad \text{II-(9)}$$

The results of calculations for a typical case are given in Fig. 16.

The values of M_0' and θ_1' used are those given in Fig. 27c. The compression

wave inclination, θ_3', was assumed to be 25° and the strength of the

compression wave corresponds to a Mach 1.005 shock. Using conditions

at the M = 1 limit, the parameters a and b can be written as:

$$a = \frac{1.085}{\tan \mu_1'} \qquad \qquad \text{II-(10)}$$

$$b = 0.158 + \frac{1.200}{\tan^2 \mu_1'} \qquad \qquad \text{II-(11)}$$

The condition for which no reflection occurs, a=b, corresponds to $M_1' = 1.016$.

Under the assumed conditions of a M = 1.005 shock, M_1' is found to be

1.0122. The reflection coefficient is calculated to be $\lambda = -0.0682$;

that is, the reflected wave for the assumed conditions in a very weak

rarefaction wave.

The Mach number after the Mach 1.012 shock is only slightly greater than unity, $M_2' = 1.005$, such that the Mach angle of the flow, which determines the position of the head of the reflected expansion wave, is quite large, $\mu_2' = 86.0°$. Figure 59, therefore, illustrates that the incident compression wave and the reflected expansion wave are nearly coincident.

As mentioned previously, no reflected wave is observed in the schlieren photographs. This could be due to the fact that the incident and reflected waves are nearly coincident; and, therefore, the two waves cannot be resolved. Even if the separation were sufficient for resolution, however, the schlieren effect produced by a rarefaction wave is extremely weak and such waves could not be expected to be visible. Fig. 16.29 of Ref. 34 illustrates this point.

Wave Strengths

The calculated density changes across the wave fronts, which influence the strengths of the schlieren effect produced by the waves, are noted in Fig. 59. The density ratio across an oblique shock wave is given by the expression:

$$\frac{\rho_2}{\rho_1} = \frac{(\gamma+1)\frac{p_2}{p_1} + (\gamma-1)}{(\gamma-1)\frac{p_2}{p_1} + (\gamma+1)} \qquad \text{II-(12)}$$

which in the weak shock limit can be differentiated to give the density

change across the compression wave in terms of the pressure change:

$$\frac{\Delta \rho}{\rho} = \frac{1}{\gamma} \left(\frac{\Delta p}{p} \right)_3 \qquad \qquad \text{II-(13)}$$

This same expression is also obtained by differentiation of the isentropic

relation which applies to the density change across the expansion wave:

$$\frac{\rho_2}{\rho_1} = \left(\frac{p_2}{p_1} \right)^{1/\gamma} \qquad \qquad \text{II-(14)}$$

To evaluate the density change across the contact discontinuity,

the change in the density behind the bow shock due to the disturbance

of the incident compression wave is calculated by use of Eq. II-(12).

For weak disturbances, differentiation yields:

$$\frac{\rho_{3B} - \rho_1}{\rho_1} = \left[\frac{\gamma+1}{(\gamma+1)\frac{p_1}{p_o} + (\gamma-1)} - \frac{\gamma-1}{(\gamma-1)\frac{p_1}{p_o} + (\gamma+1)} \right] \frac{p_{3B} - p_1}{p_1} \qquad \text{II-(15)}$$

Since the pressure difference across the contact discontinuity is zero,

from Fig. 59

$$\frac{p_{3B} - p_1}{p_1} = \frac{p_2 - p_1}{p_1} + \frac{p_{3A} - p_2}{p_1}$$

$$= (1 + \lambda)\left(\frac{\Delta p}{p} \right)_3 \qquad \qquad \text{II-(16)}$$

The net change in density across the incident compression wave and

reflected expansion wave is given by:

$$\frac{\rho_{3A} - \rho_1}{\rho_1} = \frac{1}{\gamma} \frac{p_{3A} - p_1}{p_1}$$

$$= \frac{1}{\gamma} (1 + \lambda)\left(\frac{\Delta p}{p} \right)_3 \qquad \qquad \text{II-(17)}$$

144

The density change across the contact discontinuity is then given by:

$$\frac{\rho_{3A}-\rho_{3B}}{\rho_1} = (1+\lambda)\left(\frac{\Delta P}{P}\right)_3 \left\{\frac{1}{\gamma} - \left[\frac{\gamma+1}{(\gamma+1)\frac{P_2}{P_0}+(\gamma-1)} - \frac{\gamma-1}{(\gamma-1)\frac{P_2}{P_0}+(\gamma+1)}\right]\right\} \text{II-(18)}$$

This expression indicates that the value of the density change increases with increasing bow shock strength. This trend is caused by the greater irreversibility associated with stronger shocks. The expression also indicates that for negative values of the reflection coefficient, the density change across compression wave is always greater than the change across the contact discontinuity. This is not indicated by the schlieren photographs where it is observed that the schlieren effect produced by the contact discontinuities is stronger than that produced by the compression waves. Since the schlieren effect is related to the density gradients through the wave rather than to the total density change, a difference in wave structure may be responsible for the stronger schlieren effect of the contact discontinuity.

The temperature change across the contact discontinuity can be found directly from Eq. II-(18), since the pressure change across the wave is zero. Thus the temperature in Region 3B is higher than that in 3A. As discussed in the section on the instability mechanism, the magnitude of this temperature change is important in determining the amplitude of the corrugations of the reacted gas boundary. The amplitude of the corrugations is observed to diminish with increasing reaction zone

width, implying that the magnitude of the temperature change across the contact discontinuity decreases with increasing distance from the flow field axis. This could be due either to a decay in the strength of the incident compression wave with distance from the axis or to a decrease in the strength of the contact discontinuity generated by a compression wave of a given strength as the wave moves outward from the axis.

Equation II-(18) indicates that the latter effect does indeed occur; i.e., the magnitude of the temperature change for a given $\left(\frac{\Delta P}{P}\right)_3$ decreases with decreasing $\frac{P_1}{P_0}$ and increasing λ . The pressure rise across the bow shock, $\frac{P_1}{P_0}$, is maximum on the axis and decreases to unity far from the axis. The reflection coefficient value will lie on the vertical leg of the curves of Fig. 61, but whether it increases or decreases with increasing distance from the axis must be determined from Eq. II-(3) and II-(4) which requires knowledge of the change in form taken by the interaction configuration (Fig. 59). The qualitative arguments given in the following paragraph indicate that λ does increase.

Reference to Fig. 27a and to Fig. 52, which shows the change in the compression wave contour with distance from the axis indicates that angle between the compression wave and the bow shock becomes smaller as the axis is approached; on the axis this angle is zero and the inter- action is one-dimensional. As noted previously, this results in the velocity of the interaction point becoming very large such that in the

transformed coordinate system (Fig. 27c), M_o' becomes large. But reference

to compressible flow charts, e.g., Ref. 35, indicates that as the upstream

Mach number becomes large, the value of the shock angle at the limit

of sonic flow downstream, $\Theta_1' = \Theta_1*$, increases by only a few degrees

from the value given in Fig. 27c. The density ratio across the bow shock,

$\frac{\rho}{\rho_c}$, increases from a value of approximately 3 at the downstream

location represented in Fig. 27 to a typical value of 5 on the flow field

axis. The deflection angle δ_1' is related to Θ_1' and $\frac{\rho}{\rho_o}$ by Eq. II-(8).

The changes in Θ_1', $\frac{\rho}{\rho_o}$ and δ_1' thus are small relative to the

change in $\tan\mu_1'$. Therefore, $\tan\mu_1'$ dominates the behavior of the para-

meters a and b. As the angle between S1 and S3 becomes small in Fig. 27c,

the component of M_1' normal to S3 becomes small. This component determines

the strength of the compression wave. For a given compression wave

strength then, the deviation of M_1' from unity must increase as the

interaction point approaches the axis. Thus μ_1', determined by Eq. (6),

decreases and the reflection coefficient, determined by Eqs. II-(2) to

II-(4) increases. The coefficient does not increase sufficiently to

become positive, since as indicated in Fig. 45, the one-dimensional

interaction is shown to produce a reflected rarefaction wave.

The predicted change in the strength of the contact discontinuity

with distance from the axis is therefore consistent with the observed

decrease in amplitude of the boundary corrugation with increasing

distance from the axis.

APPENDIX III

CHEMICAL KINETICS OF HYDROGEN-OXYGEN INDUCTION REACTIONS

Hydrogen-oxygen gas systems are particularly suited to experimental

investigations of exothermic flows since the kinetic mechanism of this

system has been extensively studied in the high temperature range of

interest, particularly the induction zone reactions (Ref. 36 to 39).

Numerical values of the specific reaction rate constants are thought

to be fairly well established. The induction zone kinetic mechanisms

can be represented by a set of linear first order differential equations;

therefore, detailed calculations of the progress of the reactions in

the induction region are easily performed. Presented in this appendix

are the details of the kinetic calculations. The results are used to

generate an induction time correlation which is consistent with the

experimental instability wavelength observations. The results are

also used in Appendix IV to compare the experimental reaction front

profile with that predicted analytically.

The reactions which govern the hydrogen oxidation process can be

classified as initiation reactions, induction reactions and exothermic

reactions. The initiation reactions are those which reduce a small

fraction of the oxygen and hydrogen molecules to atoms and radicals

which are in turn required to initiate the chain branching mechanism

of the induction zone. The time required to complete these reactions

is usually not significant compared to the induction time. The induction time, however, does depend strongly on these initial atom and radical concentrations; therefore, the initiation reactions must be included in the analysis. The initiation reactions together with the assumed rate constants used in the numerical calculations are given in Table II.

During the induction period, the atom and radical concentrations grow rapidly due to a branched chain mechanism. The chain carrying and branching reactions specified in Table II, Reactions I, II, and III, are important at all temperature levels of interest in the hydrogen-oxygen system (Ref. 24, p. 22). The chain breaking reaction, Reaction VI, is important at temperatures below $1200°$ K and, being a termolecular reaction, is more effective at higher pressures. Brokaw (Ref. 40) also includes the reaction,

$$\text{XI} \qquad HO_2 + H_2 \longrightarrow H_2O_2 + H$$

which is important only at low temperatures where induction times are of the order of milliseconds or greater. For purposes of these hypersonic flow experiments, only induction times on the order of microseconds are of consequence; therefore, Reaction XI was not included. Nicholls (Ref. 36) includes the reactions

$$H_2O + M \longrightarrow OH + H + M$$
$$OH + M \longrightarrow O + H + M$$
$$2OH \longrightarrow H_2O + O$$
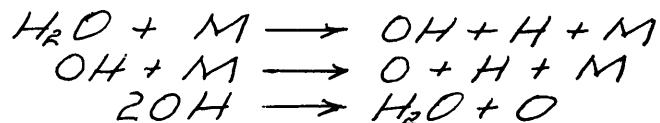
but shows that they have a negligible effect in the temperature range of interest.

The exothermic reactions become important, by definition, for times greater than the induction period. These reactions, mostly three-body recombination reactions, are much slower than the chain branching reactions, and therefore the time required for the overall reaction to be completed is generally an order of magnitude greater than the induction period (Ref. 29, 37, 39). Since the primary purpose of these calculations is to determine the induction time, these reactions are not included herein. In reality, the behavior of these reactions determines the end of the induction period; however, as will be discussed later, the knowledge that the chain branching reactions are much faster than the exothermic reactions is sufficient to establish a criterion which signifies the end of the induction period.

Equations and Initial Conditions

Using the reactions listed in Table II, the following expressions can be written for the rate of change of the atom and radical concentrations,

$$\frac{dc^*_{OH}}{dt} = -k_1' c^*_{OH} c'_{H_2} + k_2' c^*_H c'_{O_2} + k_3' c^*_O c'_{H_2} + 2k_{OH}' c'_{H_2} c'_{O_2}$$

$$\frac{dc^*_H}{dt} = k_1' c^*_{OH} c'_{O_2} - k_2' c^*_H c'_{O_2} + k_3' c^*_O c'_{H_2} - k_6' c^*_H c'_{O_2} c'_H + 2k_H' c'_{H_2} c'_H$$

$$\frac{dc^*_O}{dt} = k_2' c^*_H c'_{O_2} - k_3' c^*_O c'_{H_2} + 2k_O' c'_{O_2} c'_H \qquad \text{III-(1)}$$

$$\left(c^*_{OH}\right)_0 = \left(c^*_H\right)_0 = \left(c^*_O\right)_0 = 0$$

$$\left(c'_{H_2}\right)_0, \quad \left(c'_{O_2}\right)_0, \quad \left(c'_H\right)_0 = GIVEN$$

150

Throughout the induction period it may be assumed that the molecule

concentrations and the total concentration remain unchanged. Thus

Eqs. III-(1) represent a system of first order, linear differential

equations in the atom and radical concentrations. The system may be

written as a homogeneous set by the transformations,

$$c_i' \equiv c_i^* - s_i' \qquad\qquad i = OH, H, O \qquad\qquad \text{III-(2)}$$

Equations III-(2) are substituted into Eqs. III-(1) and the constant

terms are set equal to zero. The resulting expressions for the constant

terms are

$$-k_1 \delta_1 \qquad\qquad + k_2 \bar{x} \delta_2 \qquad + \delta_3 = -2 k_{OH}$$

$$k_1 \delta_1 + (-k_2 + k_6)\bar{x} \delta_2 \qquad + \delta_3 = -2 k_H \frac{1}{x_{H_2}} \qquad \text{III-(3)}$$

$$k_2 \bar{x} \delta_2 \qquad - \delta_3 = -2 k_0 \frac{\bar{x}}{x_{H_2}}$$

where the equations have been nondimensionalized by dividing by

$k_3' c_{H_2}'^2$ and the following definitions have been introduced:

$$\delta_i \equiv \frac{\delta_i'}{c_{H_2}'} \quad i = OH, H, O \qquad\qquad \bar{x} \equiv \frac{c_{O_2}'}{c_{H_2}'}$$

$$k_i \equiv \frac{k_i'}{k_3'} \quad i = 1,2,3,OH,H,O \qquad\qquad k_6 \equiv \frac{k_6' c_{H_2}'}{k_3'}$$

$$x_i \equiv \frac{c_i'}{c_M'} \quad (\text{mol fraction}) \quad i = OH, H, O, H_2, O_2$$

Equations III-(3) may be solved in terms of the initial concentrations:

$$\delta_1 = \frac{2\bar{x}}{k_1}\left[k_{OH} + \frac{k_0}{x_{H_2}} - 2k_2 X\right]$$

$$\delta_2 = -2X \qquad\qquad\qquad\qquad \text{III-(4)}$$

$$\delta_3 = 2\bar{x}\left[\frac{k_{O_2}}{x_{H_2}} - k_2 X\right]$$

where
$$X \equiv \frac{k_{OH} + \dfrac{k_{H_2}}{X_{O_2}} + \dfrac{k_{O_2}}{X_{H_2}}}{2k_2 - k_6}$$

The rate equations assume the form:

$$\frac{1}{k_3' c_{H_2}} \frac{dx_{OH}}{dt} = -k_1 x_{OH} \qquad\qquad + k_2 x_H + k_3 x_O$$

$$\frac{1}{k_3' c_{H_2}} \frac{dx_H}{dt} = k_1 x_{OH} - (k_2 + k_6)\bar{x} x_H + k_3 x_O \qquad \text{III-(5)}$$

$$\frac{1}{k_3' c_{H_2}} \frac{dx_O}{dt} = \qquad\qquad\qquad k_2 \bar{x} x_H - k_3 x_O$$

The equations are solved in the usual manner by the substitutions,

$$x_i = A_{ij} e^{\lambda_j' t} \qquad i = OH, H, O \quad \text{III-(6)}$$

which result in the expressions,

$$(-k_1 - \lambda_j)A_{OH,j} \qquad\qquad + k_2 A_{H,j} + A_{O,j} = 0$$

$$k_1 A_{OH,j} - \left[(k_2 + k_6)\bar{x} + \lambda_j\right]A_{H,j} + A_{O,j} = 0 \quad \text{III-(7)}$$

$$k_2 \bar{x} A_{H,j} - (1 + \lambda_j)A_{O,j} = 0$$

where the nondimensional time constant

$$\lambda_j \equiv \frac{\lambda_j'}{k_3' c_{H_2}}$$

has been introduced. Equations III-(7) possess a solution for the eigenvalues of λ given by the cubic equation:

$$\lambda_j = \frac{k_1(2k_2 - k_6)\bar{x}}{k_1 + (k_1 + 1)k_6 \bar{x} + \left[(k_1 + 1) + (k_2 + k_6)\bar{x}\right]\lambda_j + \lambda_j^2} \quad \text{III-(8)}$$

As discussed by Brokaw (Ref. 40) this equation, which was first derived

by Kondratiev (Ref. 41), has three real roots, two of which are negative
and one of which is positive. The positive root is responsible for
the exponential growth of the radical and atom concentration in the
induction period. Brokaw gives expressions for approximate solutions
for the positive root; however, the full equation is easily solved
numerically since the iteration scheme suggested by the form of
Eq. III-(8) converges in two or three steps.

After solving for the $\lambda_j's$, the values of $A_{H,j}$ and $A_{O,j}$ may
be found in terms of $A_{OH,j}$ by the expressions:

$$A_{H,j} = \frac{(k_1 + \lambda_j)(1 + \lambda_j)}{k_2 \, \Gamma \, (2 + \lambda_j)} A_{OH,j}$$

$$A_{O,j} = \frac{(k_1 + \lambda_j)}{2 + \lambda_j} A_{OH,j}$$

III-(9)

The values of $A_{OH,j}$ are found by use of the initial condition
$(c_{OH}^+)_o = 0$ which, with the use of the nondimensional form of
Eqs. III-(2), and Eqs. III-(6) can be written:

$$\sum_{j=1}^{3} A_{ij} + \delta_i = 0 \qquad \begin{array}{l} i = OH, O, H \\ j = 1, 2, 3 \end{array}$$

III-(10)

Having determined the eigenvalues, λ_j , and the constants A_{ij} ,
the atom and radical mol fractions are given at any time by Eqs. III-(6).

The solution of the equations for conditions corresponding to
temperatures behind a Mach 5.0 and Mach 4.0 shock moving in a

153

stoichiometric hydrogen-air mixture (temperatures of 1611 and 1157°K, respectively) and a pressure of 10 atmospheres is shown in Fig. 62. The dashed lines represent the contribution of the term containing the positive exponent in the expression

$$\chi_{OH} = \sum_{j=1}^{3} A_{OH,j} e^{\lambda'_j t} + \delta_{OH} \qquad \text{III-(11)}$$

The induction time is of the order of 1 microsecond for the Mach 5.0 shock and 10 microseconds for the Mach 4.0 shock, and it can be seen that the expression

$$\chi_{OH} = (\chi_{OH})_0 \, e^{\lambda' t} \qquad \text{III-(12)}$$

where λ' is the positive exponent, adequately represents the radical growth throughout all but the initial stages of the induction period.

A plot of the value of $(\chi_{OH})_0$, which is equal to the value of $A_{OH,j}$ for the positive root, is given in Fig. 63. The termolecular chain breaking reaction causes a pressure effect to become significant at temperatures below 1400°K. Also shown is the approximate value obtained by use of the expression given by Brokaw (Ref. 40),

$$(\chi_{OH})_0 = 0.296 \frac{k_1}{k_{OH}} \qquad \text{III-(13)}$$

which is derived by assuming that the only initiation reaction of significance is the one in which OH is produced and that this reaction

154

is in equilibrium with Reaction I during initiation. The agreement is excellent for the conditions assumed in the calculations.

The time constant (the positive value of λ_j) which determines the radical growth rate in the induction zone is given in Fig. 64. At low temperatures, the constant rapidly approaches zero due to the effect of the chain breaking reaction. Since this is a termolecular reaction, it is more effective at higher pressure, as indicated. The time constant actually remains nonzero at the low temperature; the curves do not intersect the x-axis but instead bend quite sharply and are **virtually** coincident with the axis for the scale of Fig. 64. The value of the positive root of Eq. III-(8) at temperatures below the critical is then of a smaller order of magnitude than that above the critical. The critical temperature corresponds to that for which

$$2 k_2' = k_6' c_M'$$

III-(14)

This is the so-called second explosion limit criterion, since it also describes the boundary between conditions for which explosions either will or will not occur in low pressure, low temperature explosion experiments (Ref. 24, p. 24). In the present experiments it is the condition which would, under certain conditions, determine the freezing point for the induction zone reactions (see Appendix IV).

The radical growth during the induction period is shown on a semi-log plot in Fig. 65 for conditions behind normal shocks in a

stoichiometric hydrogen-air mixtures having an initial pressure of 0.396 atmospheres. The actual conditions during initiation are not shown; the curves have been extrapolated to $t = 0$ in accordance with the approximation:

$$x_{OH} = (x_{OH})_0 e^{\lambda t}$$

Since one of the purposes of this work is to predict the location of the exothermic reaction front , a realistic criterion which signifies the end of the induction period, must be utilized. Much of the experimental work on determining the radical growth rate during the induction period has been based on the measurement of the OH concentration by radiation absorption techniques. Schott and Kinsey, in their experiments (Ref. 28), defined the induction period as the time required for the OH concentration to exceed the limits of detection of their apparatus, which happened to be a concentration of 10^{-6} mol/liter. There has been a tendency for other authors to apply this criterion to the determination of the time required for the exothermic effects to appear. Obviously, this criterion is not necessarily applicable unless it otherwise can be shown that it does correspond to some basis other than the sensitivity of Schott and Kinsey's apparatus. Miyama and Takeyama, in their experiments (Ref. 27), found that above a certain temperature level a sudden change in the level of OH absorption did occur at the moment when the effects of the exothermic reaction were

detected, but this did not necessarily correspond to a fixed OH concentration level.

Nicholls, Adamson, and Morrison, in their analytic treatment of the equations describing the atom and radical growth in the induction period (Ref. 36), point out that the end-of-induction criterion should be based on the rate controlling reaction in the induction period, Reaction II:

$$H + O_2 \xrightarrow{k_2'} OH + O$$
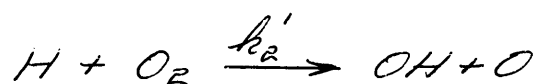
They then define the end of the induction period as that time at which the hydrogen atom mol fraction reaches its maximum. Based on their analytic expressions, they show that this occurs when the hydrogen atom mol fraction is equal to the initial oxygen molecule mol fraction:

$$t = t^* \quad when \quad x_H = (x_{O_2})_o$$

In his earlier numerical work, Duff (Ref. 37) illustrated the dependence of the induction time on the behavior of the rate limiting reaction, Reaction II, and also illustrated the now well-known overshoot of the atom and radical concentrations which leads to the maximum in the H atom concentration employed in the criterion of Nicholls et al. Duff also showed that the end of induction corresponds to the time when the net rate of the rate limiting reaction becomes slow due to the increase in the backward rate. This is caused by the build-up in the product concentrations. At this point, the exothermic reaction

rate is no longer slow compared to the chain branching rate and the temperature rise becomes perceptible. Thus the fundamental cause for the end of the induction period is the approach to equilibrium of Reaction II. This criterion is easy to apply in the case of the present numerical calculations.

The rate of production of OH atoms from Reaction II is,

$$\left(\frac{d[OH]}{dt}\right)_{PRODUCTION} = k_2''^f [H][O_2]$$

III-(15)

whereas the rate of consumption due to the reverse reaction is

$$\left(\frac{d[OH]}{dt}\right)_{CONSUMP.} = k_2''^r [OH][O]$$

III-(16)

Denoting the ratio of the reverse rate to the forward rate at the end of the induction period by α ,

$$\alpha \equiv \frac{\left(\dfrac{d[OH]_i}{dt}\right)_{PRODUCTION}}{\left(\dfrac{d[OH]_i}{dt}\right)_{CONSUMP.}}$$

III-(17)

then

$$\alpha \frac{k_2''^f}{k_2''^r} = \frac{[OH]_i [O]_i}{[H]_i [O_2]_i}$$

III-(18)

where the subscript, i , indicates the value is that at the end of induction. Introducing the equilibrium constant based on concentrations

158

and writing in terms of the mol fractions:

$$\frac{(\mathcal{X}_{OH})_i \, (\mathcal{X}_O)_i}{(\mathcal{X}_H)_i \, (\mathcal{X}_{O_2})_i} = \propto K_{eq}(T)$$

III-(19)

By use of Eq. III-(9) and the assumption that the reactant mol fractions

are unchanged through the reaction period, the following expression

can be written:

$$(\mathcal{X}_{OH})_i = \propto \frac{1+\lambda}{k_{C_2}\bar{\mathcal{X}}} \mathcal{X}_{O_2} K_{eq}(T)$$

III-(20)

The equilibrium constant is evaluated by standard methods (Ref. 42).

The resulting value of $(\mathcal{X}_{OH})_i$ for stoichiometric hydrogen-air

mixtures and for $\propto = 1.0$ is plotted in Fig. 63. Under the conditions

of the experiments, the pressure effect is seen to be neglibibly small.

The values of $(\mathcal{X}_{OH})_i$ can then be entered in Fig. 65, thus

determining the induction time. The times so determined are compared

in Fig. 66 with those given by the correlation of White and Moore

(Ref. 29) for the conditions behind normal shock waves in stoichiometric

hydrogen-air mixtures of initial pressure of 0.396 atm. The analytical

results are represented by the expression,

$$Log_{10}\left([O_2]\,\mathcal{T}\right) = -9.90 + \frac{15,100}{2.302\,RT}$$

III-(21)

This expression is compared with other correlations in Fig. 54.

It was noted above that the atom and radical growth rate in the

induction period is controlled by the rate of the chain branching

reaction, Reaction II. Indeed, one of the experimental methods of determining the specific rate constant for Reaction II, k_{c_2}', is based upon the observation of induction times behind shock waves. Values of k_{c_2}' appearing in the literature are given in the Table III. The value given by Schott and Kinsey is based upon their measurement of induction time behind shock waves. The value given by Duff is also based on shock tube work of Schott and Kinsey. Kaufman and Del Greco's value is based on discharge flow experiments. Baldwin's value is a best fit to the data from all the above experiments plus the results of flame and explosion limit studies.

The value obtained from these experiments and the value used in the kinetic calculations discussed in this appendix is:

$$k_{c_2}' = 2.6 \times 10^{14} \exp\left(-\frac{15,500}{RT}\right)$$

This value, when used in the foregoing analysis together with the other rate constants given in Table II, yields the induction time behavior shown in Figs. 54 and 66. This induction time behavior is that which produces the agreement between experiment and theory illustrated in Fig. 53. Because the correctness of this value of k_{c_2}' depends on the correctness of the instability model, of the assumed kinetic mechanism, of the criterion for the end-of-induction and, to a lesser extent, on the correctness of the other rate constants, this analysis cannot be viewed as a useful method for measuring this rate constant until the

errors involved in the individual steps have been evaluated. Indeed, the value of activation energy given by the expression for k_2', 15.5 kcal/mol, is probably somewhat low since the heat of reaction for Reaction II is approximately 16 to 17 kcal/mol in the temperature range of interest (Ref. 46) and it is unlikely that the reverse bimolecular reaction has a negative activation energy. The somewhat low value is proportional to the slope of the induction time correlation curve (Fig. 54) which is slightly smaller than the values measured by other techniques. For the purpose of this study, which was to determine the mechanism of the observed instability, the agreement between the induction times or the value of k_2' derived from these experiments and those reported previously is quite satisfactory.

APPENDIX IV

FLOW FIELD CALCULATIONS

Estimates were made of the properties of the flow field about a hypersonic sphere under conditions typical of the experiments for use in the analytical predictions of the contours of the various wave fronts generated by the exothermic reaction and by the regular periodic instability. These estimates are based on the properties of an unreacting flow field and therefore are valid only for the flow outside of the reacted gas boundary. Previously published experimental data (Ref. 43) on the properties of the subsonic and transonic regions about a Mach 5.0 sphere moving through nitrogen provides the basis for the calculations.

As is well known, the calculation of the properties of a hypersonic blunt body flow field from first principles is extremely tedious because of the mixed elliptic-hyperbolic nature of the equations describing the flow. If the flow is a nonequilibrium flow, as in the case at hand, the complexity of the system of equations is further increased. For purposes of this study it was felt that sufficiently accurate estimates of the flow properties in the regions of interest could be made by utilizing published data on the properties of an unreacting flow field. The schlieren photographs suggest that the effect of the chemical reaction on the flow outside of the reacted gas boundary is small. The bow shock shape is similar to that for unreacting flows; the effect of the exo-

thermic serves primarily to displace the bow shock outward in accordance
with the reduction in the average gas density near the surface of the
ball.

The unreacting flow field properties upon which the flow field
estimates are based are those given by Sedney and Kahl (Ref. 43). By
use of a ballistic range instrumented with an interferometer, they
obtained the density field about a Mach 5.0 sphere fired into a pure
nitrogen atmosphere. The streamline and constant Mach number contours
were then found by application of a finite difference scheme to solve
the momentum and continuity equations for the case of constant γ flow
behind the shock. The figures presented in their paper for the stream-
line and constant Mach number contours in the subsonic and transonic
regions were used to generate the data given in Figs. 20 and 66 for the
flow field of a Mach 5.0 sphere fired into a stoichiometric hydrogen-
air mixture.

The data was extended from the transonic region to a position in
the vicinity of the wake neck. This mapped a sufficiently large area
of the inviscid wake such that the pattern of the compression and
entropy waves generated by the instability could be developed. The
data was extended by application of the method of characteristics for
the axisymmetric flow of a $\gamma = 1.4$ gas in a region of varying entropy.
The boundaries of the region were taken to be the Mach 1.8 contour

given in Ref. 43, the body surface, the shear layer and the bow shock wave. The specification of the shock wave as well as the body surface and shear layer is theoretically redundant; however, this greatly reduces the calculation time. Incompatibilities introduced by the redundancies were quite small and were smoothed during the calculation. The location and shape of the shear layers was based on those observed in the schlieren photographs; the bow shock was extended downstream according to the correlation, Eq. (1), which was found to be compatible with the experimentally observed contours.

The equations and techniques describing the application of the method of characteristics to rotational axisymmetric flows are described in standard texts (e.g., Ref. 44). The technique used herein was a semigraphical one in which the streamlines and characteristic lines were extrapolated downstream from previously determined points. The properties at the intersection of two characteristic lines were found from the equation:

$$\frac{(d M^*)_{I, II}}{M^* \tan \nu} = \mp (d\delta)_{I, II} + \frac{\sin \nu \, \sin \delta}{\sin(\delta \mp \nu)} \frac{(dr)_{I, II}}{r} - \frac{\sin \nu \, \cos \delta}{r} \, d\left(\frac{s}{R}\right)_{I, II}$$

IV-(1)

where I denotes right running waves

II denotes left running waves

$M^* = v/c^*$

r = radial coordinate

s/R = dimensionless entropy

164

and the other symbols have their usual meaning. The entropy distribution

is determined by the entropy change across the bow shock and the knowledge

that flow along a streamline is isentropic. The mesh size chosen was

sufficiently small such that the errors introduced by the extrapolations

were quite small. Errors were smoothed by keeping running plots of the

significant parameters along each streamline as a function of the axial

coordinate. Five mesh points were chosen on the initial Mach contour,

a total of 60 points were involved in the calculation. The calculated

characteristic net is shown in Fig. 66; the streamline and Mach contours

are shown in Fig. 20. Since the flow is homoenergetic, the temperature

is a unique function of the Mach number. All other properties of

interest can be found from the known values of temperature (constant

on a Mach contour) and entropy (constant on a streamline).

With the properties of the flow field known, the development of

the wave front produced by infinitesimal disturbance can be traced by

application of Huygen's Principle (Ref. 45). The result of such a con-

struction for the case of an infinitesimal point generated at the bow

shock apex is shown in Fig. 25. Also shown in the figure are the con-

tours of the contact discontinuities produced by the interaction of the

acoustic wave front with the bow shock. The time interval between

successive positions of the wave fronts was arbitrarily chosen in this

example. A further discussion of Fig. 25 is given in Section 2. A

similar construction for the case of a normal wave front on the axis of symmetry is shown in Fig. 52; this figure is discussed in Section 4.

The theoretical location of the reaction front can be determined if the properties in the unreacted gas region are known. In applying the results of the flow field calculations described above, it is assumed that the exothermic reaction has no effect on the properties in the unreacted region.

As detailed in Appendix III, the reaction front location is determined by the attainment of a specified OH radical mol-fraction $(\mathcal{X}_{OH})_i$. The initial value is determined by the strength of the bow shock wave and the initial pressure. The value $(\mathcal{X}_{OH})_i$ is a function of the local gas properties and is independent of the history of the gas particles. The radical growth is governed by the expression:

$$\ln \mathcal{X}_{OH} = \ln (\mathcal{X}_{OH})_0 + \lambda'(P,T)\, t \qquad \text{IV-(2)}$$

For any time period that is sufficiently short such that the changes in gas properties are small, the change in the radical mol fraction is given by

$$\Delta \log_{10} (\mathcal{X}_{OH})_n = 2.302\, \lambda'_n(P,T)\, \Delta t_n \qquad \text{IV-(3)}$$

Thus the location of the reaction front on a given streamline may be found by summing the incremental changes in the radical mol fraction

166

along the streamline until

$$\sum_{n=1}^{N} \lambda_n'(P,T) \Delta t_n = \frac{\log_{10}(X_{OH})_i - \log_{10}(X_{OH})_o}{2.303}$$ IV-(4)

The value of λ' is found from Fig. 64 and the value of initial and final

OH mol fractions are given in Fig. 63.

A comparison of the calculated and experimental reaction front

boundaries for a Mach 5.0, 1/2-inch diameter sphere moving in a stoi-

chiometric hydrogen-air mixture with an initial pressure of 0.395 atm.

is given in Fig. 51.

The bow shock position assumed for the analytic calculations and

the calculated reaction front position are indicated by solid lines; the

experimental results are shown by dashed lines. The effect of the exo-

thermic reaction is to displace the shock and reaction front away from

the body surface. At points in the vicinity of the body shoulder, the

induction zone reactions cease to be significant; the chain branching

reaction is essentially frozen. At this point, the reaction front, or

more precisely the reacted gas boundary, is assumed to become coincident

with a streamline. As discussed below, the hot gas behind the boundary

causes the reaction to continue to proceed but at an extremely slow rate.

For a given mixture and projectile velocity, the cessation of the

branching reaction can either be a sudden freezing or a relatively

gradual approach to zero depending on the level of the initial pressure.

Sudden freezing occurs when the second limit condition, Eq. III-(14),

is satisfied. This corresponds to the time constant, λ', effectively

reaching zero as the temperature decreases due to expansion. If the

pressure is high, the slope of the λ vs. T curve is large (Fig. 64)

such that the dimensional time constant, λ', drops precipitiously to

near zero as the critical temperature is passed. On the other hand,

if the initial pressure is relatively low, the λ vs. T curve has a smaller

slope and the dimensional time constant, which is proportional to pressure,

gradually approaches zero.

For example, at the point where the particular streamline sketched

in Fig. 51 intersects the bow shock, the following conditions exist:

$T = 1368°K$; $p = 9.95$ atm. From Fig. 62, the initial OH mol fraction

generated by the initiation processes corresponds to $\log_{10} (\chi_{OH})_o = -10.4$.

(The initiation time can be estimated from Fig. 63 to be of the order

of 0.25μsec.) The time interval chosen for the stepwise calculation

of OH radical growth corresponded to a distance along the streamline of

0.025 diameters or approximately 0.3μsec. During the first time interval,

immediately behind the shock, the growth in $\log_{10}(\chi_{OH})$ is found to be

2.00. At the point where the reaction front and the streamline approach

one another, point F in Fig. 51, the conditions are: $T = 1019°K$; $p = 3.16$ atm.

The OH radical mol fraction has grown to a value corresponding to $\log_{10}$

$(\chi_{OH}) = -3.1$, while the value at the end of induction (Fig. 63) corres-

ponds to $\log_{10}(\chi_{OH})_i = -2.9$. During the last time interval considered,

the growth in $\log_{10}(\chi_{OH})$ is 0.15. At this slow rate of growth the

reaction front and the streamline approach one another very slowly and

the reaction, for practical purposes, can be considered frozen. Thus,

in this case, the cessation of the branching reaction corresponds to a

gradual decrease to zero. For this example then, the second limit

condition $2k_2' = k_6'C_M$ is not encountered. Only at higher initial

pressures than those used in the experiments will this limit be encountered.

For these experiments, the second limit condition thus plays no part in

determining the location of the flow regime boundaries.

Although the chain branching reactions become so slow in the outer

streamtubes that the OH concentration marking the end of induction is

not attained, the reacted gas boundary (reaction front) must continue

to propagate outward into the unreacted gas because of transport effects.

The photographs indicate the propagation rate is very small compared to

the local gas velocity since the reacted gas boundary appears to have

the same contour as a streamline. It should be noted that propagation

rates due to diffusion effects can be quite rapid if the property gradients

through the front are sufficiently large. Apparently, in the cases

where the exothermic flow field about the sphere is stable or is experien-

cing the regular periodic instability, the magnitude of the property

changes across the reaction front is sufficiently small such that the

diffusive effects are small. Previous investigators measured the rate

of propagation of the reacted gas boundary in the far wake (Ref. 4) and
found under their experimental conditions (H_2-Air Φ = 1.0; p=0.55 atm)
a propagation rate of 15 m/sec compared to the ball velocity of approxi-
mately 2000 m/sec. A propagation rate of this order is not significant
in the time scale of interest.

TABLE I

EXPERIMENTAL DATA

NOTE: Sphere diameter = 0.500 in. unless noted otherwise

Abbreviations: P_T = Mixture total pressure in mm Hg

M = Mach number

Regime	Remarks
P - Periodic	H - Horizontal Knife Edge
T - Turbulent	Pr - Probe Data Recorded
S - Stable	Q - Questionable Data
W - Wake	D - Dual Schlieren
	I - Irregular Pattern
	Wk - Weak Schlieren Effect

| Run | Mixture | | | Velocity | | Regime (λ/D) | Remarks |
	Gases	Ratio	P_T	fps	M		
1	$C_2H_2:O_2$	1:15	50	6300	5.87	S	Wk
2	"	"	100	6200	5.78	P-0.098	Wk,I
3	"	"	150	5480	5.11	P-0.163	
4	"	"	150	5950	5.55	P-0.245	Wk,I
5	"	"	100	5480	5.11	P-0.206	Wk
6	"	"	100	5460	5.09	P-0.214	Wk
7	"	"	"	5960	5.56	P-0.130	Wk
8	"	"	"	5850	5.45	P-0.150	Wk
9	"	"	"	6340	5.91	S	
10	"	1:10	"	5570	5.19	T	Wk

| | | Mixture | | Velocity | | | |
Run	Gases	Ratio	P_T	fps	M	Regime (λ/p)	Remarks
11	$C_2H_2:O_2$	1:10	100	6250	5.83	P-0.096	
12	"	1:8	"	6360	5.94	T	
13	"	"	"	6090	5.68	T	
14	"	"	"	6150	5.74	T	
15	"	"	50	5600	5.22		Wk
16	"	"	150	6210	5.80	T	
17	"	1:10	100	5550	5.18	T	Q
18	"	"	"	5280	4.93	P-0.240	
19	"	"	"	4980	4.65	P-0.288	
20	"	"	"	5215	4.82	P	Ir,Q
21	"	"	"	5880	5.48	T	H,Q
22	"	"	"	4900	4.57	P-0.528	H
23	"	"	"	4560	4.26	W	H
24	"	"	"	--	--	P	H,Q
25	"	"	"	--	--	T	H,Q
26	"	1:15	"	6250	5.83	T	H
28	"	"	"	5260	4.90	P-0.253	H
29	"	"	"	6150	5.73	P-0.075	Q
30	"	"	"	5210	4.86	P-0.243	D
31	"	"	"	--	--	P-0.209	D,Q
32	"	1:20	"	6010	5.61	P-0.051	

| | Mixture | | | Velocity | | | |
Run	Gases	Ratio	P_T	fps	M	Regime (λ/D)	Remarks
33	$C_2H_2:O_2$	1:20	100	5560	5.18	P-0.204	D
34	"	1:15	"	--	--	P-0.120	Q
35	"	"	"	6270	5.85	P-0.065	Q
36	"	"	"	4950	4.61	P-0.471	Q,D
37	"	"	"	6210	5.80	P-0.098	Q,D,Wk
38	"	"	"	5710	5.32	--	Q,D,Wk
39	"	"	"	6160	5.75	P-0.077	Q,Pr
40	"	"	"	6050	5.66	P-0.098	Q,D,Pr
41	"	"	150	5515	5.15	P-0.162	Q,Pr
41a	"	1:10	100	5100	4.75	P-0.278	Q,D,Pr
42	"	1:20	100	5680	5.29	S	Q,Wk
43	"	"	150	5425	5.05	P-0.205	Q,D,Pr
44	"	"	"	5700	5.31	P-0.130	Q,D,Wk
45	"	1:10	75	5370	5.05	P-0.242	Q,D,Pr
46	"	"	"	6180	5.75	P-0.143	Q,D
47	"	"	50	5760	5.37	P-0.157	Q,D
48	"	1:8	"	6325	5.80	P-0.132	D,Ir,Wk
49	"	"	"	5450	5.08	P-0.186	D,Wk
50	$C_2H_2:O_2:N_2$	1:2.5:12.5	100	5650	4.98	W	D,Wk
51	$C_2H_2:O_2$	1:15	"	5280	4.91	W	0.375" Dia.
52	"	"	"	5530	5.16	P-0.255	

| | Mixture | | | Velocity | | | |
Run	Gases	Ratio	P_T	fps	M	Regime (λ/σ)	Remarks
53	$C_2H_2:O_2$	1:15	150	6590	6.15	S	0.375" Dia.
54	"	"	"	6500	6.05	S	0.250" Dia.
55	"	"	200	6200	5.78	P-0.128	
56	"	"	"	5790	5.40	P-0.220	
57	"	"	"	6150	5.73	T	
58	"	"	"	5930	5.53	T	
59	"	"	150	4280	3.99	W	
60	"	"	200	5500	5.13	T	
61	"	"	150	6220	5.80	T	
62	"	"	"	5250	4.90	P-0.254	
63	"	"	"	5250	4.90	P-0.252	
64	"	"	100	6090	5.68	P-0.126	
65	"	"	"	5810	5.42	P-0.150	
66	"	"	"	5660	5.28	P-0.199	
67	"	"	200	5950	5.55	P-0.194	0.250" Dia.
68	"	"	"	5600	5.23	P-0.230	0.250" Dia.
69	"	"	"	5080	4.73	P-0.560	0.250" Dia.
70	"	"	"	6315	5.89	P/S	0.250" Dia.
71	"	"	"	5860	5.47	P-0.158	0.250" Dia.
72	"	"	"	5500	5.13	P-0.256	0.250" Dia.
73	"	"	"	5910	5.50	P-0.160	0.250" Dia.

| | Mixture | | | Velocity | | | |
Run	Gases	Ratio	P_T	fps	M	Regime (λ/ϖ)	Remarks
74	$C_2H_2:O_2$	1:15	200	6300	5.86	P-0.108	0.250" Dia.
78	$H_2:O_2:N_2$	2:1:3.76	150	5980	4.48	W	Wk
79	"	"	200	6680	5.00	P	Wk
80	"	"	300	6180	4.64	P-0.281	Pr
81	"	"	200	5530	4.15	W	
82	"	"	"	6100	4.58	W	Pr
83	"	"	250	7080	5.31	S	Pr
84	"	"	200	5580	4.19	W	Pr
85	"	"	300	5865	4.40	P-0.161	Pr
86	"	"	"	6710	5.04	P-0.160	Pr
87	"	"	"	6790	5.10	P-0.164	Pr
88	"	"	"	6230	4.67	P-0.285	Pr
89	"	"	"	6610	4.96	P-0.184	Pr
90	"	"	"	6300	4.73	P-0.240	Pr
91	$H_2:O_2$	1:2	100	6280	4.83	--	D,Wk
92	"	"	"	6240	4.79	--	D,Wk
93	"	"	"	5810	4.47	--	D,Wk
94	"	"	"	6780	5.20	T	
95	"	"	"	6700	5.15	S	
96	"	"	"	5700	4.38	W	Wk
97	"	1:2.39	300	5580	4.39	T	
98	"	"	"	5800	4.57	T	Pr

	Mixture			Velocity			
Run	Gases	Ratio	P_T	fps	M	Regime (λ/D)	Remarks
99	$H_2:O_2$	1:2.39	300	6910	5.45	T	
100	"	"	200	6730	5.30	P/T	Ir,Pr
101	"	"	"	7010	5.53	T	Pr
102	"	"	"	5750	4.53	P	Ir,Pr
103	$H_2:O_2:N_2$	2:1:3.76	300	6850	5.14	S	0.375" Dia.
104	"	"	"	6630	4.98	S	0.375" Dia.
105	$H_2:O_2:Ar$	"	286	6800	5.60	S	Pr
106	"	"	300	6380	5.26	S	Pr
107	"	"	"	5160	4.25	P-0.254	Pr,Ir
108	"	"	"	6080	5.02	P-0.071	Pr
109	"	"	"	6150	5.07	T	Pr,Ir
110	"	"	"	5750	4.73	P-0.105	Pr
111	"	"	"	5460	4.50	P-0.110	Pr
112	"	"	"	5450	4.50	P-0.156	Pr
126	$C_2H_2:O_2:N_2$	1:2.5:12.5	150	6500	5.72	P	Pr,Ir
127	"	"	200	6360	5.59	P-0.148	Pr
128	$C_2H_2:O_2:Ar$	"	"	5715	5.49	T	Pr
129	"	"	148	5790	5.55	T	Pr
130	"	"	100	5800	5.56	P-0.115	Pr
131	"	"	"	5440	5.21	P-0.171	Pr
132	"	"	"	5000	4.80	P-0.279	Pr

	Mixture			Velocity			
Run	Gases	Ratio	P_T	fps	M	Regime (λ/D)	Remarks
133	$C_2H_2:N_2:Ar$	1:2.5:12.5	150	5850	5.47	--	Pr
134	"	"	"	5680	5.40	--	Pr
135	$C_2H_2:O_2:H_e$	"	"	6670	3.25	W	Pr
136	$C_2H_2:O_2:Ar:H_e$	1:2.5:4:8.5	"	7215	4.86	P-0.238	Pr
137	"	"	"	7020	4.73	P-0.308	Pr,Ir
138	$C_2H_2:O_2$	1:15	"	4600	4.28	W	Pr
139	"	"	"	5380	5.01	P-0.228	D,Pr
140	"	"	"	5600	5.22	P-0.158	Pr
141	"	"	"	5940	5.53	T	Pr
142	"	"	"	4910	4.58	P-0.54,0.60	Pr
143	"	"	"	6000	5.58	T	Pr
144	"	"	125	4340	4:05	W	Pr
145	"	"	"	6890	6.43	S	Pr
146	"	"	100	6160	5.75	P-0.105	Pr
147	"	"	"	4890	4.55	W	Pr
148	"	"	"	6150	5.73	P-0.112	Pr
149	"	"	"	6115	5.70	P	Ir,Pr
150	"	"	"	5720	5.34	P	Ir,Pr
151	"	"	150	5060	4.71	P-0.30,0.15	Pr,Q,Wk
152	"	"	"	--	--	P-0.23	Q,Pr
153	"	"	"	5915	5.52	T	D,Pr

177

| un | Mixture | | | Velocity | | Regime (λ/D) | Remarks |
	Gases	Ratio	P_T	fps	M		
54	$C_2H_2:O_2$	1:15	150	5690	5.30	P-0.160	D,Pr
55	"	"	"	5720	5.33	P-0.151	D,Pr
56	"	"	"	5710	5.33	P-0.151	Pr
57	"	"	"	5545	5.16	P-0.211	D,Pr,Ir
58	"	"	"	5150	4.80	P-0.179	**D**,Pr
59	"	"	"	5100	4.75	P-0.390	H,Pr
60	"	"	"	5800	5.40	T	H,Pr
61	"	"	"	5540	5.16	P-0.20/0.17	H,Pr
62	"	"	"	5430	5.02	P-0.220	H,Pr
63	"	"	"	5440	5.07	P-0.203	H,Pr
64	"	"	"	7480	6.98	T	
65	"	"	100	7150	6.66	S	Q,Ir
66	"	"	50	7290	6.80	S	
67	"	"	"	6800	6.35	S	Q
68	"	"	"	5930	5.53	S	Q,Wk
69	"	"	"	5850	5.45	S	Q,Wk
170	"	"	200	5050	4.70	P	Ir
171	"	"	"	4950	4.61	P-0.42	Ir
172	"	"	100	6245	5.81	P-0.101	
173	"	"	200	4310	4.01	W	
174	"	"	"	5250	4.89	P-0.229	Ir

	Mixture			Velocity		Regime	Remarks
un	Gases	Ratio	P_T	fps	M	(λ/D)	
75	$C_2H_2:O_2$	1:8	50	5330	4.97	S	Q
76	"	"	100	5820	5.43	T	
77	$H_2:O_2:N_2$	2:1:3.76	250	6840	5.13	S	
78	"	"	"	6710	5.03	S	
79	"	"	"	6715	5.04	P-0.157	
80	"	"	200	6650	5.00	P-0.249	
81	"	"	250	6360	4.77	P-0.255	
82	"	"	200	6450	4.84	P-0.260	
83	"	"	150	6470	4.85	S	
84	"	"	250	6800	5.10	S	Ir
85	"	"	200	6900	5.18	S/P	Ir
86	"	"	300	6815	5.11	P-0.156	
87	"	"	"	6880	5.15	P-0.121	
88	"	"	"	6890	5.16	P-0.120	
89	"	2:1:3.76	"	7130	5.35	P-0.117	Wk
90	"	"	"	7750	5.80	S	
91	"	"	200	7290	5.47	S	
92	"	"	"	6510	4.89	P-0.255	
93	"	"	300	6550	4.91	P-0.174	
194	"	"	250	6560	4.92	P-0.227	Wk
195	"	"	"	6460	4.85	P-0.235	

Run	Mixture			Velocity		Regime (λ/D)	Remarks
	Gases	Ratio	P_T	fps	M		
196	$H_2:O_2:N_2$	2:1:3.76	250	6850	5.15	P-0.155	Wk
197	"	"	"	7110	5.33	S	
198	"	"	200	6780	5.09	S	
199	"	"	300	6480	4.86	P-0.215	
200	"	"	"	6470	4.86	P-0.205	
201	"	"	"	6430	4.82	P-0.228	
202	"	"	250	6510	4.89	P-0.236	
203	"	"	200	6510	4.89	P-0.248	Wk
204	"	"	"	6740	5.05	S	
205	"	"	250	6550	4.91	P-0.232	Wk
206	"	"	300	6155	4.62	P-0.270	
207	"	"	250	6110	4.59	P	Wk
208	"	"	200	6200	4.65	W	
209	"	"	250	6380	4.78	P-0.246	
210	"	"	200	6150	4.61	W	
211	"	"	250	6735	5.05	P-0.164	
213	$C_2H_2:O_2$	1:15	50	6640	6.19	S	
214	"	"	100	6630	6.18	S	
215	"	"	150	6760	6.30	T	
216	"	"	"	7140	6.65	T	
217	"	"	100	7060	6.59	S	

	Mixture			Velocity			
ın	Gases	Ratio	P_T	fps	M	Regime (λ/D)	Remarks
18	$C_2H_2:O_2$	1:15	75	5200	4.85	S	Wk
19	"	"	100	5570	5.20	P-0.198	
20	"	"	"	5100	4.75	P-0.139	Wk,Q
21	"	"	"	5815	5.43	P-0.143	
22	"	"	"	6220	5.80	P-0.010	
23	"	"	"	6445	6.01	P-0.081	
24	"	"	"	5880	5.48	P-0.134	
25	"	"	"	5690	5.30	P-0.159	
26	"	"	"	5720	5.34	P-0.155	
27	"	"	75	5715	5.34	P-0.201	
28	"	"	125	5665	5.28	P-0.149	
29	"	"	100	5940	5.54	P-0.135	
30	"	"	75	5630	5.25	P-0.221	
31	"	"	50	5720	5.34	S	
32	"	"	75	5415	5.05	P-0.170	
33	"	"	"	5910	5.51	S/P	Ir
34	"	"	"	5950	5.55	P-0.144	
35	"	"	100	5355	5.00	P-0.233	
36	"	"	"	5320	4.96	P-0.243	
37	"	"	"	5845	5.45	P-0.135	
38	"	"	"	6210	5.80	P-0.094	

Run	Mixture			Velocity		Regime (λ/D)	Remarks
	Gases	Ratio	P_T	fps	M		
239	$C_2H_2:O_2$	1:15	100	7200	6.80	S	
240	"	"	"	5265	4.91	P-0.166	
241	"	"	125	5200	4.85	P-0.133	
242	"	"	"	5330	4.97	P-0.231	
243	"	"	75	5380	5.01	P	Wk
244	"	"	200	5530	5.16	T	
245	"	"	100	4810	4.49	W	Wk
246	"	"	150	4860	4.54	P-0.583	
247	"	"	"	5260	4.90	P-0.230	
248	"	"	200	5050	4.70	P	Ir
249	"	"	75	5140	4.79	S	Wk
250	"	"	100	5100	4.75	W	
251	"	"	"	5130	4.78	P-0.145	Wk,Q
252	"	"	"	5450	5.08	P-0.226	
253	"	"	75	5460	5.09	S	
254	"	"	200	5270	4.91	P/T	Ir
255	"	"	75	5815	5.42	S	
256	"	"	"	5580	5.20	P-0.229	
257	"	"	100	5050	4.70	W	Wk
258	"	"	"	5230	4.88	P-0.173	
259	"	"	"	5120	4.78	P-0.214	Wk

Run	Mixture		P_T	Velocity		Regime (λ/D)	Remarks
	Gases	Ratio		fps	M		
260	$C_2H_2:O_2$	1:15	175	4790	4.46	P-0.605	
261	"	"	125	6150	5.73	P-0.083	
262	"	"	175	4990	4.65	P-0.375	
263	"	"	150	5000	4.67	P-0.37,0.19	
264	"	"	75	5615	5.24	P-0.222	
265	"	"	175	5140	4.80	P-0.240	
266	"	"	150	4820	4.49	P-0.63,0.54	
267	"	"	175	5300	4.94	P-0.222	
268	"	"	100	5260	4.90	P-0.170	
269	"	"	75	5690	5.30	P-0.207	

TABLE II

ASSUMED HYDROGEN-OXYGEN KINETIC MECHANISM

Initiation Reactions		Specific Rate Constant	Ref.
OH	$H_2 + O_2 \rightarrow 2OH$	$k'_{OH} = 1.0 \times 10^{14} T^{-1} \exp(-70,000/RT)$	37
H	$H_2 + M \rightarrow 2H + M$	$k'_H = 1.85 \times 10^{17} T^{-1} \exp(-54,000/RT)$	38
O	$O_2 + M \rightarrow 2O + M$	$k'_O = 5.8 \times 10^{16} T^{-1} \exp(-60,600/RT)$	38

Chain Carrying Reactions

I	$OH + H_2 \rightarrow H_2 + H$	$k'_1 = 6.3 \times 10^{13} \exp(-5,900/RT)$	46

Chain Branching Reactions

II	$H + O_2 \rightarrow OH + O$	$k'_2 = 2.6 \times 10^{14} \exp(-15,500/RT)$	Table III
III	$O + H_2 \rightarrow OH + O$	$k'_3 = 2.5 \times 10^{12} \exp(-7,700/RT)$	46

Chain Breaking Reactions

VI	$H + O_2 + M \rightarrow HO_2 + M$	$k'_6 = 3.27 \times 10^{21}(x_{H_2} + 0.35x_{O_2} + 0.43x_{N_2} + 0.2x_{Ar})T^{-1.92}$	40

Units:

Concentration - $mol\ cm^{-3}\ sec^{-1}$

Temperature - $^\circ K$

TABLE III

KINETIC DATA FOR REACTION II

II: $H + O_2 \longrightarrow OH + O$
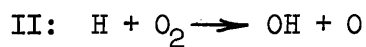
Units: $cm^3 mol^{-1} sec^{-1}$

Source	Specific Reaction Rate, k'_2
Schott and Kinsey, Ref. 28	$3 \times 10^{14} \exp\left[-(17.5 \pm 0.3)10^3/RT\right]$
Duff, Ref. 37	$4 \times 10^{14} \exp(-18{,}000/RT)$
Kaufman and Del Greco, Ref. 46	$1.7 \times 10^{16} \exp(-18{,}100/RT)$
Baldwin, Ref. 47	$(2.14 \pm 0.3)10^4 \exp\left[-(16.6 \pm 0.8)10^3/RT\right]$
Momtchiloff, et al., Ref. 39	$5.64 \times 10^{13} \exp(-15{,}100/RT)$
These experiments	$2.6 \times 10^{14} \exp(-15{,}500/RT)$

FIGURE 1

REGULAR PERIODIC INSTABILITY

Run No. 132: $C_2H_2:O_2:Ar:$ 1:2.5:12.5

Mach No.:   4.80

Pressure: 0.132 atm
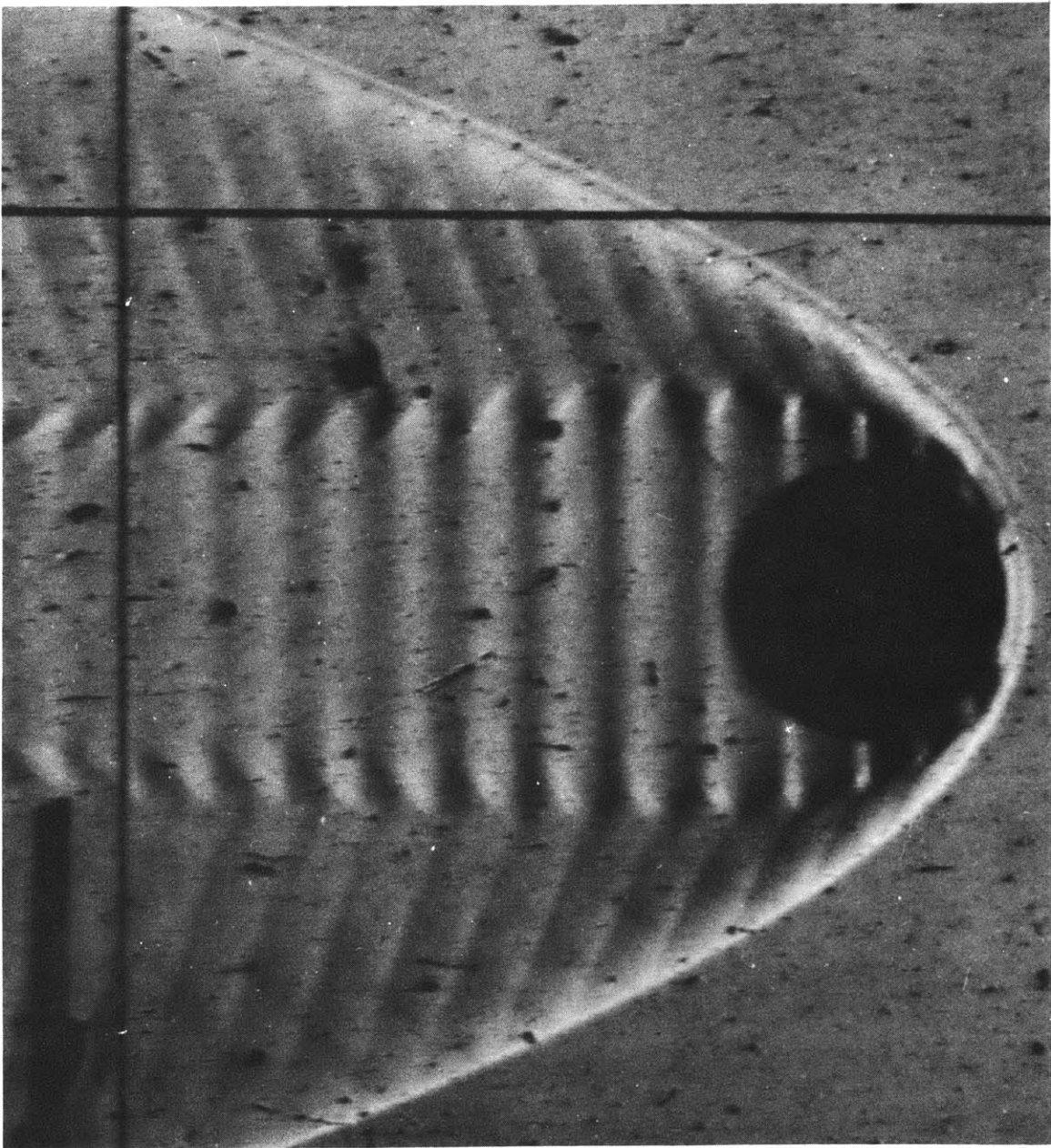
FIGURE 2

OVERALL VIEW OF BALLISTIC RANGE
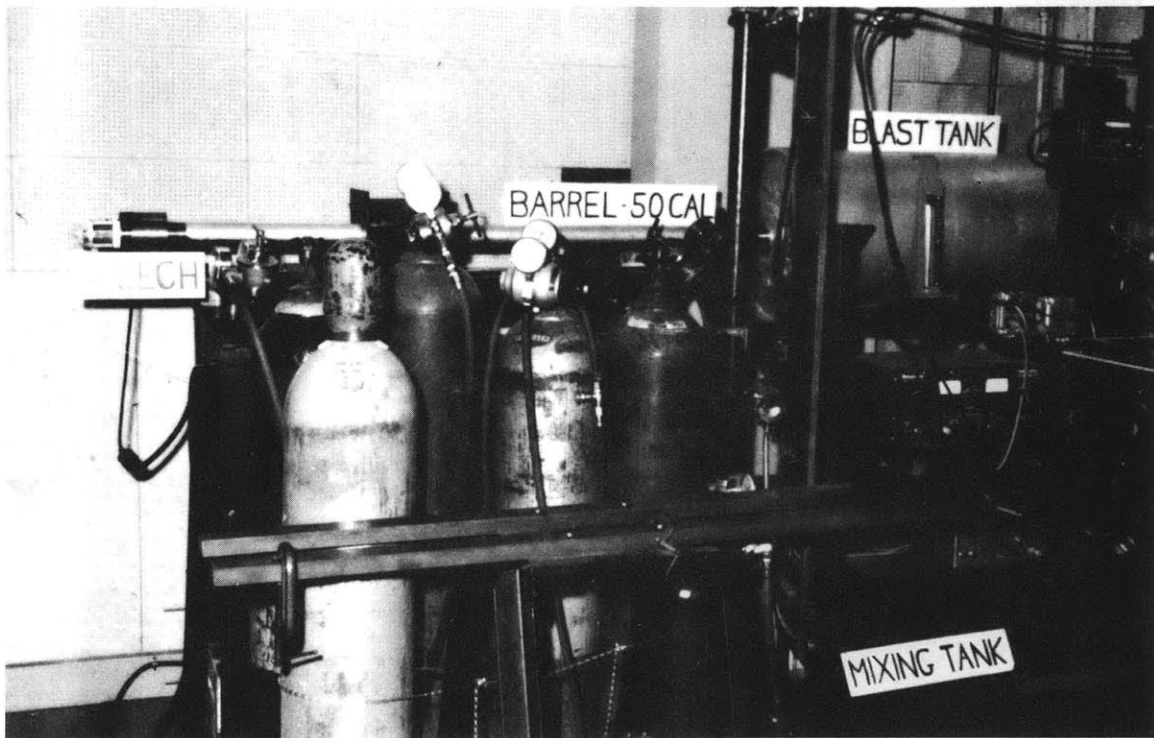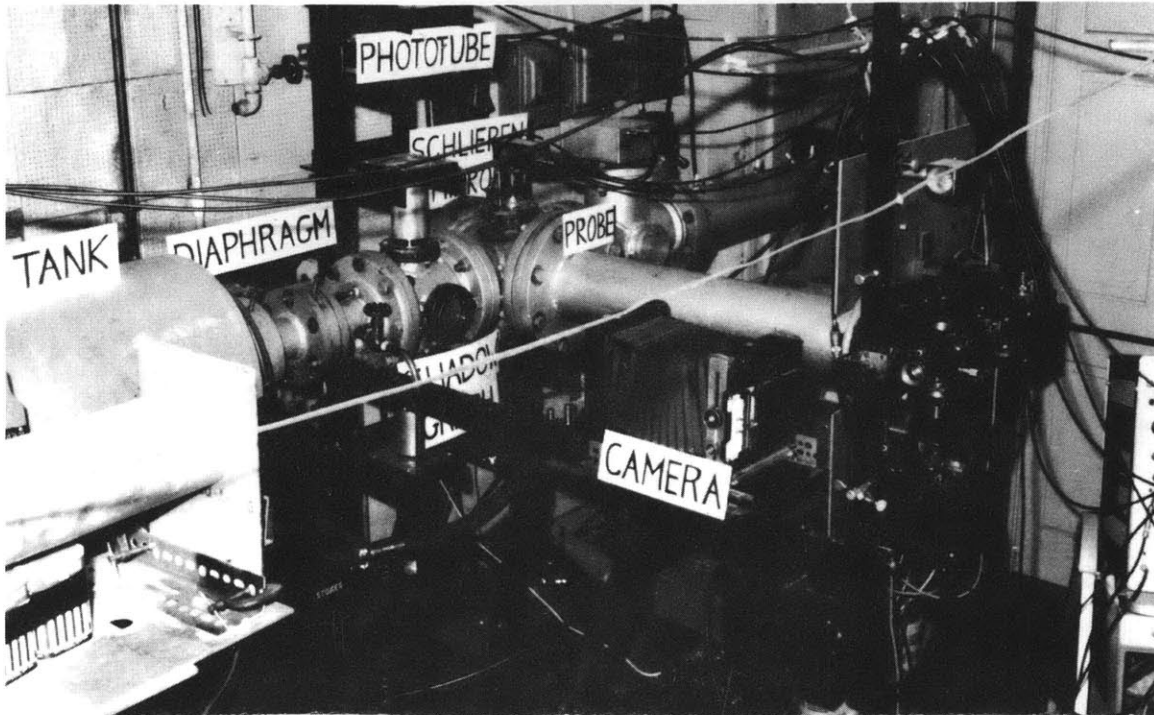
FIGURE 3

CLOSEUP VIEW OF SCHLIEREN SYSTEM COMPONENTS
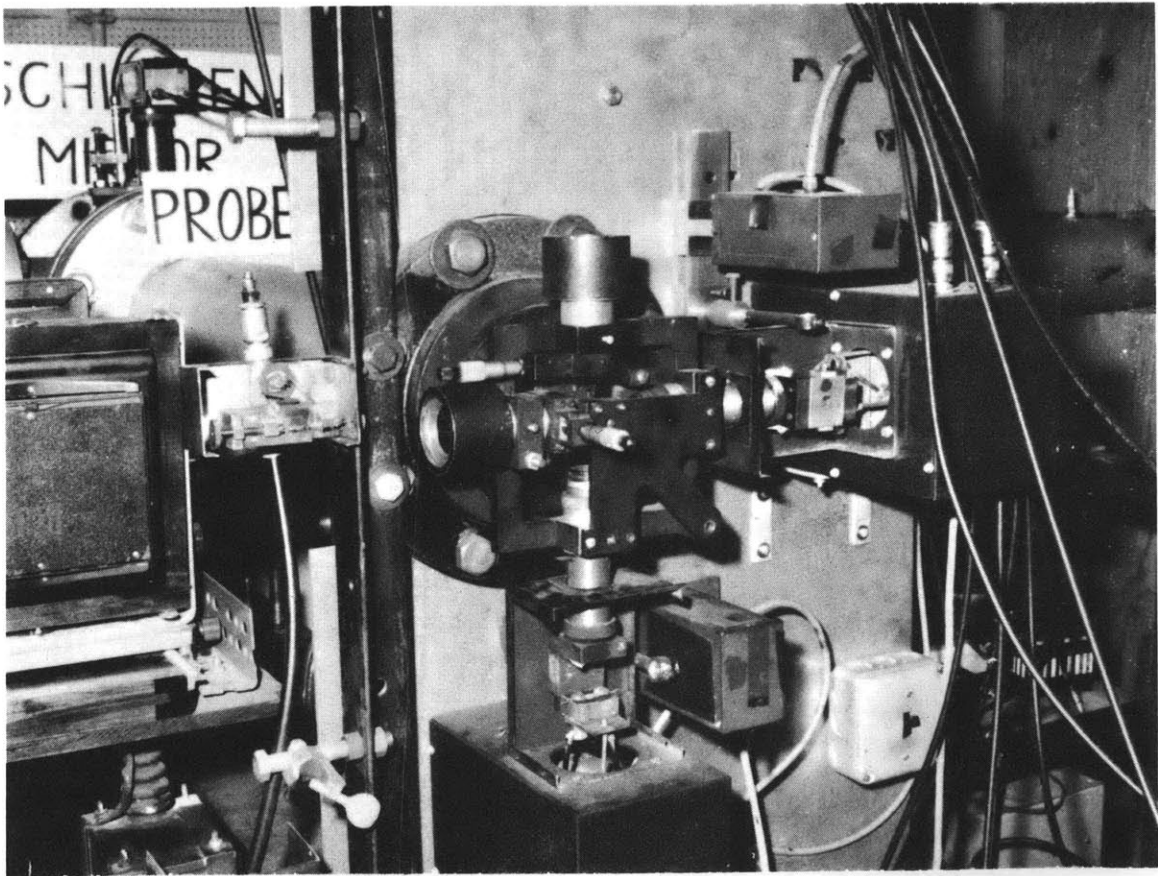
FIGURE 4

CHARACTERISTICS OF EXOTHERMIC HYPERSONIC BLUNT-BODY FLOW FIELDS
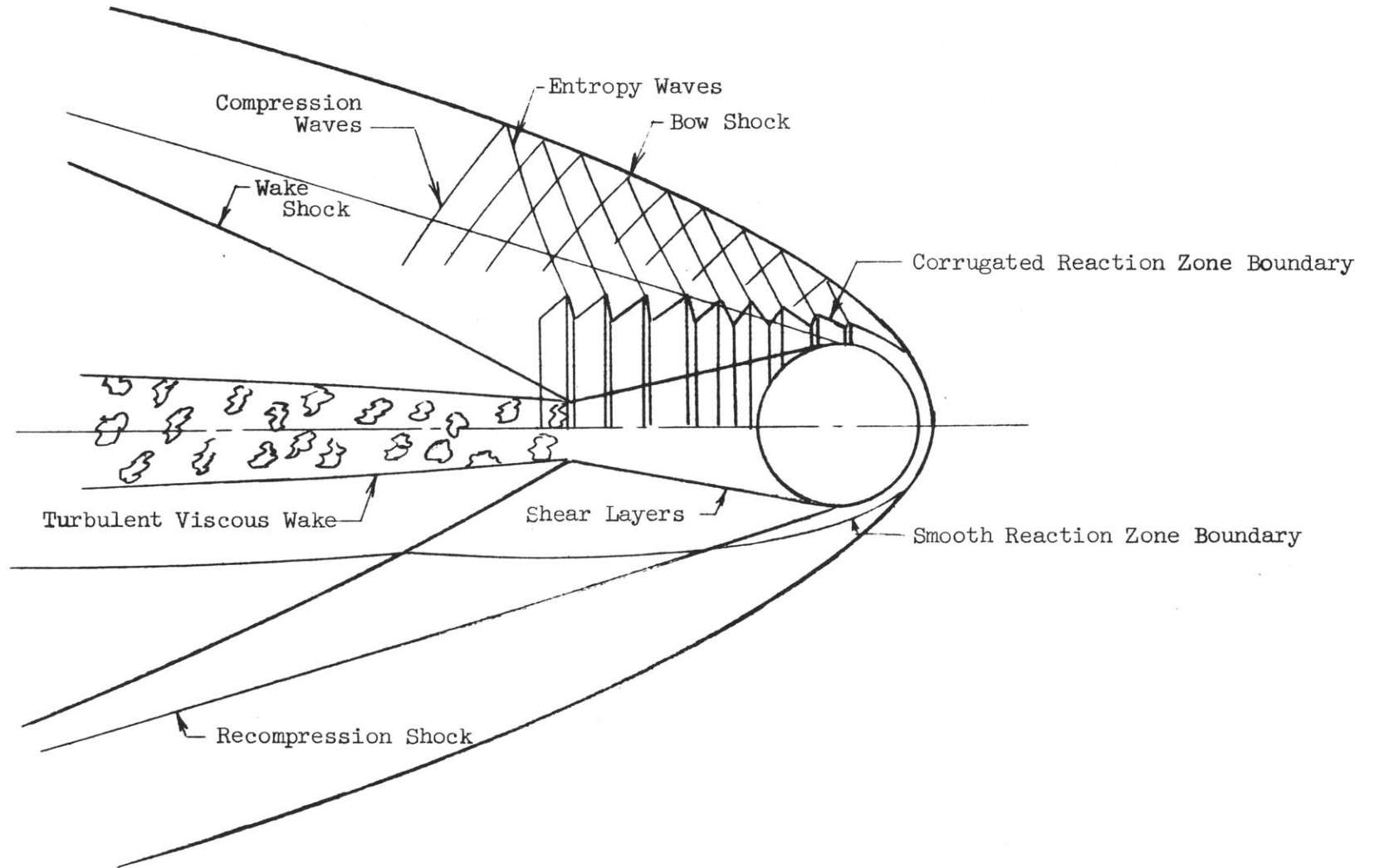
FIGURE 5

INTERMITTENT STABLE/PERIODIC FLOW

Run No. 87: $H_2:O_2:N_2$: 2:1:3.76

Mach No.: **5**.10

Pressure: 0.396 atm
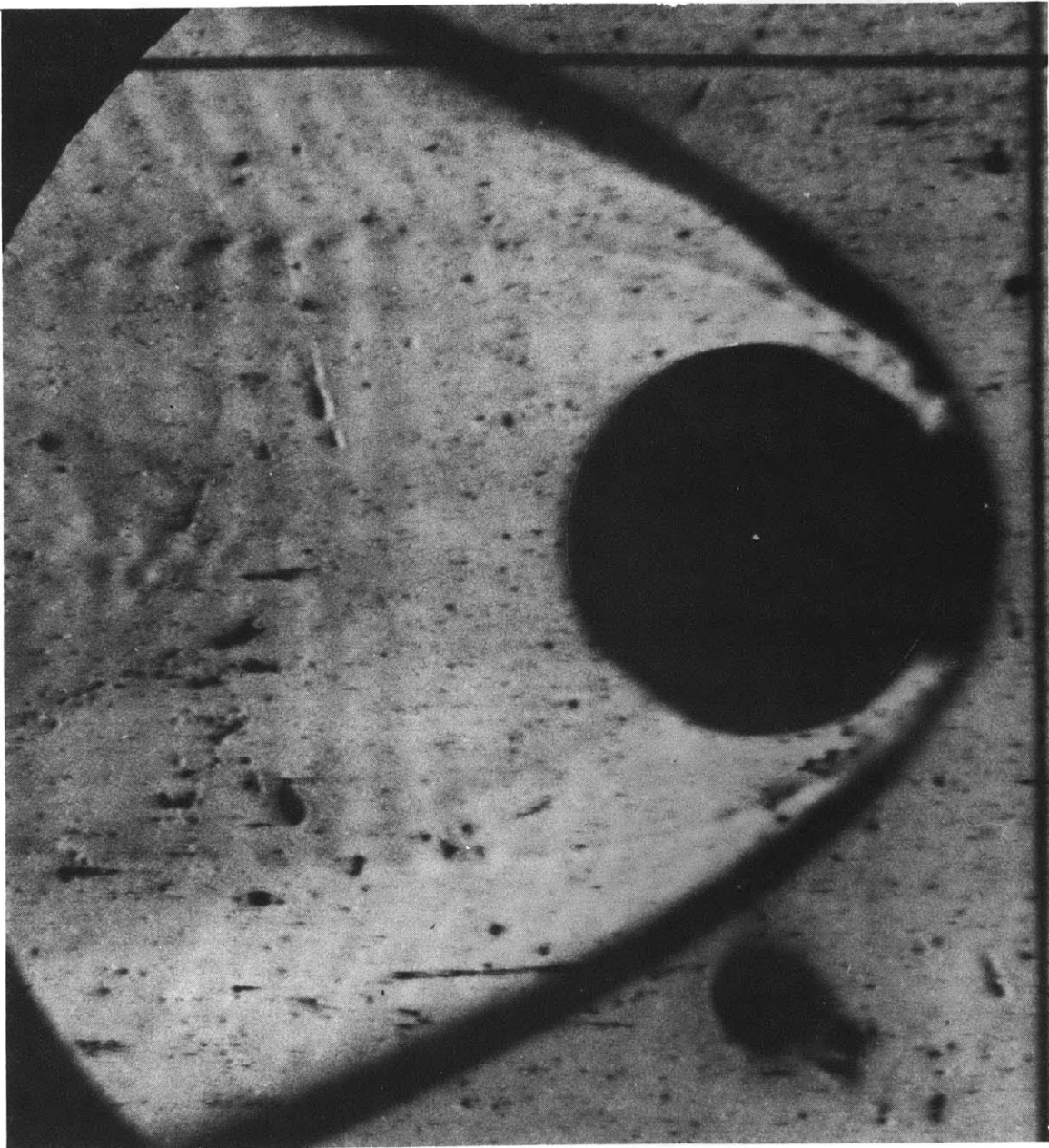
FIGURE 6

BOW SHOCK PROFILE CORRELATION

——————— Experiment - Run No. 87 (Fig. 5)

⊙ Correlation: $\dfrac{r}{D} = 1.14\left(\dfrac{x}{D}\right)^{0.49}$
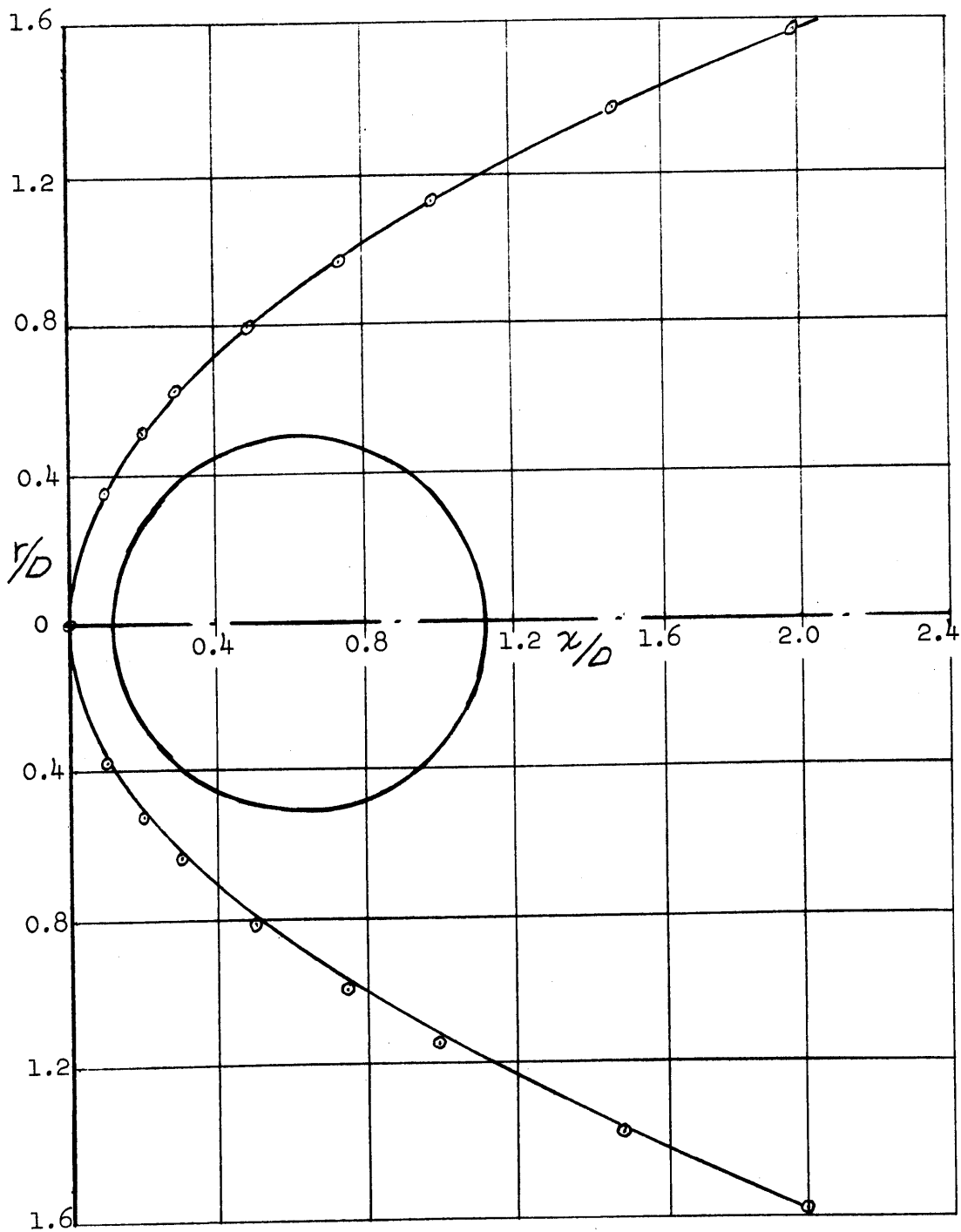
FIGURE 7

OVERTAKING DETONATION WAVE

Run No. 12: $C_2H_2:O_2$: 1:8

Mach No.: 5.94

Pressure: 0.132 atm

FIGURE 8

TURBULENT REGIME

Run No. 128: $C_2H_2:O_2:Ar$:   1:2.5:12.5

Mach No.:   5.49

Pressure: 0.264 atm
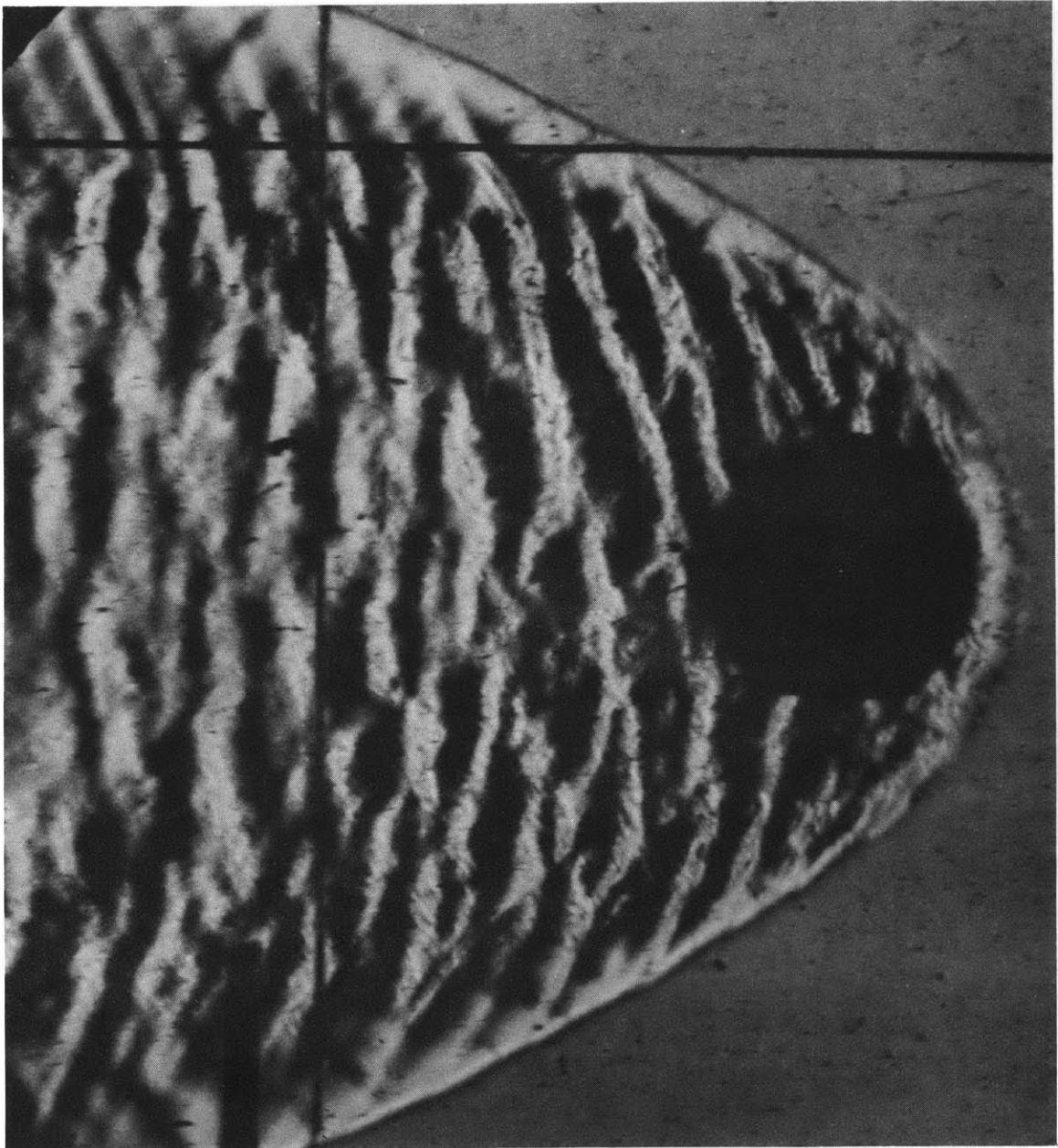
FIGURE 9

ANOMALOUS HIGH FREQUENCY OSCILLATION

Run No. 85: $H_2:O_2:N_2$: 2:1:3.76

Mach No.: 4.40
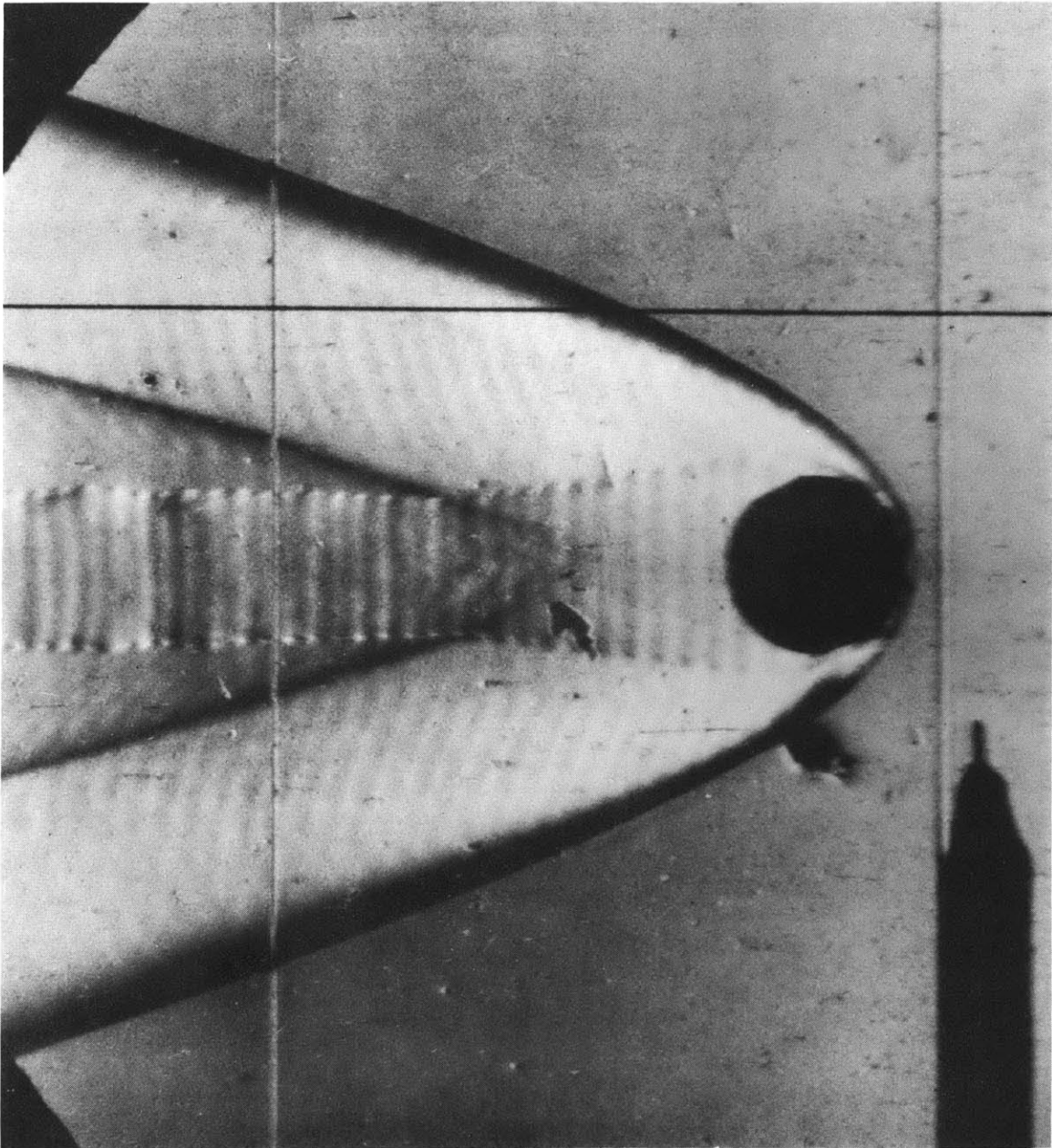
Pressure: 0.396 atm

FIGURE 10

VERY HIGH FREQUENCY PERIODIC INSTABILITY

Run No. 108: H_2:O_2:Ar: 2:1:3.76

Mach No.: 5.02

Pressure: 0.396 atm
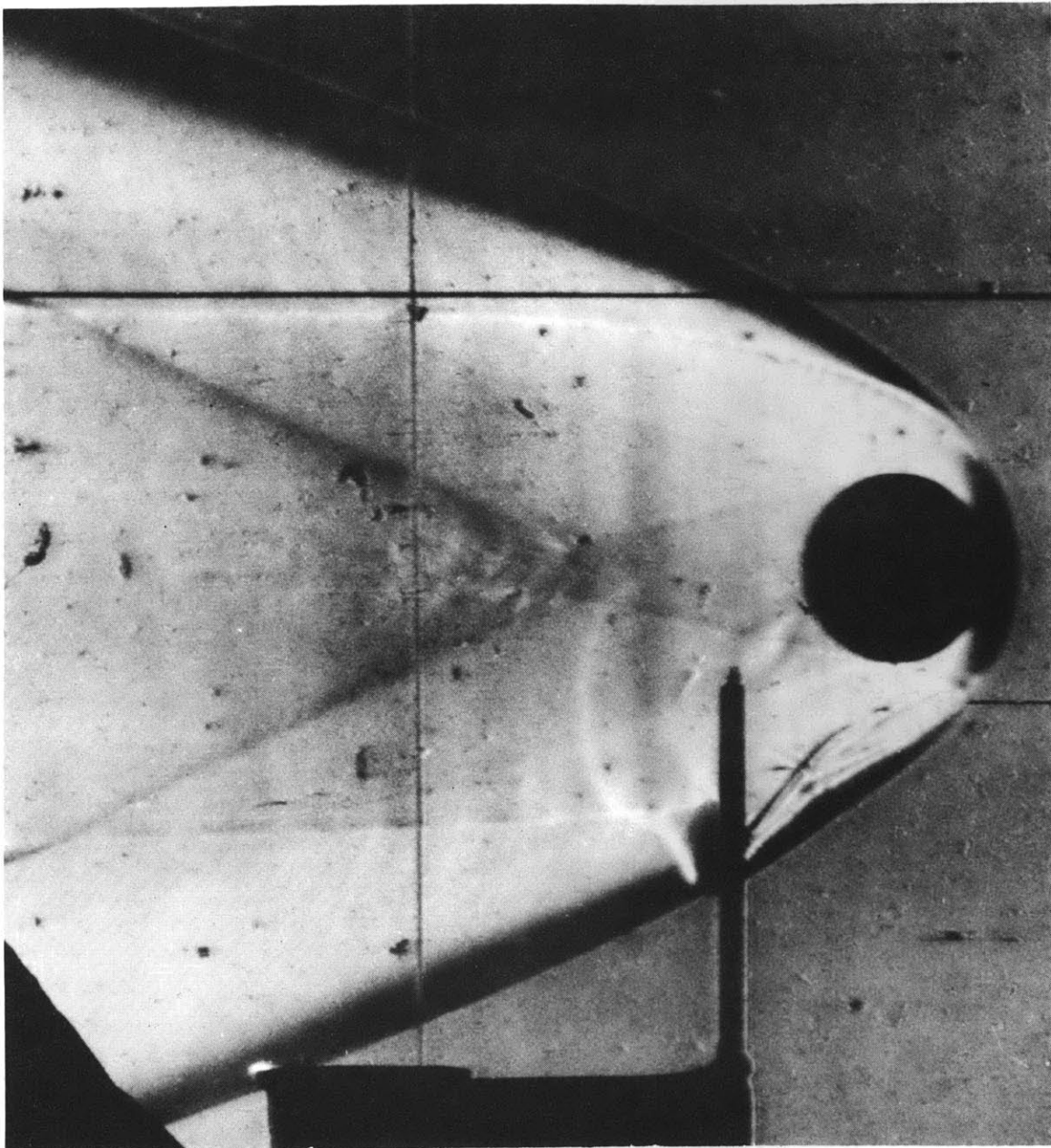
FIGURE 11

WAKE COMBUSTION REGIME

Run No. 144: $C_2H_2:O_2$: 1:15

Mach No.: 4.05

Pressure: 0.165 atm
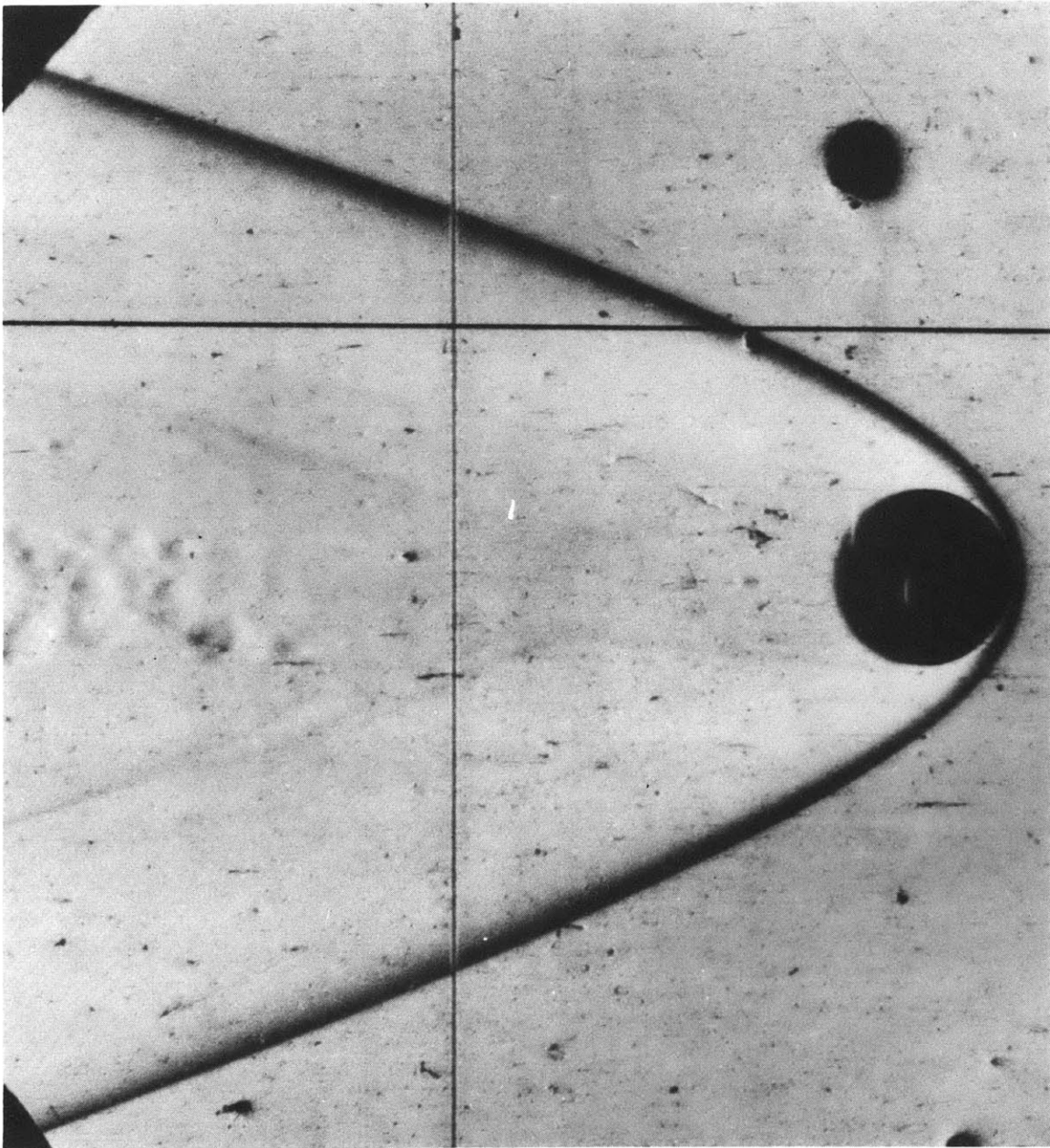
FIGURE 12

WAKE COMBUSTION REGIME

Run No. 84: $H_2 : O_2 : N_2$: 2:1:3.76

Mach No.: 4.19

Pressure: 0.264 atm
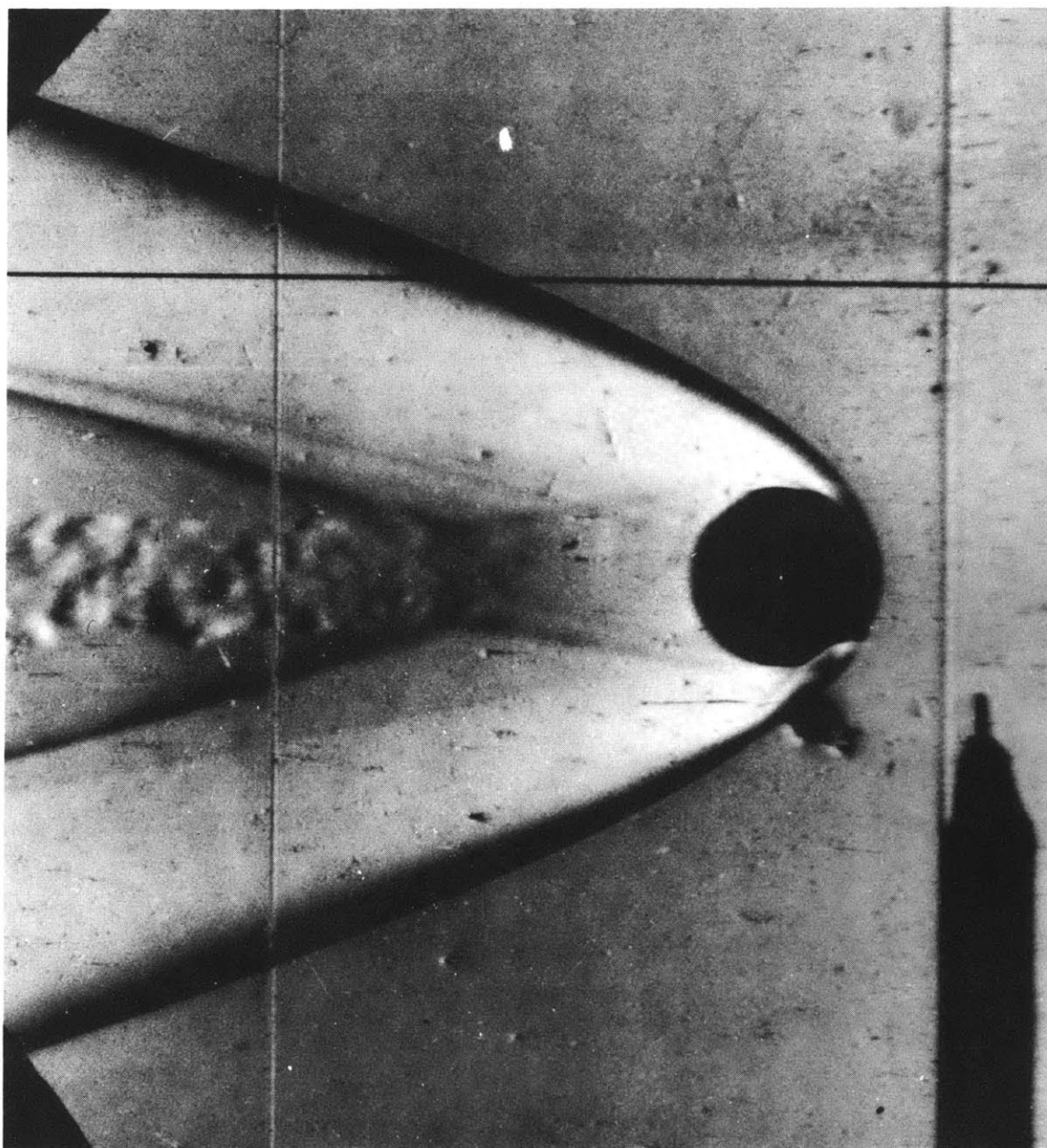
FIGURE 13

CORRUGATED REACTED GAS BOUNDARY CONFIGURATION

Run No. 88: $H_2:O_2:N_2$: 2:1:3.76

Mach No.: 4.67

Pressure: 0.396 atm
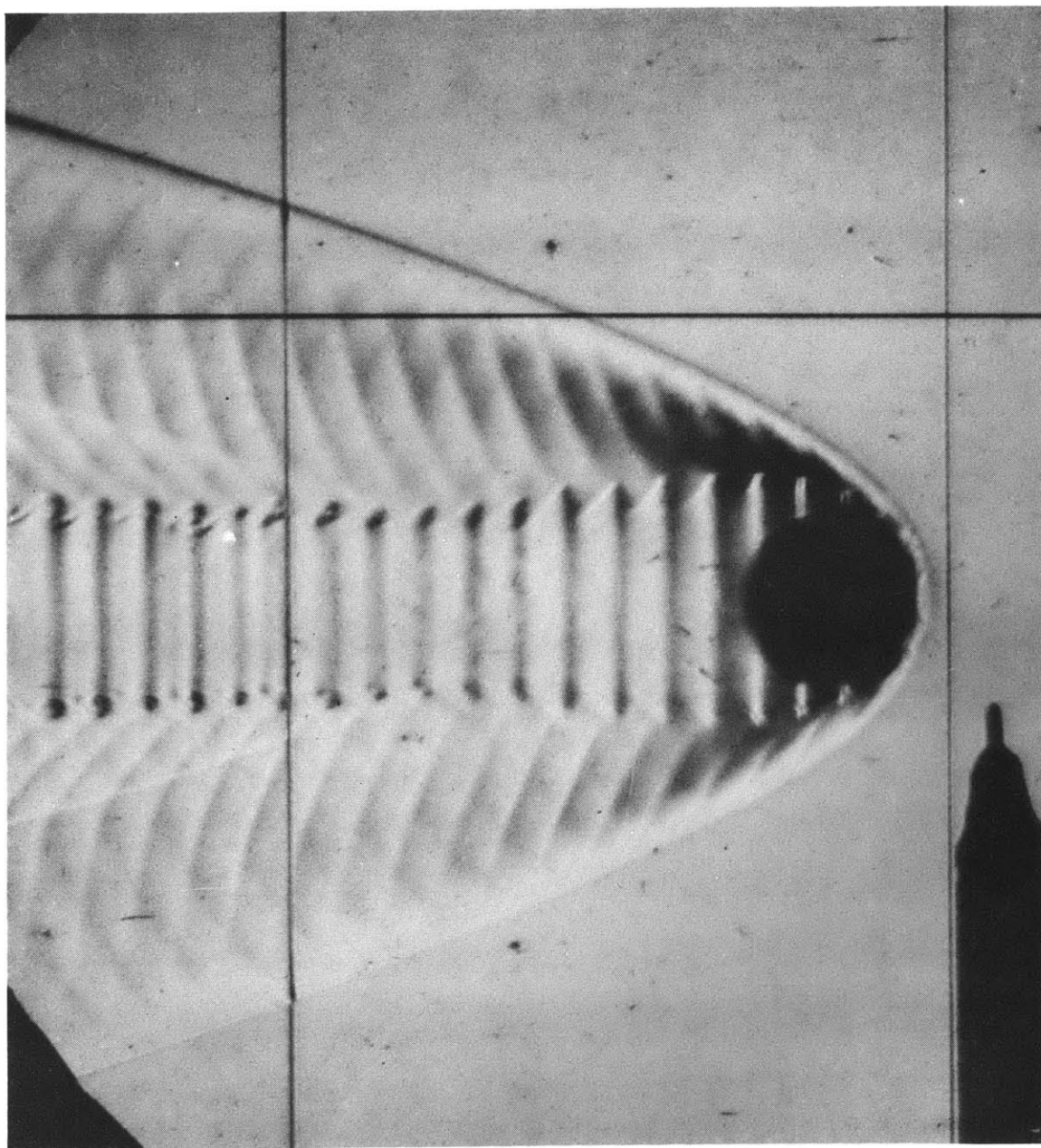
FIGURE 14

STABLE COMBUSTION REGIME

Run No. 106: $H_2:O_2:Ar$: 2:1:3.76

Mach No.: 5.26

Pressure: 0.396 atm
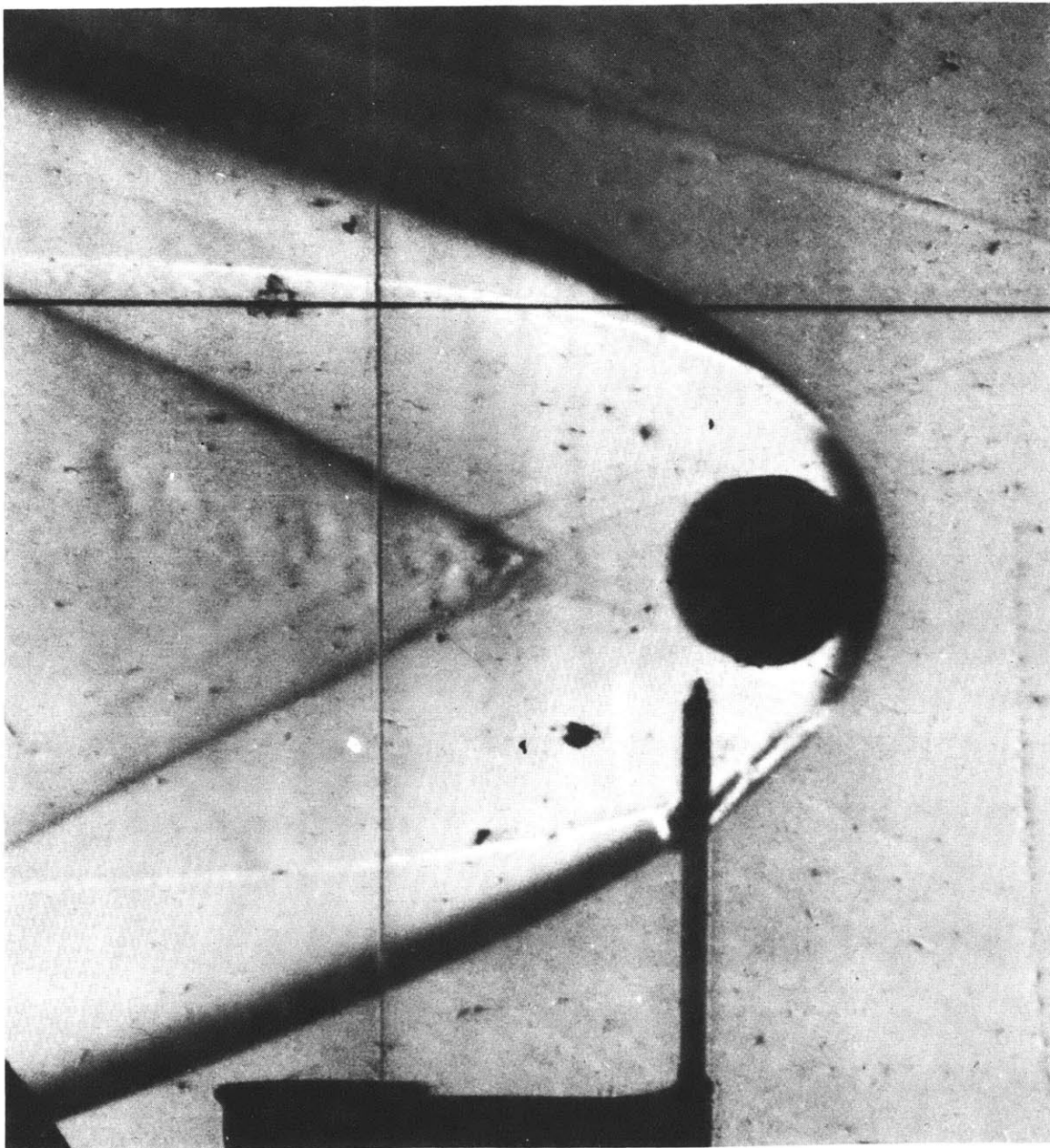
FIGURE 15

IONIZATION PROBE - ZERO SIGNAL

Run No. 151: C_2H_2:O_2 :   1:15

Mach No.:   4.71

Pressure: 0.198 atm

Normal component of bow shock Mach No. at probe intersection point = 3.2
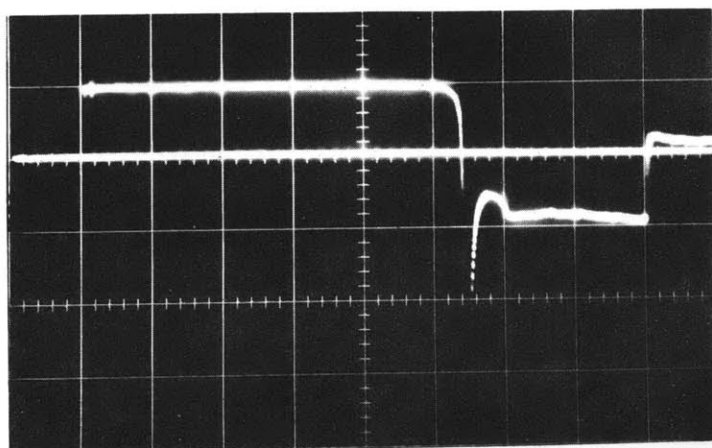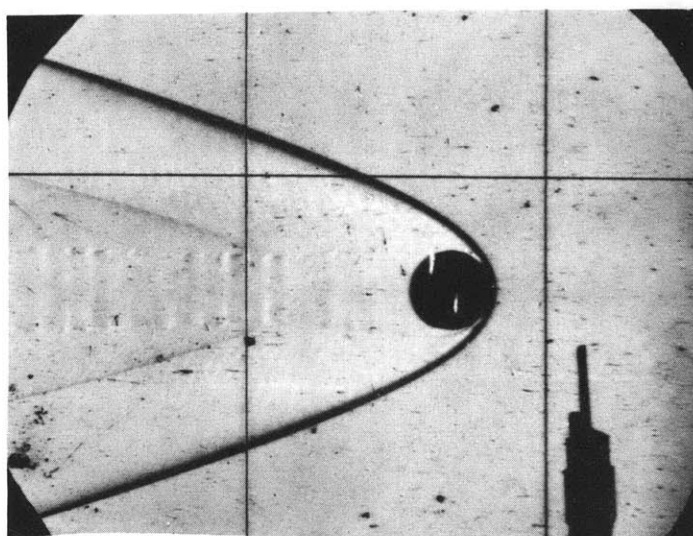
Schlieren Phototube
($40.0 \, \mu$ sec/cm)

Probe ($10.4 \, \mu$ sec/cm)

-1 0 1 2 3 4 5 6 7 8 9

Distance from intersection point to probe -
lower trace (diameters)

FIGURE 16

IONIZATION PROBE - DELAYED SIGNAL

Run No. 139: C_2H_2:O_2 : 1:15

Mach No.: 5.01

Pressure: 0.198 atm

Normal component of bow shock Mach No. at probe intersection point = 3.5
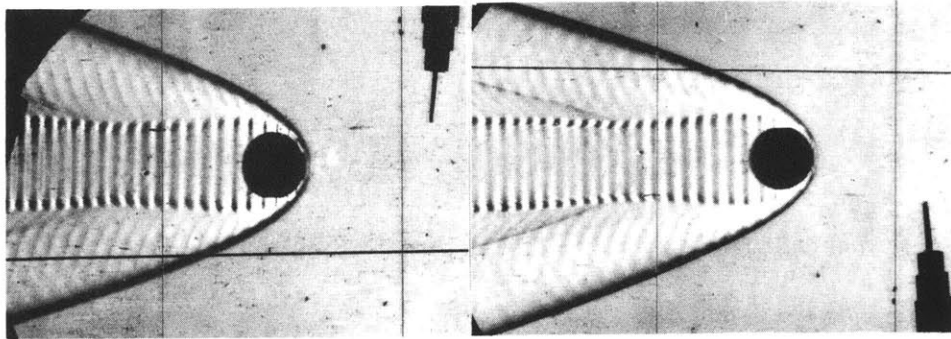
Time between photographs: 1.6 μsec

Schlieren phototube
(40.0μsec/cm)

Probe (10.4 μsec/cm -
sweep begins when first
Photograph is exposed)

Distance from intersection point to probe - lower trace (diameters)
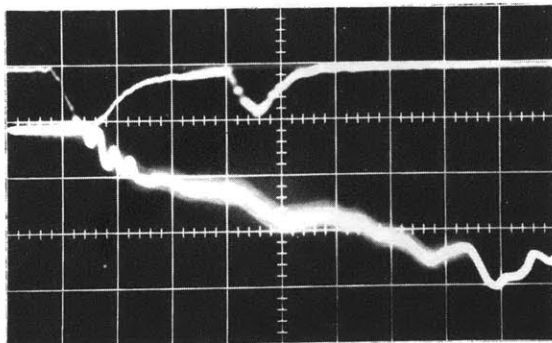
Spark phototube
(0.52 μsec/cm)

Probe (53 μsec/cm -
sweep begins when
second photograph
exposed)

FIGURE 17

IONIZATION PROBE - PROMPT SIGNAL

Run No. 157: $C_2H_2:O_2$:   1:15

Mach No.:   5.16

Pressure: 0.198 atm

Normal component of bow shock Mach No.
at probe intersection point = 3.6
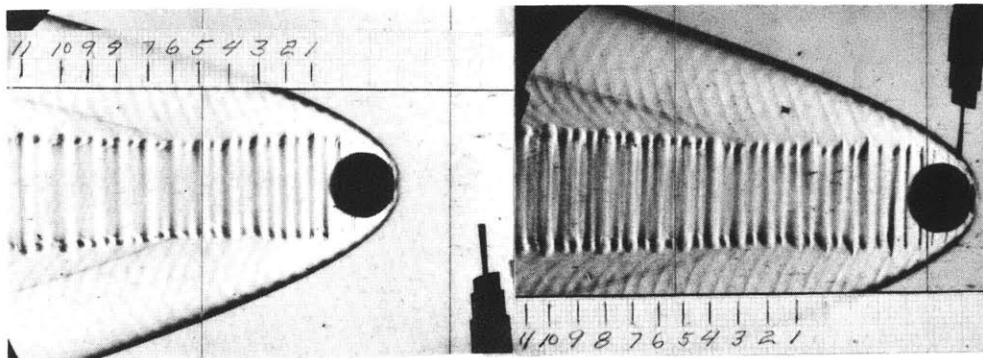
Time between photographs: 11.9 μ sec
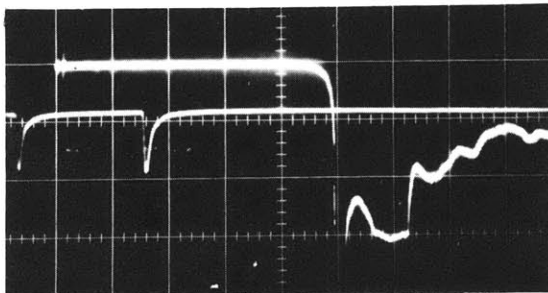
Schlieren phototube
(40.3 μ sec/cm)

Spark phototube
(5.3 μ sec/cm)
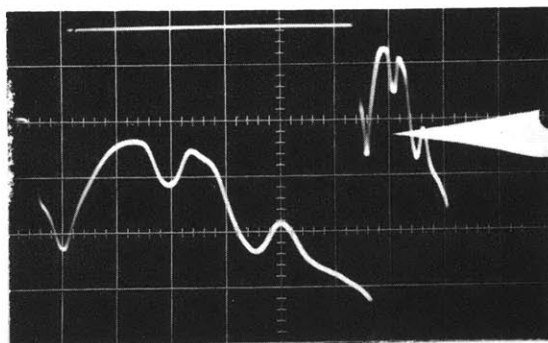
Probe (41 μ sec/cm)
Sweep begins 198 μ sec
before first photo exposed.

Probe (10.6 μ sec/cm)
Sweep begins when second
photo exposed.

FIGURE 18

DUAL SCHLIEREN MEASUREMENT OF REACTED
GAS BOUNDARY STREAMWISE VELOCITY

Note: Velocity measured relative to
laboratory observer
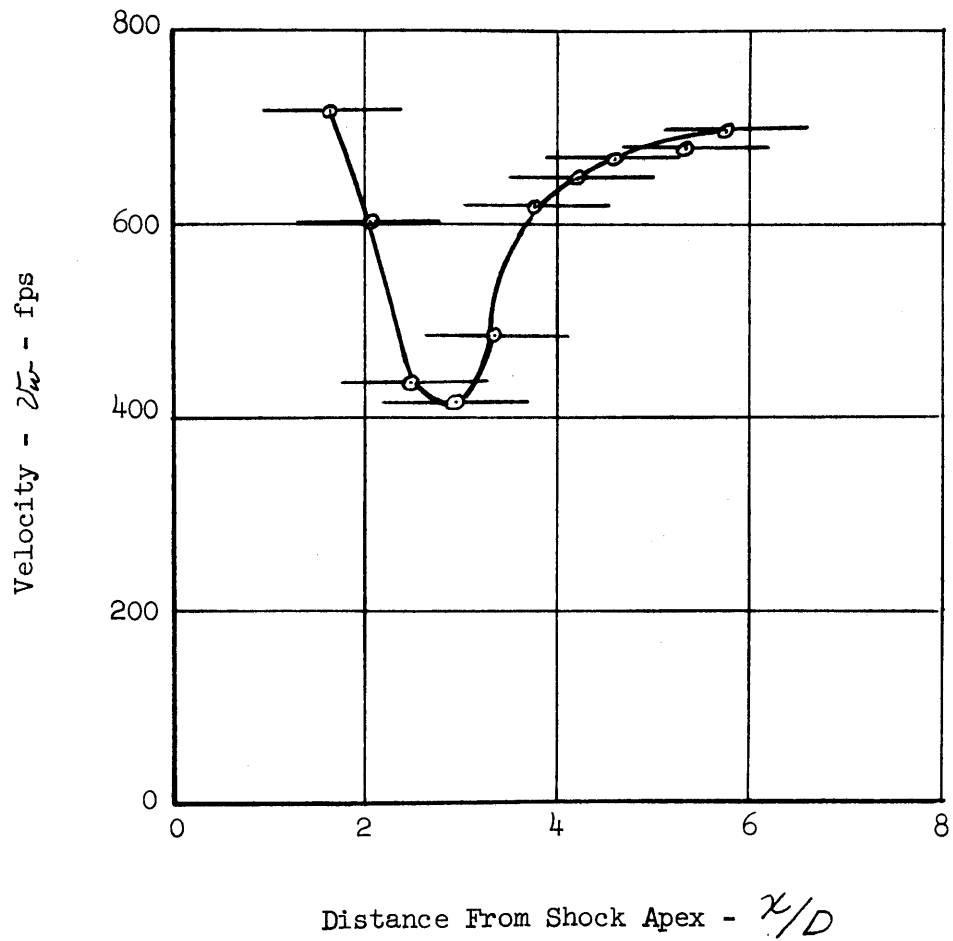
FIGURE 19

SCHLIEREN PHOTOTUBE MEASUREMENT OF REACTED GAS BOUNDARY
STREAMWISE VELOCITY

Run No. 142: C_2H_2:O_2 : 1:15

Mach No.: 4.58

Pressure: 0.198 atm
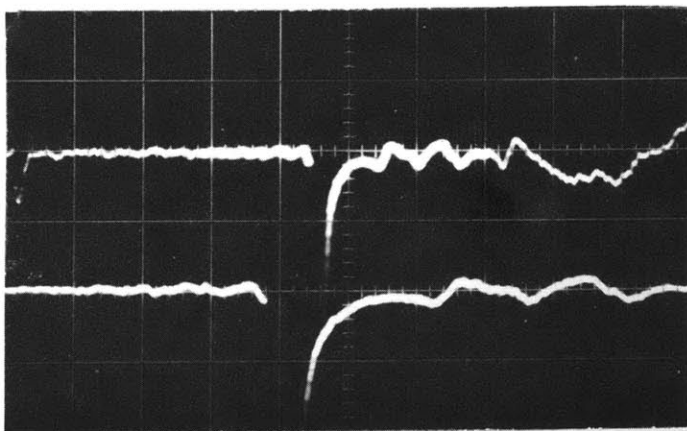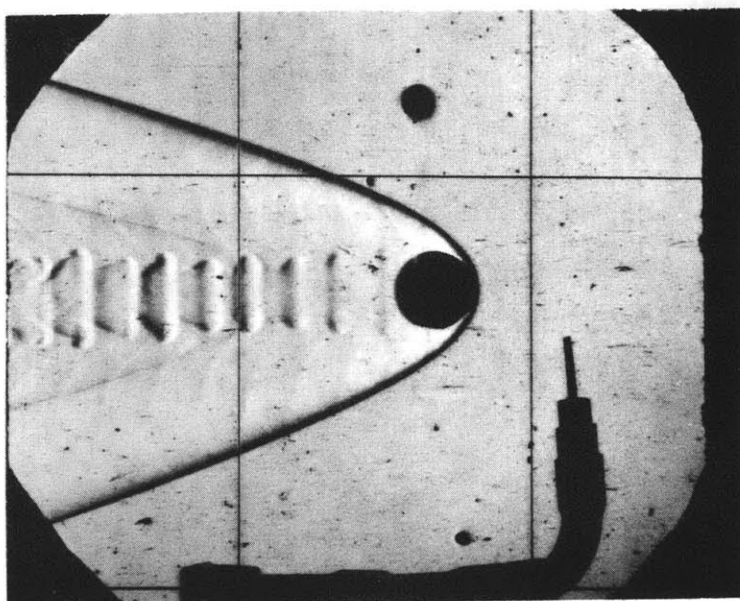
Sweep rate: 51 μsec/cm

Sweep rate: 21 μsec/cm

Phototube Output

FIGURE 20

STREAMLINES AND CONSTANT MACH NUMBER CONTOURS

Note: $M_o = 5.0$
$\gamma = 1.4$
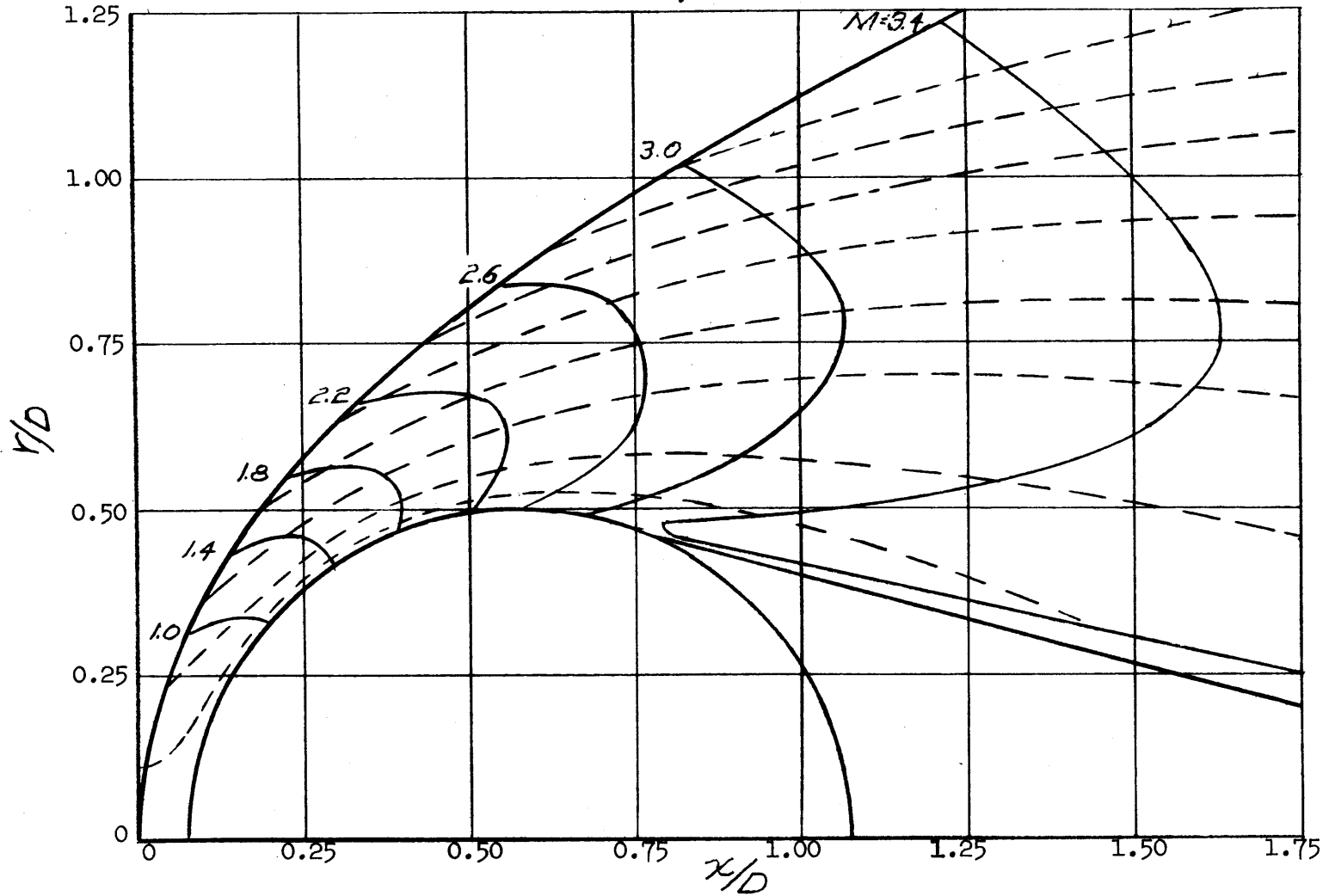
FIGURE 21

REGULAR PERIODIC INSTABILITY

Run No. 86: $H_2:O_2:N_2$: 2:1:3.76

Mach No.: 4.40
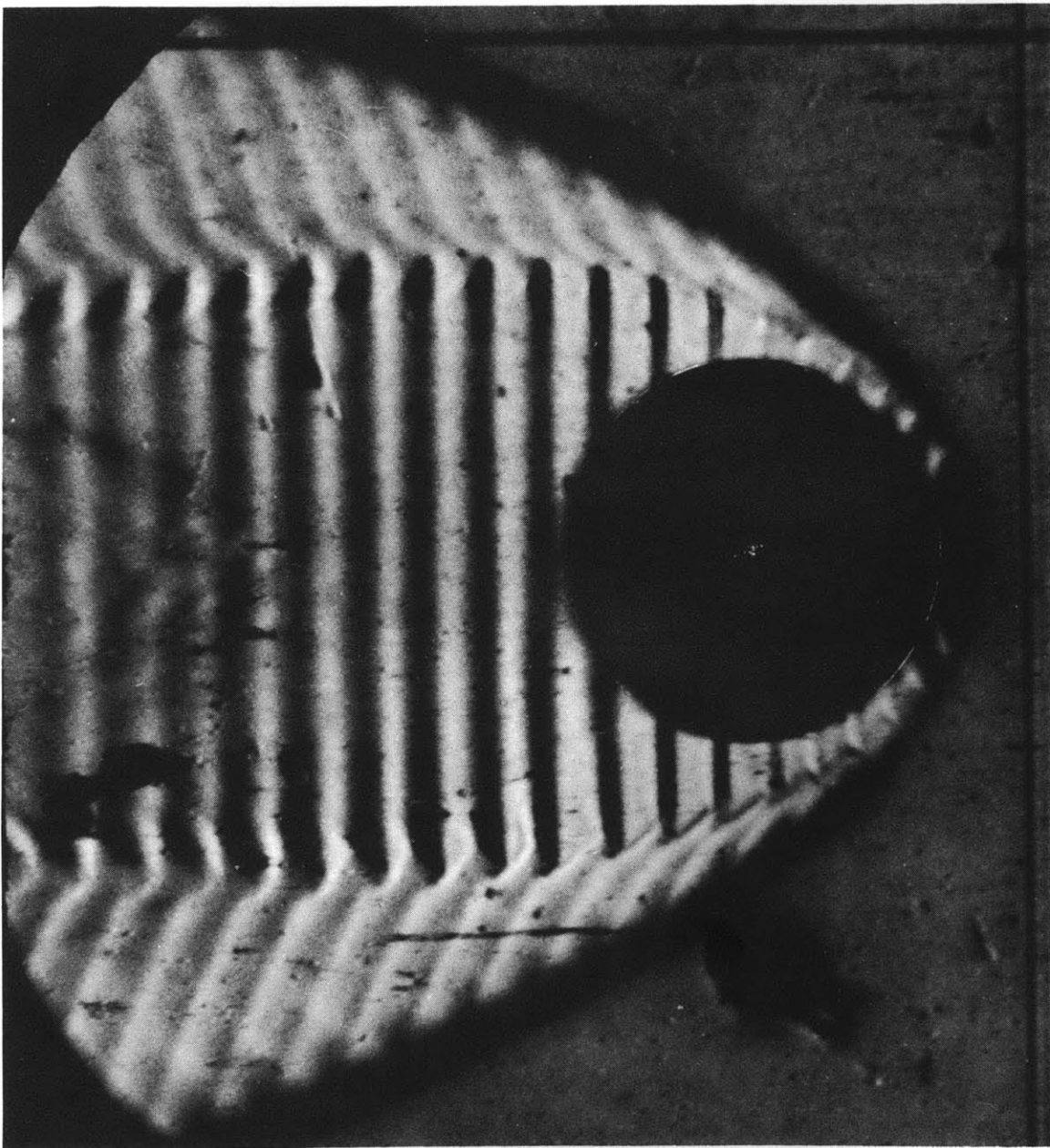
Pressure: 0.396 atm

FIGURE 22

EXISTENCE OF STRIATIONS IN NOSE REGION

Run No. 111: $H_2:O_2:Ar$: 2:1:3.76

Mach No.: 4.50

Pressure: 0.396 atm
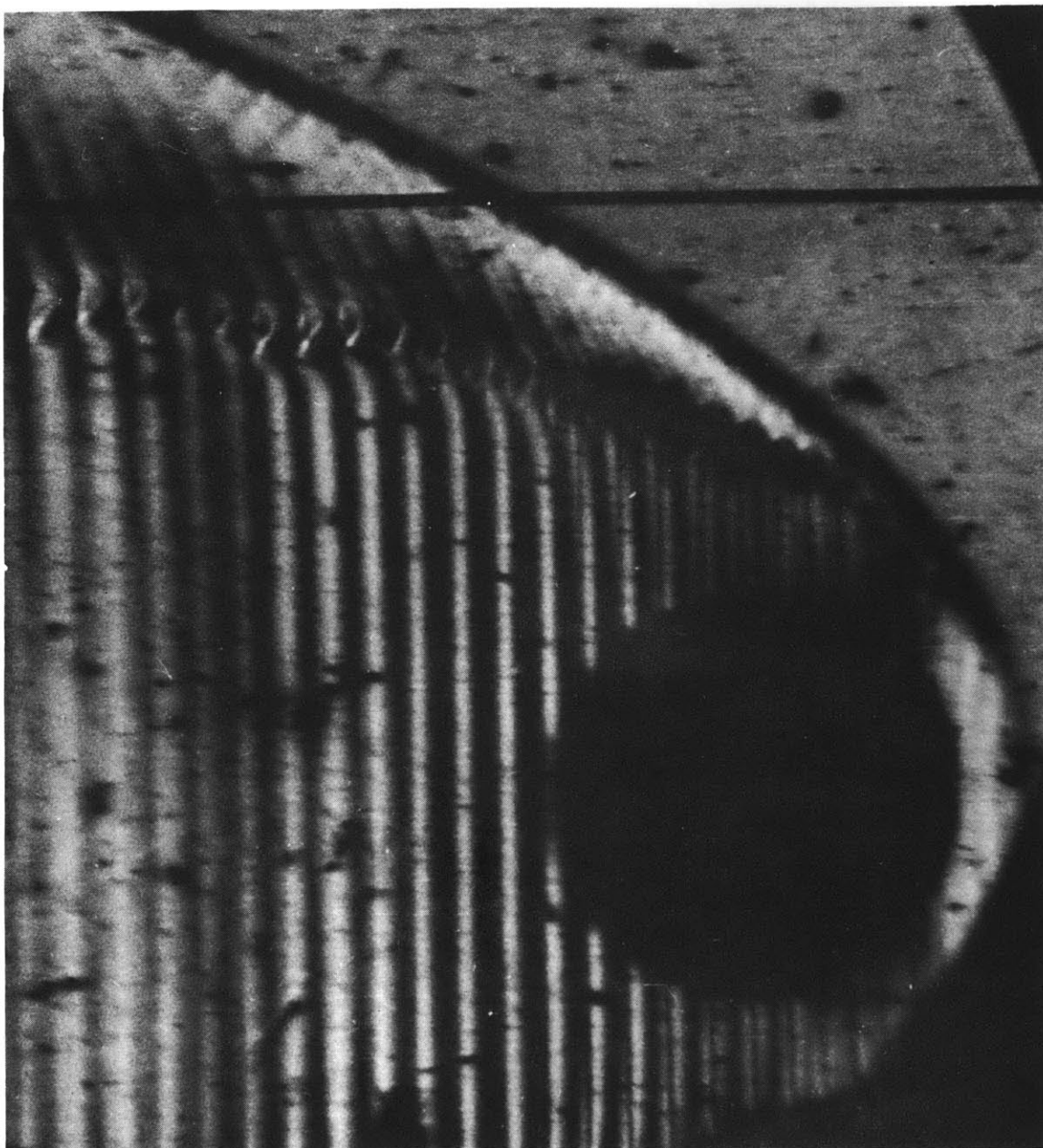
FIGURE 23

WAVEFORM DISTORTION AT HIGH PRESSURE

Run No. 248: $C_2H_2:O_2$: 1:15

Mach No.: 4.70

Pressure: 0.264 atm
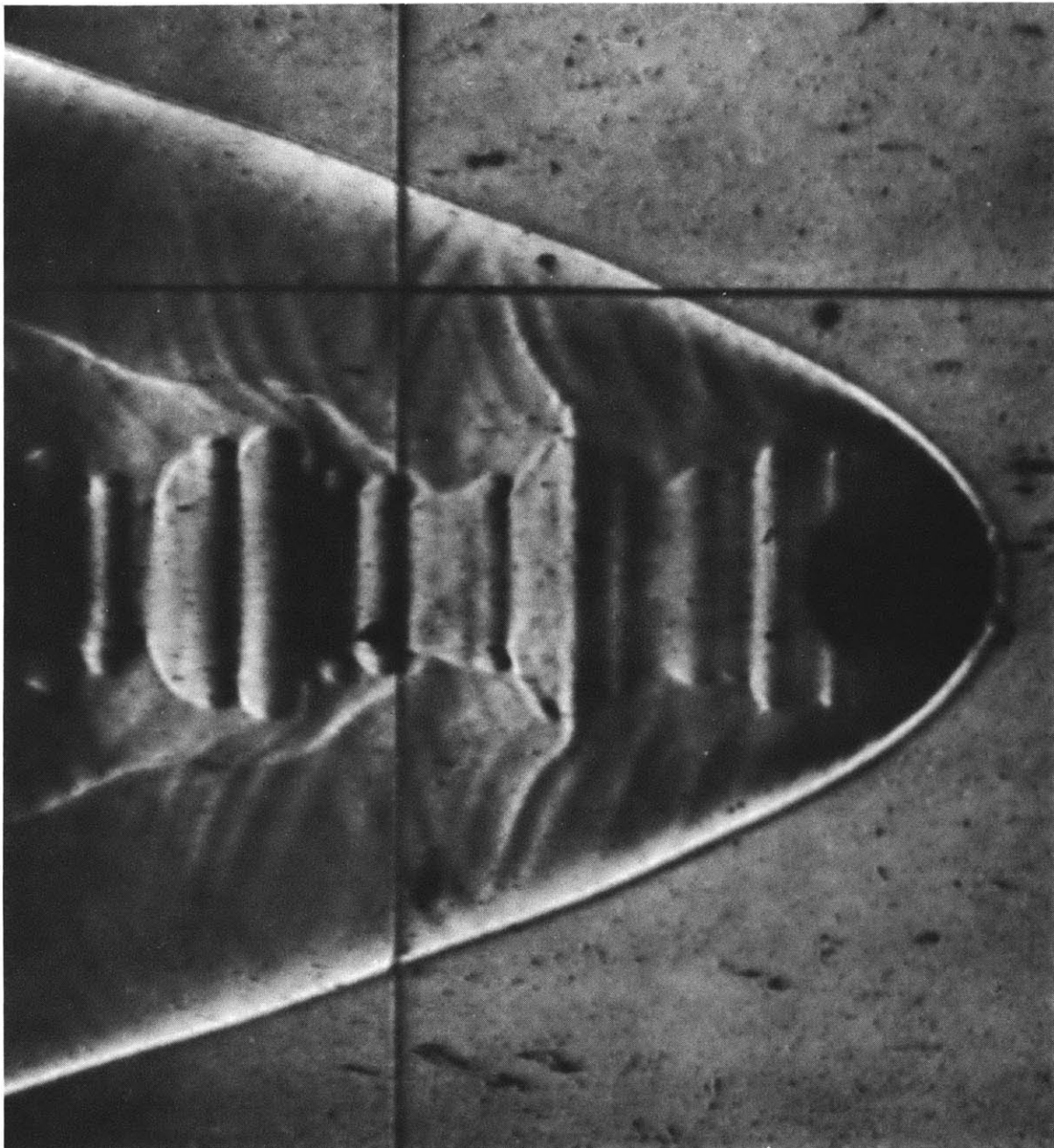
FIGURE 24

PROPAGATION RATE OF COMPRESSION WAVES IN INVISCID WAKE

Note: Data from Run No. 157
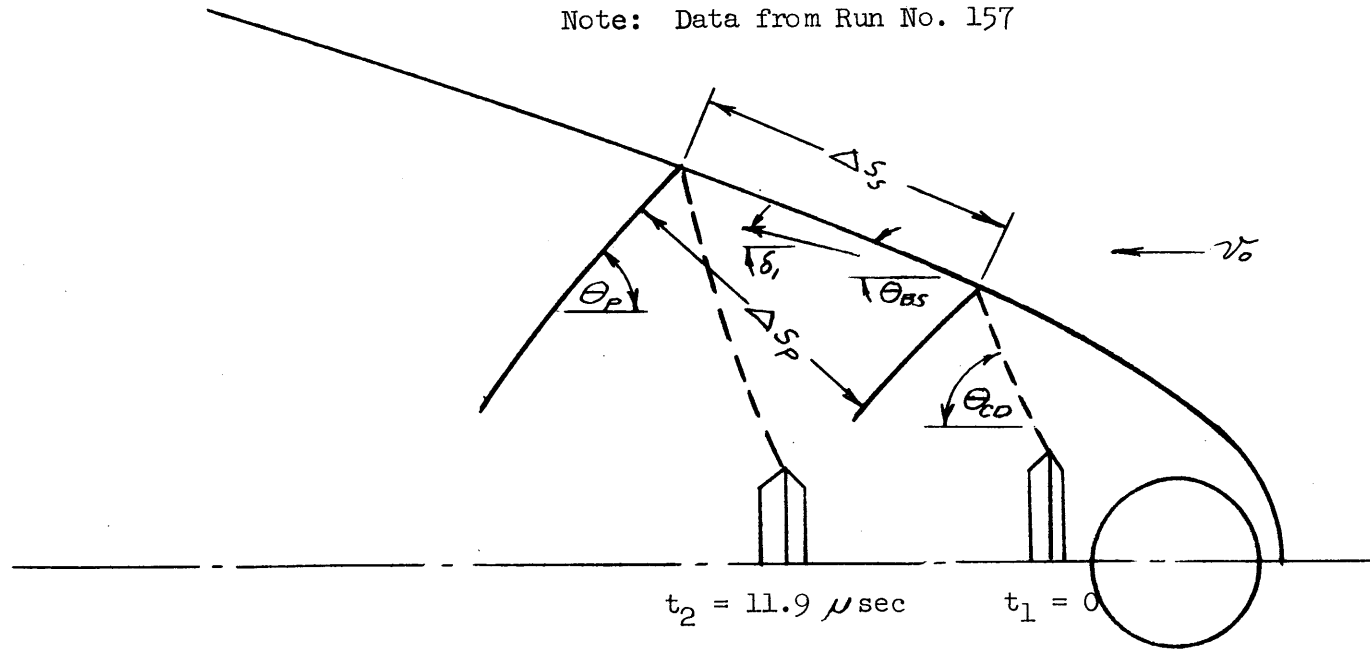
Measured Values	Calculated Values	Comparison
$\mathcal{V}_o$ = 5540 fps	$\mathcal{V}_1$ = 5180 fps	a_{meas} = 1400 fps
ΔS_s = 0.77 inches	δ_1 = 13.3°	a_{calc} = 1375 fps
Δt = 11.9 μ sec	a_1 = 1375 fps	
θ_{BS} = 22.3°		
θ_P = 45°		
θ_{CO} = 72°		

FIGURE 25

COMPRESSION WAVE AND ENTROPY WAVE CONTOURS

Note: M_0 = 5.0
γ = 1.4
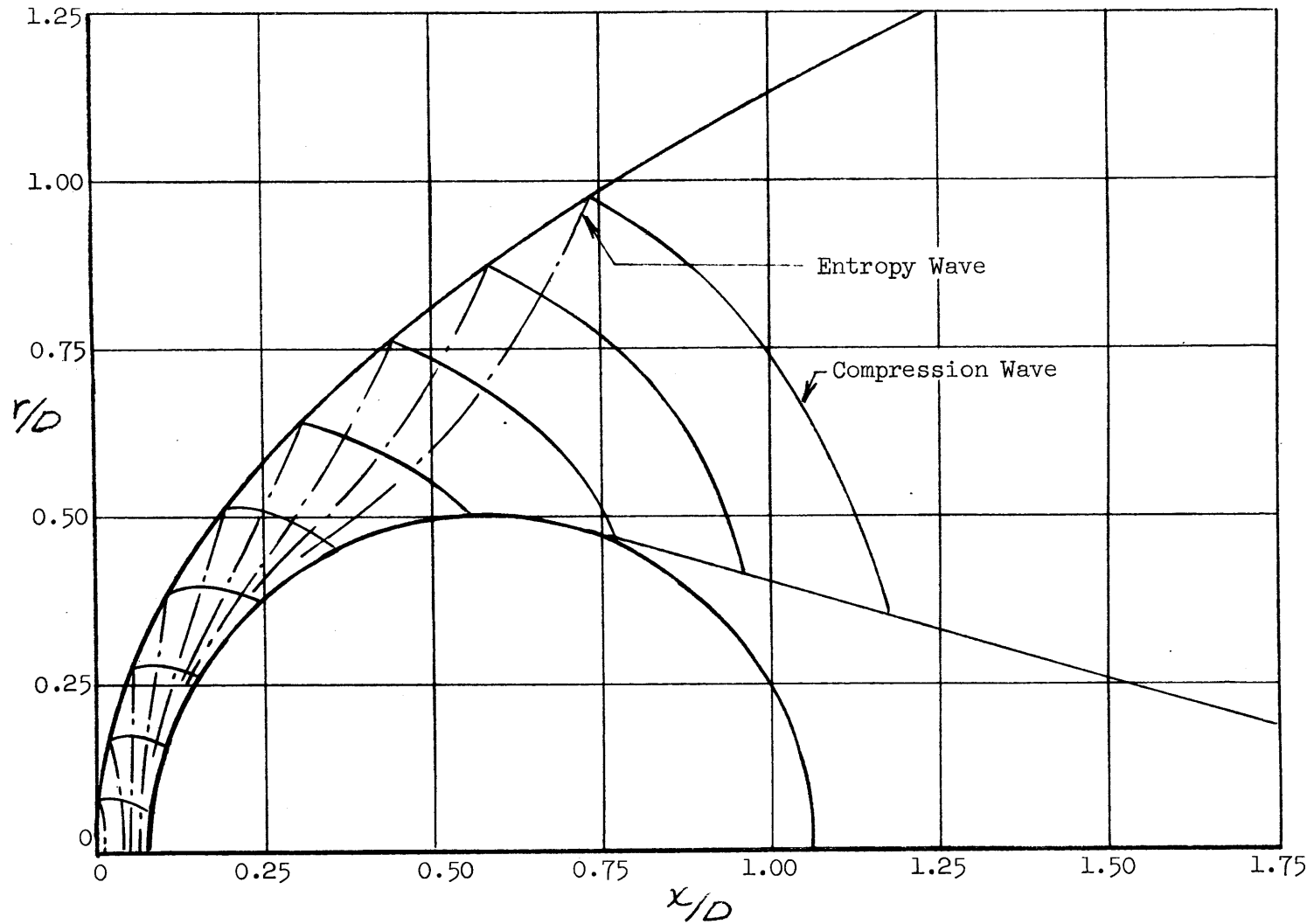
FIGURE 26

REGULAR PERIODIC INSTABILITY

Run No. 62: $C_2H_2:O_2$: 1:15

Mach No.: 4.90

Pressure: 0.198 atm
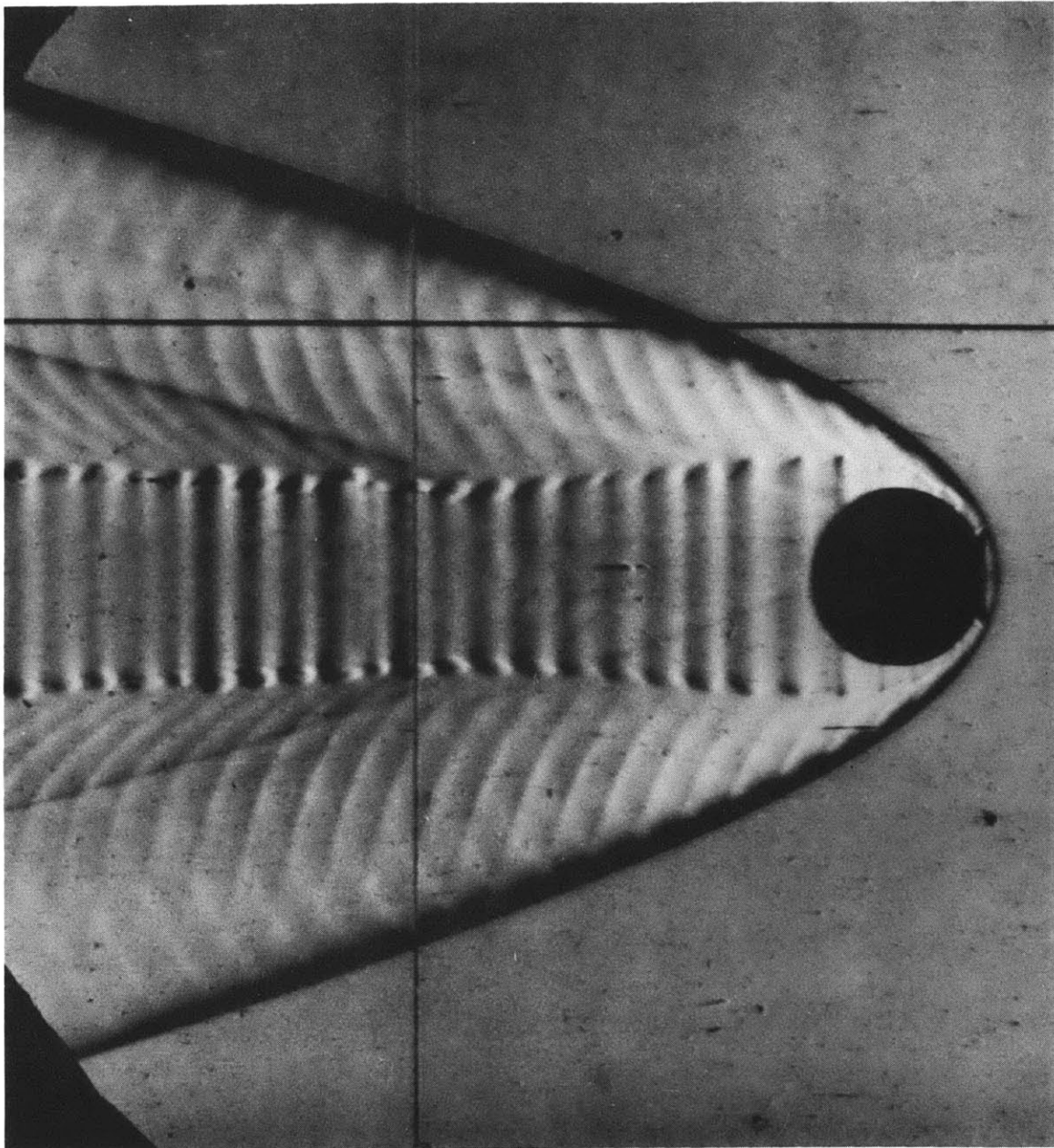
FIGURE 27

COMPRESSION WAVE - BOW SHOCK INTERACTION

Note: Numerical data corresponds to Run No. 154, x/D = 1.5
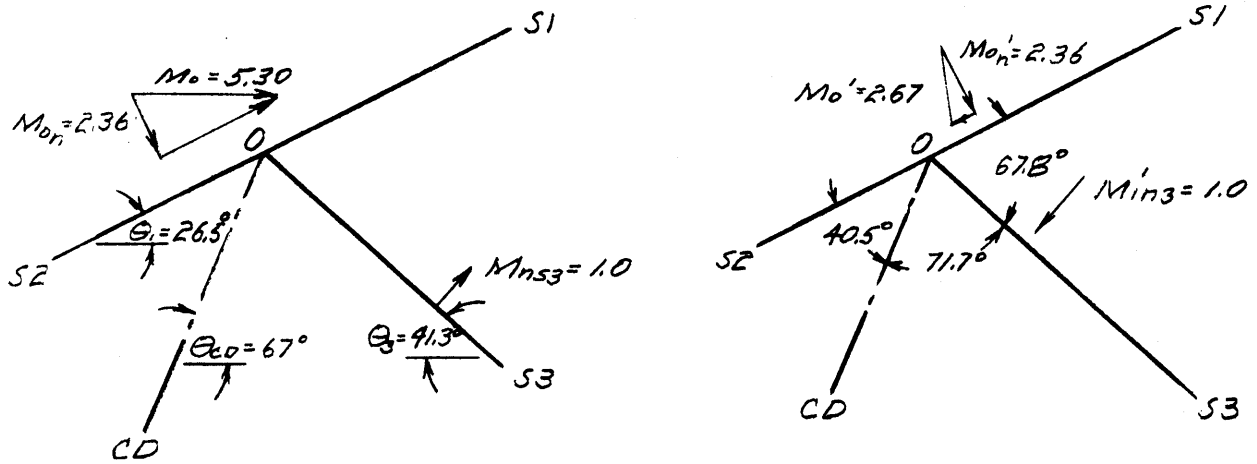
(a) Coordinates Fixed to Ball

(b) Coordinates Fixed to Intersection Point
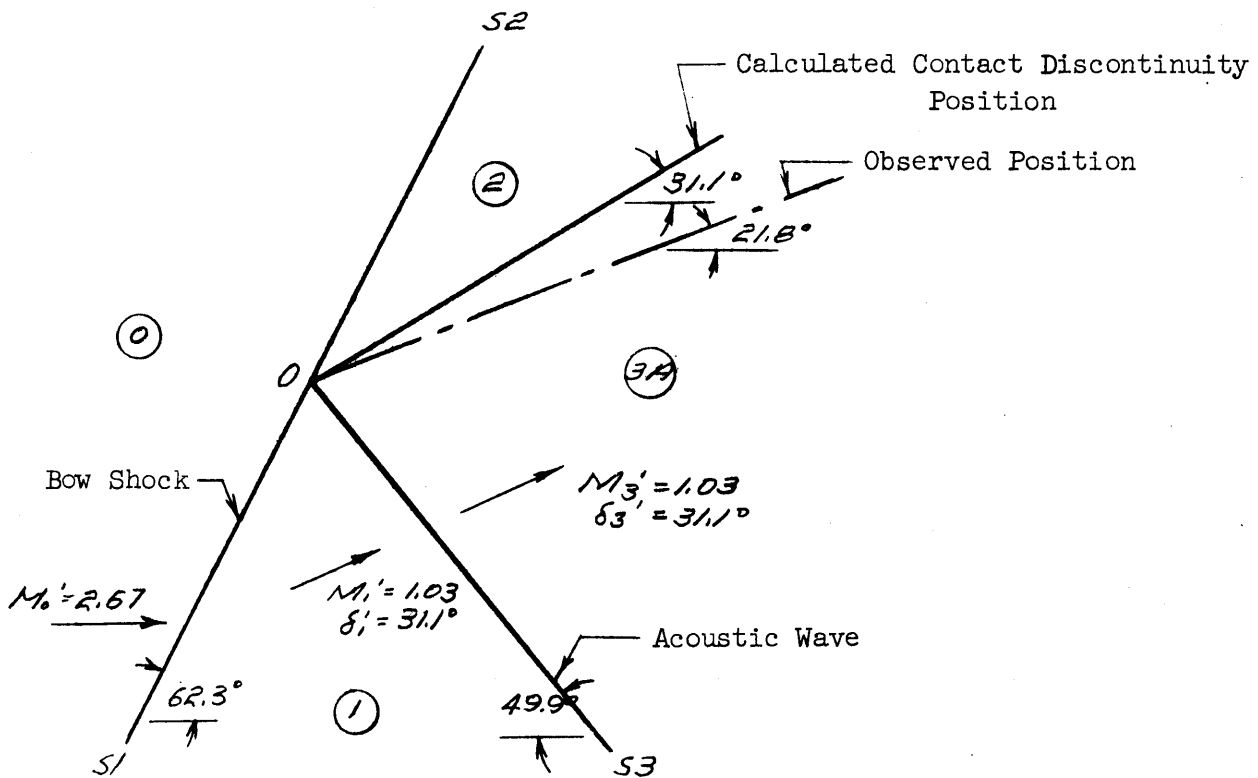
(c) Coordinates Fixed to Intersection Point, M_o' Parallel to x-Axis

FIGURE 28

FLOW FIELD REGIMES   ACETYLENE-OXYGEN Φ = 0.167

1/2" Diameter Spheres
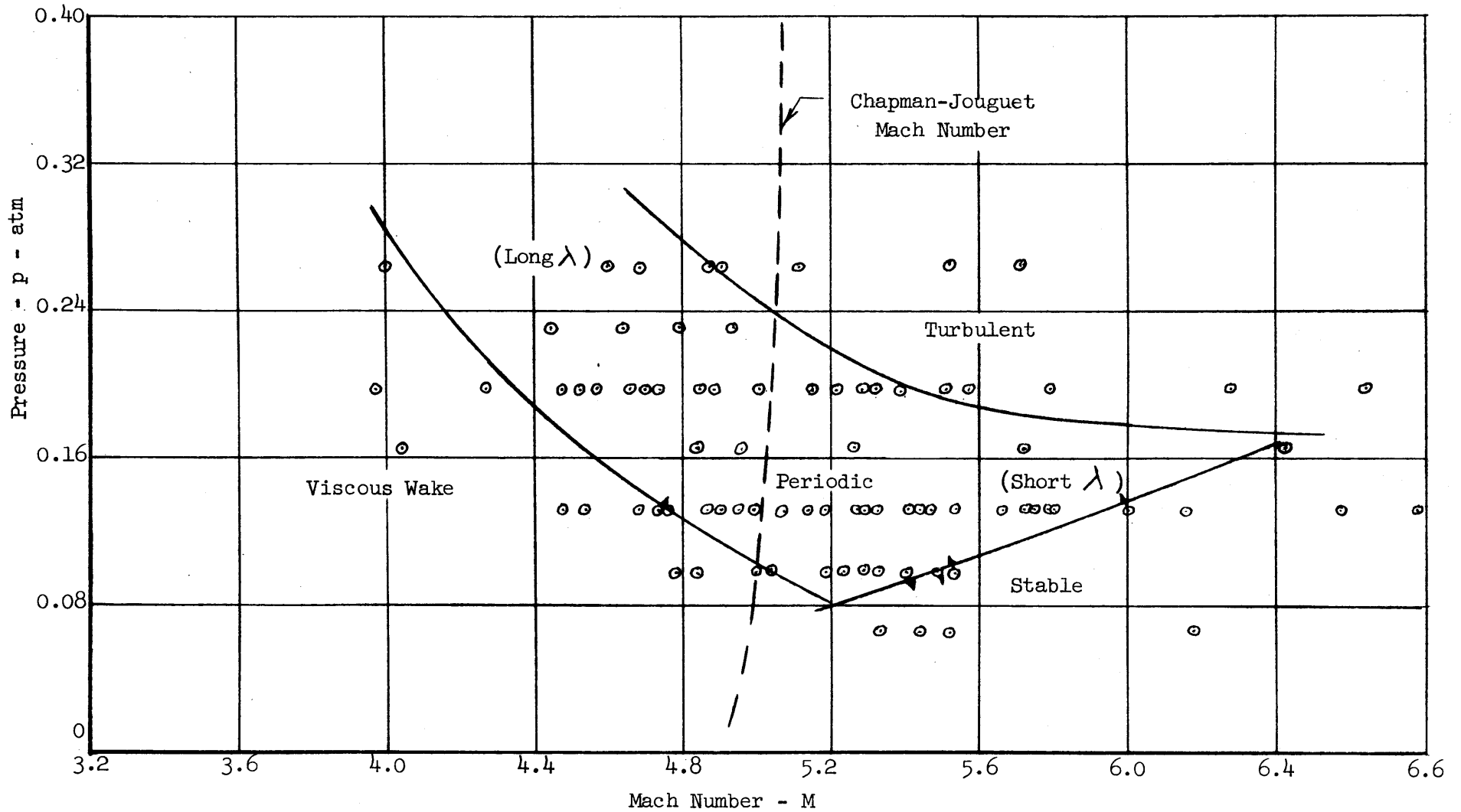
FIGURE 29

FLOW FIELD REGIMES
HYDROGEN-AIR Φ = 1.0
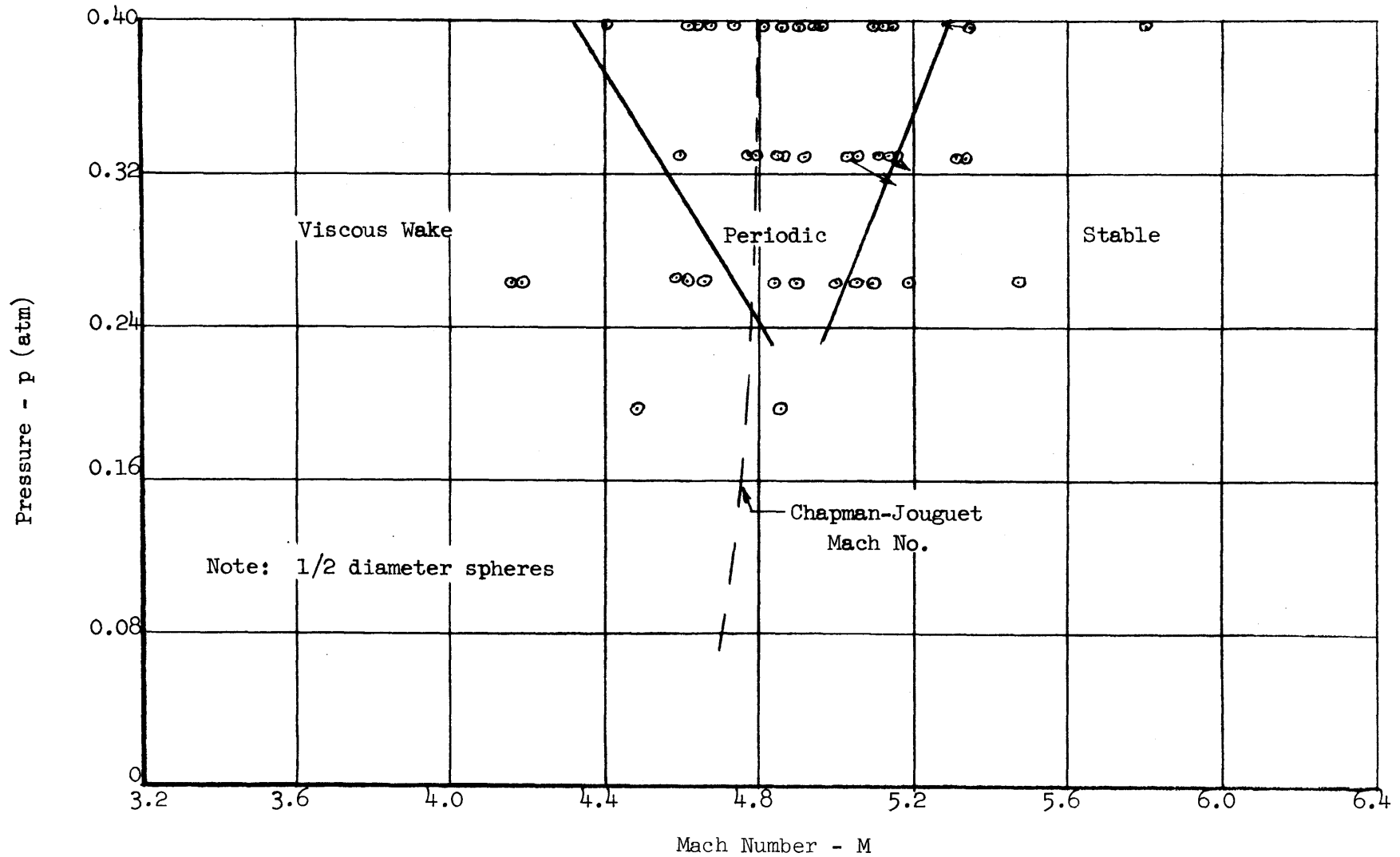
FIGURE 30

LONG WAVELENGTH REGULAR PERIODIC INSTABILITY

Run No. 260: $C_2H_2:O_2$: 1:15

Mach No.: 4.46

Pressure: 0.230 atm
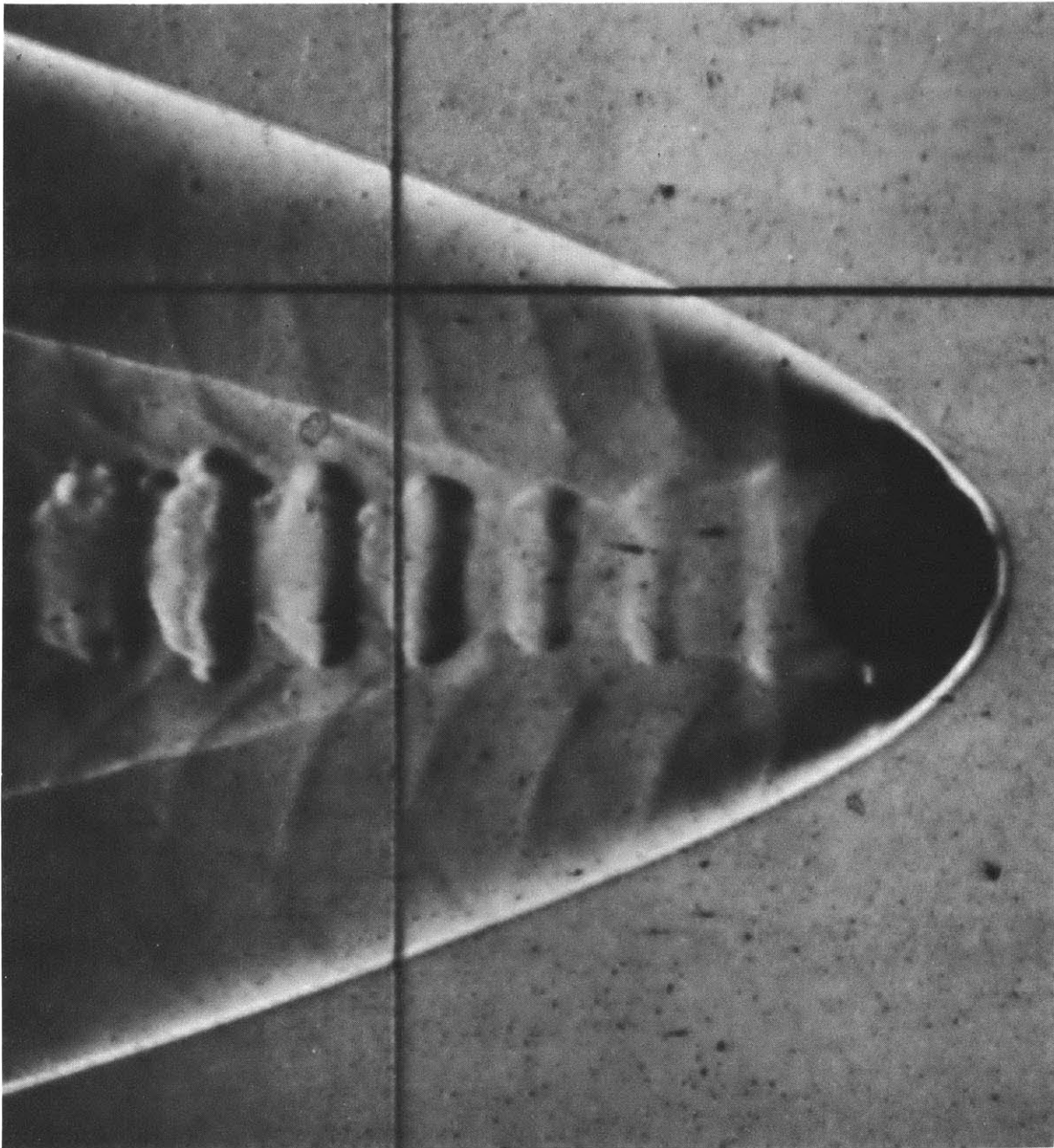
FIGURE 31

TURBULENT COMBUSTION NEAR REGIME BOUNDARY

Run No. 129: $C_2H_2:O_2:Ar:$ 1:2.5:12.5

Mach No.:   5.59

Pressure: 0.198 atm.
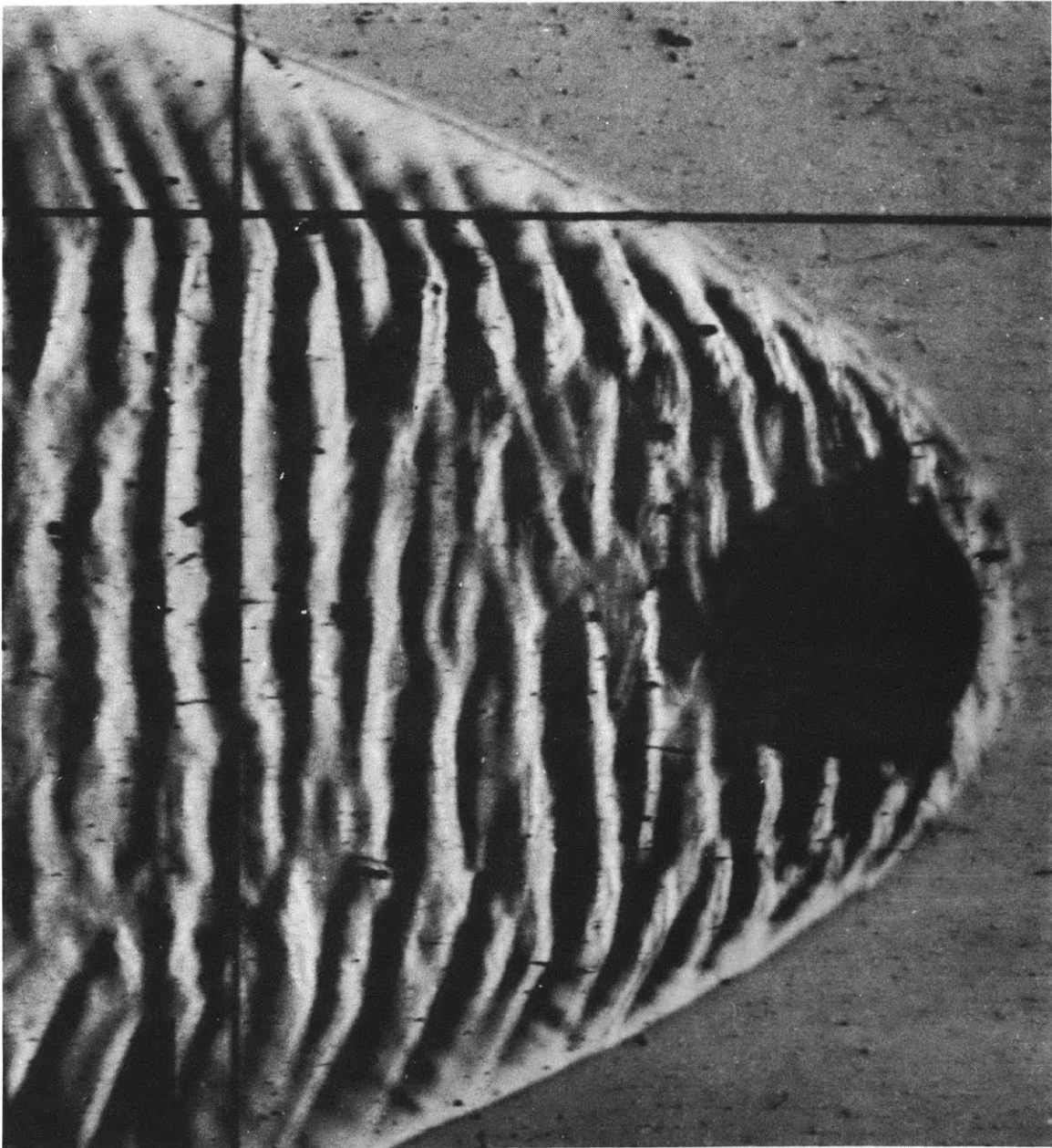
FIGURE 32

INTERMITTENT TURBULENT/PERIODIC FLOW

Run No. 254: $C_2H_2:O_2$:   1:15

Mach No.:   5.42

Pressure: 0.264 atm
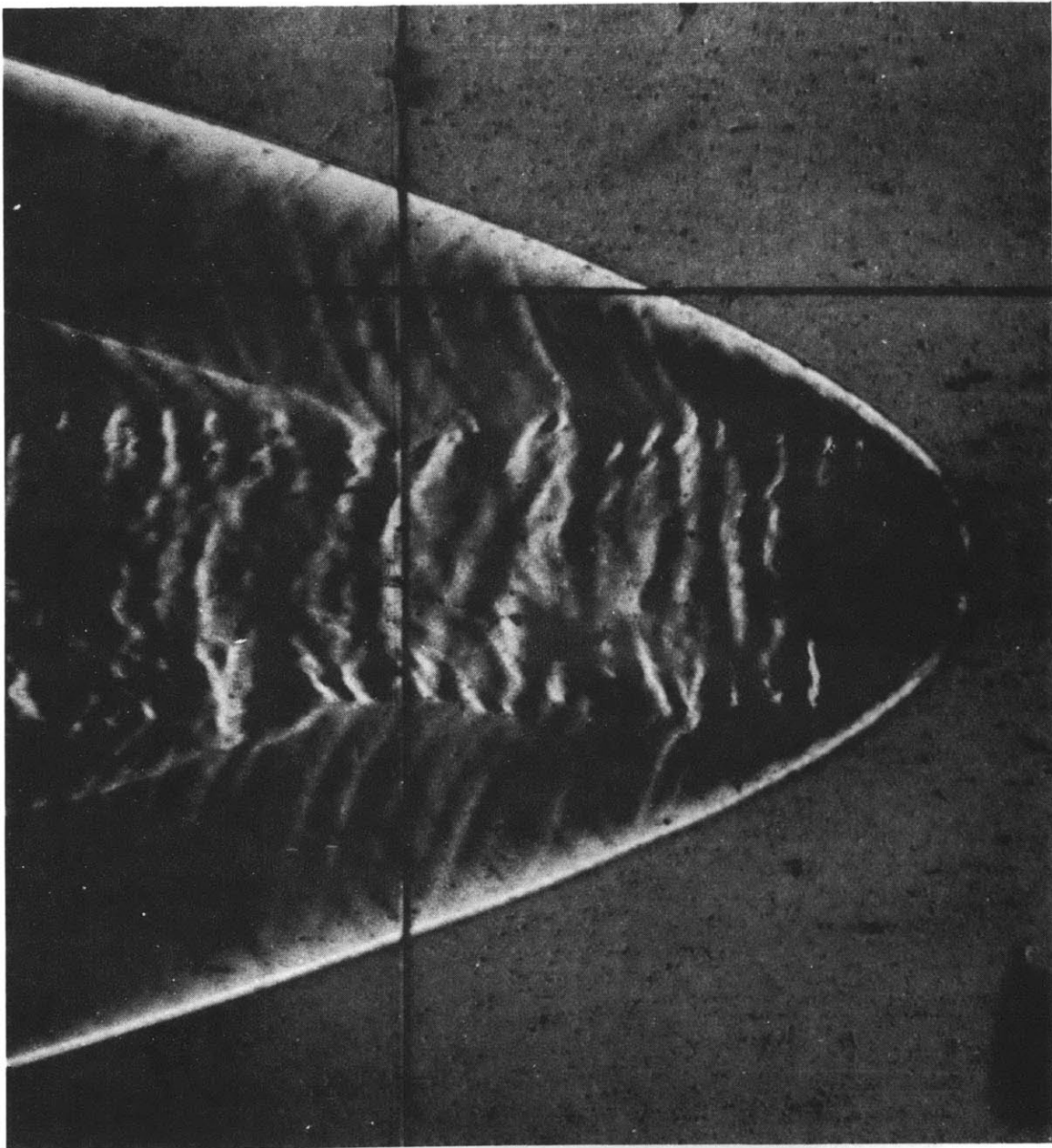
FIGURE 33

PERIODIC INSTABILITY NEAR REGIME BOUNDARY

Run No. 130: $C_2H_2:O_2:Ar$:   1:2.5:12.5

Mach No.:   5.56

Pressure: 0.132 atm
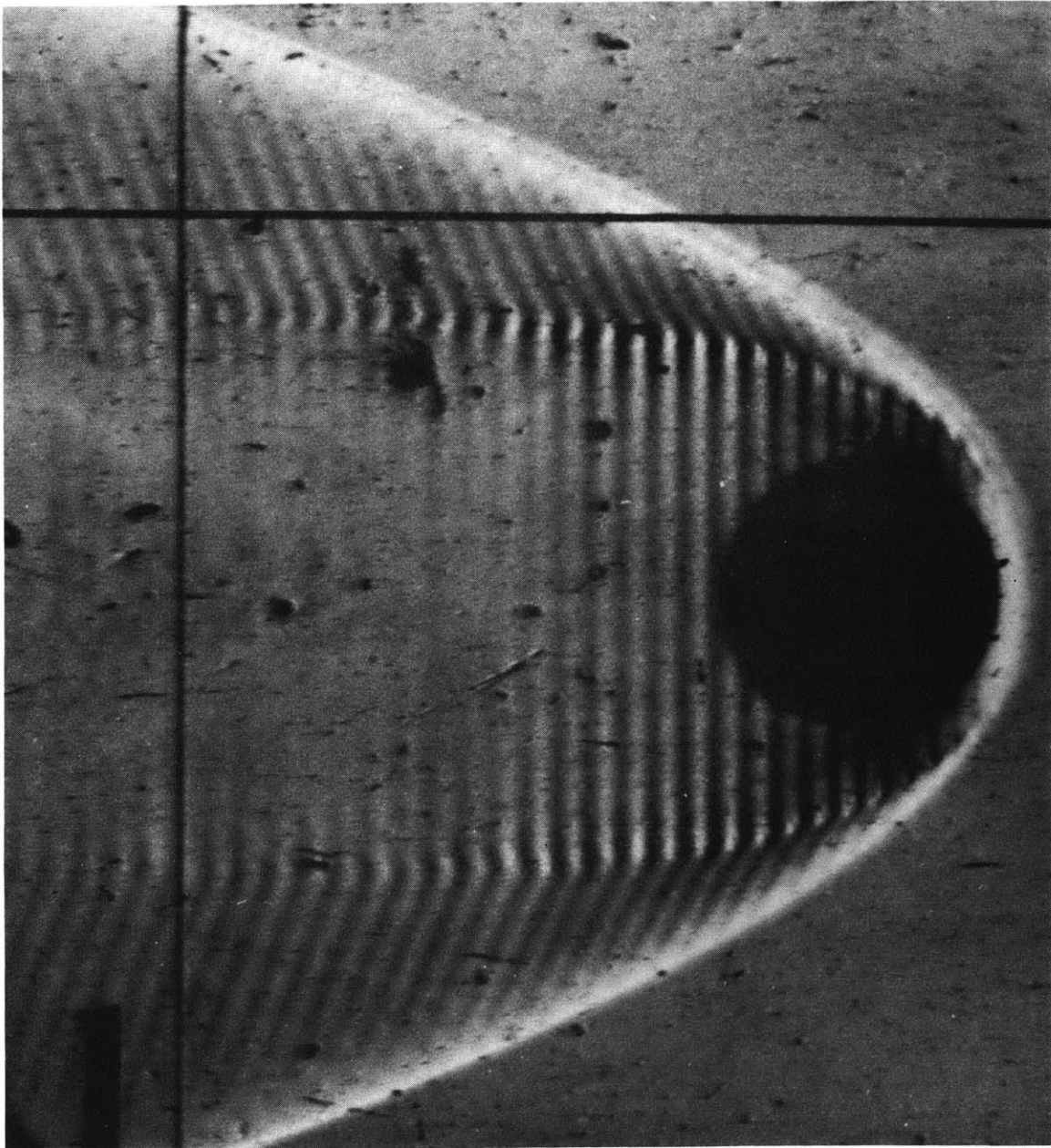
FIGURE 34

TURBULENT REGIME AT HIGH VELOCITY

Run No. 216: C_2H_2:O_2 : 1:15

Mach No.: 6.65

Pressure: 0.198 atm
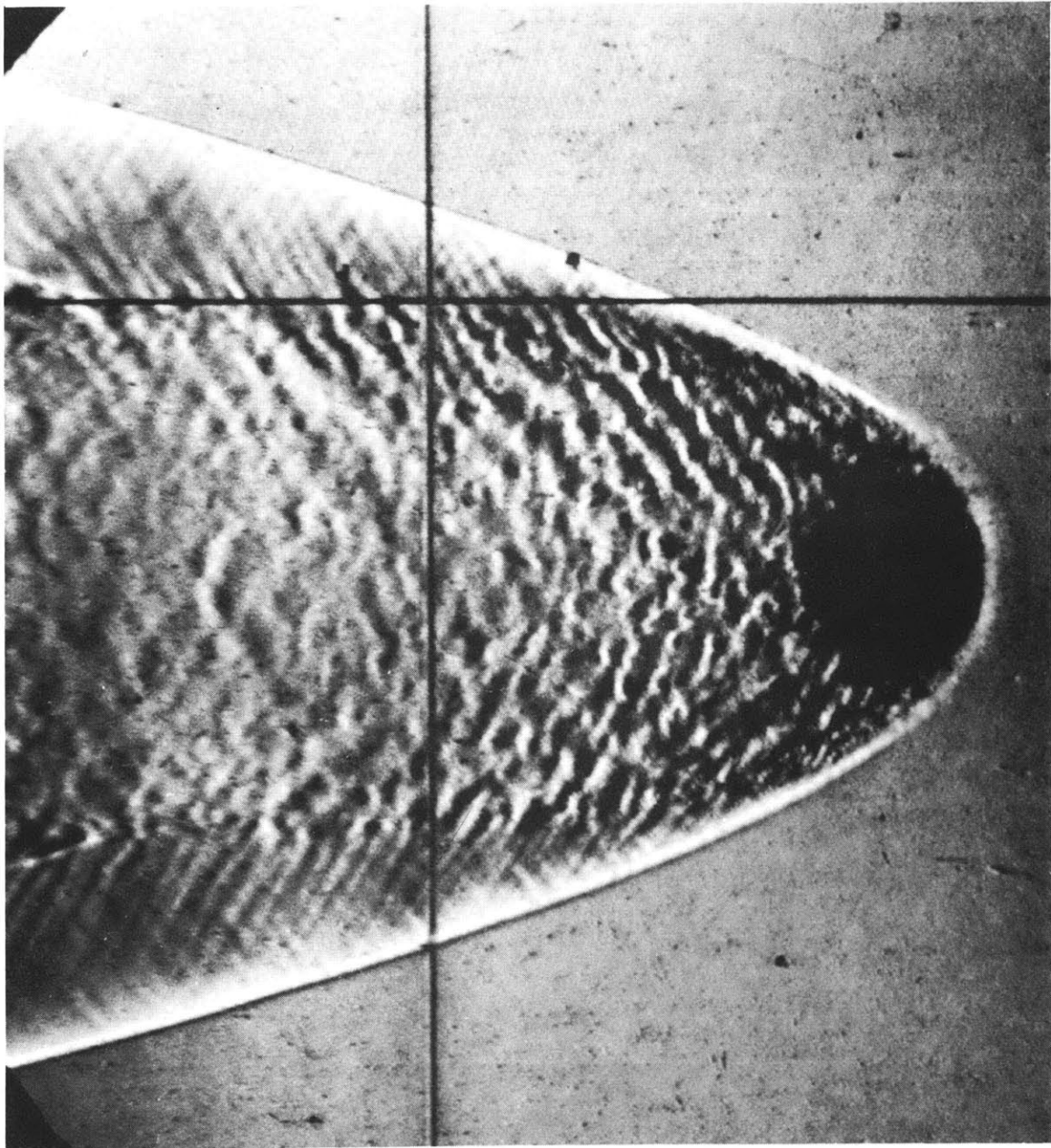
FIGURE 35

EFFECT OF DIAMETER ON REGIME BOUNDARIES
ACETYLENE-OXYGEN $\frac{F}{P}$ = 0.167

Note: o - 3/8" Dia Sphere
         □ - 1/4" Dia Sphere

$$D = \frac{\rho w_o}{R} = 0.187$$

Turbulent

Periodic

Stable

Viscous Wake

Mach Number - M
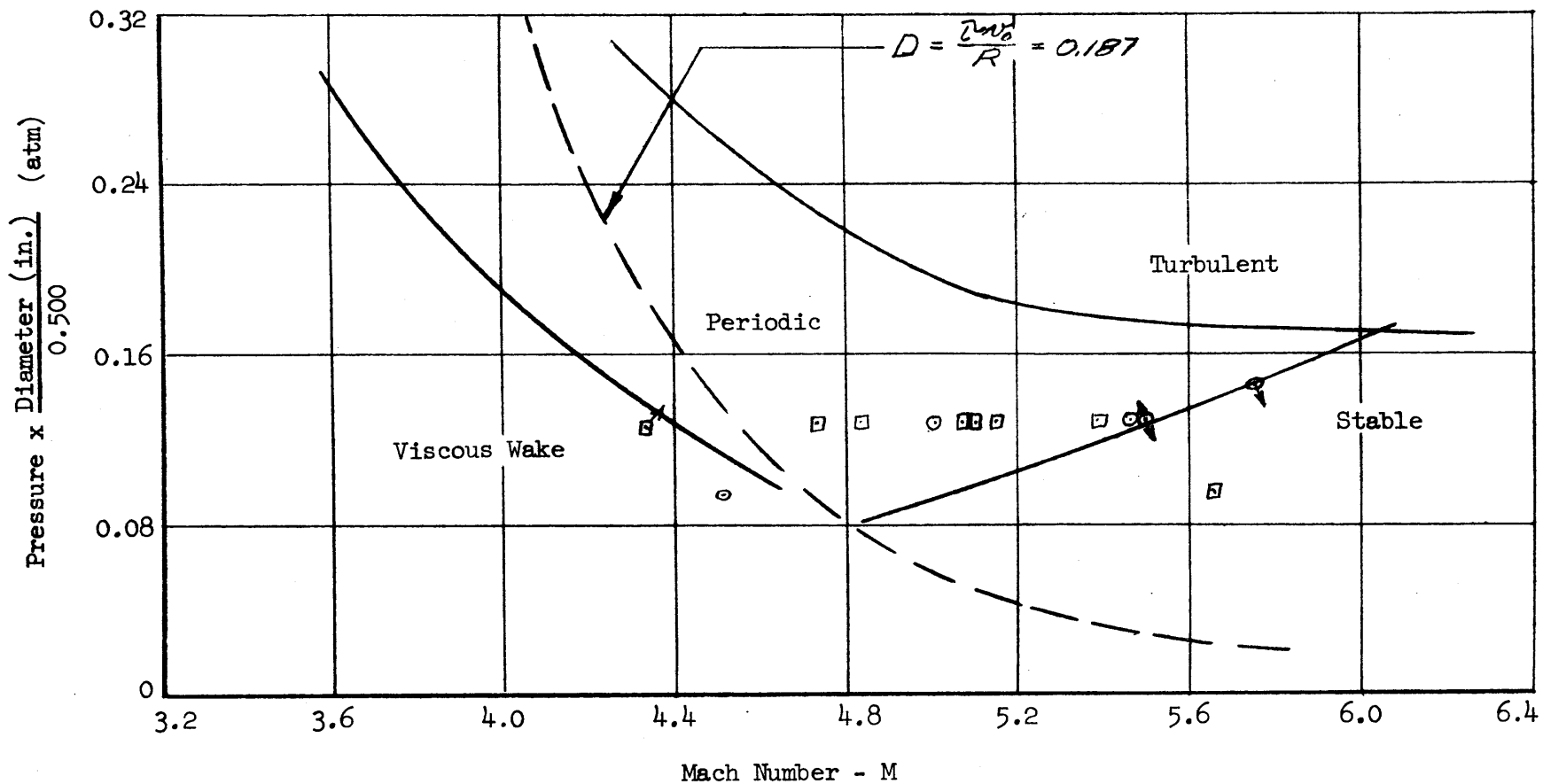
FIGURE 36

EFFECT OF DIAMETER ON REGIME BOUNDARIES

HYDROGEN-AIR Φ = 1.0

Note: Ruegg and Dorsey (Ref. 2)
20 mm dia Nylon Spheres

Behrens, Struth and Wecken (Ref. 4)
9 mm dia Plastic Spheres
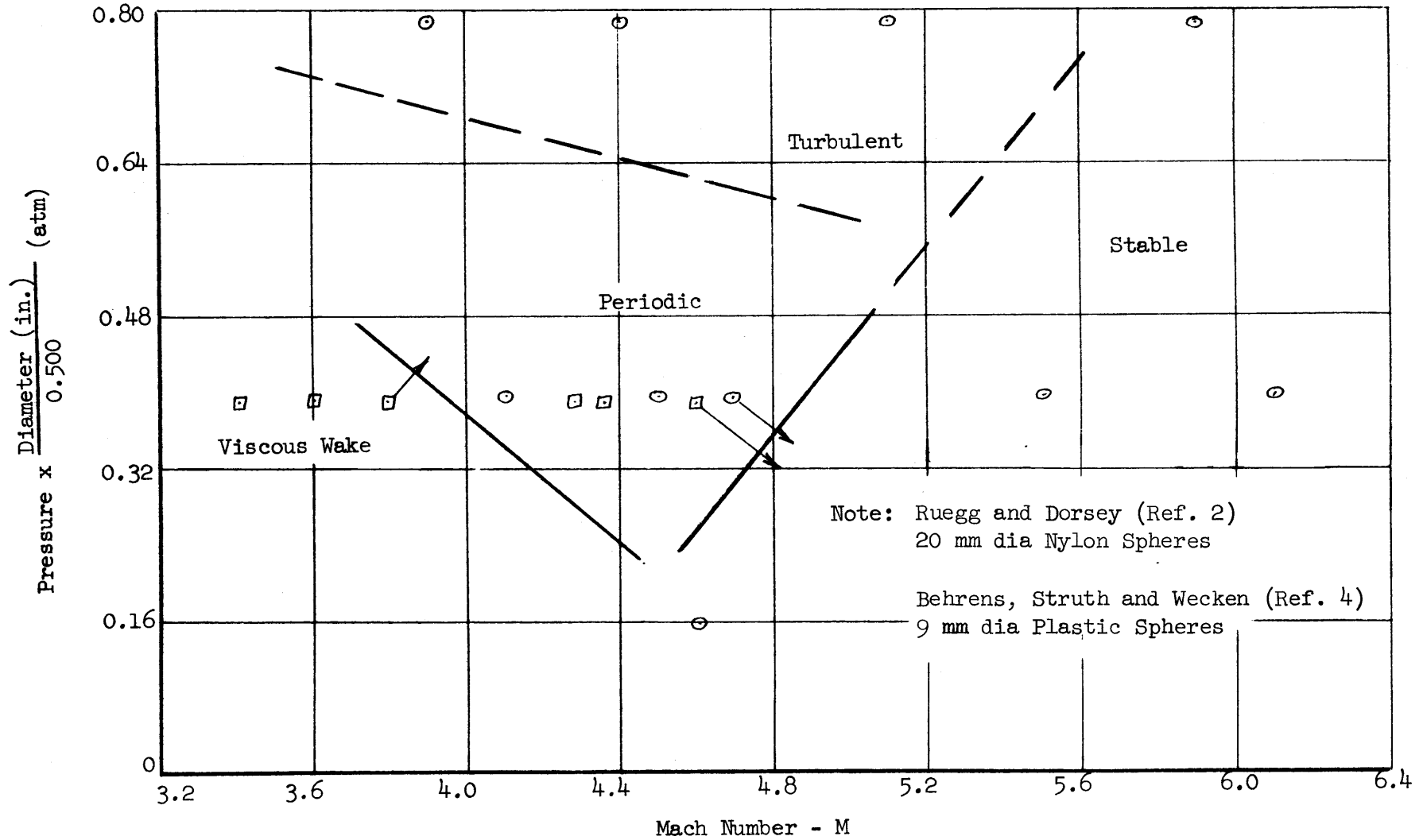
FIGURE 37

EXPERIMENTAL INSTABILITY WAVELENGTH
ACETYLENE-OXYGEN $\Phi = 0.167$
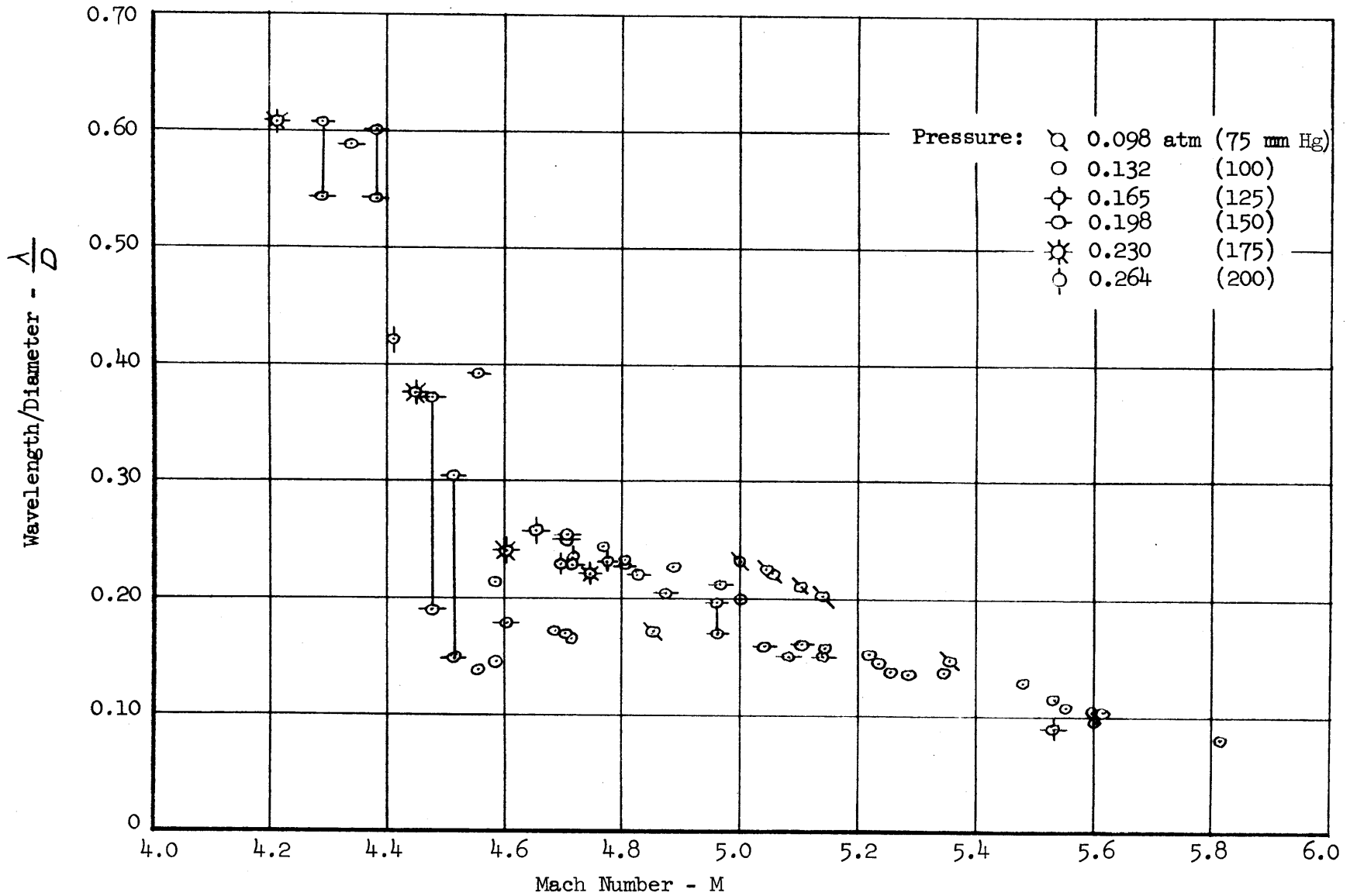
FIGURE 38

EXPERIMENTAL INSTABILITY WAVELENGTH

HYDROGEN-AIR Φ = 1.0
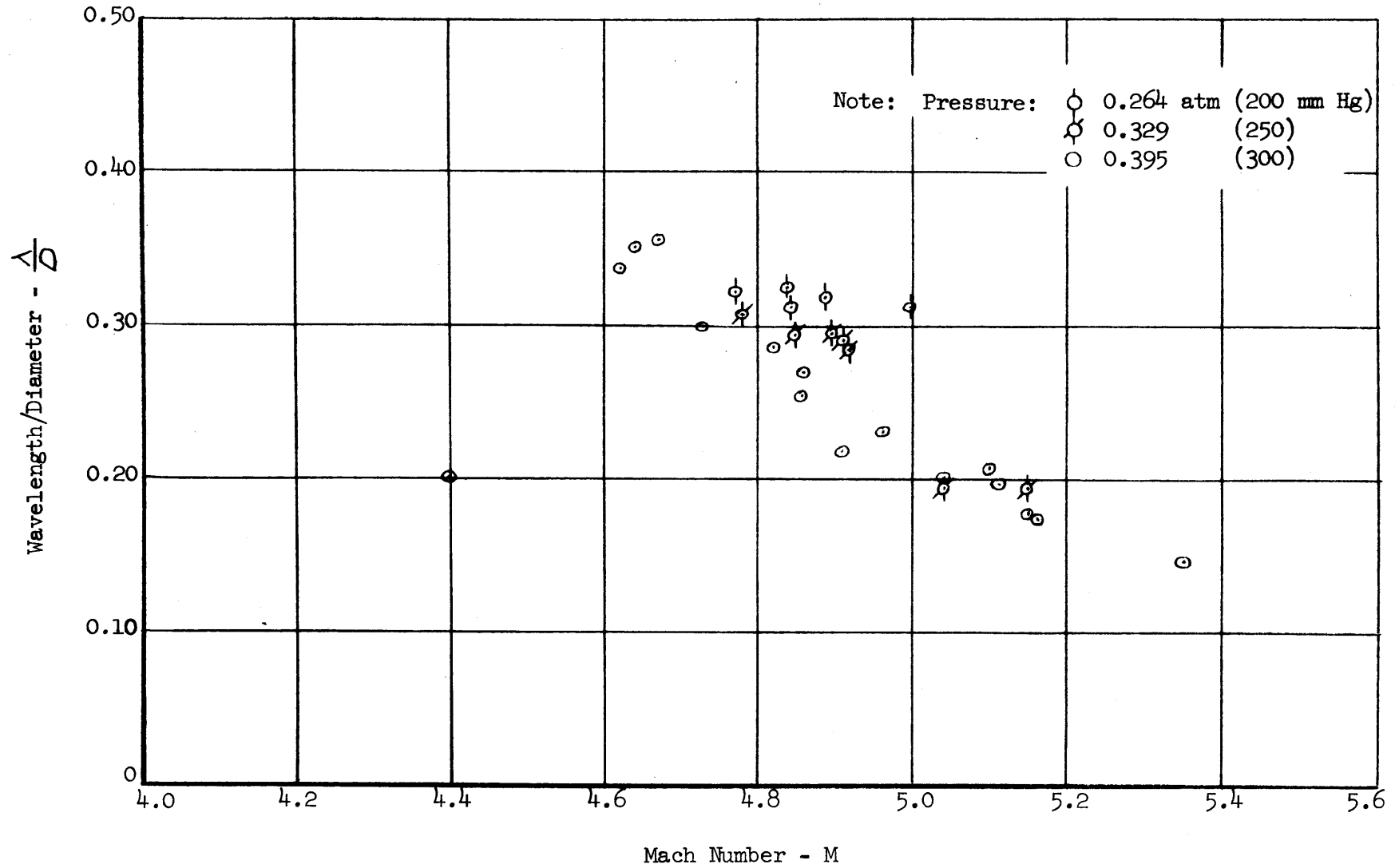
FIGURE 39

SCHLIEREN EFFECT PRODUCED BY HORIZONTAL KNIFE EDGE

Run No. 161: C_2H_2:O_2 : 1:15

Mach No.: 5.16
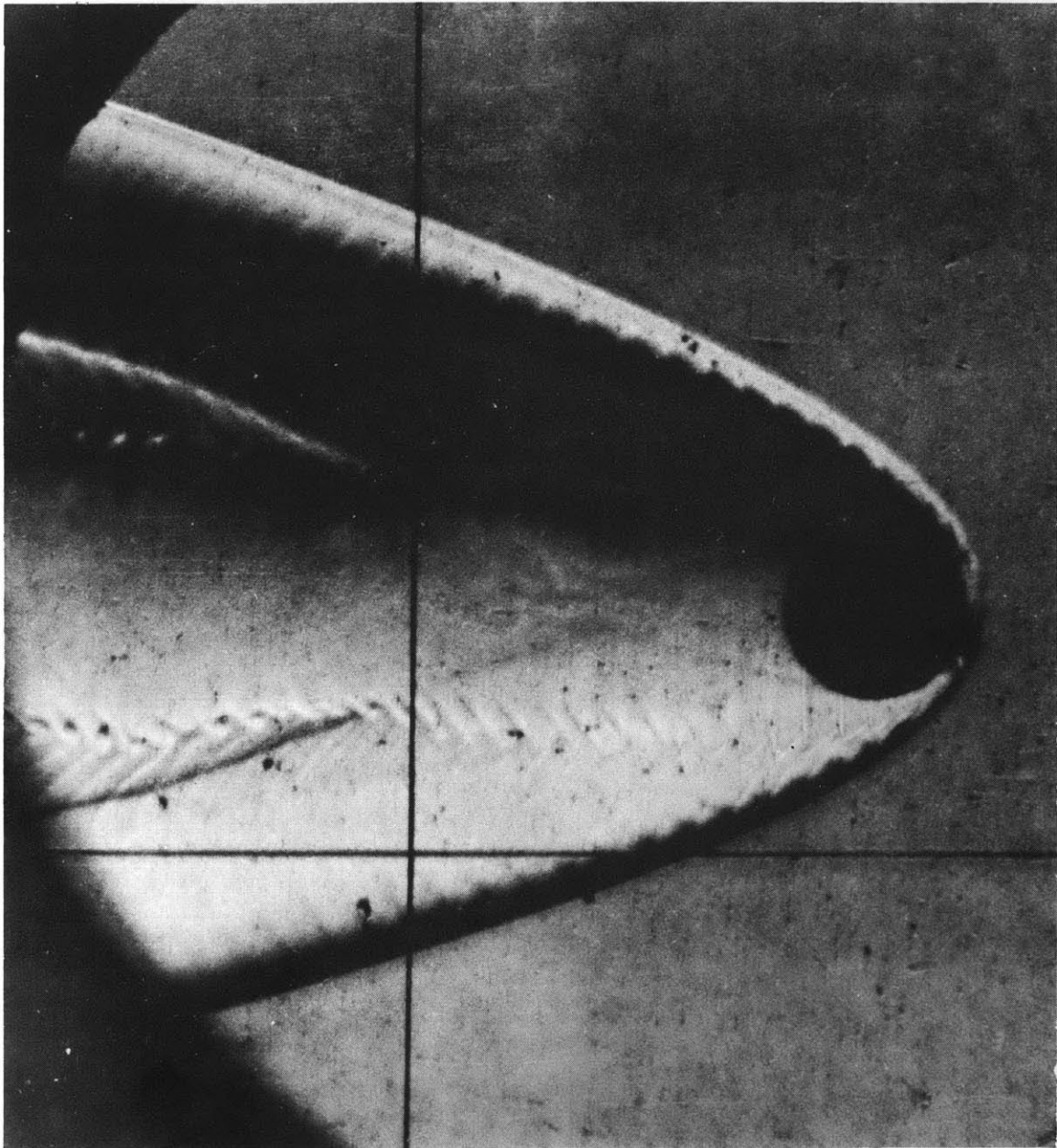
Pressure: 0.198 atm

FIGURE 40

DOUBLE-VALUED BOUNDARY CORRUGATION WAVELENGTH

Run No. 263: $C_2H_2:O_2$: 1:15

Mach No.:   4.67

Pressure: 0.198 atm
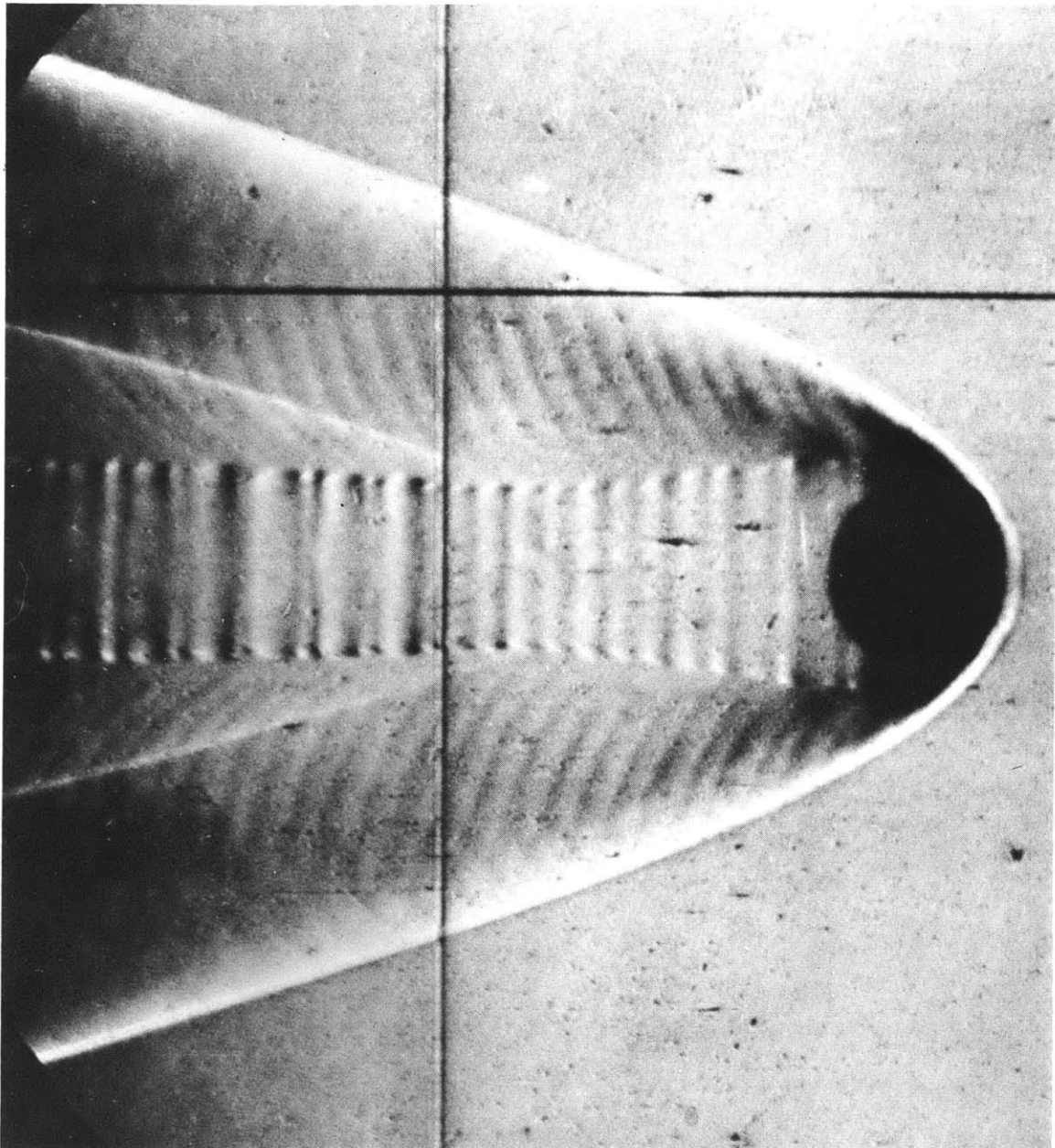
FIGURE 41

PERIODIC INSTABILITY EXHIBITING DOUBLE SET OF ENTROPY WAVES

Run No. 262: $C_2H_2:O_2$: 1:15

Mach No.: 4.65

Pressure: 0.230 atm
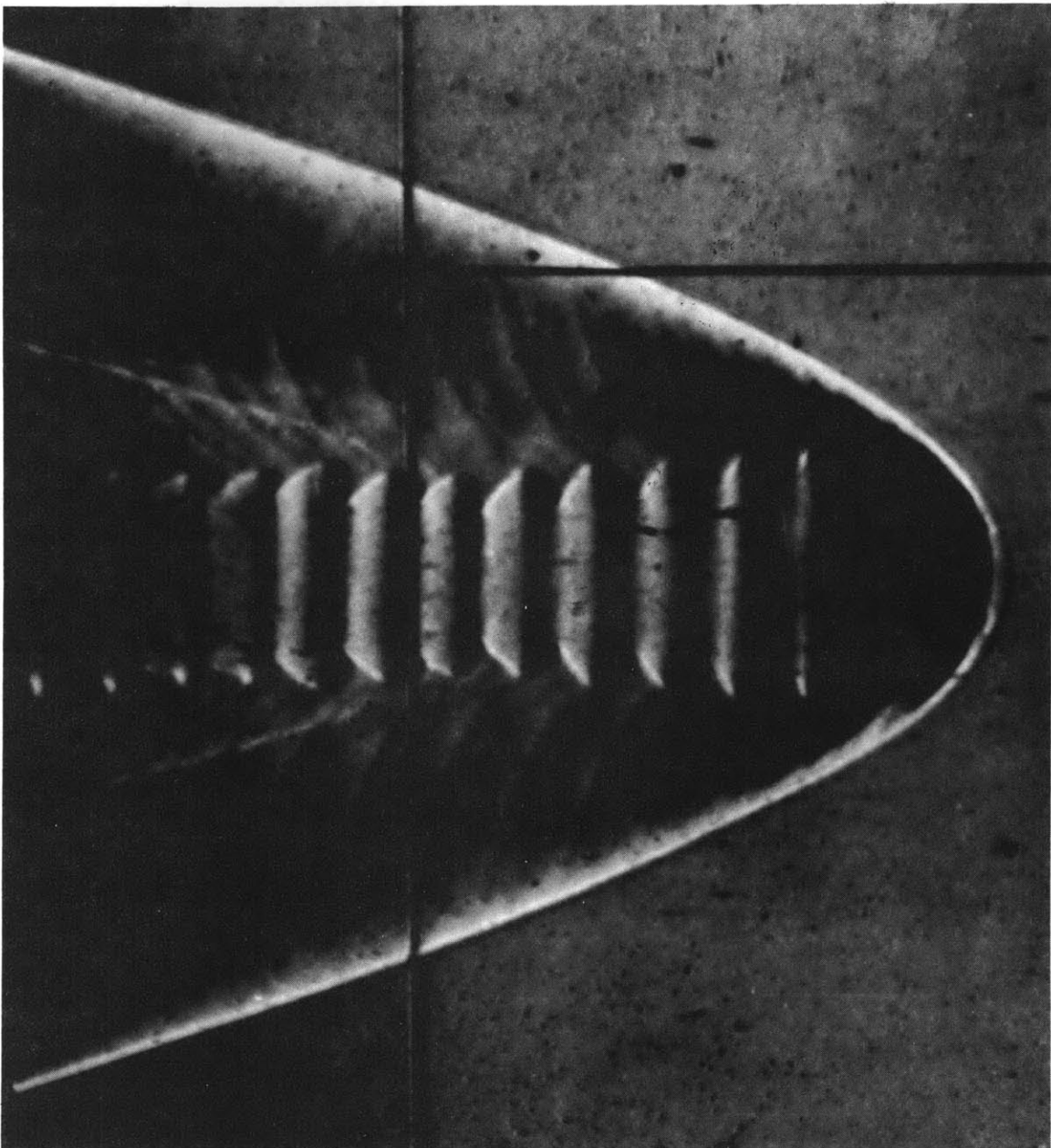
FIGURE 42

EFFECT OF BALL DIAMETER ON INSTABILITY WAVELENGTH
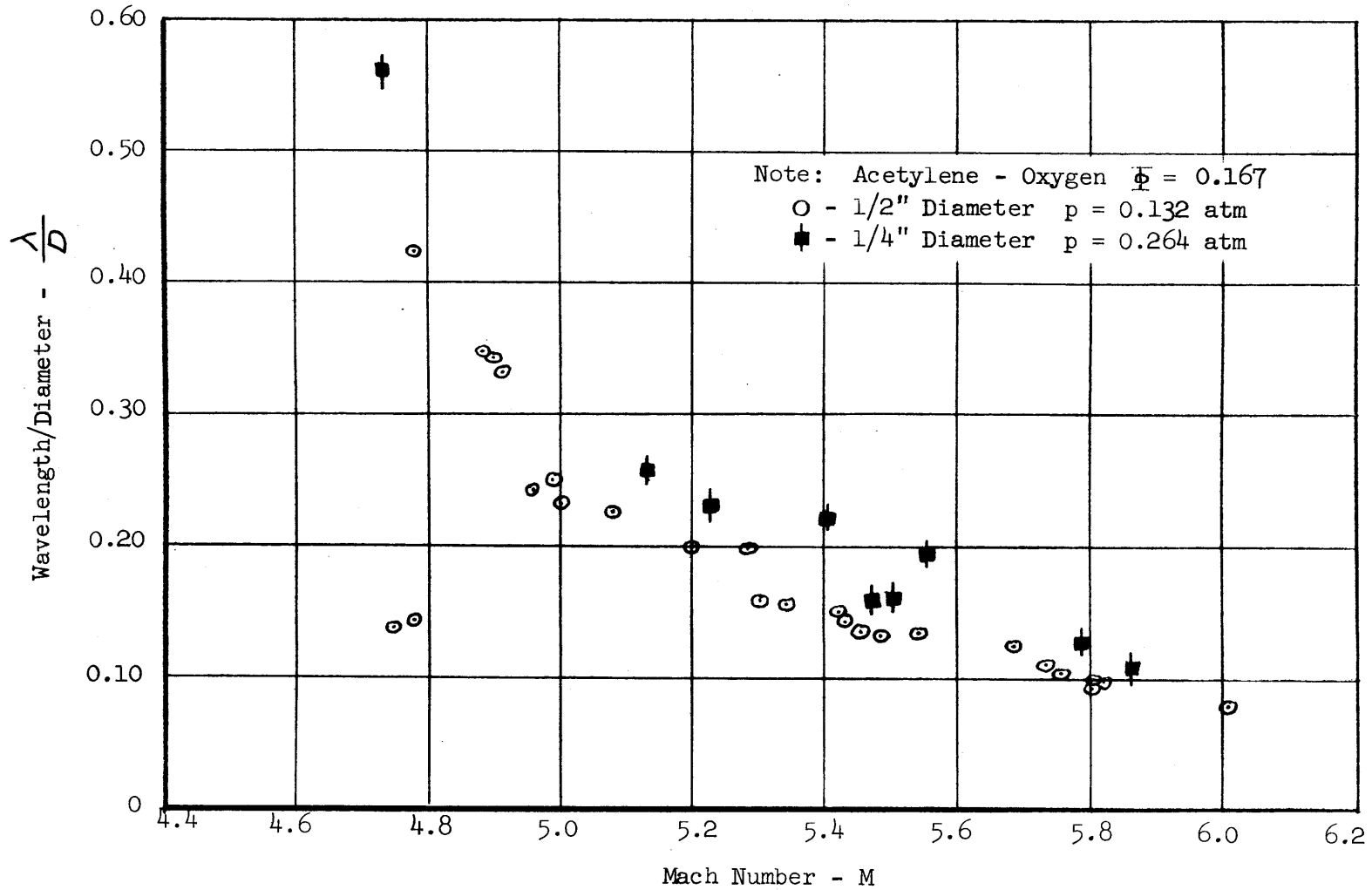
FIGURE 43

ASSUMED STAGNATION STREAMLINE VELOCITY DISTRIBUTION

Sphere
Surface

Reaction
Front

Bow
Shock

v_u v_u v_s v_o

$$v = \frac{\Delta' - x}{\Delta'} v_s$$

x

Δ_u

Δ'
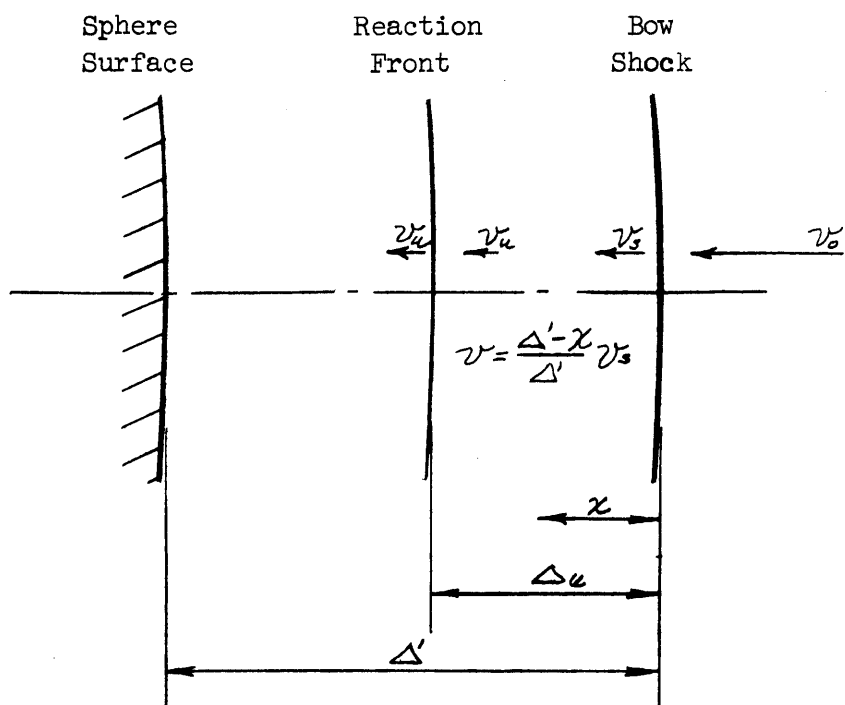
(a) Zero Heat Release

v_R v_u v_s v_o

$$v = \frac{\Delta}{\Delta'}\left(1 - \frac{x}{\Delta}\right) v_s$$

x

Δ_R

Δ_u

Δ
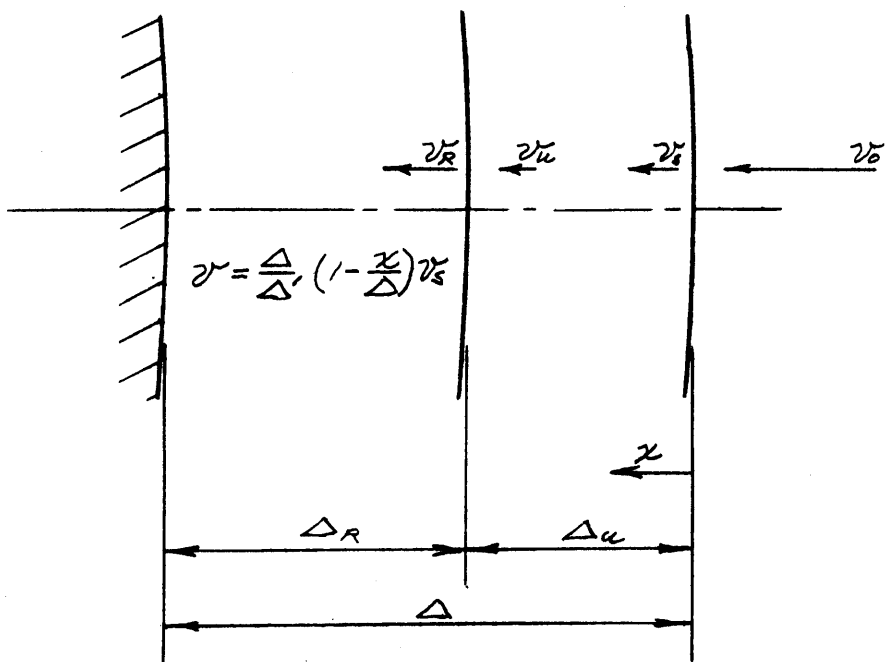
(b) Finite Heat Release

FIGURE 44

THEORETICAL INSTABILITY WAVELENGTHS
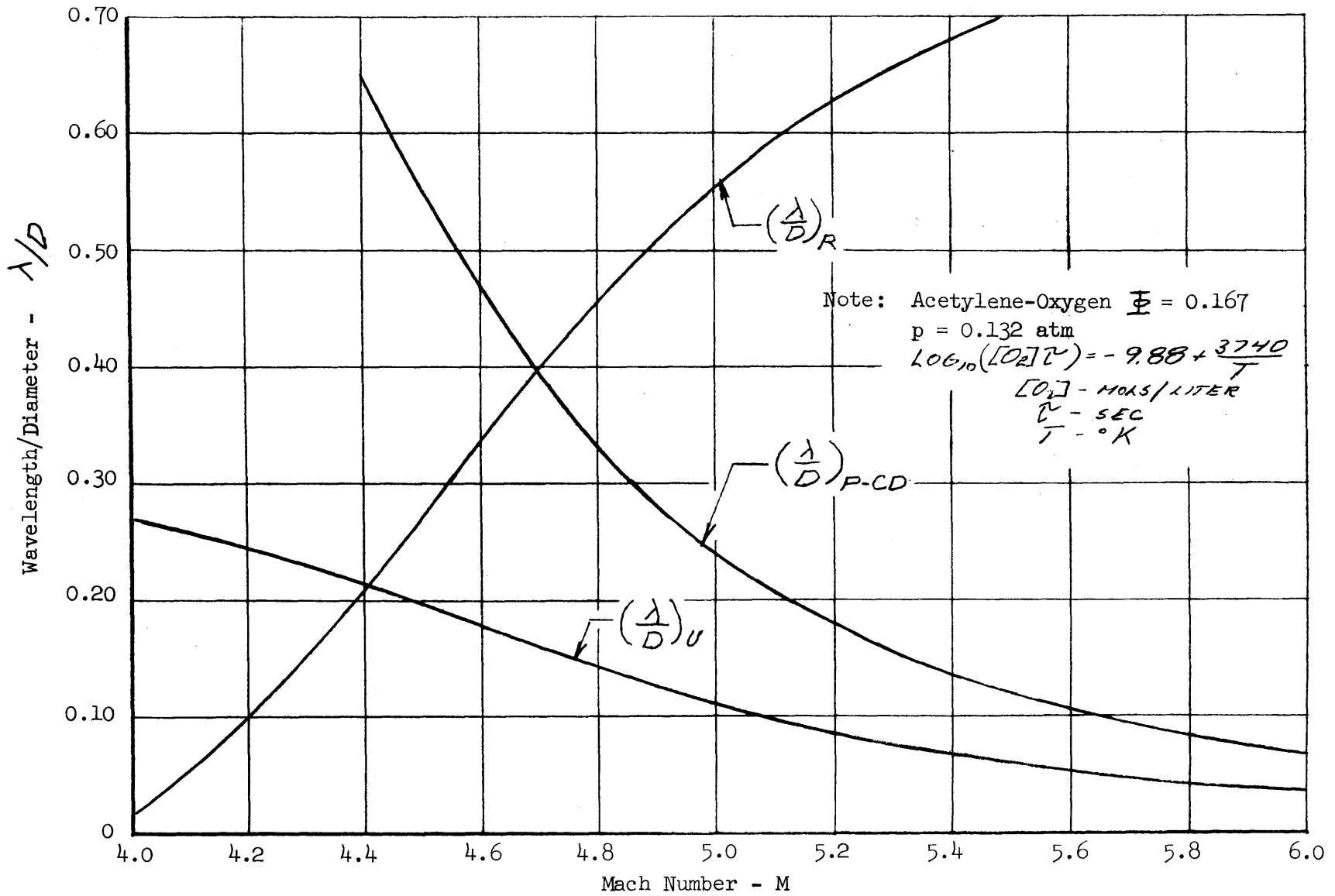
FIGURE 45

COMPRESSION WAVE - SHOCK WAVE INTERACTION

Coordinates Fixed With Respect To Undisturbed Bow Shock

Note: τ - Induction time for stoichiometric H_2-air mixture
according to correlation: $log_{10}([O_2]\tau) = -9.90 + \frac{3290}{T}$

Mach Number of Incident Compression Wave = 1.05

$\gamma = 1.4$
P - Compression Wave
BS - Bow Shock
R - Rarefaction Wave
CD - Contact Discontinuity

(a) Before Interaction

$v_P = 1.53\,a_o$
$M_c = 1.05$
$v_{BS} = 0$

(b) After Interaction

$v_R = -3.25\,a_o$
$v_{BS} = 0.06\,a_o$
$v_{CO} = -0.78\,a_o$
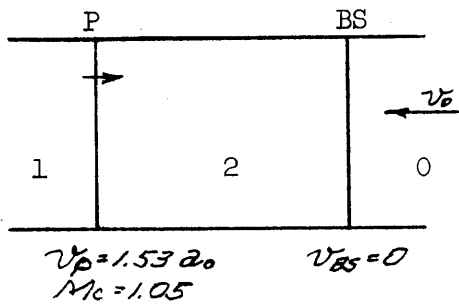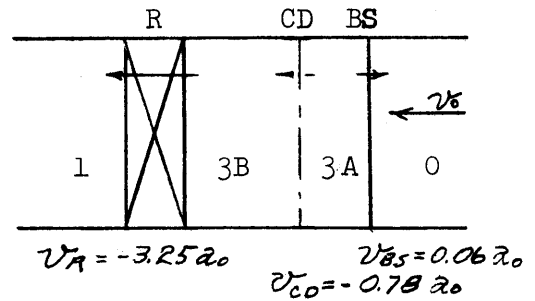
Region	M	v/a_o	P/P_o	T/T_o	τ/τ_2
0	5.0	-5.0	1.00	1.00	--
1	0.327	-0.80	32.48	5.99	0.80
2	0.415	-1.0	29.00	5.80	1.00
3A	0.312	-0.79	32.10	6.33	0.68
3B	0.321	-0.79	32.10	5.97	0.82

FIGURE 46

x-t DIAGRAM FOR THE P-CD INSTABILITY MODEL

Note: BS = Bow Shock
       RF = Reaction Front
       CD = Contact Discontinuity
        P = Compression Wave
        R = Rarefaction Wave
        Z = Entropy Zone
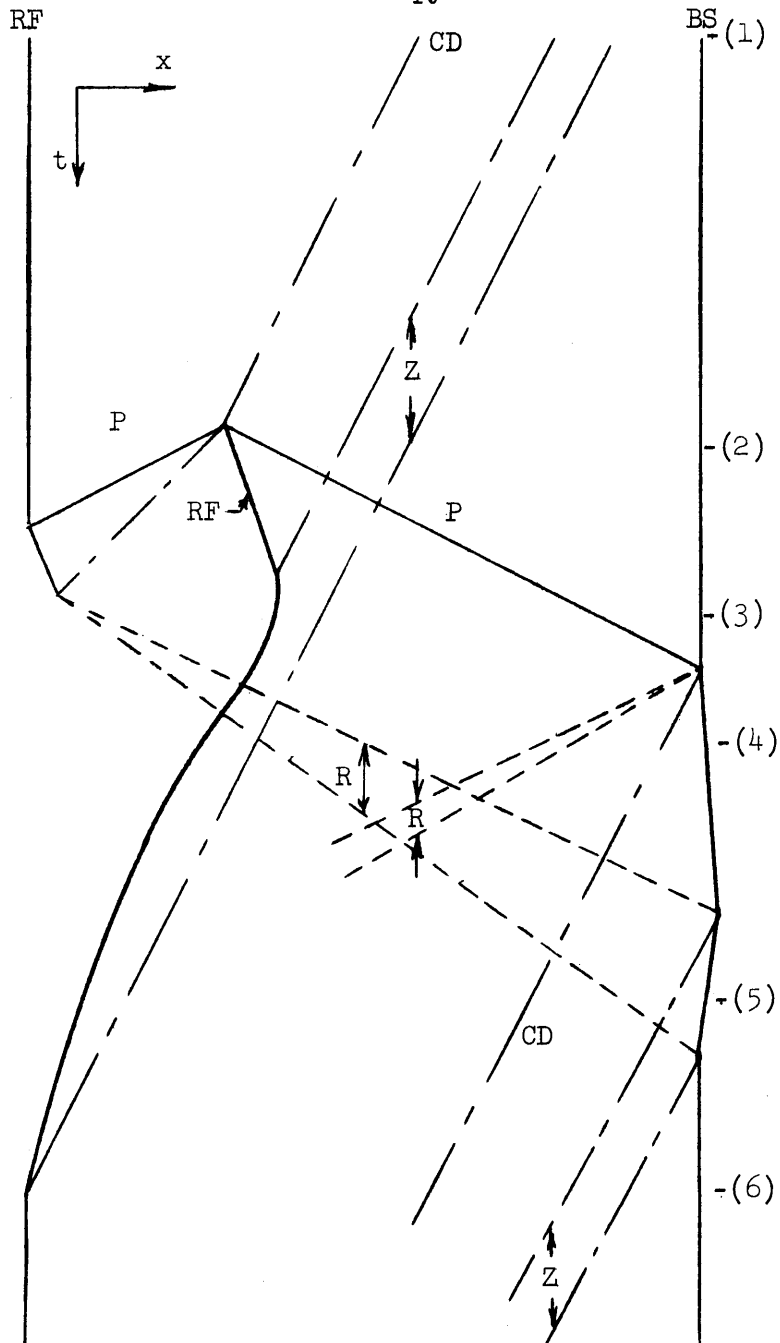
FIGURE 47

EFFECT OF REDUCED INDUCTION TIME ON ENERGY RELEASE RATE

Note: BS = Bow Shock
        RF = Reaction Front
        CD = Contact Discontinuity
         P = Compression Wave
         R = Rarefaction Wave
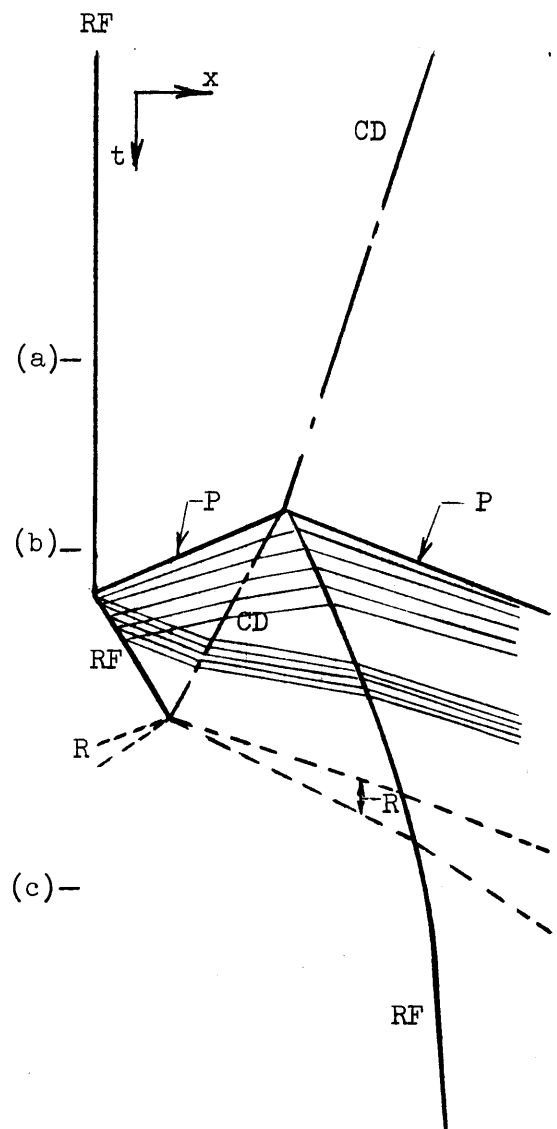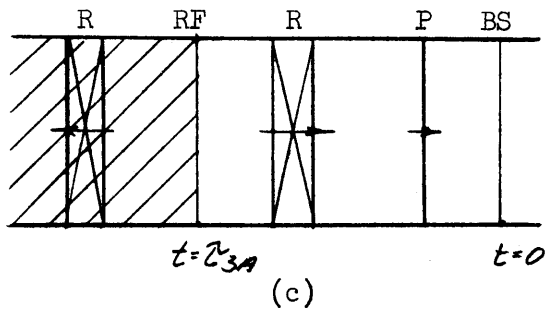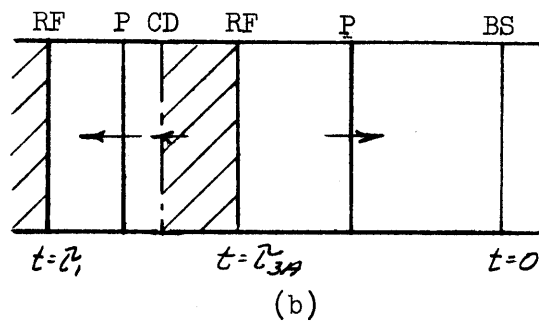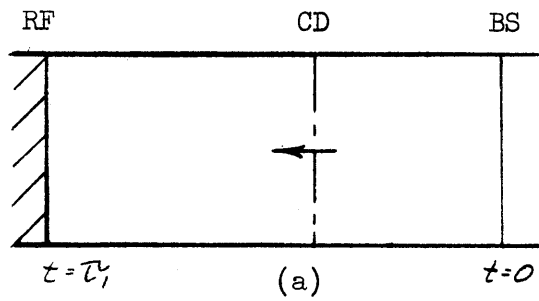
FIGURE 48

CYCLE OF EVENTS IN P-CD INSTABILITY MODEL
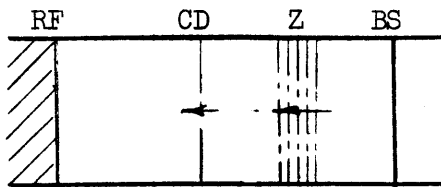
(1) A contact discontinuity followed by a zone of decreasing entropy approaches the reaction front.
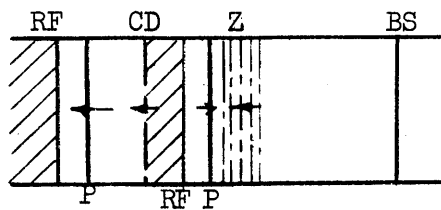
(2) The hot gas behind the CD reacts, creating a reaction front upstream of the original front, thereby doubling the reaction rate and generating compression waves which propagate upstream and downstream.
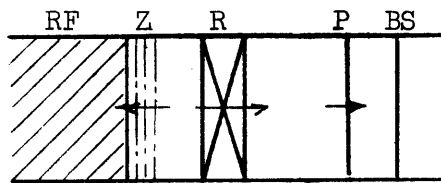
(3) The original reaction front is extinquished, halving the reaction rate and generating rarefaction waves which propagate upstream and downstream. The zone of decreasing entropy begins to penetrate the upstream reaction front.
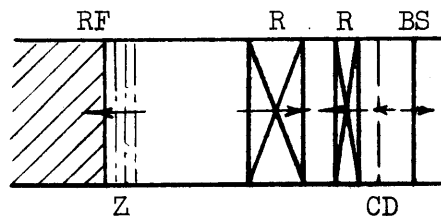
(4) The compression wave generated in Step (2) interacts with the bow shock producing a weak reflected rarefaction wave and generating a contact discontinuity. The bow shock is strengthened.
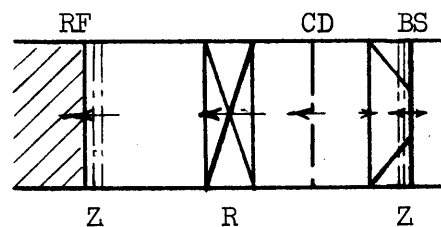
(5) The rarefaction wave generated in Step (3) penetrates the bow shock, weakening it and generating a zone of increasing entropy and a chain of weak reflected compression waves.
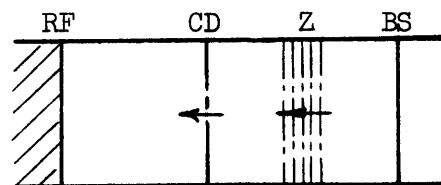
(6) The weak reflected rarefaction and compression waves have a negligible effect on the reaction front. The next cycle begins.

FIGURE 49

COMPARISON OF EXPERIMENTAL AND THEORETICAL INSTABILITY WAVELENGTHS
ACETYLENE-OXYGEN $\bar{\Phi}$ = 0.167

Note: _____ Theory, P-CD Model
      -------- Experiment (See Fig. 37)
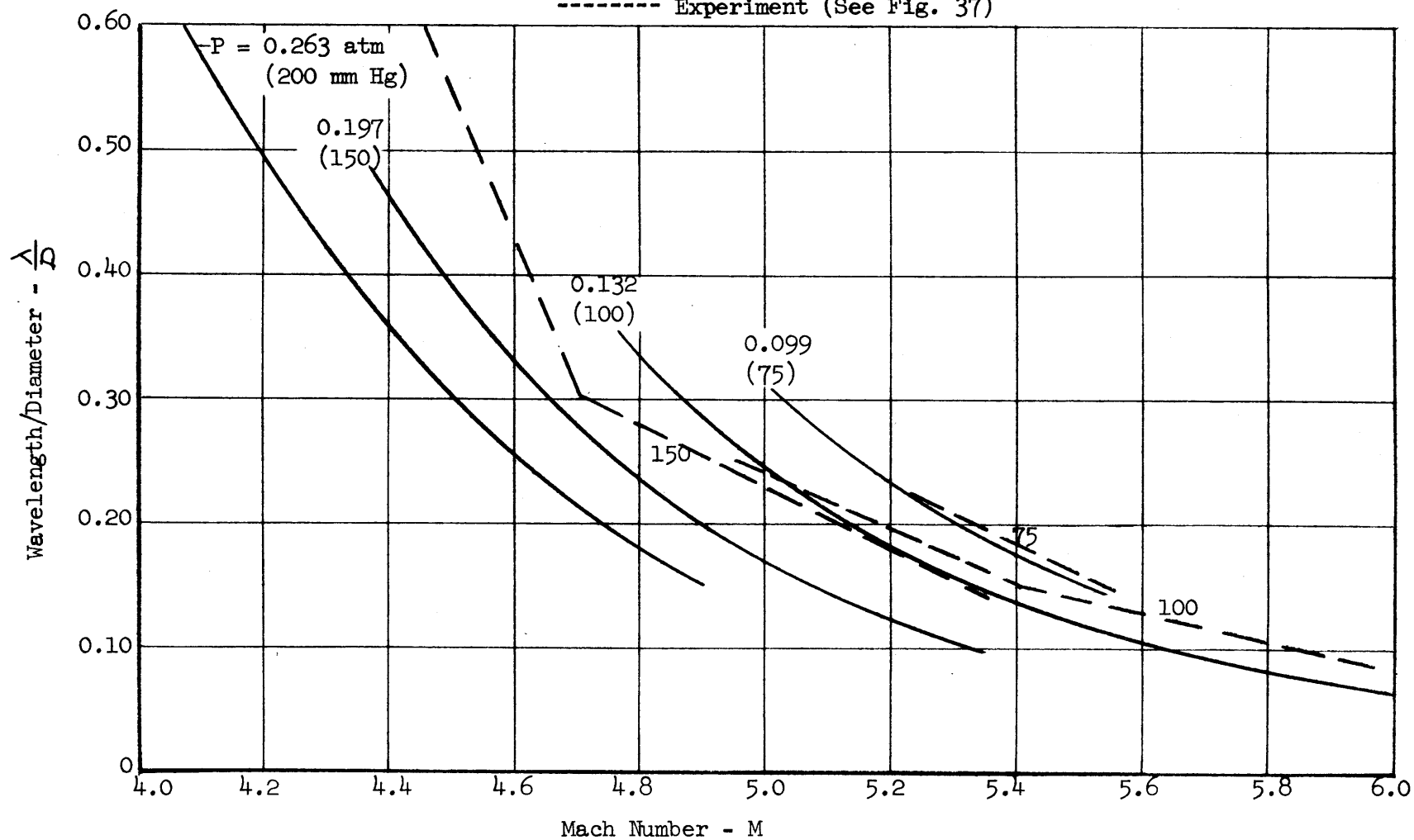
FIGURE 50

CORRELATION OF INSTABILITY WAVELENGTH WITH REACTION ZONE WIDTH
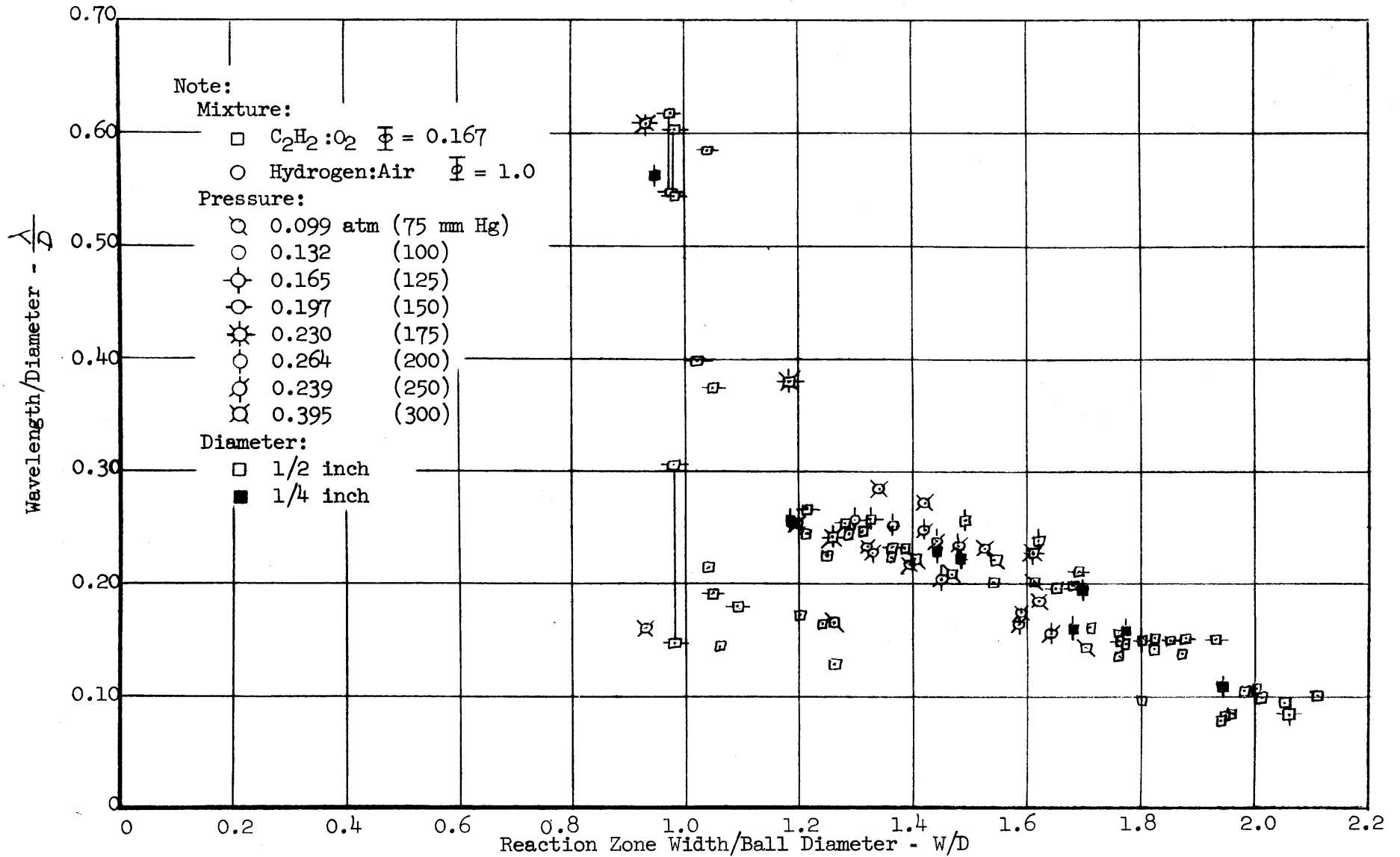
FIGURE 51

COMPARISON OF ANALYTICAL AND EXPERIMENTAL REACTION FRONT PROFILES

Bow Shock

Reaction Front

Streamline
(Analytical)

Note: Hydrogen-Air Φ = 1.0

p = 0.396 atm

M_σ = 5.0

—— —— ——Experimental (Run No. 87, Fig. 21)

——————Analytical (No Heat Release)

$\dfrac{r}{D}$

x/D
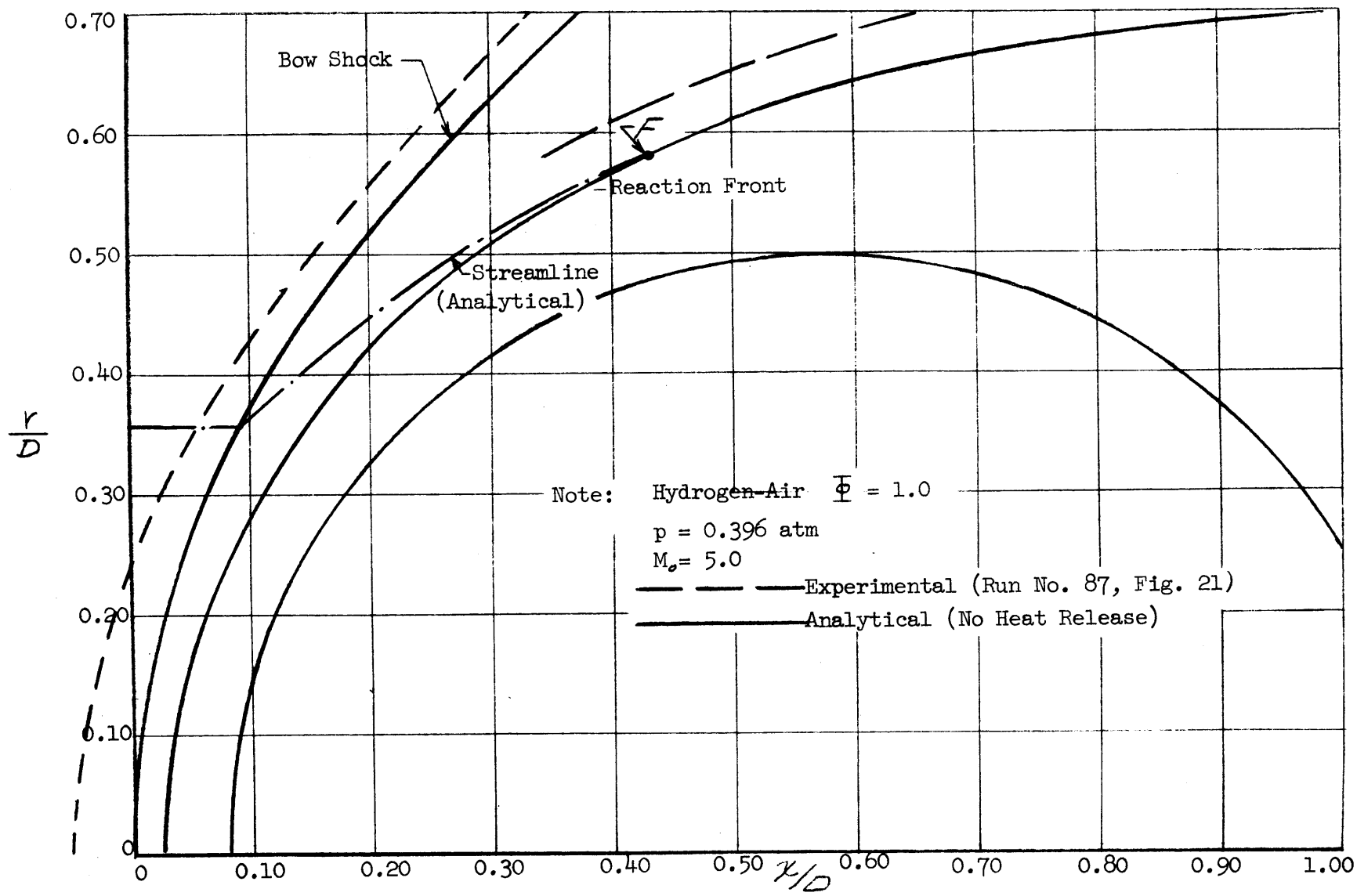
FIGURE 52

DEVELOPMENT OF CORRUGATED REACTED GAS BOUNDARY
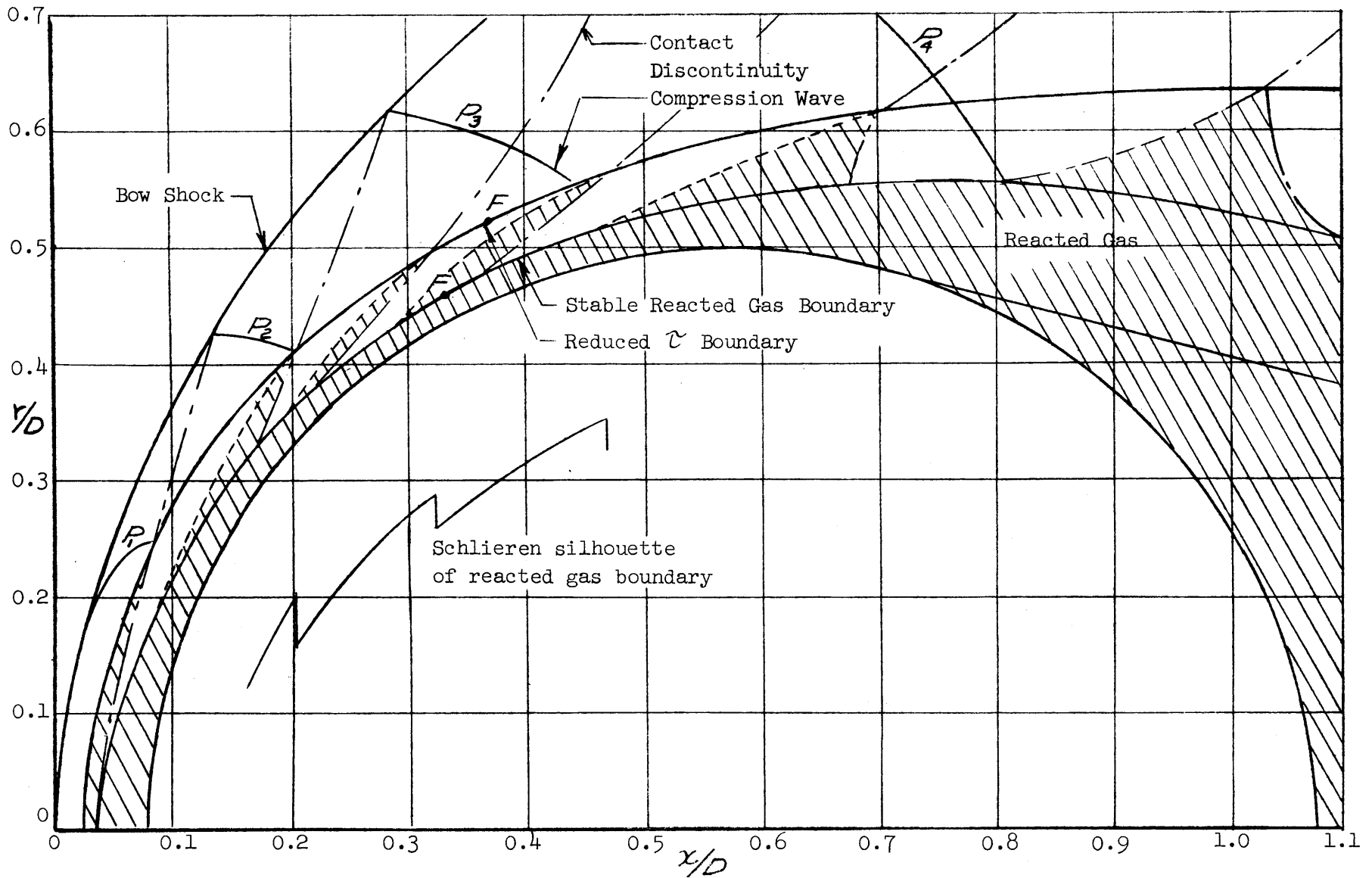
FIGURE 53

COMPARISON OF EXPERIMENTAL AND THEORETICAL INSTABILITY WAVELENGTHS

HYDROGEN-AIR Φ = 1.0

Note: $log_{10}\left([O_2]\tau\right) = -9.90 + \dfrac{3300}{T}$

$[O_2]$ — $MOLS/LITER$
τ — SEC
T — $^\circ K$
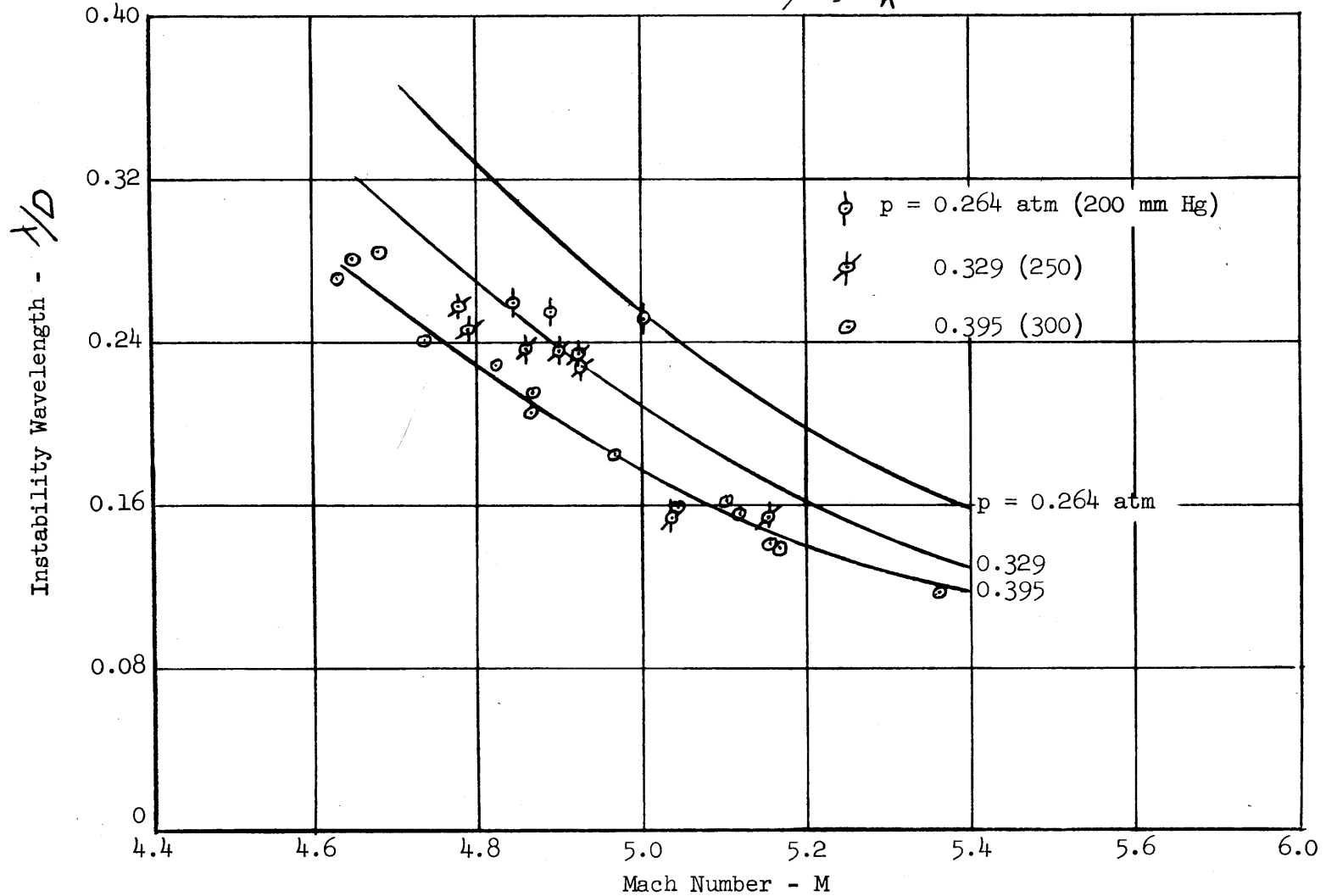
FIGURE 54

HYDROGEN-OXYGEN INDUCTION TIME CORRELATIONS
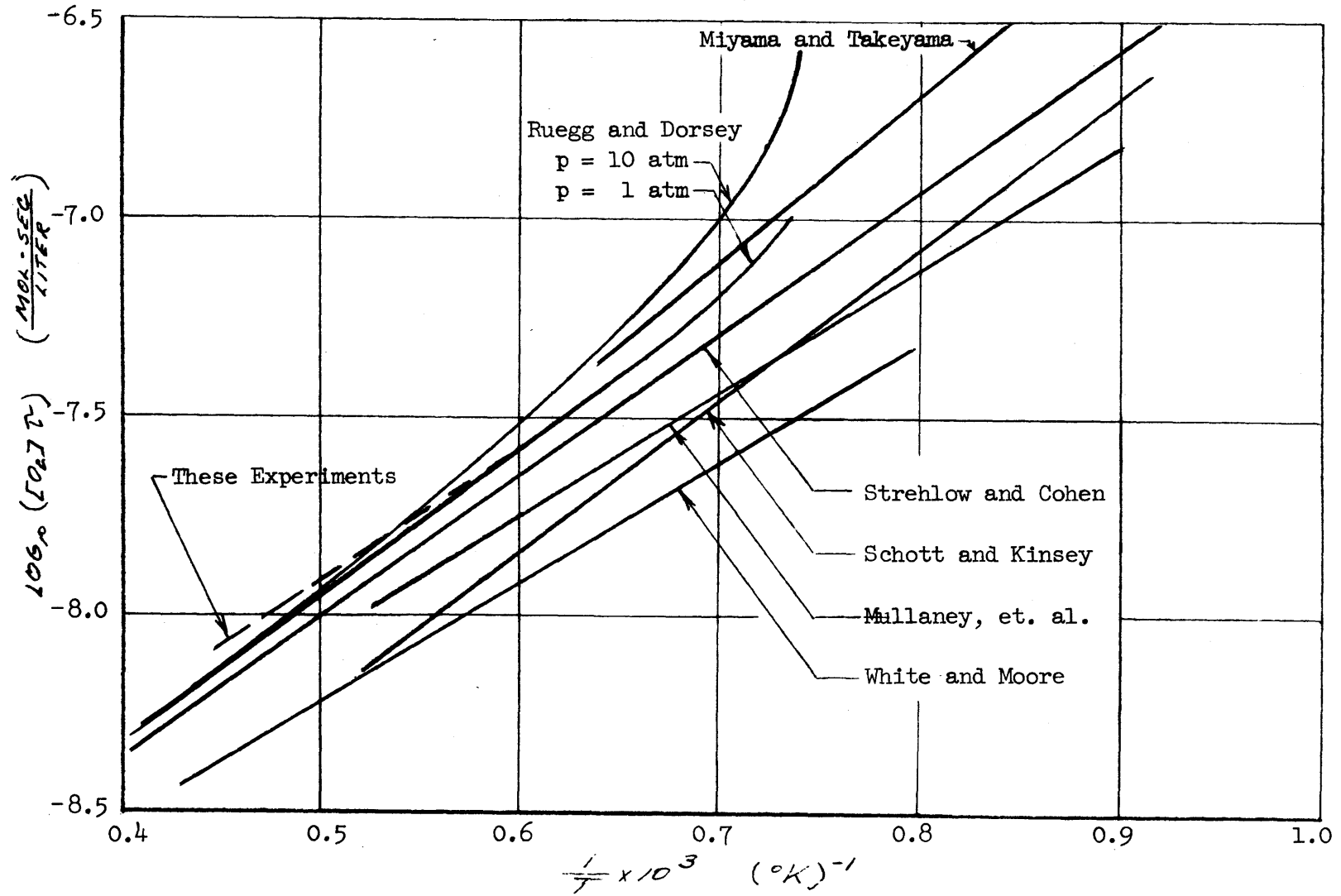
FIGURE 55

SCHLIEREN SYSTEM PRINCIPLES

Spherical Mirror

Test Area

Knife Edge →   Light Source

Viewing Screen
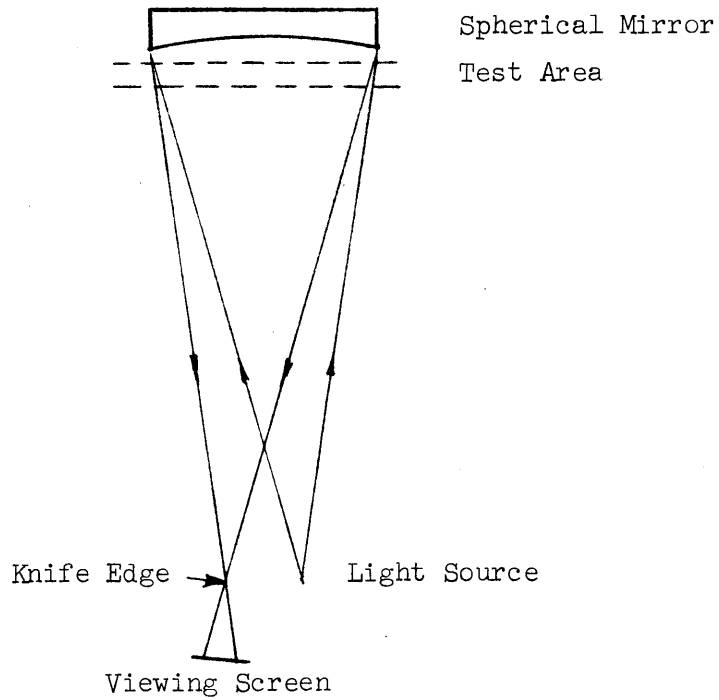
(a)   Arrangement of a Double Pass Schlieren System
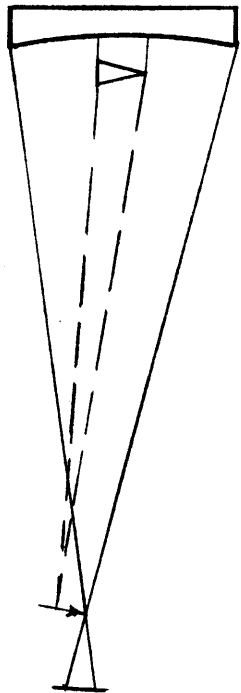
(b) Ray Deflection Producing
     Darkened Image

$$z = -x \tan \alpha_1$$
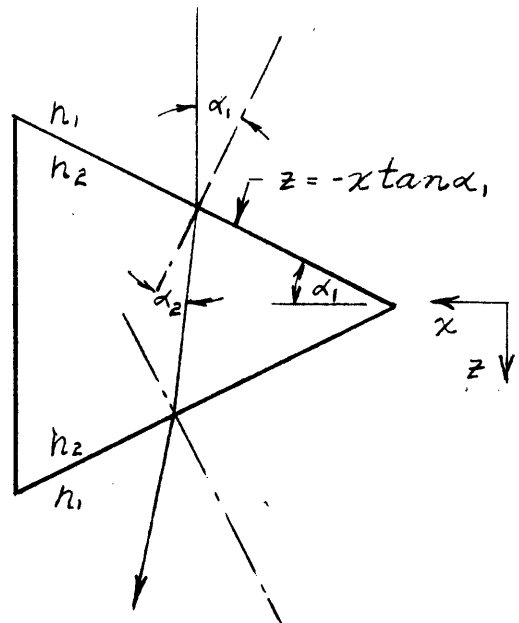
(c)   Refraction Due to a Wedge

FIGURE 56

SCHLIEREN CHARACTERISTICS OF BOW SHOCK WAVE

Note: Vertical Knife Edge

$y = y_0$

y

x

(a) Viewing Plane Image

x

z

x_3 x_2 x_1

(b) Plane $y = y_0$

$\int \Delta \rho \, dz$

$\frac{\partial}{\partial x} \int \Delta \rho \, dz$

x_3 x_2 x_1

x_3 x_2 x_1
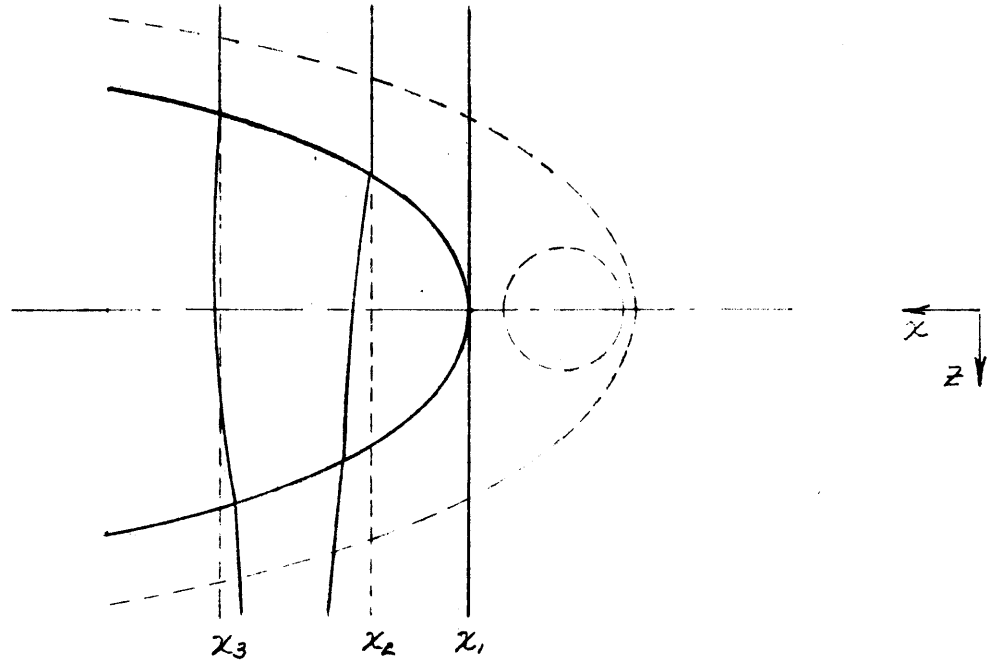
(c) Integrated Optical Path

(d) Relative Brightness

FIGURE 57

SCHLIEREN CHARACTERISTICS OF CORRUGATED
REACTED GAS BOUNDARY
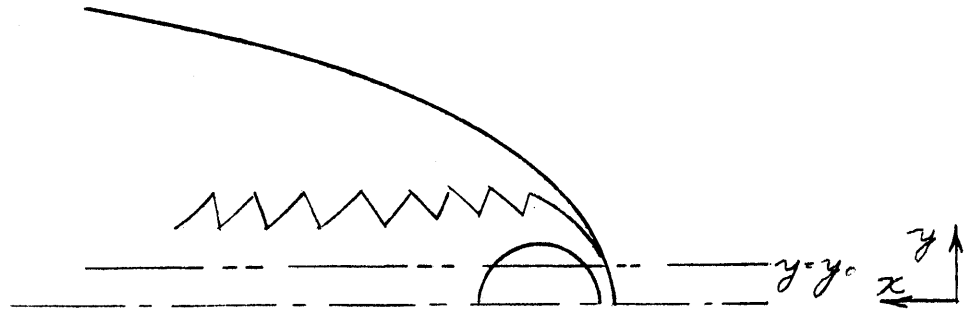
(a) Viewing Plane Image
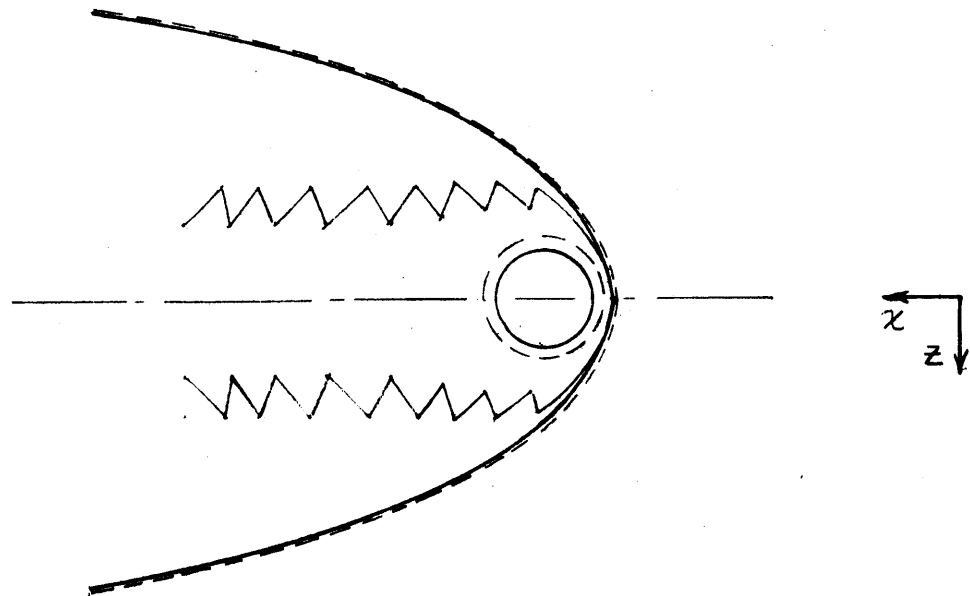
(b) Plane $y = y_0$
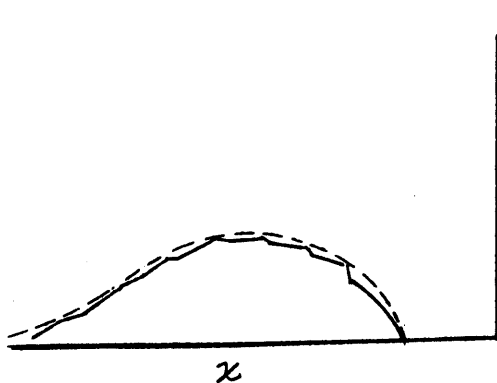
(c) Integrated Light Path
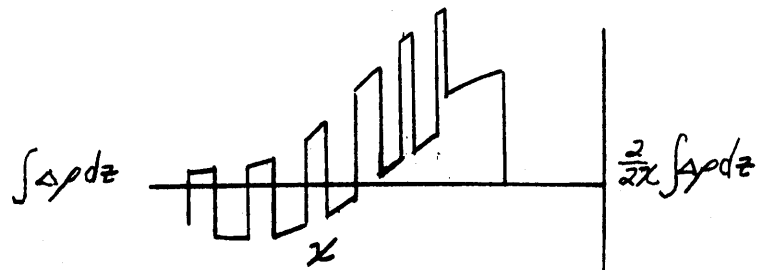
(d) Relative Brightness

FIGURE 58

SCHLIEREN CHARACTERISTICS OF COMPRESSION AND
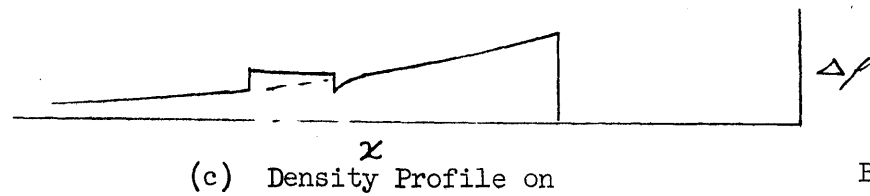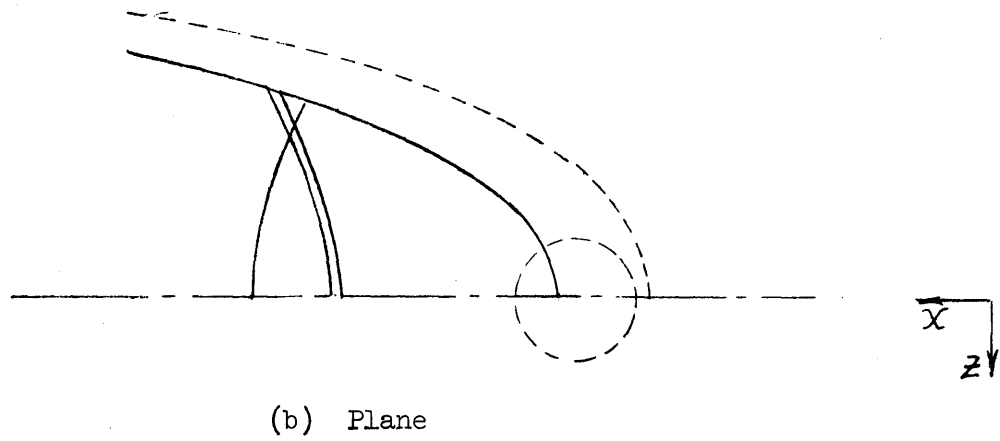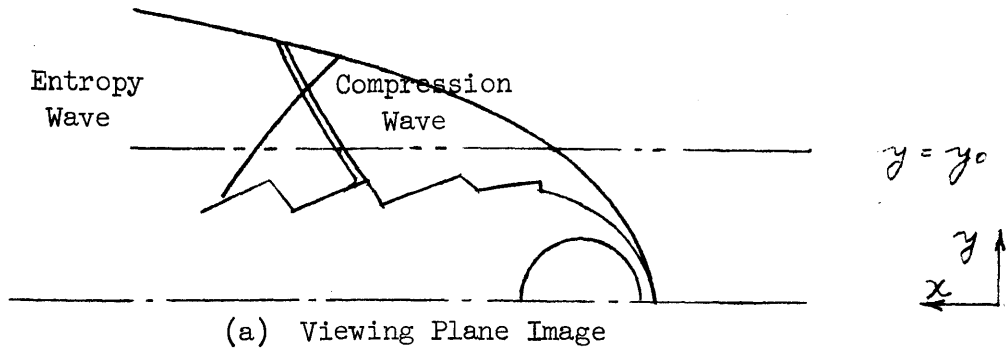ENTROPY WAVES IN THE INVISCID WAKE

Entropy
Wave

Compression
Wave

$y = y_0$

y

x

(a)   Viewing Plane Image

x

z

(b)   Plane

$\Delta \rho$

x

(c)   Density Profile on

$\int \Delta \rho \, dz$

Entropy Wave
(Bright)

Bow
Shock
(Bright)

$\frac{\partial}{\partial z} \int \Delta \rho \, dz$

x

Compression
Wave
(Bright)

Entropy
Wave
(Dark)

x

(d)   Integrated Optical Path

(e)   Relative Brightness
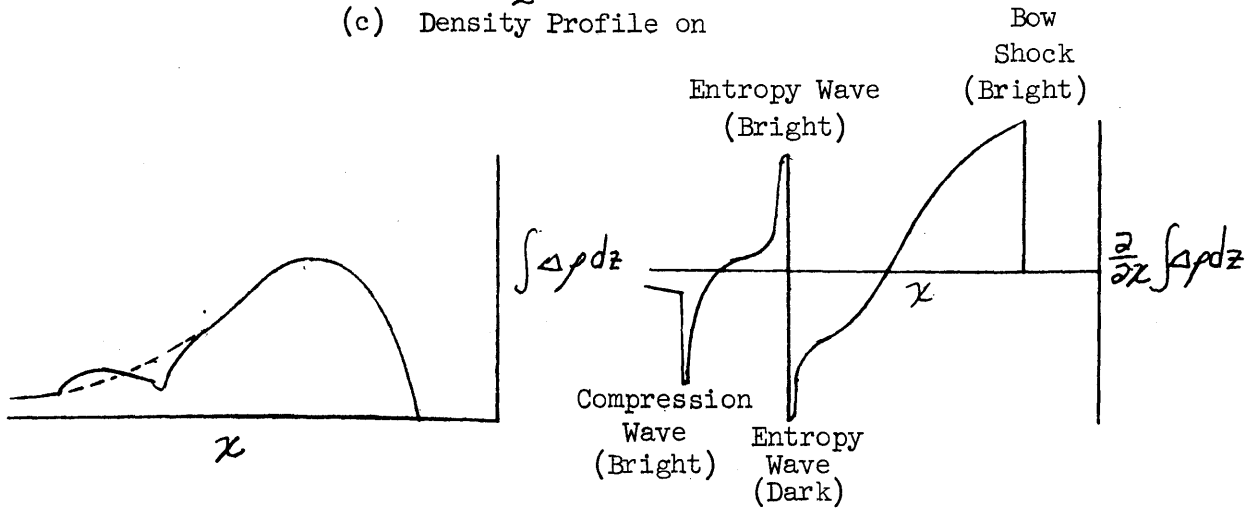
FIGURE 59

REFLECTED WAVE CALCULATION

$M_0' = 2.658$
$\delta_0' = 0$

$\left(\dfrac{\Delta\rho}{\rho}\right)_{CD} = 0.0027$

$\Delta\rho_{CD} \equiv \rho_{3A} - \rho_{3B}$

$M_1' = 1.0122$
$\delta_1' = 31.2°$

$M_2' = 1.005$

$\theta_1' = 62.8°$

$\dfrac{P_1}{P_0} = 6.32$

$\dfrac{\rho_1}{\rho_0} = 3.16$

$\dfrac{T_1}{T_0} = 1.414$

$\theta_3' = 65.7°$

$\left(\dfrac{\Delta P}{P}\right)_3 = 0.01167$

$\left(\dfrac{\Delta\rho}{\rho}\right)_3 = 0.00831$

$\theta_4' = 62.7°$

$\left(\dfrac{\Delta P}{P}\right)_4 = -0.00080$

$\left(\dfrac{\Delta\rho}{\rho}\right)_4 = -0.00057$
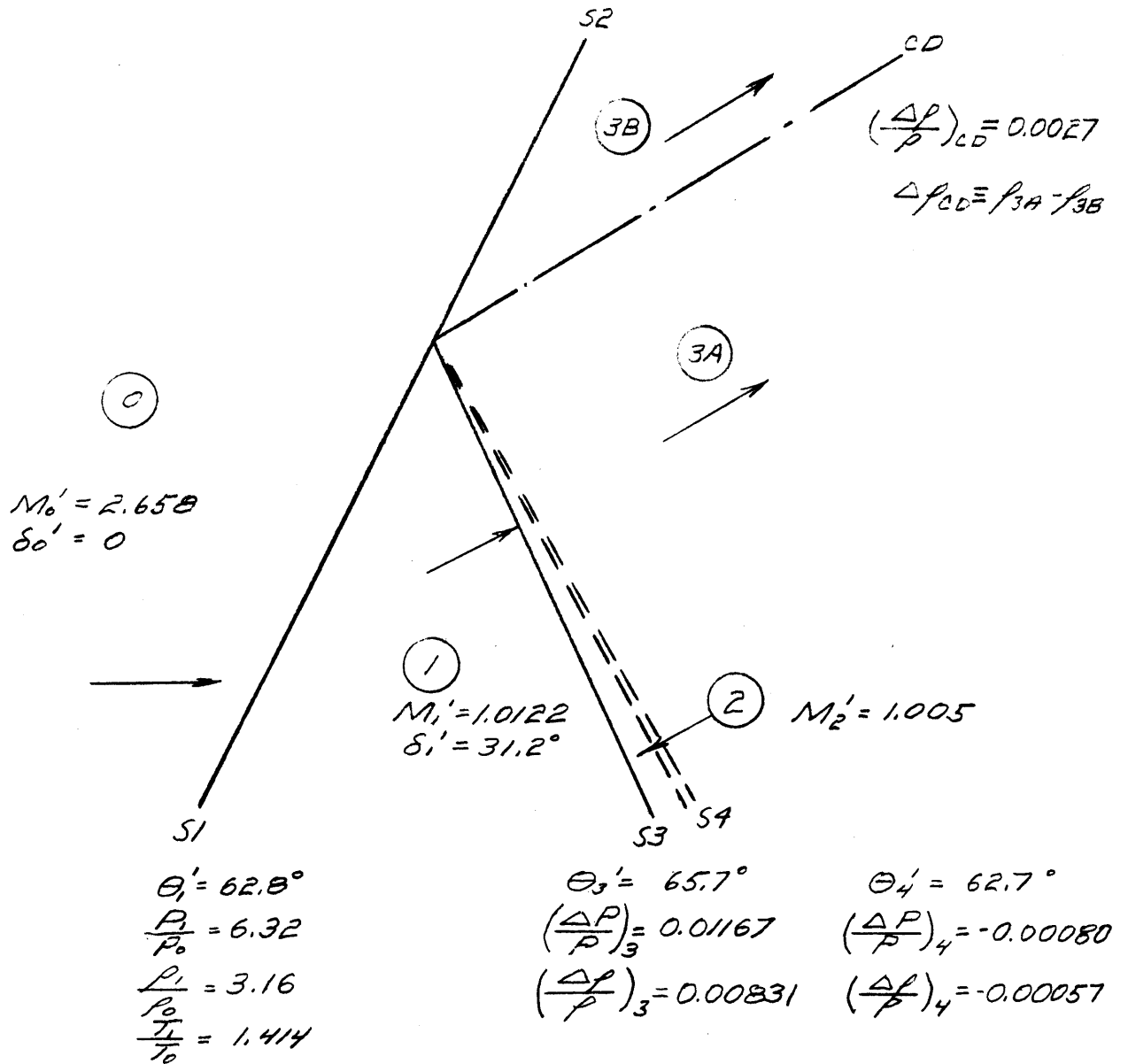
FIGURE 60

WAVE INTERACTION GEOMETRY

——— Experimental - Run No. 154
------- Analytical M_o = 5.30
                        $C_2H_2:O_2$ $\bar{\Phi}$ = 0.167
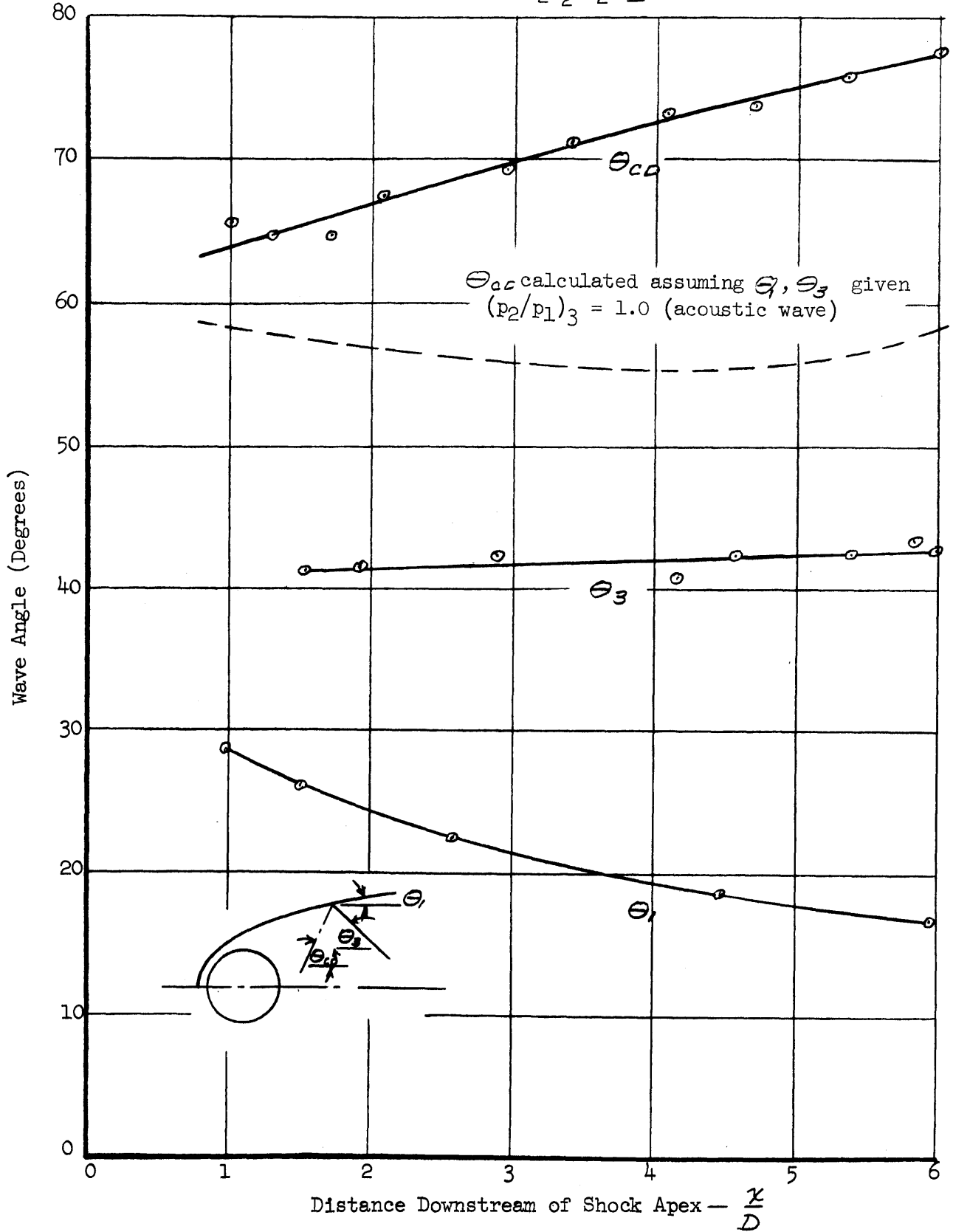
FIGURE 61

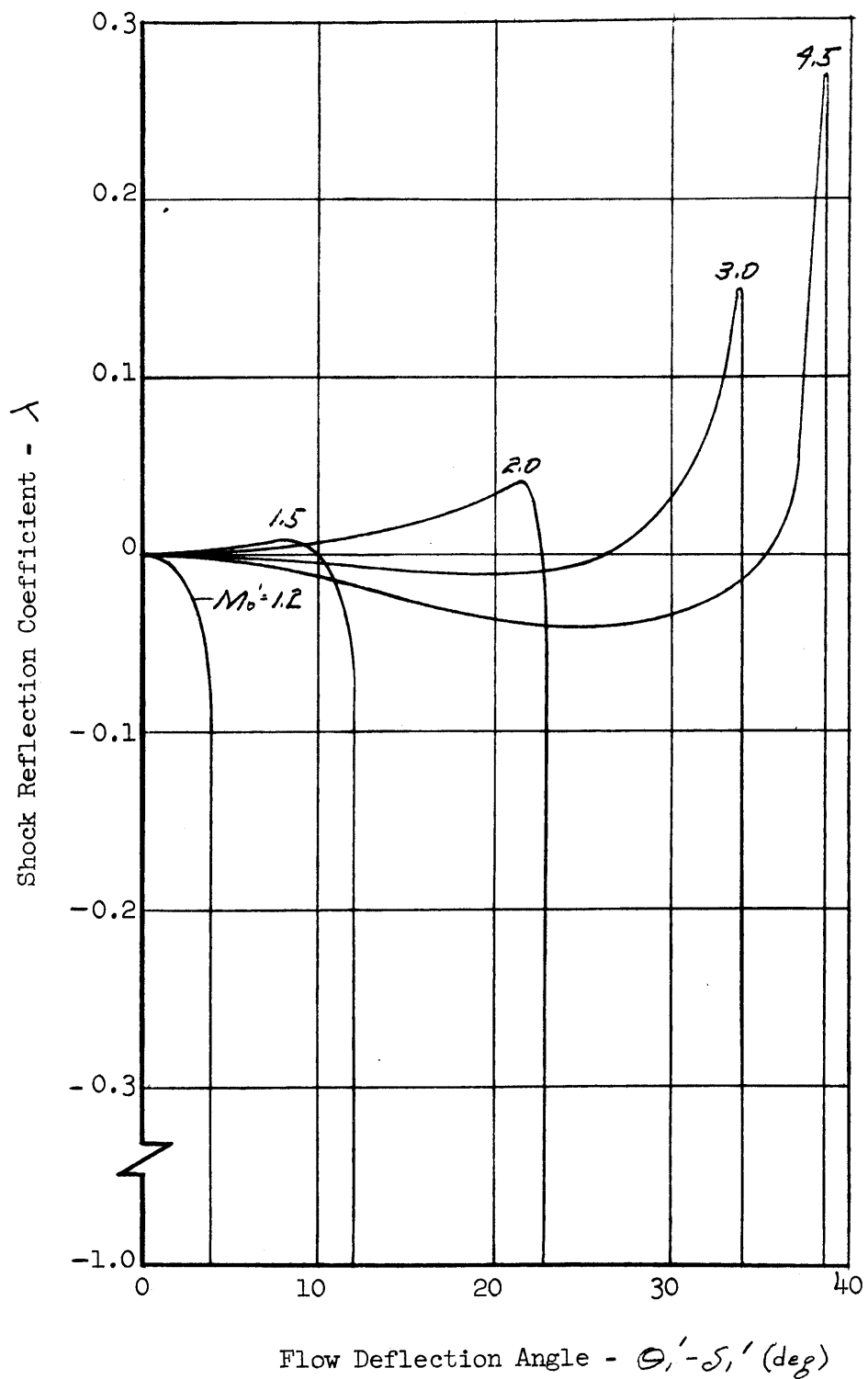SHOCK REFLECTION COEFFICIENT

Note: Data from Ref. 33
$\gamma = 1.4$

Flow Deflection Angle - $\Theta_1' - \delta_1'$ (deg)
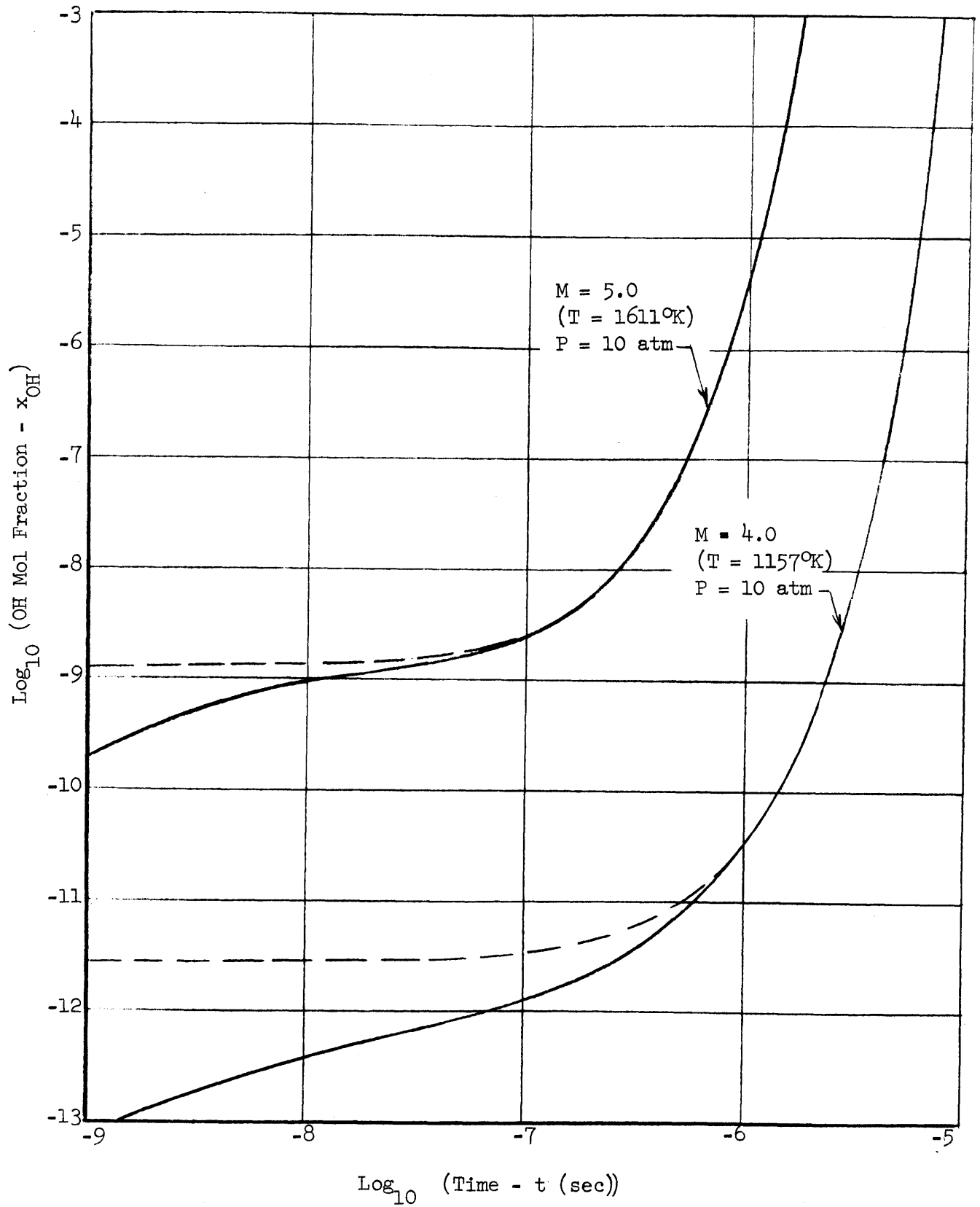
FIGURE 62

OH RADICAL GROWTH DURING INITIATION PERIOD

FIGURE 63

INITIAL AND FINAL OH MOL FRACTIONS

Note: Hydrogen-Air $\bar{\phi}$ = 1.0
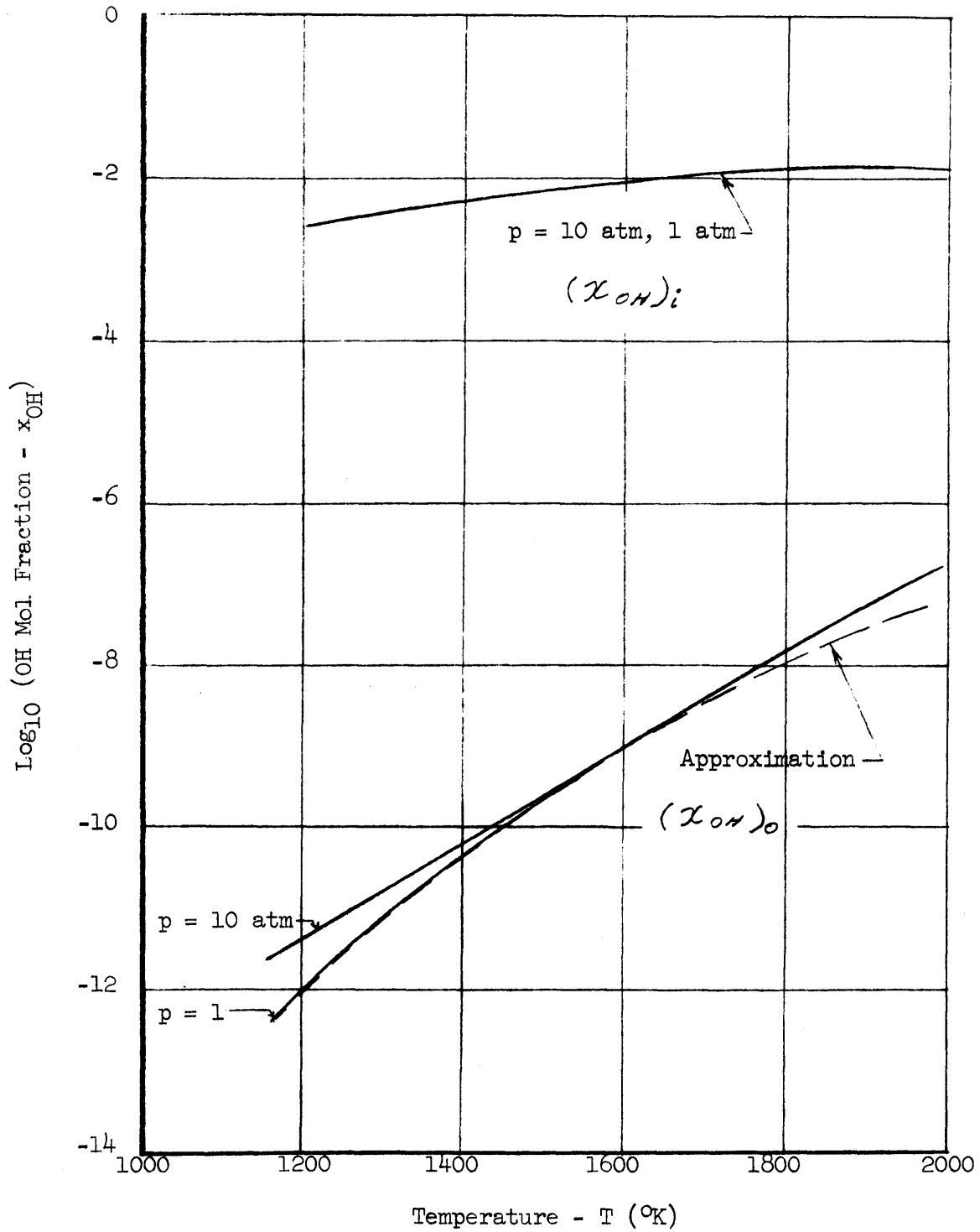
FIGURE 64

INDUCTION PERIOD TIME CONSTANT
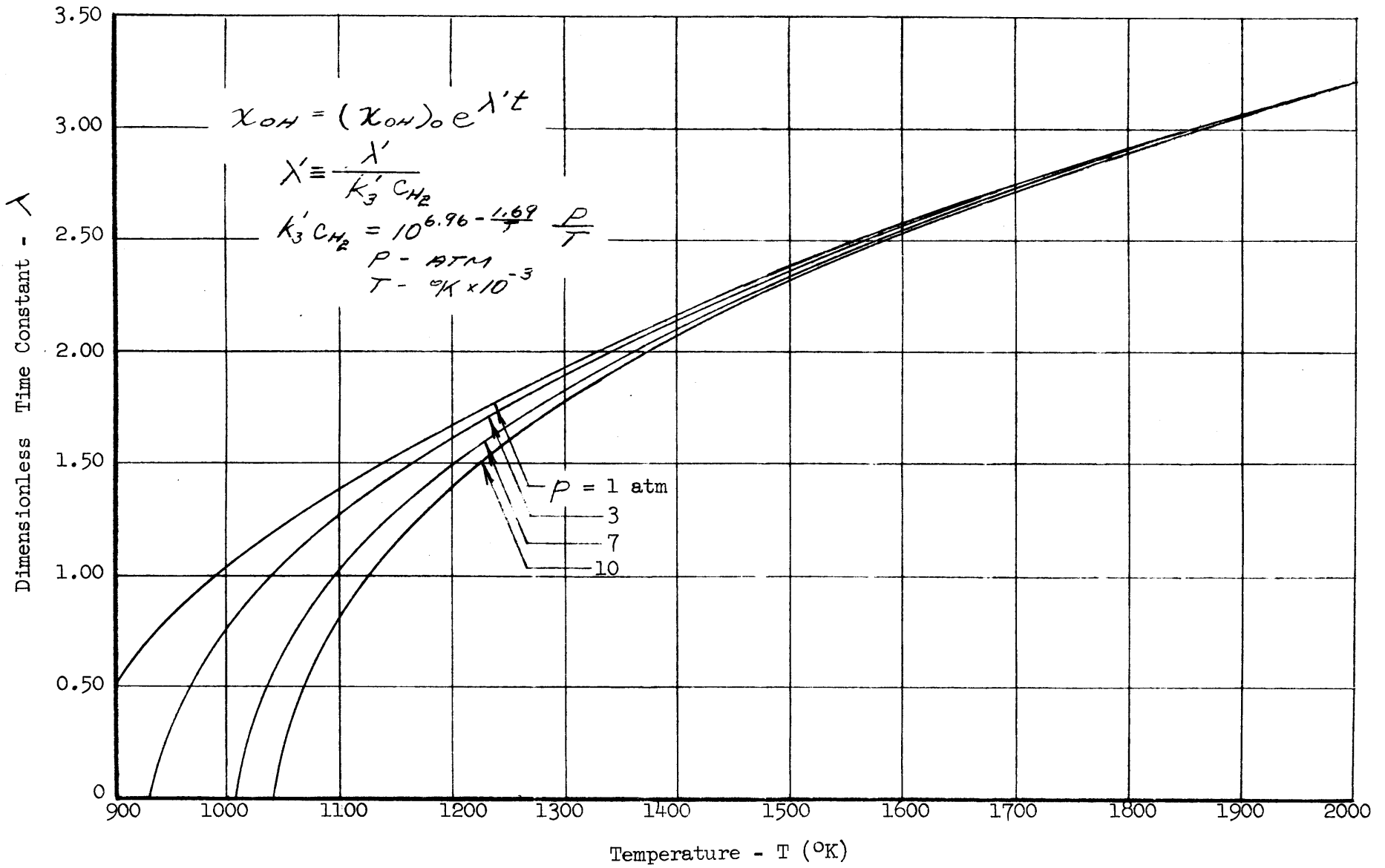HYDROGEN-AIR $\Phi = 1.0$

$$x_{OH} = (x_{OH})_0\, e^{\lambda' t}$$

$$\lambda' \equiv \frac{\lambda'}{k_3'\, c_{H_2}}$$

$$k_3'\, c_{H_2} = 10^{6.96 - \frac{1.69}{T}}\, \frac{P}{T}$$

$$P - ATM$$
$$T - {}^\circ K \times 10^{-3}$$

$P = 1$ atm
3
7
10

Dimensionless Time Constant - λ

Temperature - T ($^\circ$K)

FIGURE 65

OH RADICAL GROWTH DURING INDUCTION PERIOD

Note: Hydrogen-Air $\Phi = 1.0$
Conditions correspond to those behind a
  normal shock with pso = 0.396 atm
End of induction period based on equilib-
  rium of Reaction II
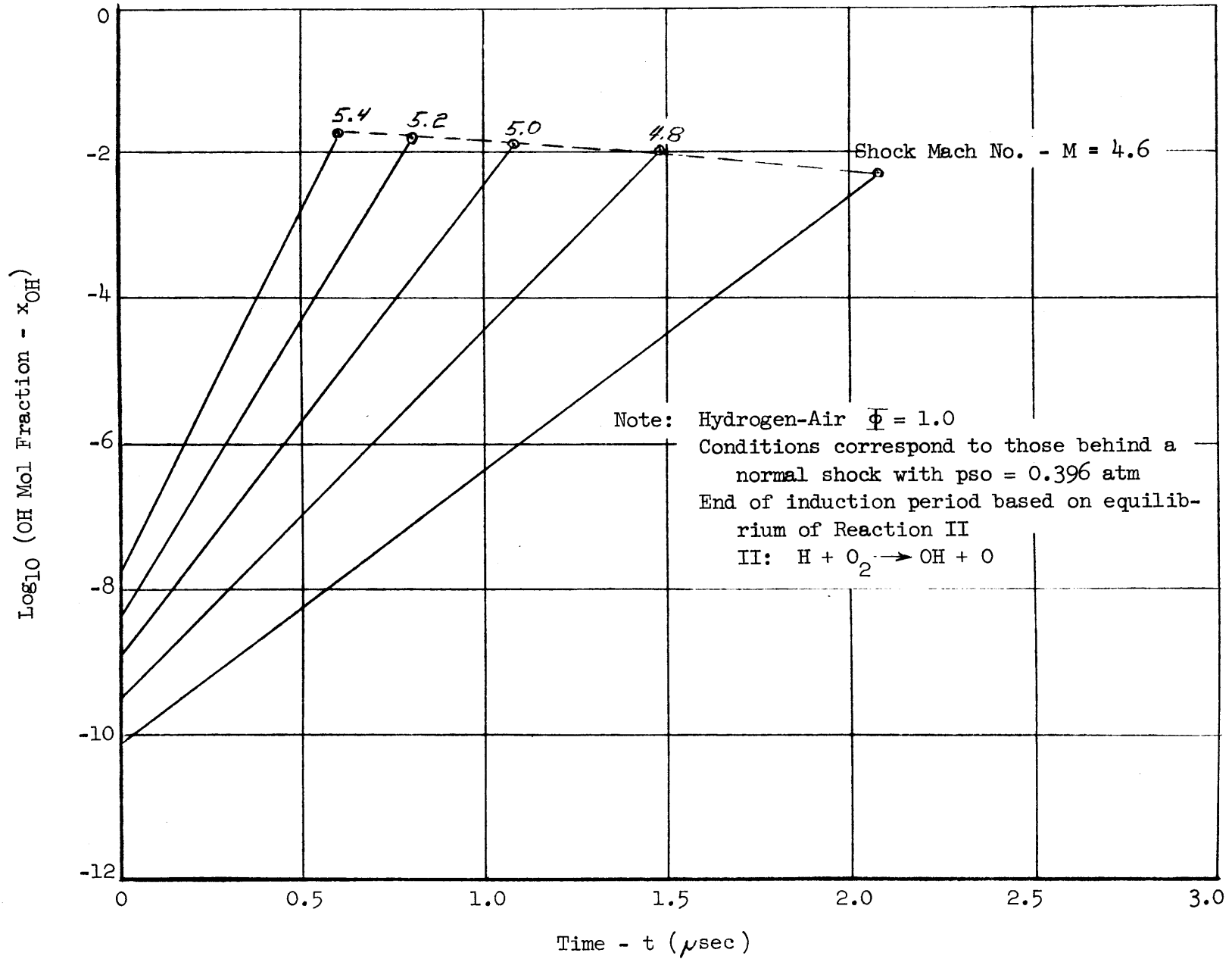 II: $H + O_2 \longrightarrow OH + O$

FIGURE 66

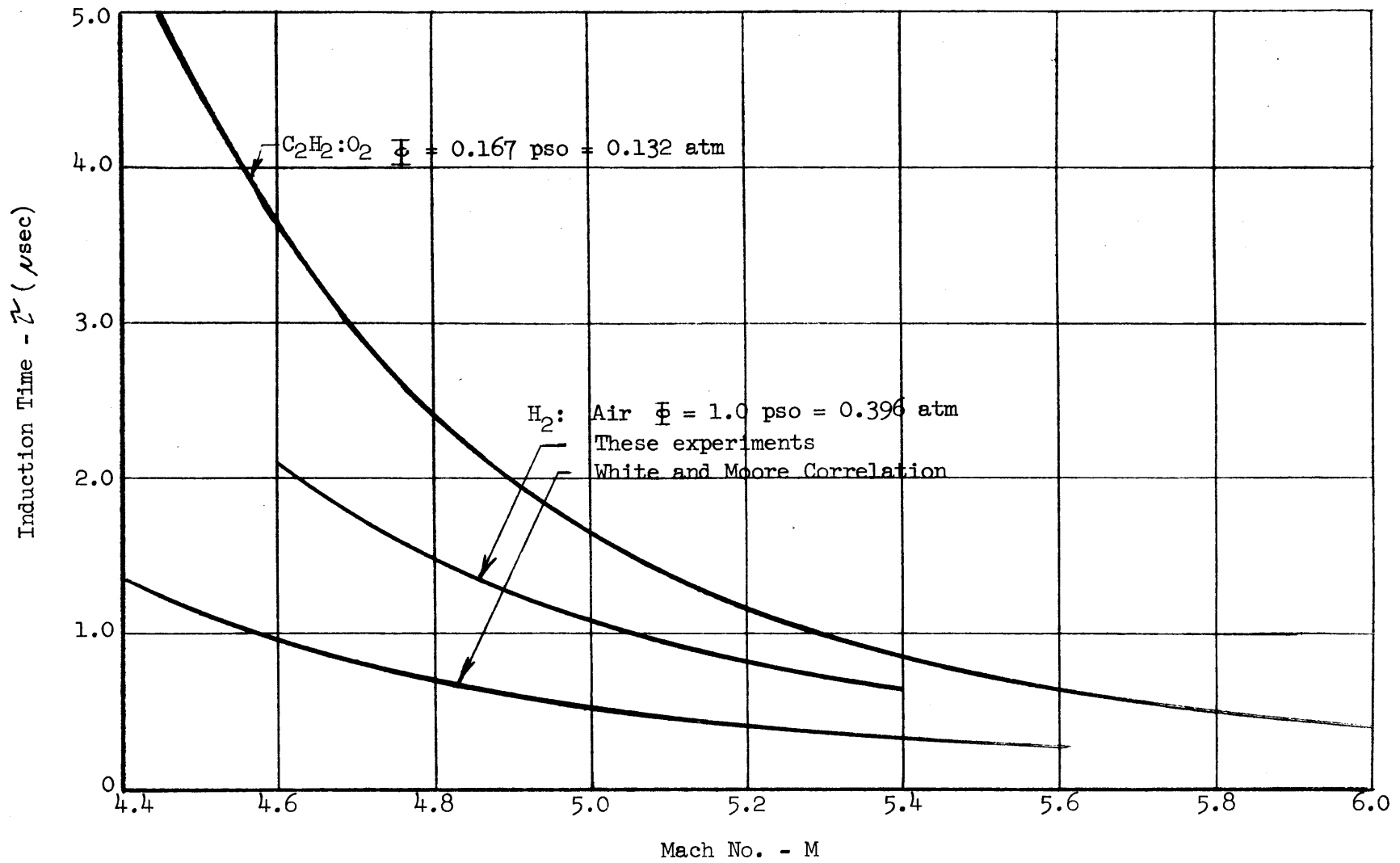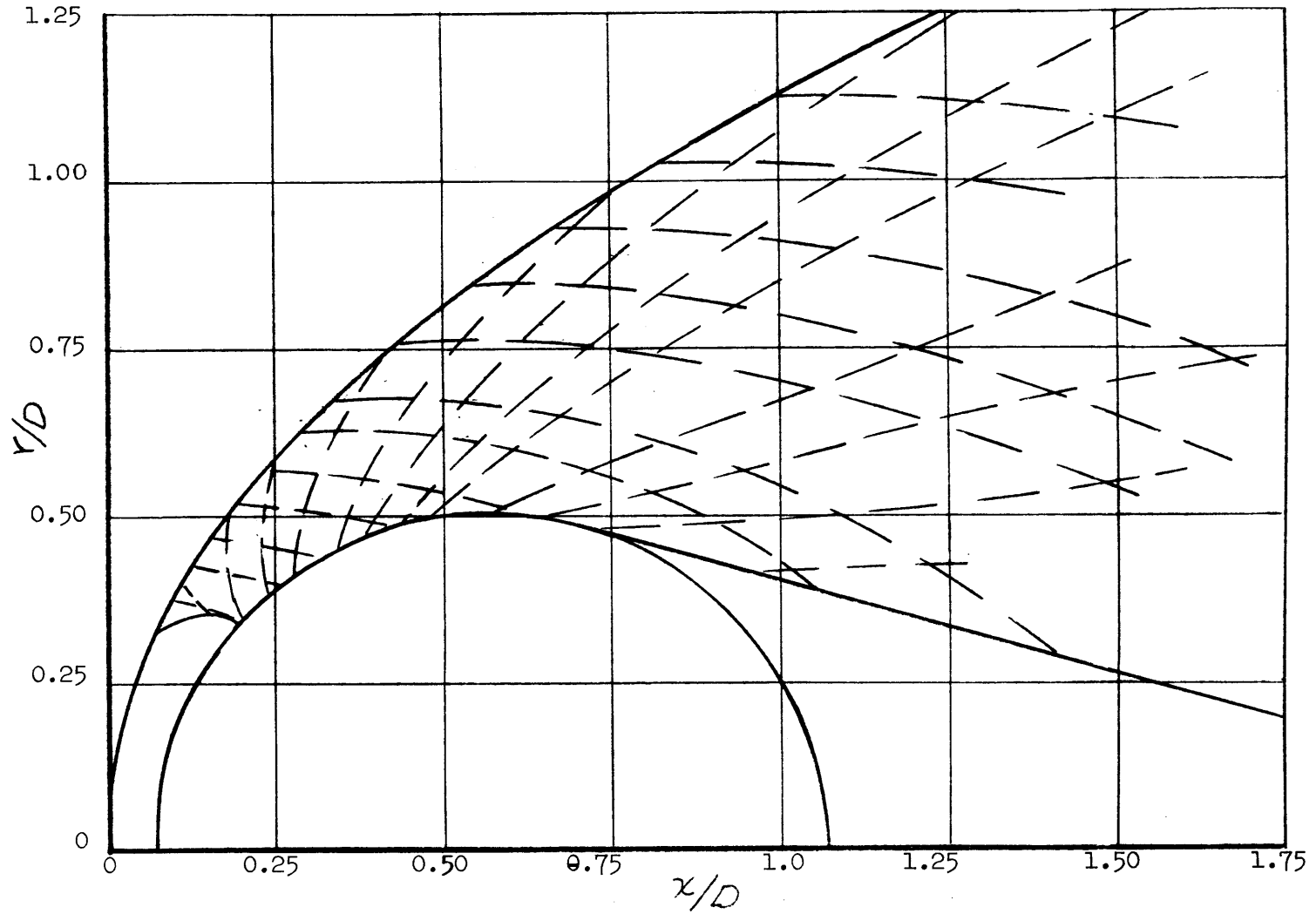INDUCTION TIMES BEHIND NORMAL SHOCK WAVES

Figure 3|

CHARACTERISTIC NET

Note: $M_o = 5.0$
$\gamma = 1.4$

BIOGRAPHICAL SKETCH

John B. McVey was born in Allentown, Pennsylvania on March 29, 1933
and received his secondary school education in the Catasauqua, Pennsylvania
public school system. He entered Lehigh University, Bethlehem, Pennsylvania
in September 1951 and received a B.S. degree in Mechanical Engineering in
June 1955 and an M.S. degree in Mechanical Engineering in June 1956. He
was then employed by the United Aircraft Corporation Research Laboratories
where he performed analytical studies of the performance of hypersonic
air-breathing engines and of aircraft environmental control systems.
He entered M.I.T. in September, 1962 and as a Research Assistant in the
Department of Mechanical Engineering performed a study of the effects of
electric and magnetic fields on the characteristics of laminar flames.
The doctoral thesis program reported herein was begun in October 1963.